ORGANIC MOLECULES ON METAL AND OXIDE SEMICONDUCTOR SUBSTRATES: ADSORPTION BEHAVIOR AND ELECTRONIC ENERGY LEVEL ALIGNMENT

By

CHARLES M. RUGGIERI

A dissertation submitted to the

Graduate School—New Brunswick

Rutgers, The State University of New Jersey

In partial fulfillment of the requirements

For the degree of

Doctor of Philosophy

Graduate Program in Physics and Astronomy

Written under the direction of

Robert A. Bartynski

And approved by

_____

_____

_____

_____

_____

New Brunswick, New Jersey

May, 2016

ABSTRACT OF THE DISSERTATION

Organic Molecules on Metal and Oxide Semiconductor Substrates: Adsorption Behavior and Electronic Energy Level Alignment

By CHARLES M. RUGGIERI

Dissertation Director:

Robert A. Bartynski

Modern devices such as organic light emitting diodes use organic/oxide and organic/metal interfaces for crucial processes such as charge injection and charge transfer. Understanding fundamental physical processes occurring at these interfaces is essential to improving device performance. The ultimate goal of studying such interfaces is to form a predictive model of interfacial interactions, which has not yet been established. To this end, this thesis focuses on obtaining a better understanding of fundamental physical interactions governing molecular self-assembly and electronic energy level alignment at organic/metal and organic/oxide interfaces. This is accomplished by investigating both the molecular adsorption geometry using scanning tunneling microscopy, as well as the electronic structure at the interface using direct and inverse photoemission spectroscopy, and analyzing the results in the context of first principles electronic structure calculations.

First, we study the adsorption geometry of zinc tetraphenylporphyrin (ZnTPP) molecules on three noble metal surfaces: Au(111), Ag(111), and Ag(100). These surfaces were chosen to systematically compare the molecular self-assembly and adsorption behavior on two metals of the same surface symmetry and two surface symmetries of one metal. From this investigation, we improve the understanding of self-assembly at organic/metal interfaces and the relative strengths of competing intermolecular and molecule-substrate interactions that influence molecular adsorption geometry.

We then investigate the electronic structure of the ZnTPP/Au(111), Ag(111), and Ag(100) interfaces as examples of weakly-interacting systems. We compare these cases to ZnTPP on TiO_2(110), a wide-bandgap oxide semiconductor, and explain the intermolecular and molecule-substrate interactions that determine the electronic energy level alignment at the interface. Finally we study tetracyanoquinodimethane (TCNQ), a strong electron acceptor, on TiO_2(110), which exhibits chemical hybridization accompanied by molecular distortion, as well as extreme charge transfer resulting in the development of a space charge layer in the oxide. Thus, we present a broad experimental and theoretical perspective on the study of organic/metal and organic/oxide interfaces, elucidating fundamental physical interactions that govern molecular organization and energy level alignment.

Acknowledgments

I would like to acknowledge the time, effort, care, and consideration put into this work by Robert Bartynski and Sylvie Rangan. Their tireless efforts were essential in the completion of the work presented in this thesis and in helping me grow as a physicist. I would also like to acknowledge the vital insights and contributions from our collaborators, Elena Galoppini, Fernando Flores, José Martínez, and José Ortega, as well as my fellow lab members for helping to keep the lab running smoothly. Additionally, I would like to thank funding sources from the NSF, DOE, as well as the Rutgers Department of Physics and Astronomy for awarding me the inaugural Peter Lindenfeld Graduate Fellowship for the 2015-2016 academic year.

Dedication

This work is dedicated to my amazing wife, my family, and my friends. Their unwavering support and patience during this difficult period gave me the strength and motivation to press on.

Table of Contents

Abstract ii

Acknowledgments iv

Dedication v

List of Tables viii

List of Figures ix

1. Introduction 1

1.1. Role of Organic Molecules in Modern Electronics 1

1.2. Organic/Noble Metal Interfaces 3

1.3. Organic/Oxide Semiconductor Interfaces 8

1.4. Molecular Adsorption Behavior and Self-Assembly 14

1.5. Thesis Outline 17

2. Experimental and Theoretical Methods 19

2.1. Introduction 19

2.2. Ultrahigh Vacuum 20

2.3. Photoemission Spectroscopy 23

2.4. Inverse Photoemission Spectroscopy 34

2.5. Scanning Tunneling Microscopy 40

2.6. Computational Methods 42

3. Molecular Self-Assembly on Noble Metals 45

3.1. Introduction 45

3.2. ZnTPP on Au(111) 47

3.3. ZnTPP on Ag(111) 62

3.4. ZnTPP on Ag(100) 68

3.5. Conclusions . . . 76

4. Molecular Dehydrogenation on Ag(100) and Ag(111) . . . 81

4.1. Introduction . . . 81

4.2. ZnTPP Dehydrogenation on Ag(100) and Ag(111) . . . 83

4.3. ZnPC on Ag(100) . . . 89

4.4. Photoemission and Electronic Structure Calculations . . . 93

4.5. Conclusions . . . 104

5. Organic/Oxide Interfaces: Adsorption Geometry and Electronic Energy Level Alignment . . . 106

5.1. Introduction . . . 106

5.2. ZnTPP on TiO_2(110) . . . 109

5.3. TCNQ on TiO_2(110) . . . 119

5.4. Conclusions . . . 129

Bibliography . . . 131

Appendix A. Hartree-Fock and DFT: Formulation and Calculational Insights . . . 151

A.1. Introduction . . . 151

A.2. The Hamiltonian of a Solid . . . 151

A.3. Hartree Approximation . . . 152

A.4. Hartree-Fock Approximation . . . 153

A.5. Density Functional Theory . . . 155

A.6. Basis Sets . . . 158

A.7. FIREBALL . . . 160

A.8. Quantum ESPRESSO . . . 166

Appendix B. UPS Spectrum Calibration and Work Function Measurement . . . 167

B.1. UPS Calibration: Obtaining Binding Energies . . . 167

B.2. UPS Work Function Measurement: Secondary Electron Cutoff . . . 168

B.3. UPS Molecular States: Subtracting the Substrate Signal . . . 171

Appendix C. IPS Spectrum Calibration . . . 173

C.1. IPS Calibration . . . 173

List of Tables

2.1. Vacuum types from greatest to least pressures. 21

List of Figures

1.1. Skeleton diagrams of (a) ZnTPP and (b) TCNQ molecules. 2

1.2. Schematic energy level diagram of (a) a metal and (b) an isolated molecule. 4

1.3. Pillow effect diagram showing charge density and electrostatic potential energy plots. 5

1.4. Energy level alignment diagram of a clean metal and a metal with adsorbed molecules depicting the pillow effect. 6

1.5. Schottky barrier heights at the organic/metal interface 7

1.6. Energy level alignment of an oxide semiconductor and organic interface. 9

1.7. (a-c) Universal energy level alignment plots of ΔE_H versus $\phi - IE_{org}$. 10

1.8. Universal energy level alignment theory of ionized molecule formation. 11

1.9. Energy level alignment diagram showing molecular orbital energy shifting upon adsorption to an oxide. 12

1.10. Energy level alignment diagram showing oxide band bending upon molecular adsorption. 13

2.1. Rotary vane pump diagram. 22

2.2. Turbomolecular pump diagram. 23

2.3. Ion pump diagram. 24

2.4. Photoemission process diagram. 25

2.5. Electron inelastic mean free path. 26

2.6. Cylindrical mirror analyzer diagram. 31

2.7. Electron multiplier diagram. 33

2.8. Inverse photoemission process energy diagram. 35

2.9. Inverse photoemission experimental chamber diagram. 37

2.10. Spherical diffraction grating diagram. 38

2.11. IPS two-dimensional detector diagram. 39

2.12. IPS detector coordinate determination diagram. 40

2.13. STM diagram. 41

3.1. ZnTPP skeleton molecule. 45

3.2. Clean Au(111) STM. 48

3.3. Clean Au(111) STM and schematic. 49
3.4. ZnTPP/Au(111) STM step edge coverage. 50
3.5. ZnTPP/Au(111) STM sub-monolayer. 51
3.6. ZnTPP/Au(111) STM near-monolayer. 52
3.7. ZnTPP/Au(111) STM step-edge comparison. 53
3.8. ZnTPP/Au(111) STM monolayer high resolution. 54
3.9. ZnTPP/Au(111) monolayer binding model. 55
3.10. ZnTPP/Au(111) STM reorganized high resolution. 57
3.11. ZnTPP/Au(111) reorganized binding model. 58
3.12. ZnTPP/Au(111) STM herringbone periodicity. 59
3.13. Clean Ag(111) STM. 62
3.14. ZnTPP/Ag(111) STM low coverage. 63
3.15. ZnTPP/Ag(111) STM near-monolayer domains. 64
3.16. ZnTPP/Ag(111) STM monolayer high resolution. 65
3.17. ZnTPP/Ag(111) STM monolayer via multilayer desorption. 66
3.18. ZnTPP/Ag(111) binding model. 67
3.19. Clean Ag(100) STM large scale. 69
3.20. Clean Ag(100) STM atomic resolution. 70
3.21. ZnTPP/Ag(100) STM low coverage. 70
3.22. ZnTPP/Ag(100) STM monolayer. 71
3.23. ZnTPP/Ag(100) STM monolayer high resolution. 72
3.24. ZnTPP/Ag(100) binding model for directly-deposited monolayer. 73
3.25. ZnTPP/Ag(100) STM 510K annealed monolayer. 74
3.26. ZnTPP/Ag(100) STM 530K annealed monolayer. 75
3.27. ZnTPP/Ag(100) STM monolayer via 470K multilayer desorption. 76
3.28. ZnTPP/Ag(100) STM monolayer via 500K multilayer desorption. 77
3.29. ZnTPP/Ag(100) binding model of monolayer via multilayer desorption. 78
4.1. Intact and dehydrogenated ZnTPP skeleton models. 81
4.2. Dehydrogenated ZnTPP/Ag(100) STM monolayer annealed to 610K. 84
4.3. Dehydrogenated ZnTPPs on Ag(100) and Ag(111), STM monolayer annealed to 640K with binding model. 85
4.4. Dehydrogenated ZnTPPs on Ag(100), STM images of each type. 86

4.5. Dehydrogenated ZnTPP/Ag(100) STM of ZnTPP chain. 87
4.6. ZnPC and ZnTPP skeleton models. 89
4.7. ZnPC/Ag(100) STM monolayer. 90
4.8. ZnPC/Ag(100) STM high resolution monolayer. 91
4.9. ZnPC/Ag(100) binding model. 92
4.10. ZnPC/Ag(100) STM monolayer annealed to 650K. 94
4.11. ZnTPP/Au(111) UPS and IPS summary. 95
4.12. Intact ZnTPP calculated DOS. 96
4.13. ZnTPP on Au(111) energy level alignment summary. 97
4.14. Substrate screening model depiction. 98
4.15. Dehydrogenated ZnTPP calculated DOS. 99
4.16. ZnTPP on Ag(100) and Ag(111) UPS and IPS summary. 100
4.17. ZnTPP/Ag(100) C1s and SECO measurements. 101
4.18. ZnTPP/Ag(111) C1s and SECO measurements. 102
4.19. ZnTPP on Ag(100) and Ag(111) energy level alignment diagrams. 103
5.1. Energy level alignment of TiO_2(110) with isolated TCNQ and ZnTPP. 108
5.2. ZnTPP/TiO_2(110) STM and binding model. 109
5.3. ZnTPP/TiO_2(110) theoretical binding model. 110
5.4. ZnTPP/TiO_2(110) STM experiment and theory comparison. 111
5.5. ZnTPP/TiO_2(110) XPS core level band bending test. 112
5.6. ZnTPP/TiO_2(110) SECO, UPS, IPS summary. 113
5.7. ZnTPP/TiO_2(110) energy alignment experiment and theory comparison. 114
5.8. ZnTPP/TiO_2(110) calculated DOS. 115
5.9. TCNQ/TiO_2(110) UPS and IPS summary. 120
5.10. TCNQ/TiO_2(110) XPS core level band bending test. 121
5.11. TCNQ/TiO_2(110) adsorption model. 122
5.12. TCNQ/TiO_2(110) theoretical energy alignment at 0K and room temperature. 124
5.13. TCNQ/TiO_2(110) XPS coverage determination. 127
5.14. TCNQ/TiO_2(110) UPS and IPS summary for low temperature multilayer. 128
5.15. TiO_2(110) band edge determination via UPS and IPS. 129
5.16. TCNQ/TiO_2(110) calculated DOS. 130
B.1. Metal and semiconductor occupied states measurements. 168

B.2. Energy level alignment diagram depicting significant values. 170
B.3. SECO of Au(111) sample and spectral width determination. 171
B.4. Energy level alignment depicting important values for metals and semiconductors. . 172
B.5. Substrate spectrum substraction from total spectrum, giving the molecular contribution.172
C.1. IPS spectrum of Au foil. 173
C.2. IPS spectra of Au foil taken at varying electron energies. 175

Chapter 1
Introduction

1.1 Role of Organic Molecules in Modern Electronics

Modern electronic devices such as organic light emitting diodes, organic field effect transistors, and organic solar cells utilize organic molecules in some form. For example, state-of-the-art displays in smart phones consist of organic light emitting diodes. Organic molecules are relatively inexpensive to produce, as they do not contain rare elements, and are commercially available. Each device using organic molecules contains a material on which the organic molecules adhere, such as a metal electrode or a semiconductor substrate. These organic/metal and organic/semiconductor interfaces perform a specific function such as a medium for charge transport or charge injection and greatly influence the overall efficiency of the device. Understanding how these interfaces form and function on the atomic and molecular scale is essential to improving device performance.

A potential first step in learning about the atomic-scale functionality of organic/metal and organic/semiconductor interfaces is to investigate properties of organic molecules adsorbed to metal and semiconductor substrates in a clean environment, separate from the device. In this way, crucial information regarding the organic interactions with the metal or semiconductor substrate can be extracted without interference from other device components. Particularly important characteristics are the electronic structure and adsorption behavior of the organic molecule when adsorbed to the metal or semiconductor substrate. Investigating the electronic structure of the organic/metal and organic/semiconductor system provides insight into charge transport barriers and charge injection barriers at the interface. Atomic-scale properties at the interface such as the molecular conformation to the substrate surface and the orientation of the molecule upon adsorption to the surface are obtained by studying the adsorption behavior. This information can then be used to accurately model charge transport pathways across the interface.

Rather than studying a specific organic/metal or organic/oxide interface from a particular device, we focus on two molecules found in nature exhibiting several interesting functions that have been applied to many modern electronic devices. The first molecule is known as zinc tetraphenylporphyrin, shown as Figure 1.1a, which is in the porphyrin class of molecules. Porphyrins are found in nature

with a wide variety of functions from light absorbers in chlorophyll[138] to electron sources/sinks during electron transfer or redox chemistry and even oxygen transport in hemoglobin[30]. Additionally, porphyrins are extremely versatile molecules that can be utilized in the laboratory to probe a variety of topics such as supramolecular chemistry[11], biomimetic redox and rearrangement catalysis[202], and molecular electronics such as organic light emitting diodes[63], field-effect transistors[12, 42, 78, 82, 127, 161, 190, 193], and dye-sensitized solar cells[70, 110, 134]. We also discuss tetracyanoquinodimethane (TCNQ) which is easily reduced to its radical anion and is primarily of interest as a charge transfer salt with high electrical conductivity. TCNQ (strong electron acceptor) combined with the tetrathiafulvalene molecule (TTF, a strong electron donor) crystallizes into a salt that forms a one-dimensionally stacked polymer that is comprised of cations of the donors (TTF) and anions of the acceptors (TCNQ). This complex is an organic semiconductor that shows electrical conductivity similar to that of metals.[97, 175, 183]

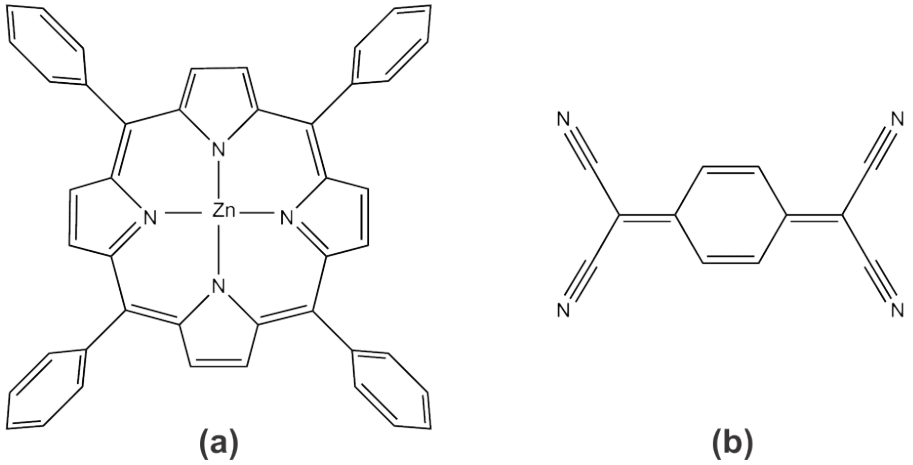

Figure 1.1: Skeleton diagrams of (a) ZnTPP and (b) TCNQ molecules.

We start our investigation with the adsorption behavior of ZnTPP molecules on a weakly-interacting metal surface to promote molecular self-assembly. Noble metal substrate surfaces are generally known for their low reactivity with a wide variety of adsorbates. As such, they provide an ideal surface on which to study fundamental molecular adsorption properties including molecular self-assembly. In this work, we investigate the adsorption behavior and self-assembly characteristics of ZnTPPs on three noble metal surfaces: Au(111), Ag(111), and Ag(100). We systematically compare the influence of subtle differences in molecule-surface interaction strength using Au(111) and Ag(111). Additionally, we investigate the influence of substrate surface atomic symmetry on the ZnTPP adsorption behavior using Ag(111) and Ag(100). From this work, we hope to gain insight

into the relative influence of molecule-substrate and molecule-molecule interactions on the adsorption behavior of the ZnTPPs. The information gathered from this study can then be extended to other weakly-interacting organic/metal interfaces.

Electronic structure properties of organic/metal and organic/semiconductor interfaces determine charge injection and charge transport barriers across the interface. In general, these aspects of the interface depend on the particular molecule and metal or semiconductor used, as some organic/metal and organic/semiconductor pairings can strongly interact such that their combined electronic structure is vastly different from their isolated electronic structures. Due to such interactions, it is difficult to predict the electronic behavior of a particular organic/metal and organic/semiconductor interface. Insight into charge transport and charge injection energy barriers is gained by studying the electronic energy level alignment at these interfaces. To help understand subtle influences of the molecule-substrate interaction on the electronic energy level alignment, we first measure the weakly-interacting ZnTPP/Au(111), ZnTPP/Ag(111), and ZnTPP/Ag(100) interfaces. Then, to better understand the impact of a more reactive substrate on the electronic structure of the molecule, ZnTPP is studied on the wide-bandgap transition metal oxide semiconductor, TiO_2(110). This case functions as an intermediate interaction strength molecule-substrate system, whereas ZnTPP/noble metals represents the minimally-interacting regime. Finally, we study TCNQ/TiO_2(110) which is a strongly-interacting system due to the combination of the high electron affinity of TCNQ with the n-type doping nature of TiO_2(110). In each case, the impact of molecule-molecule and molecule-substrate interactions on the electronic structure and electronic energy level alignment are discussed. From this broad perspective we hope to obtain a more general understanding of the fundamental physical interactions that influence the charge transport and charge injection properties at organic/metal and organic/semiconductor interfaces.

1.2 Organic/Noble Metal Interfaces

To understand the electronic energy level alignment at the interface of an organic semiconductor and a metal, it is first necessary to understand the two materials individually. Figure 1.2a shows an energy level diagram of a typical metal with occupied states, unoccupied states, Fermi energy (E_F) or the energy of the highest occupied states, and work function (ϕ). ϕ is defined as the amount of energy required to excite an electron from the highest occupied state energy, E_F, to the vacuum level (VL) with zero kinetic energy, where the VL is the electrostatic potential energy of the vacuum just outside of the metal. Figure 1.2b shows a schematic energy level diagram of a typical molecule with the highest occupied molecular orbital (HOMO), lowest unoccupied molecular orbital (LUMO), and

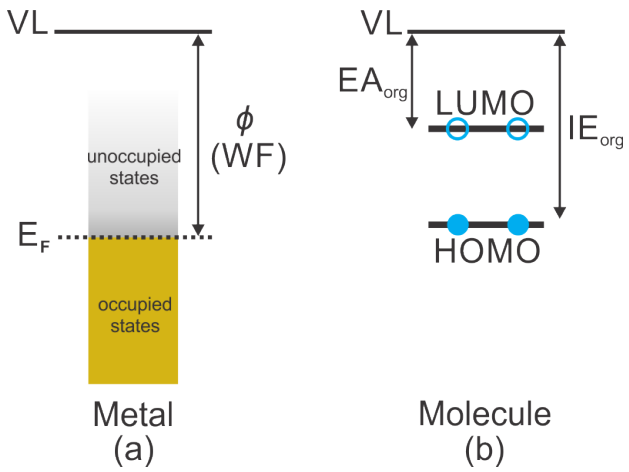

Figure 1.2: Schematic energy level diagram of (a) a metal and (b) an isolated molecule.

VL, as well as the ionization energy (IE_{org}) and electron affinity (EA_{org}). IE_{org} is defined as the energy required to excite an electron from the HOMO to the vacuum just outside the molecule with zero kinetic energy, and EA_{org} is the change in energy of an electron at the VL with zero kinetic energy upon relaxing to the LUMO.

Figure 1.3a shows for a clean metal substrate surface the electron density as a function of distance from the surface, $\rho(z)$. When the bulk metal is cut to form this surface, the charge density that previously formed atomic bonds must come to an equilibrium density distribution in the absence of the atomic bonds that were broken. The surface atoms equilibrate after the charge density near the surface rearranges to the distribution shown in the figure, in which the electron charge density decays exponentially into the vacuum and leaves a positive charge density just inside the substrate surface. This charge rearrangement creates a dipole layer at the metal surface, which can be approximated by a dipole layer of finite length as shown in the lower portion of Figure 1.3a. Then, the approximate electrostatic potential energy felt by an electron close to the surface is described by $V(z)$ shown at the bottom of Figure 1.3a.

When an organic molecular layer adsorbs to the metal surface, the metal surface dipole changes due to the molecular presence. The electron density trailing into the vacuum is effectively repelled by approaching molecules. Compared to the electron density distribution of the clean metal, the electron density with adsorbed molecules decreases in the space just outside the metal surface but increases just inside the metal, resulting in a net negative charge just inside the metal surface and a net positive charge just outside the metal. This phenomenon is known as the push-back or pillow effect.[93, 98, 178] The interfacial dipole due to the pillow effect is shown in Figure 1.4 as Δ^{pillow} for an organic monolayer adsorbed to a metal substrate. In this figure, VL_1 represents the vacuum level of the clean metal surface, and VL_2 the vacuum level of the system after a monolayer

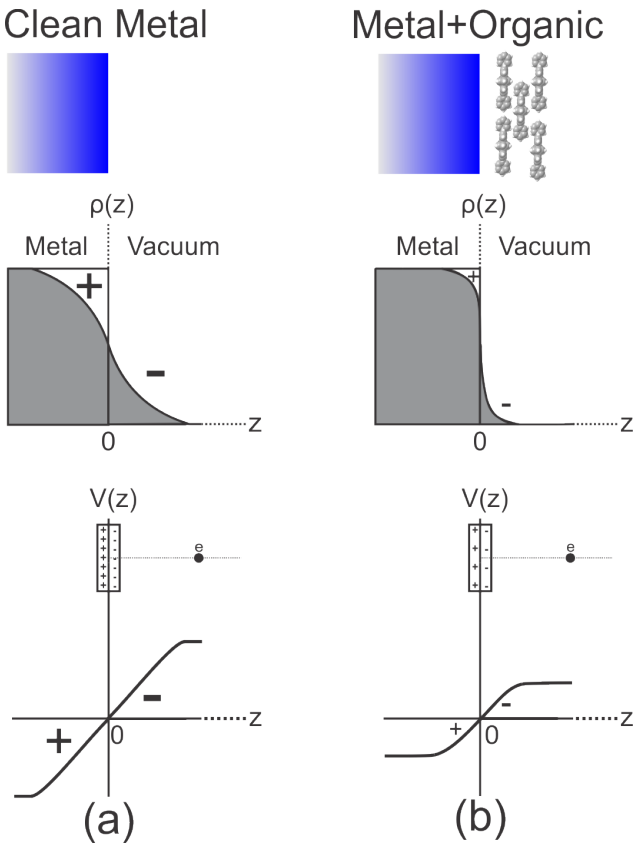

Figure 1.3: Diagram showing the electron density as a function of distance from the substrate surface, $\rho(z)$, with the metal/vacuum interface at z=0 for (a) a clean metal surface and (b) an organic layer adsorbed to a metal surface. Also shown is the potential energy as a function of distance from the surface, $V(z)$, felt by a test electron due to a simplified dipole layer of fixed length.

of molecules have adsorbed to the surface. The pillow effect is a common occurrence and is the primary contributor to the development of an interfacial dipole in weakly-interacting organic/metal interfaces. The interfacial dipole produced by the pillow effect varies with the system and the coverage of molecules, however typical values are around 1.0 eV.

Figure 1.5 shows an energy alignment diagram after molecules make contact with a metal substrate. In this diagram, Φ_B^n and Φ_B^p are the electron and hole injection barriers, respectively. Additionally the total interfacial dipole is shown as Δ, which in principle includes other effects beyond the pillow effect, such as charge transfer. The direction of charge flow at the metal/organic interface can be described by the barrier heights: a low electron injection barrier, Φ_B^n, promotes electron flow from the metal to the molecule LUMO, and a low hole injection barrier, Φ_B^p, promotes electron flow from the HOMO to the metal unoccupied states, or, equivalently, hole flow from the metal to the molecule HOMO. The electron and hole barrier heights can be written in terms of the metal work

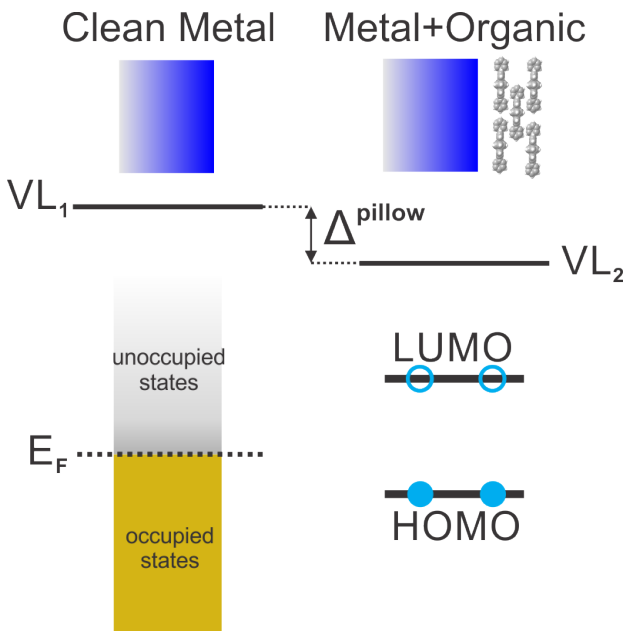

Figure 1.4: Energy level alignment diagram of a clean metal substrate and a metal surface covered with adsorbed molecules. The change in charge density at the interface due to the pillow effect, Δ^{pillow}, causes a decrease in vacuum level from VL_1 to VL_2, which are the vacuum levels of the clean surface and after adsorbing molecules, respectively.

function (ϕ), organic ionization energy (IE_{org}), and electron affinity (EA_{org}) as:

$$\Phi_B^n = \phi - \Delta - EA_{org}, \tag{1.1}$$

$$\Phi_B^p = IE_{org} + \Delta - \phi, \tag{1.2}$$

Equation 1.2 can be rewritten in terms of Φ_B^n as:

$$\Phi_B^p = E_{HOMO-LUMO} - \Phi_B^n, \tag{1.3}$$

where $E_{HOMO-LUMO}$ is the difference between the organic ionization energy and electron affinity, $IE_{org} - EA_{org}$.

Upon contact there are two types of electron flow that depend on the relative energy level alignment of a metal with a given semiconductor, including semiconducting organic molecules if the layer of organics is sufficiently thick. An Ohmic contact is such that an applied voltage produces a current that depends linearly on the voltage. On the other hand, a Schottky barrier follows non-Ohmic behavior (i.e., non-linear current response to an applied voltage). In terms of the barriers defined by equations 1.1 and 1.2, barriers having a value much greater than kT, where k is the Boltzmann constant and T the temperature, are typically Schottky barrier contacts. For smaller barrier values, such as on the order of kT, the interface is described by an Ohmic contact. According to the Schottky-Mott rule, the electron barrier height at the metal/semiconductor interface is predicted to

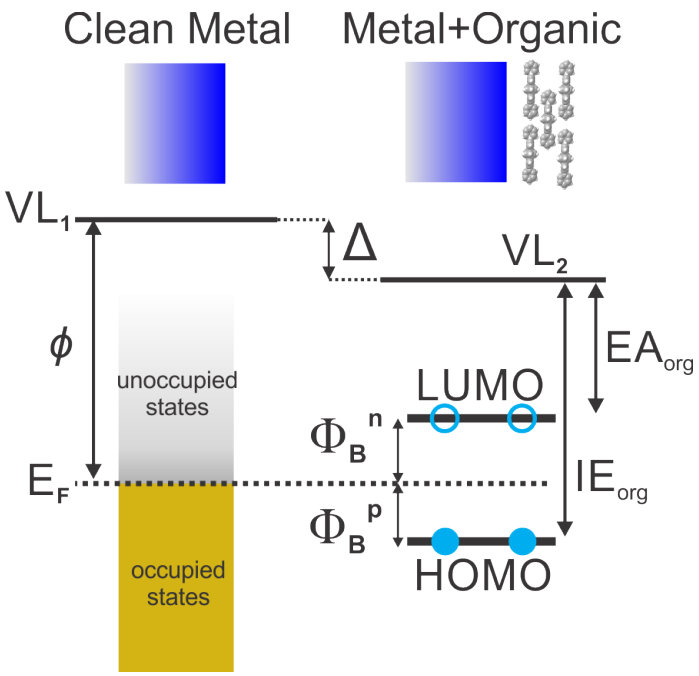

Figure 1.5: Energy level alignment diagram of a metal/organic interface showing Schottky barrier heights for electron (Φ_B^n) and hole (Φ_B^p) injection. Here, Δ represents the total interfacial dipole after the organics make contact with the metal surface.

be proportional to the difference of the metal work function and the semiconductor electron affinity. In practice, most metal/semiconductor interfaces do not follow this rule because it does not account for localized states that can be filled or emptied, and exist at the semiconductor surface within the band gap. These states arise either due to chemical bonding with the metal surface (metal-induced gap states) or due to charge defects or vacancies at the semiconductor surface prior to metal contact (surface states). Such states can absorb a large quantity of charge from the metal and become pinned to the metal Fermi level which causes a deviation from the Schottky-Mott rule.

In this work, molecular layers are typically in the monolayer range which is far too small a quantity to exhibit bulk semiconductor electronic behavior. For example, band bending is only possible when a sufficient density of charge carriers is available in the material, such as in a thick organic layer or organic layers that are good semiconductors. In interfaces where sub-monolayer, monolayer, or only a few multilayers of organic molecules are adsorbed onto a substrate in UHV, band bending is generally not expected in the organic layer. Our experiments involve sub-monolayer to multilayers of molecules, and while the presence of band bending is checked for multilayers it has not been observed for any of the systems discussed in this thesis. Therefore, for the measurements of organics on metals presented here, a flat-band picture is assumed for the metal/organic interfaces, such as that shown in Figure 1.5.

1.3 Organic/Oxide Semiconductor Interfaces

Organic/oxide interfaces were first used in organic light-emitting diodes after the discovery that some oxides decrease the hole-injection barrier when inserted between a metal anode and an organic compound.[174] This landmark discovery decreased the contact resistance in organic electronic devices and greatly improved efficiencies as a result. The ability of two materials to efficiently transfer charge strongly depends on the relative energy alignment of the electron donor and acceptor states, which in a molecule are the HOMOs and LUMOs, respectively. A schematic electronic energy level alignment diagram for the organic/oxide interface is shown as Figure 1.6. In this diagram, ϕ is the oxide work function, E_F is the Fermi level located at mid-gap for an intrinsic semiconductor at zero temperature, IE is the oxide ionization energy, and EA is the oxide electron affinity. For the organic, IE_{org} is the ionization energy and ΔE_H is the binding energy of the HOMO, or the energy difference between the HOMO and Fermi level of the system. Note that the vacuum levels of the two materials are different due to a presumed interfacial dipole, Δ, that may be the result of charge transfer, charge redistribution within the molecule, or chemical bonding for example. Additionally, for organic/oxide interfaces characterized by significant charge redistribution upon contact, band bending in the oxide can occur which further complicates the energy alignment. To make use of the full potential of organic/oxide interfaces, interactions that strongly effect energy level alignment must be understood.

To date, there exist several empirical models describing organic/oxide interface energy level alignment. Models have been proposed describing the interfacial pinning parameter[81, 88], induced density of interface states[177, 179], charge neutrality level[177, 178], integer charge transfer model[32, 171], pillow effect[93, 98, 178], and interfacial dipole[46]. Another empirical model with a universally-applicable scope was developed by investigating the role of the oxide work function and the organic ionization energy. Each of several molecules with a range of ionization energies were adsorbed onto many oxide semiconducting substrates with a wide range of work functions. An empirical trend was found by measuring the HOMO binding energy ΔE_H as a function of the energy difference between the oxide work function ϕ and the ionization energy of the organic IE_{org}, where ΔE_H and IE_{org} were measured directly for the organic/oxide system such as that shown in Figure 1.6b.[67] Figure 1.7a-c show the data acquired from this work for each of three molecules on top of many substrates. Figure 1.7d combines the data from 1.7a-c into one plot and rescales the x-axis to be the energy difference between the oxide work function and the ionization energy of the organic, $\phi - IE_{org}$.

To help understand the concept behind the energy alignment behavior observed in the empirical

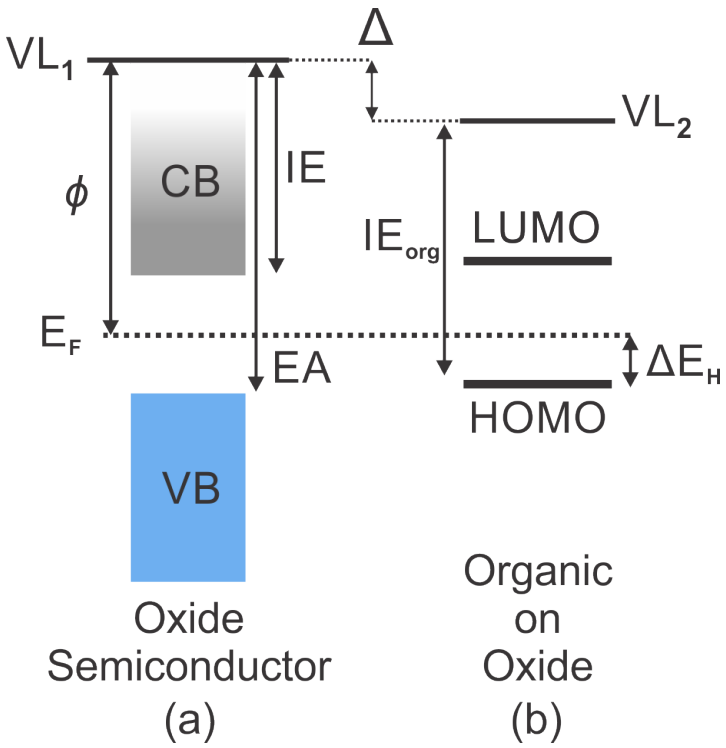

Figure 1.6: Energy alignment diagram depicting (a) a typical oxide semiconductor and (b) an organic molecule, with relevant energy levels indicated.

model described above, energy alignment diagrams representing each energy alignment regime, $\phi > IE_{org}$ and $\phi < IE_{org}$, are shown in Figure 1.8. The left diagram represents an organic molecule with ionization energy IE_{org} adsorbed to Oxide 1 with work function ϕ_1 with $\phi_1 < IE_{org}$, and the right diagram represents the same organic molecule on Oxide 2 with work function $\phi_2 > \phi_1$, such that $\phi_2 > IE_{org}$. These diagrams assume that IE_{org} has the same value when adsorbed to both oxides, which is an acceptable assumption as the systems studied in this work are weakly-interacting, meaning the gas-phase molecular electronic structure is not significantly altered upon adsorption to the oxide. On Oxide 1, with $\phi_1 < IE_{org}$, the Fermi level, $E_F(1)$, resides above IE_{org} and within the HOMO-LUMO energy gap of the molecule. In this case the neutral molecular species, M^0, is thermodynamically favorable and no charge transfer occurs between the molecule and oxide, so the component of the total interface dipole due to charge transfer will be zero. Then, ΔE_H will change linearly with ϕ until $\phi = IE_{org}$, as shown experimentally in the left side of each Figure 1.7a-d. That is, since ΔE_H is the HOMO binding energy, or the energy of the HOMO with respect to the Fermi level of the oxide, if the oxide work function is increased (for example by substituting an oxide with larger work function) then ΔE_H will decrease by the same amount up until the Fermi level aligns with IE_{org}.

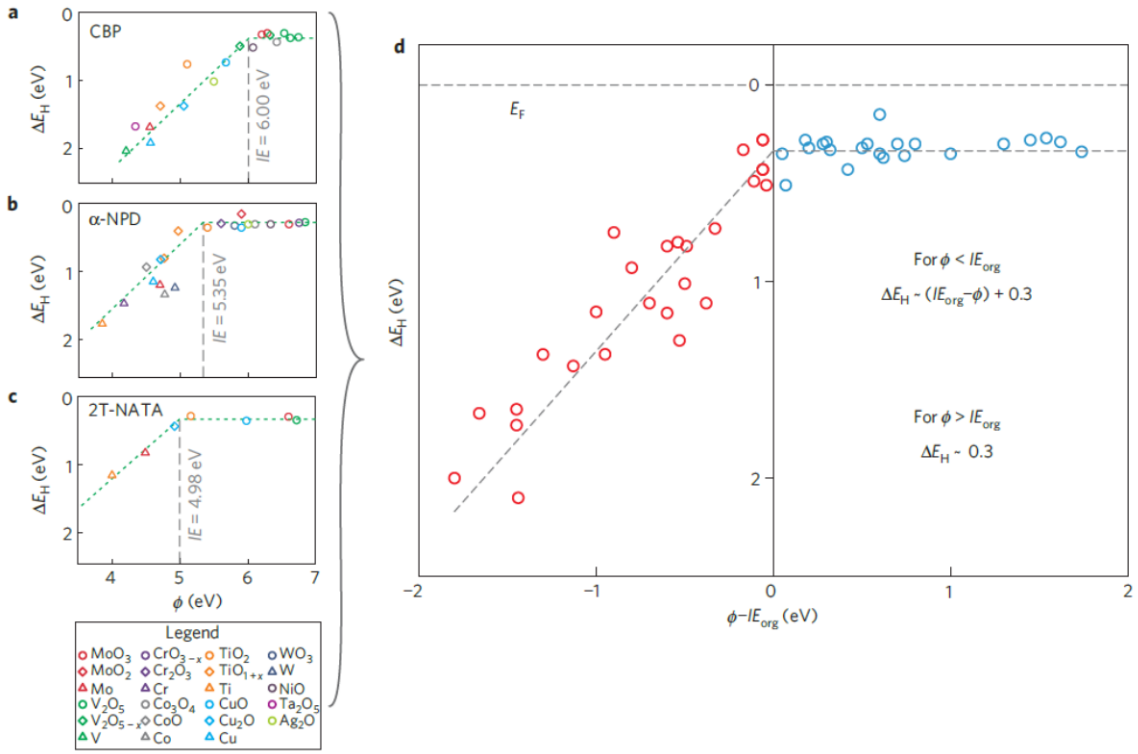

Figure 1.7: (a-c) Plots of HOMO binding energy (ΔE_H) versus substrate work function for a set of three molecules on a series of transition-metal oxide and transition-metal substrates. (d) Universal plot combining plots a-c and rescaling the x-axis to $\phi - IE_{org}$. The dashed line for $\phi > IE_{org}$ was determined by calculating the average ΔE_H value, and the dashed line for $\phi < IE_{org}$ was determined using a least-squares regression fit, with the restriction that $\Delta E_H = 0.3$ when $\phi = IE_{org}$. Adapted from reference [67].

In the regime where $\phi > IE_{org}$, shown for the molecule on Oxide 2 in the right energy alignment diagram of Figure 1.8, electron transfer from the organic to Oxide 2 is thermodynamically favorable and the positively charged molecular species, M^+, will form. As ϕ is further increased, the concentration of positively charged molecules increases. This creates an interfacial dipole Δ that is proportional to the change in ϕ and results in the HOMO binding energy, ΔE_H, remaining constant as ϕ is increased, shown experimentally in the right sides of Figures 1.7a-d. This is an example of Fermi level pinning since the HOMO-E_F energy separation is fixed. In general, the observed trend is governed by the equilibration of the substrate electron chemical potential with the oxidation/reduction potential of the adsorbed molecule.

The above empirical model describes a trend for weakly-interacting organic/oxide semiconductor interfaces, however in cases of strong organic-oxide interactions that involve chemical bonding, large molecular deformation upon adsorption, or large quantities of charge transferred upon adsorption, the energy alignment behavior becomes more complicated and system-dependent. Figures 1.9a and

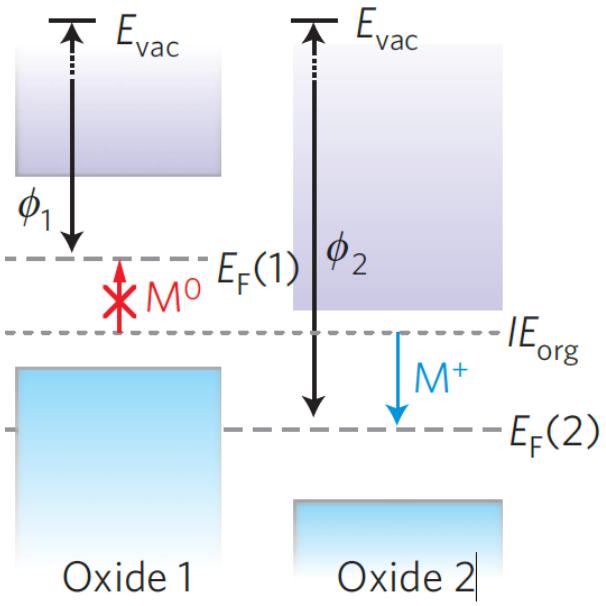

Figure 1.8: Energy level alignment of a molecule of ionization energy IE_{org} with two oxide semiconductors of different Fermi levels, $E_F(1)$ and $E_F(2)$, and work functions ϕ_1 and ϕ_2, with $\phi_2 > \phi_1$. For $\phi > IE_{org}$, ionized molecule species M^+ form by transferring electrons from the molecule to the oxide. For $\phi < IE_{org}$, assuming the oxide Fermi level resides within the HOMO-LUMO gap of the molecule, the neutral molecular species, M^0, is stable. Adapted from reference [67].

b show the relative energy level alignment of an isolated n-type oxide semiconductor and an isolated organic molecule, respectively, with vacuum levels aligned since there is no charge transfer or charge redistribution. If we consider the molecule adsorbed onto the semiconductor at zero temperature, chemical bonding occurs between the molecule and substrate surface. This bonding alters the electronic structure of the isolated molecule to stabilize the system such that the new HOMO and LUMO binding energies shift by an amount Δ^{bond}, shown in Figure 1.9c. In this case, such chemical bonding can cause molecular distortion and subsequent charge reorganization, which results in the formation of an interfacial dipole, Δ^{ID}, shown in Figure 1.9d. In the charge reorganization picture shown at the top of the figure representing a side view of a distorted molecule after bonding to an oxide surface, a positive interfacial dipole forms, $\Delta^{ID} > 0$, which shifts the orbital energies toward lower binding energies, counteracting part of the chemical bonding effect. It is important to note that VL_2 serves to keep track of all molecular orbital energy shifts, in this case the sum of the energy shifts due to bonding and charge reorganization from molecular distortion, $\Delta^{bond+ID}$. However only the interfacial dipole, Δ^{ID}, effects vacuum level measurements of the system. For example, in the case shown in Figure 1.9d, the measured vacuum level for this organic/oxide system will be greater than the vacuum level measured on the clean oxide substrate by an amount Δ^{ID}.

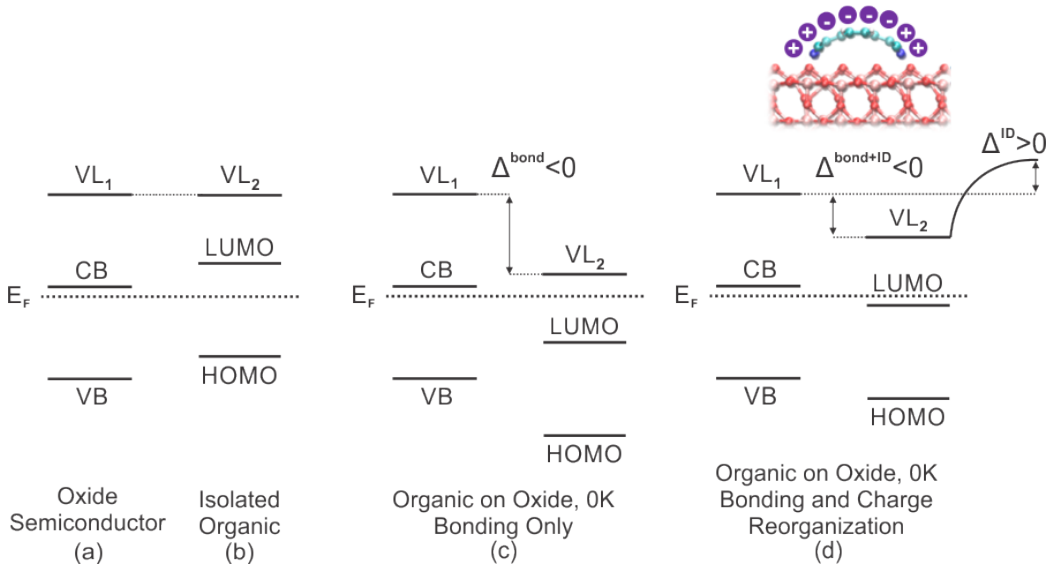

Figure 1.9: Energy level alignment of (a) an isolated n-doped oxide semiconductor and (b) an isolated organic molecule, before adsorption to the oxide. (c) Energy level alignment for the organic/oxide system at zero temperature showing an energy shift of Δ^{bond} due to organic-oxide chemical bonding, and (d) after including an interfacial dipole due to charge reorganization, Δ^{ID}.

In addition to the above considerations at zero temperature, at elevated temperature band bending in the oxide can occur. Figures 1.10a and b show the relative energy level alignment of an isolated n-type oxide semiconductor and an isolated molecule with large electron affinity, respectively, at room temperature prior to adsorption. The n-doping of the semiconductor results from localized filled oxygen impurity states just below the Fermi level. A dynamic equilibrium is established at room temperature in which electrons are thermally excited from localized impurity states into the delocalized conduction band and relax back into the emptied oxygen impurity states, indicated by the blue arrow. After the molecule comes into contact with the semiconductor surface at room temperature, thermally excited delocalized electrons in the semiconductor conduction band can fill the molecular LUMO, shown in Figure 1.10c. What was once a dynamic equilibrium in the isolated semiconductor is now disrupted by semiconductor conduction band electrons filling the molecular LUMO rather than relaxing into emptied oxygen impurity states. In effect, there are not enough electrons to fill the unoccupied impurity states since they are now filling the molecular LUMO, causing positive charge accumulation at the semiconductor surface. This positive charge accumulation results in a space charge layer that bends the oxide bands upward by an energy V^{SCL}. Furthermore, a large positive interfacial dipole develops due to charge transfer to the molecular LUMO, Δ^{CT}, shifting the vacuum level upward. The occurrence of band bending strongly depends on the energy alignment characteristics of the organic and oxide, as well as the charge carrier density of the oxide itself. In the relatively extreme band bending case shown in Figure 1.10a-c, the organic

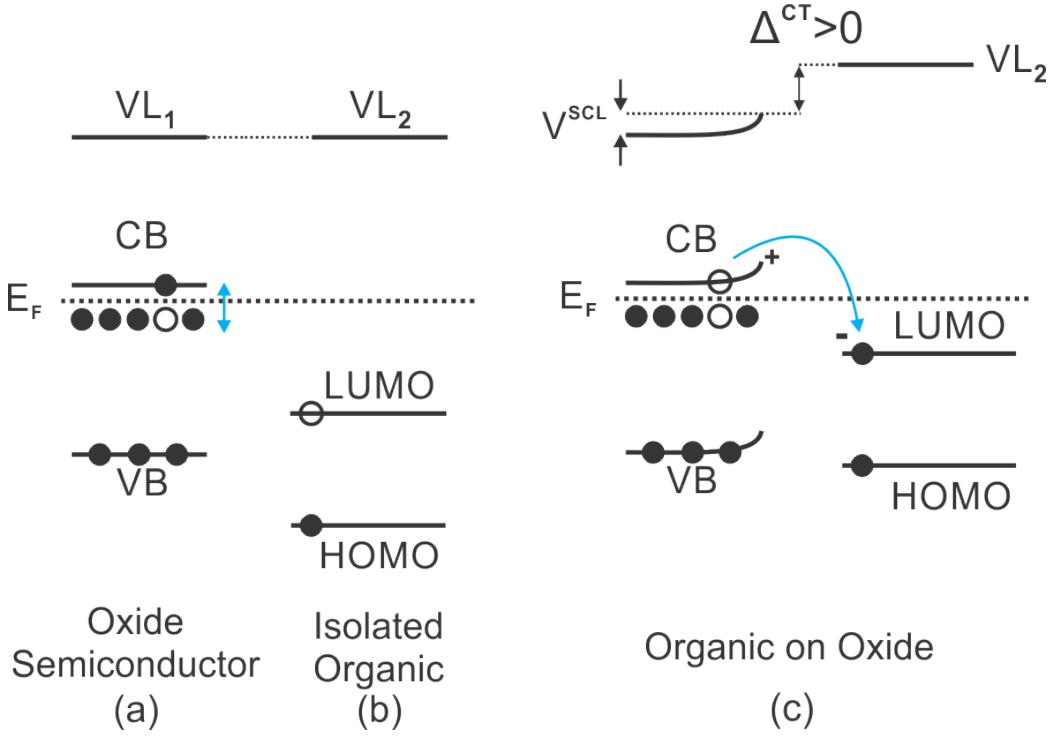

Figure 1.10: Energy level alignment of (a) an isolated n-doped oxide semiconductor and (b) an isolated organic molecule with high electron affinity, before adsorption to the oxide at room temperature. (c) Energy level alignment for the organic/oxide system at room temperature showing electron transfer from the oxide conduction band to the partially-filled organic LUMO, and the subsequent development of a space charge layer of energy V^{SCL} and oxide band bending. The interfacial dipole due to charge transfer, Δ^{CT}, is positive in this case, since electrons are transferred from the oxide to the organics which raises the energy levels of the organics in the process.

molecule has a large electron affinity such that the LUMO situates below the oxide Fermi level, creating a thermodynamically favorable environment for electron transfer from the oxide conduction band to the organic LUMO.

Despite these many efforts toward understanding aspects of the energy alignment problem, there is no definitive first-principles model to predict the final energy alignment of organic/oxide semiconductor interfaces. Weakly-interacting organic/oxide interfaces tend to follow the empirical trend of Figure 1.7. However more strongly interacting interfaces exhibiting large charge transfer, oxide band bending, chemical bonding, and large changes in the molecular conformation upon adsorption do not follow this trend and have not yet been studied enough to find universal behavior. In this work, we study two molecules with different ionization energies and electron affinities adsorbed to the wide bandgap semiconductor, TiO_2(110). One molecule, ZnTPP, represents a weakly-interacting case in which no chemical bonding is expected to develop with TiO_2. The other molecule, TCNQ, has a large electron affinity compared to ZnTPP, and since TiO_2(110) is typically an n-type semiconductor with E_F just 0.2-0.3eV below the conduction band minimum, we expect strong interactions and

charge transfer at the interface. By studying organic/oxide interfaces at extremes of interaction strength, we hope to gain insight into the electronic processes that are most influential to the final electronic energy level alignment and how these electronic processes compare for such drastically different cases.

1.4 Molecular Adsorption Behavior and Self-Assembly

In organic electronic devices, optimizing energy level alignment at the organic/oxide or organic/metal interface is an important issue, however there is also molecular aggregation and arrangement to consider. For example, a given organic/oxide interface can exhibit desirable energy alignment characteristics for a device, however in practice the organics may aggregate on the surface into disordered clumps potentially decreasing the charge transfer efficiency or light absorbtion probability, for example. It would be beneficial to understand how molecules arrange on a given substrate and to take advantage of these behaviors and acquire the best possible organization. Additionally, experimentally studying molecular adsorption geometry provides a starting point for electronic structure calculations of the molecule/substrate system. An experimentally determined binding geometry can help to calculate charge transfer, charge redistribution, and molecular conformation at the molecule/substrate interface with greater ease and accuracy than assuming a binding geometry in the absence of experimental insight. The calculated electronic structure, charge redistribution, and molecular conformation behavior at the interface can then be used to model electronic energy level alignment, which can then be compared to experimental results. Furthermore experimental studies of molecular adsorption behavior places limits on the relative strengths of intermolecular interactions and molecule-substrate interactions. For example, for an organic/metal system in which isolated molecules are observed and there is no long range molecular assembly, one can deduce that the molecule-substrate interaction is likely stronger than the molecule-molecule interaction. Alternatively, if molecules readily self-assemble into large structures and are never observed in an isolated state, one can infer that the molecule-molecule interaction dominates the molecular adsorption behavior. The study of molecular adsorption behavior provides many benefits that improve the overall understanding of molecule/substrate interface interactions.

A first step in considering molecular organization is to understand molecular ordering in the monolayer regime since the monolayer interacts most directly with the substrate and can influence the growth of multilayers. Due to ease of surface preparation and low chemical reactivity with a broad range of molecular species, noble-metal substrates typically are used when studying fundamental interactions that govern molecular self-assembly. Many molecules self-assemble into highly ordered

arrays at room temperature on noble metal substrates (e.g., TPP[13, 20, 33, 35–38, 52, 74, 128, 143, 144, 146, 156, 160, 163, 173, 186, 187, 194, 197, 199], TCNQ[65, 182, 184, 196]). While molecules can exhibit ordered structures on oxide semiconductor surfaces, the organization behavior tends to be dominated by strong molecule-substrate interactions.[133, 137, 140, 170]

Self-assembly of molecules on noble metal surfaces is the result of many competing interactions. When a single molecule adsorbs to the surface it experiences a molecule-substrate attraction that can range from relatively weak van der Waals interactions to strong covalent bond formation and hybridization or even molecular dissociation. Furthermore, molecules that remain intact can deform from their gas-phase conformation, for example by bending or twisting upon adsorption. Molecules can also be highly mobile atop the substrate surface if the molecule-substrate interaction is sufficiently weak. Increasing the coverage beyond a single molecule to near-monolayer introduces the potential for intermolecular interactions in addition to molecule-substrate interactions. In cases where attractive intermolecular interactions are present, for example through van der Waals forces, mobile molecules can assemble into highly ordered, weakly-bound structures (i.e., no covalent bonding between molecules). Noble metal surfaces such as Au and Ag are typically used to study self-assembly of molecular monolayers since they tend to interact weakly with many adsorbates. In the self-assembly and adsorption behavior work presented in this thesis, ZnTPPs, a weakly-interacting molecule, is adsorbed to the noble metal Au(111), Ag(111), and Ag(100) surfaces. Self-assembly is likely to occur in these systems, and the molecule-substrate interaction is strong enough to influence the molecular adsorption behavior, but not so strong as to completely inhibit molecular organization. Additionally, as mentioned earlier, these three systems enable a comparison of the role of molecule-substrate interaction in the organization process by investigating two different metals of the same surface symmetry (Au(111) and Ag(111)), as well as two surfaces of the same metal however with different symmetry (Ag(111) and Ag(100)).

To study self-assembly at organic/metal interfaces, it is essential to obtain sub- or near-monolayer molecular coverage. Two UHV molecular monolayer preparation techniques typically used are known as direct deposition and multilayer desorption. For direct deposition, molecules are sublimated in UHV until a monolayer is reached, however this method is inherently inconsistent since deposition rates of sublimation sources are difficult to control. For multilayer desorption, a multilayer of molecules is deposited, followed by annealing to desorb weakly-bound overlayers until the monolayer is reached. While both methods are acceptable monolayer preparations, the incorporation of heat and the presence of multilayers in the multilayer desorption method can effect the system such that the monolayer may not be equivalent to that obtained from direct deposition. Molecular monolayers can take forms that are metastable which reorganize when thermal energy is introduced to the

system via annealing. Such metastable organizations typically involve significant contributions from both the molecule-substrate and molecule-molecule interactions. Additionally, annealing the system permits a reorganization not only of the molecular layer, but also of the substrate surface atoms until a lower energy molecule-substrate configuration is reached. In the self-assembly work presented here, we investigate the stability of a ZnTPP monolayer on Au(111), Ag(111), and Ag(100) as a function of annealing temperature. In addition, monolayers obtained from direct deposition and multilayer desorption are compared for each case.

Annealing the organic/metal system at too high a temperature induces molecular desorption or decomposition and loss of long range intermolecular order. However, there exists an intermediate molecular behavior at annealing temperatures slightly below what would decompose the molecule, in which the weakest atomic bonds of the molecule are broken due to the added thermal energy. For example, molecular dehalogenation and dehydrogenation can occur during such intermediate anneals. In dehalogenation, relatively weak carbon-halogen bonds are broken creating active covalent bonding sites on the molecule at the previous location of the halogen. Dehydrogenation is a similar process to dehalogenation, except C-H bonds are broken typically at higher temperature anneals than dehalogenation due to the stronger carbon-hydrogen bond. These bond-breaking processes provide a controllable pathway to creating covalently bonded molecular chains and networks starting from self-assembled van der Waals organizations. In a recent work, TPP molecules with iodine and bromine atoms bonded to opposing phenyl ligand sites of the molecule self-assemble into a net-like organization on a Au(111) surface via van der Waals interactions. Due to the different bond dissociation energies of C-I and C-Br, the C-I bonds are controllably broken by annealing the system to 120°C, and the newly active bond sites of adjacent molecules create C-C covalent bonds. Since the C-I bonds were located on opposing phenyl groups, molecules covalently bond into chains. Subsequently annealing the system to 250°C induces C-Br bond breaking along a direction perpendicular to the C-I bonds and creates two more active bond sites per molecule. Adjacent molecular chains can then bond together to form a 2D covalent molecular net.[105]

Similarly, dehydrogenation is a pathway to create long-range 2D covalent order starting from self-assembled van der Waals molecular networks. In this case, inducing hydrogen loss in the molecule by breaking C-H bonds via annealing creates active bond sites. However, dehydrogenation can cause intra- and intermolecular rehybridization, where in the former C-H bond breaking creates new C-C bonds within a single molecule that result in an altered molecular conformation, which has been observed for TPPs[52, 143, 194]. Molecular dehydrogenation and subsequent conformational changes is a relatively new field of study and has so far only been shown for isolated molecules in the sub-monolayer range. In this work, we study dehydrogenation of ZnTPPs on Ag(100) and

Ag(111) starting from intact highly-ordered monolayers obtained via multilayer desorption and show that intermolecular effects significantly contribute to the dehydrogenation process. Furthermore, we show that ZnTPP chains form by the dehydrogenation process, indicating the potential for forming molecular networks using this method.

1.5 Thesis Outline

The work in this thesis concentrates on obtaining a better understanding of the fundamental physical interactions governing energy level alignment and molecular self-assembly at organic/metal and organic/oxide interfaces by investigating both the electronic structure of the interface as well as the molecular adsorption geometry on the substrate for select organic/metal and organic/oxide systems. We seek to simplify the systems by minimizing contaminants and using atomically flat single-crystal substrates in UHV while adsorbing molecules via *in situ* vapor deposition to ensure clean interface preparation. Furthermore, the electronic behavior upon adsorption is directly probed for both occupied and unoccupied states and combined with molecular adsorption geometry to create a comprehensive description of the system. Such experimental characterization of electronic energy level alignment correlated with binding geometries greatly facilitates the development of theoretical models that can give insight into fundamental physical interactions at organic/metal and organic/oxide interfaces. Once a given system is understood at the level of fundamental interactions perhaps global trends can be extrapolated for similar systems, and in this way we hope to develop a more broadly applicable understanding of organic/metal and organic/oxide interfaces.

This thesis is organized in the following way. In Chapter 2, experimental and theoretical techniques are discussed, including ultraviolet, X-ray, and inverse photoemission spectroscopies (UPS, XPS, IPS, respectively), scanning tunneling microscopy (STM), as well as density functional theory (DFT) calculational methods to aid in interpreting the experimental results. In Chapter 3 a complete study of the self-assembly behavior of a ZnTPP monolayer obtained via direct deposition and multilayer desorption on Au(111), Ag(111), and Ag(100) is presented. The stability and evolution of the monolayer as a function of annealing temperature is also investigated for each surface. In Chapter 4, ZnTPP dehydrogenation reaction on the Ag(111) and Ag(100) surfaces is investigated using STM and photoemission spectroscopies, and compared to dehydrogenation of the zinc phthalocyanine molecule to elucidate important aspects of the dehydrogenation behavior. In Chapter 5, electronic energy level alignment of a ZnTPP monolayer on Au(111), Ag(111), and Ag(100) is discussed which represents a relatively weakly-interacting organic/metal interface. These results are interpreted with DFT calculations of the gas-phase ZnTPP density of states. Additionally, energy level alignment of a

ZnTPP monolayer on the transition metal oxide semiconductor $TiO_2(110)$ is studied and compared to a more strongly interacting system, $TCNQ/TiO_2(110)$. These two molecules span a wide range of electron affinities and ionization energies as well as molecule-substrate interaction strengths. Where applicable, the experimental results are interpreted with the aid of gas-phase DFT density of states calculations. In addition, collaboration with theoretical physicists permits a deeper understanding of the fundamental interactions that govern the energy level alignments through advanced DFT electronic structure calculation methods of the organic/oxide system. These calculations permit an interpretation of the final energy alignment and a decomposition of the interfacial dipole that develops at the organic/oxide interface due to contributions from molecule-substrate charge transfer, charge redistribution due to molecular conformation to the substrate surface, as well as intermolecular effects within the monolayer plane. In this way, we present a broad experimental and theoretical perspective on the study of organic/metal and organic/oxide interfaces and elucidate fundamental physical interactions that govern energy level alignment and molecular organization.

Chapter 2
Experimental and Theoretical Methods

2.1 Introduction

Precise experimental work on organic molecules adsorbed to clean, atomically flat surfaces of noble metals and transition metal oxide semiconductors is accomplished in the extremely clean environment of ultrahigh vacuum (UHV). Working in a UHV environment permits an examination of the interactions between the molecule and substrate surface of consideration without the addition of contaminants present in ambient air. Furthermore, the spectroscopic measurements used in this work involve electrons traveling distances of millimeters to centimeters from sample to detector(or from electron gun to sample if the electron is the incident particle), and the electrons must travel to the detector or the sample without inelastically scattering. The lower the pressure of the environment through which the electrons travel, the greater distance they can travel before colliding with ambient gaseous atoms or molecules. Additionally, some of the measurement systems themselves must be operated in UHV due to the application of high voltage to either the electron or photon source or the detector, which would arc and damage the systems at higher pressures. Experiments were performed primarily in two separate UHV systems, one of which houses both direct and inverse photoemission capabilities, and another which houses a scanning tunneling microscope. Both chambers were equipped with sample-cleaning tools, such as an argon-ion sputter source and sample heater for annealing, as well as molecular sublimation sources. The substrate surface is cleaned in UHV and exposed to the molecules of interest via sublimation deposition without ever leaving the UHV environment, creating an extremely clean and pure system with minimal contaminants. This permits a thorough investigation of fundamental physical and chemical interactions that would otherwise be masked by impurities in systems exposed to ambient air.

The experimental techniques used in this work include direct photoemission such as ultraviolet photoemission spectroscopy (UPS) and X-ray photoemission spectroscopy (XPS), inverse photoemission spectroscopy (IPS), and scanning tunneling microscopy (STM). This suite of measurements permits a complete characterization of the system's electronic structure (occupied and unoccupied electronic states) and topography of both the clean substrate surfaces and molecular monolayers or

sub-monolayers. Through these experiments the adsorption geometry of the organic molecules on the substrate surface is linked to the electronic structure. This experimental pairing is well-suited for theoretical analysis; for example one can propose a binding model for the molecules on top of the substrate surface and calculate the theoretical density of states of the individual molecule as well as the monolayer system to be compared with that measured in direct and inverse photoemission spectroscopies.

Density functional theory methods are used to perform electronic density of states calculations to determine the electronic structure of both the occupied and unoccupied states of the isolated molecule as well as a single molecule and a monolayer of molecules on the substrate surface, and the results of these calculations are compared to experiment. The GAMESS software package is used for density of states calculations for the isolated or gas-phase molecules, as well as for determining the shape of the electronic states and their distribution across the molecules. Our collaborators on several of the works presented in this thesis used the FIREBALL code and Quantum ESPRESSO code suite to obtain the energy-minimized adsorption geometry of the molecule on the substrate surface, to model the electronic energy level alignment of the system, and also to simulate STM images. FIREBALL and Quantum ESPRESSO incorporate the effects of the substrate surface on the system at zero temperature and room temperature to characterize charge transfer between molecule and substrate, as well as charge reorganization within the molecule or substrate. This theoretical analysis permits the assignment of specific charge reorganization and charge transfer processes to phenomena such as molecular distortion, overlap of electronic states between substrate and molecule, and intermolecular effects in the monolayer that are absent for a single molecule on the surface, and also elucidates the impact of these phenomena on the experimental spectra. Thus, density of states calculations provide valuable insight into the fundamental physical interactions between the molecules and the substrate, as well as the molecules with other molecules in the monolayer where applicable. What follows in this chapter is a discussion of how UHV conditions are obtained, an explanation of the direct- and inverse-photoemission processes and equipment used, a brief review of scanning tunneling microscopy, as well as a discussion of the theoretical methods used in this work.

2.2 Ultrahigh Vacuum

There are many levels of vacuum that can be achieved in the laboratory, as shown in Table 2.1. Different levels of vacuum may be appropriate for a particular experiment depending on the vulnerability of the experimental technique or the system being studied to the surrounding gas pressure.

The mean free path of a particle (e.g., atom or molecule) is the average distance travelled before scattering or interacting with another particle. At atmospheric pressures the mean free path is on the order of nanometers, but in UHV it is on the order of kilometers. For example, high vacuum or better is necessary for any measurements requiring electrons to travel unimpeded to a sample or a detector that is typically millimeters to centimeters away from the source. At atmospheric pressure, the electron would inelastically scatter many times, altering its kinetic energy, and it would likely not reach the detector at all. Furthermore, in experiments requiring pristine surfaces UHV is necessary to maintain a clean surface for the duration of time required to perform experiments. At atmospheric pressures a monolayer of adsorbates can form on a pristine surface in a matter of nanoseconds. This time scale is far too short to perform meaningful experiments, however in ultrahigh vacuum that time increases to hours or even days.

Table 2.1: Vacuum types from greatest to least pressures.

Vacuum Quality	**Pressure (Torr)**	**Particles/cm^3**	**Mean free path**
Atmospheric pressure	760	10^{19}	$\sim$ 1 nm
Low vacuum	760 - 25	10^{19}-10^{16}	0.1-100 μm
Medium vacuum	25 - 10^{-3}	10^{16}-10^{13}	0.1-100 mm
High vacuum	10^{-3} - 10^{-9}	10^{13}-10^{9}	10 cm - 1 km
Ultra high vacuum	10^{-9} - 10^{-12}	10^{9}-10^{4}	1 km - 10^5 km
Extremely high vacuum	$< 10^{-12}$	$< 10^{4}$	$> 10^5$ km

UHV pressures in our stainless steel vacuum chambers are achieved using multiple stages of pumping. The first pumping stage uses a rotary vane pump to give a rough vacuum on the order of 1-10 mTorr. This is occasionally referred to as a rough pump since it achieves at best a rough or medium vacuum. A diagram showing the operating principle of the rotary vane pumping cell is shown as Figure 2.1. As the blue circle (2) rotates counterclockwise in place, the vanes extend and contract against the cell walls (1) through the action of the spring (4). Gas is forced in (blue arrows) via vacuum suction due to the constantly increasing volume until the maximum volume is reached, at which point the vane has rotated beyond the inlet (green arrow). This volume of gas is then pushed by the vane behind it toward the outlet (red arrow) and effectively pumped out of the system. The ratio of exhaust pressure (atmospheric pressure) to base pressure (the lowest pressure obtained at the pump inlet) is referred to as the compression ratio. The base pressure of most rotary vane pumps is in the 10 mTorr range (10^{-3}Torr), and atmospheric pressure is 760 Torr,

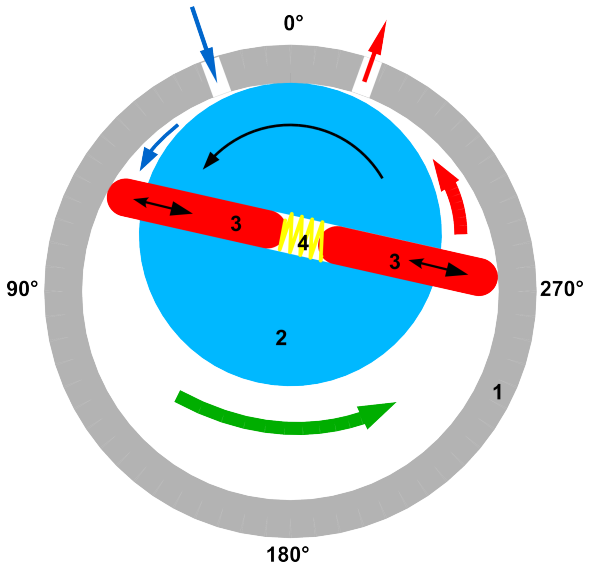

Figure 2.1: Diagram of the pumping cell in a rotary vane pump depicting (1) the pump, (2) rotor, (3) vanes, and (4) spring.[24]

giving a compression ratio of about 76,000. The second stage of pumping is accomplished using a turbo-molecular pump, shown in Figure 2.2a. This pump typically operates below 100 mTorr, and pumps down to 10^{-7}-10^{-10} Torr, depending on the pumping capacity and the size of the chamber being pumped. Gases in the chamber collide with rotating blades spinning on the order of 1000 Hz which impart a large amount of momentum to the gases outward from the chamber, as shown in Figure 2.2b. These pumped gases build up in the bottom of the turbomolecular pump and must be evacuated using a backing pump (rotary vane pump). The compression ratio of turbomolecular pumps varies exponentially with the square root of the molecular weight of the gas being pumped; for hydrogen the compression ratio is on the order of 10^7, whereas for nitrogen it is around 10^{11}.

Another optional stage of pumping commonly used beyond the turbomolecular pump is the ion pump. The pumping element and surrounding components are shown as Figure 2.3. The ion pump consists of a cloud of electrons in a magnetic field that travel in helical paths in the anode region. These electrons ionize incoming gas atoms and molecules, and the newly formed ions are accelerated to the titanium cathode. Upon striking the cathode, the ions either become buried in the cathode material and are effectively removed from the chamber pressure, or they sputter cathode material onto the walls of the pump. The sputtered titanium further evacuates gas via both chemisorption and physisorption, resulting in a net pumping effect. Due to the nature of the pumping mechanism and the requirement of high voltage (3-7 kV), this pump is typically only operated below 10^{-7} Torr, and can bring the chamber pressure down into the 10^{-11} Torr range. Finally, another technique to aid in obtaining low chamber pressures is the titanium sublimation pump (TSP). Coils of titanium wire

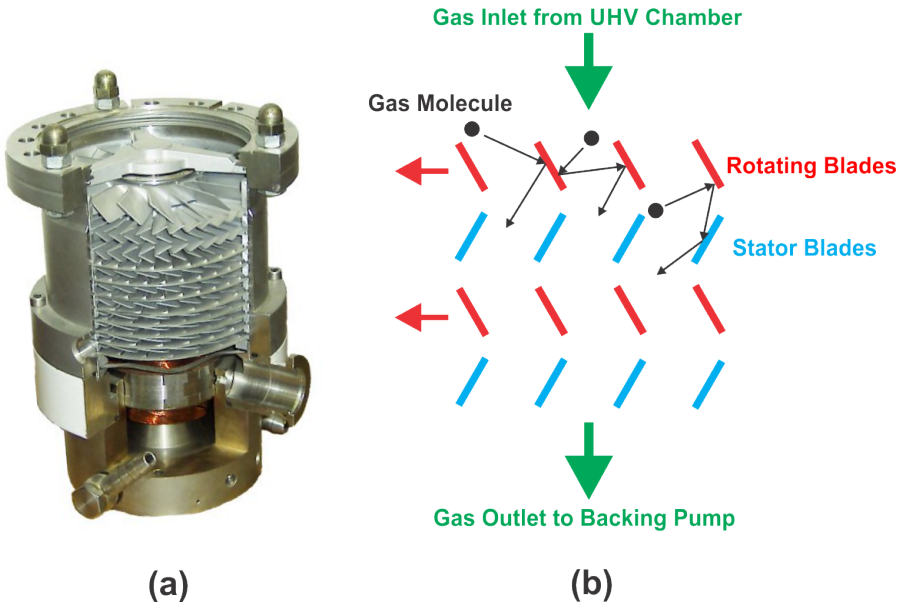

Figure 2.2: (a) Interior view of a turbomolecular pump showing the turbine blades that pump air in from the top through the blades and out the bottom to the backing pump (rotary vane pump)[111]. (b) Illustration of the pumping principle; gas molecules fed in from the top and are imparted with downward momentum via collisions with rotating and stator blades and are pumped out from the bottom via a backing pump.

in the vacuum system have a large current of 50-70A driven through them, causing Ti sublimation and Ti coating of the walls of the chamber. Gases that collide with the Ti-coated chamber walls stick via chemisorption and physisorption as in the ion pump, and are effectively removed from the chamber pressure. This procedure is done periodically to maintain a working ultrahigh vacuum pressure of 10^{-10}-10^{-11} Torr. In practice, the process of obtaining such low pressures is expedited by uniformly heating up the vacuum chamber up to increase the rate of outgassing of chamber walls and components. The vacuum chamber is heated to around 100°C while being continuously pumped for a few days. This is typically done after exposing a UHV chamber to atmospheric pressures and through this process UHV conditions are achieved after several days.

2.3 Photoemission Spectroscopy

2.3.1 Photoemission Process

Photoemission spectroscopy is an experiment by which a photon of some energy is incident on the sample of interest and absorbed by an electron in the occupied states of the sample, and the electron is emitted from the sample. This emitted photoelectron is guided to a detector by applied voltages that only let electrons of a desired energy pass through, and electrons of too low or too high kinetic energy collide with the analyser walls and are therefore unable to reach the detector.

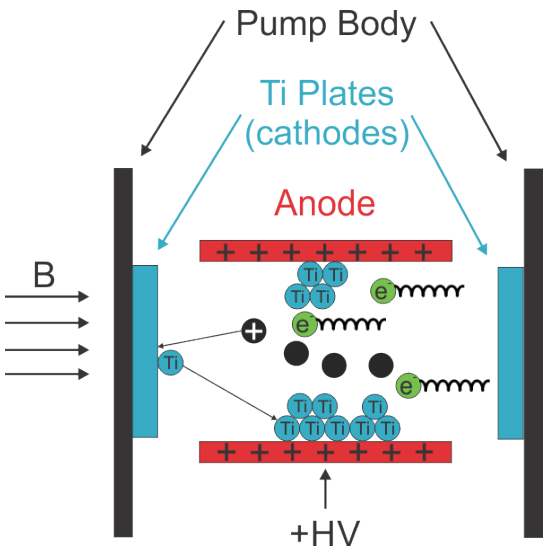

Figure 2.3: Schematic diagram of a sputter ion pump depicting electrons traversing a helical path in the applied magnetic field, which then ionizes gaseous species in the cavity. The ions are accelerated to the titanium cathodes and collide, sputtering off titanium atoms and clusters.

When many electrons are counted over a period of time for a range of electron kinetic energies, a spectrum of the number of electrons collected versus electron kinetic energy is obtained. The photoemission process is depicted in Figure 2.4 for a metal sample. A photon of energy $h\nu$ is absorbed by an electron e_1^- originating from a bound state with energy $E_{B,1}$. The photon imparts on the electron enough energy to overcome its binding energy, $E_{B,1}$, and the work function of the metal, $e\phi$, while having enough kinetic energy remaining, $E_{K,1}$ to reach the detection system. Photoelectrons generated by this process contain information about the occupied states from which they came such that the kinetic energy distribution of the collected electrons effectively maps the occupied states of the sample. Indeed, another electron, e_2^-, residing in a more deeply bound state, $E_{B,2}$, photoexcited by a photon of energy $h\nu$ will leave the sample with less kinetic energy than the first case, $E_{K,2} < E_{K,1}$. However, many photoelectrons undergo inelastic scattering processes upon photoexcitation and during transport to the sample surface. Inelastic scattering results in the photoelectron leaving the sample with less kinetic energy than the ideally photoexcited electron (i.e., a photoelectron that retains all energy imparted to it by the absorbed photon) and some scatter enough times that they never leave the sample. The average length an electron can travel in a solid before undergoing an inelastic collision is known as the inelastic mean free path (IMFP), and this length depends on the energy of the electron. Figure 2.5 shows the depth from which electrons may escape a material (in angstroms) as a function of the electron kinetic energy in electron volts. Typical energies for photons in photoemission spectroscopy range from 21.2-40.8eV for ultraviolet light (HeIα-HeIIα, respectively) to 1486.7eV for X-ray light (Al Kα). The range of electron kinetic

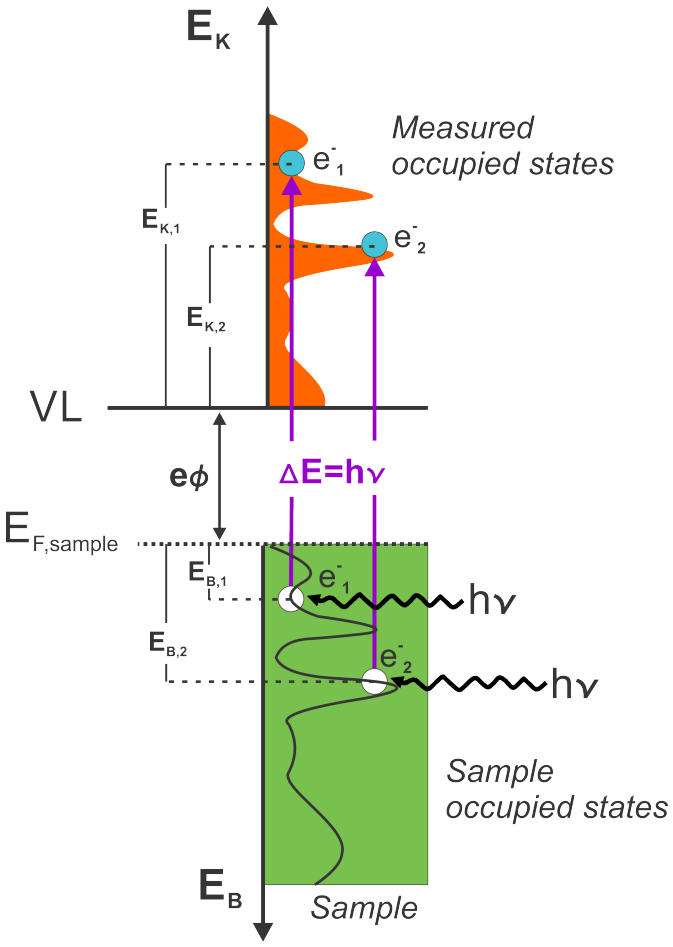

Figure 2.4: Energy diagram depicting the photoemission process, by which an electron in an occupied state of the sample, $E_{B,1}$ is excited by absorbing an incident ultraviolet photon. Once excited, the electron may then leave the sample and arrive at the detector with some kinetic energy, $E_{K,1}$ which can then be converted back to a binding energy scale since the incident photon energy is known ($h\nu = 40.8eV$ for He II emission).

energies in our photoemission experiments are roughly 20-1500 eV, where photoelectrons with the lowest kinetic energies originate from the valence band (probed by ultraviolet and X-ray photons) and the highest kinetic energies originate from core levels (probed by X-rays). For example, the C1s core level is around 1185eV kinetic energy when excited by Al Kα photons, corresponding to around 285eV binding energy. However the binding energy varies according to the local chemical environment of the carbon atom, for example 285eV is for simple carbon-carbon sp^3 bonding, but for carbon-oxygen single and double bonds the binding energy is around 287.5eV and 289eV, respectively. The IMFP for electrons in the range probed by photoemission spectroscopy is 5-20 Å, which means the elastically-scattered electrons detected originate from the first 5-20 Å of the sample, making these techniques extremely surface-sensitive.[191]

A discussion of energetics is necessary to gain quantitative insight into the photoemission process.

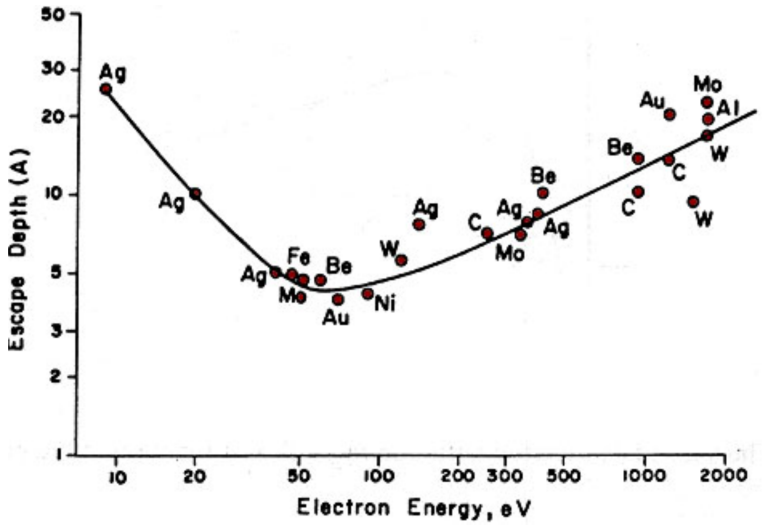

Figure 2.5: Universal electron inelastic mean free path as a function of electron energy.

The total energy of the system before photoexcitation, E, is equal to the photon energy, $\hbar\omega$, plus the energy of the system with N electrons, E_N: $E_{system} = \hbar\omega + E_N$, for a single incident photon and an N-electron solid. After photoexcitation the total energy transforms to the kinetic energy of the photoelectron (E_K) plus the energy of the $N-1$ electron system (E_{N-1}). Following the law of energy conservation, it follows that:

$$\hbar\omega + E_N = E_K + E_{N-1}, \tag{2.1}$$

$$E_K = \hbar\omega + (E_N - E_{N-1}). \tag{2.2}$$

The term in parentheses is defined as the binding energy E_B of the initial electronic state with respect to the vacuum level and is a negative quantity. It is convenient write the binding energy with respect to the Fermi level of the sample rather than the vacuum level, since the Fermi level will be common for all materials in thermal equilibrium with the sample (e.g., the vacuum chamber sample holder). The equation for the electron kinetic energy after these considerations is written as:

$$E_K = \hbar\omega + E_B - e\phi, \tag{2.3}$$

where ϕ is the work function of the sample being measured. This formulation in which we define energies with respect to the Fermi level works well for metal samples due to their well-defined Fermi levels in both ultraviolet and inverse photoemission spectroscopies. However, for semiconductors and insulators with band gaps, a different formulation proves beneficial since the Fermi level resides within the band gap of the material, that is, between the valence band maximum (VBM) and conduction band minimum (CBM). The procedure for addressing band gap materials is discussed further in Appendix B.

The derivation above from equations 2.1 to 2.3 uses the Hartree-Fock approximation (see Appendix A), in which Koopmans' Theorem is exact [77]. Koopmans' theorem assumes that the orbitals of the ionized system are identical to those of the neutral system, i.e., that the orbitals are frozen and do not include relaxation effects around the hole generated in the photoemission process. Two main sources of error in this method result from orbital relaxation, or the response of the system to changing the number of electrons, and the electron correlation, or the electron-electron interactions between all electrons in the system, such as Coulomb repulsion. Koopmanns' Theorem gives accurate results for some systems since the energetic corrections for relaxation and electron correlation are of similar magnitude and opposite sign, and thus nearly cancel each other. It is assumed that Koopmanns' Theorem applies to the photoemission measurements presented in this thesis.

2.3.2 Photoemission Probability

Photoemission spectra are represented as the intensity of photoexcited electrons, $I(E)$, with sufficient energy to arrive at the detector as a function of electron kinetic energy. This intensity is proportional to the density of occupied electronic states, $N(E)$, multiplied by the photoabsorption cross section, $\sigma_{abs}(E)$, for a given photoelectron energy, E[192]:

$$I(E) \propto N(E)\sigma_{abs}(E), \tag{2.4}$$

To find the density of states (DOS), the photoabsorption cross section must be known. This value can be derived using Fermi's golden rule, which describes the rate of transition for the electronic photoexcitation process. The average transition rate, Γ, or the probability of photoabsorption per unit time, is given by:

$$\Gamma = \frac{2\pi}{\hbar} |\left\langle \Psi_f^0 \right| H^{int} \left| \Psi_i^0 \right\rangle|^2 \delta(E_f^0 - E_i^0 - \hbar\omega), \tag{2.5}$$

where Ψ_i^0 and Ψ_f^0 are the initial and final unperturbed states, and H^{int} is the interaction Hamiltonian describing the first-order perturbation theory. In this case, the interaction Hamiltonian describes the incident electromagnetic radiation interacting with the electron of consideration. The delta function enforces conservation of energy for this transition, such that $E_f^0 = E_i^0 + \hbar\omega$.

The Hamiltonian for electrons in a solid may be written as:

$$H^0 = \frac{\mathbf{p} \cdot \mathbf{p}}{2m} + V(\mathbf{r}), \tag{2.6}$$

where $\mathbf{p}$ is the momentum operator of the electron with m the mass of the electron, and $V(\mathbf{r})$ is the potential felt by the electrons due to the nuclei and other electrons. When an electromagnetic field is present, the Hamiltonian changes to:

$$H = H^0 + H^{int} = \frac{[\mathbf{p} - \frac{e}{c}\mathbf{A}(\mathbf{r}, t)]^2}{2m} + e\phi(\mathbf{r}, t) + V(\mathbf{r}), \tag{2.7}$$

and after expanding the quadratic term gives:

$$H = H^0 + H^{int} = \frac{\mathbf{p}\cdot\mathbf{p}}{2m} + V(\mathbf{r}) + \left(\frac{e^2}{2mc^2}\right)\mathbf{A}\cdot\mathbf{A} - \left(\frac{e}{2mc}\right)[\mathbf{A}\cdot\mathbf{p} + \mathbf{p}\cdot\mathbf{A}] + e\phi(\mathbf{r},t), \tag{2.8}$$

where

$$H^{int} = \left(\frac{e^2}{2mc^2}\right)\mathbf{A}\cdot\mathbf{A} - \left(\frac{e}{2mc}\right)[\mathbf{A}\cdot\mathbf{p} + \mathbf{p}\cdot\mathbf{A}] + e\phi(\mathbf{r},t), \tag{2.9}$$

where $\mathbf{A}$ is the vector potential and ϕ is the electric potential due to the electromagnetic field. Using commutator relationship between the vector potential and momentum gives

$$[\mathbf{A}\cdot\mathbf{p} - \mathbf{p}\cdot\mathbf{A}] = -i\hbar\nabla\cdot\mathbf{A}, \tag{2.10}$$

which implies that

$$\mathbf{p}\cdot\mathbf{A} = i\hbar\nabla\cdot\mathbf{A} + \mathbf{A}\cdot\mathbf{p}. \tag{2.11}$$

Then if we choose a transverse gauge in which $\phi = 0$ and $\nabla\cdot\mathbf{A} = 0$ while keeping only terms that are linear in $\mathbf{A}$, and using the commutator relationship above, H^{int} reduces to

$$H^{int} = -\left(\frac{e}{mc}\right)\mathbf{A}\cdot\mathbf{p}. \tag{2.12}$$

Inserting this interaction hamiltonian into equation 2.5 for Fermi's golden rule gives

$$\Gamma = \frac{2\pi}{\hbar}\left(\frac{-e}{mc}\right)^2 |\langle\Psi_f^0|\,\mathbf{A}\cdot\mathbf{p}\,|\Psi_i^0\rangle|^2\delta(E_f^0 - E_i^0 - \hbar\omega). \tag{2.13}$$

The spatial dependence of $\mathbf{A}$ is given by $e^{-i\mathbf{k}\cdot\mathbf{r}}$, and considering that for ultraviolet radiation the wavelength ($\lambda \approx 10 - 400$nm) is much greater than the Bohr radius ($a_0 \approx 0.0529$nm) then the exponential dependence may be approximated by 1 and $\mathbf{A}$ can be considered spatially uniform (i.e., $\mathbf{A}$ may be taken as a constant) over the unit cell. This is known as the dipole approximation. Then in this approximation the transition rate becomes[90]

$$\Gamma = \frac{2\pi}{\hbar}\left(\frac{e}{mc}\right)^2 |\langle\Psi_f^0|\,\hat{\epsilon}\cdot\mathbf{p}\,|\Psi_i^0\rangle|^2\delta(E_f^0 - E_i^0 - \hbar\omega), \tag{2.14}$$

where $\hat{\epsilon}$ is the polarization vector of the incident light. From equation 2.14 for Fermi's Golden Rule in the dipole approximation, the differential absorption cross section per unit solid angle can be obtained as the following[90]:

$$\frac{d\sigma_{abs}}{d\Omega} = \frac{\alpha k}{mh\omega}|\langle\Psi_f^0|\,\hat{\epsilon}\cdot\mathbf{p}\,|\Psi_i^0\rangle|^2, \tag{2.15}$$

where $\alpha = \left(\frac{e^2}{\hbar c}\right) \approx \frac{1}{137}$ is the fine structure constant and k is the magnitude of the electron wave vector. The differential cross section is obtained as a function of incident photon energy which is useful in determining the orbital character of a particular spectral feature by observing the energy dependence of its cross section.

2.3.3 Three-Step Model of Photoemission

One may approach the interpretation of photoemission spectra using the three-step model.[23] In this model, the intensity of emitted electrons in valence band measurements is given by:

$$I(E, h\nu) = I_p(E, h\nu) + I_s(E, h\nu), \tag{2.16}$$

where I is the total photoelectron intensity measured, I_p is the intensity of primary photoexcitation events, and I_s is the intensity of secondary inelastically scattered photoelectrons. The primary photoelectron intensity may be treated as a product of three contributions:

$$I_p(E, h\nu) = J(E, h\nu)T(E_f, h\nu)D(E_f), \tag{2.17}$$

where $J(E, h\nu)$ is the absorption of the incident photon by the electron, $T(E_f, h\nu)$ is the transportation of the photoelectron to the sample surface, and $D(E_f)$ is the photoelectron escaping the sample and entering the vacuum. For $T(E_f, h\nu)$, a classical treatment of the electron mean free path shows that the transport of an electron to the solid surface can be described by the fraction of the total number of photoelectrons created within one mean free path, λ_e, from the surface. Then, $T(E_f, h\nu)$ is given by:

$$T(E_f, h\nu) = \frac{\lambda_e(E_f)/\lambda_{ph}(h\nu)}{1 + \lambda_e(E_f)/\lambda_{ph}(h\nu)}, \tag{2.18}$$

where $\lambda_e(E_f)$ is the inelastic mean free path of the electron with kinetic energy E_f and $\lambda_{ph}(h\nu)$ is the penetration depth of the incident photon with energy $h\nu$.[85] In the limit $\lambda_e/\lambda_{ph} << 1$, the mean free path of the electron is much smaller than the penetration depth of the light, one obtains $T(E_f, h\nu) \rightarrow \lambda_e/\lambda_{ph}$. To cross the surface of the solid into the vacuum, an electron must have enough energy to overcome the work function (i.e., possesses the minimum energy of $E_F + \Phi$) and a component of its wave vector normal to the surface. Then,

$$D(E_f) = 1/2 \left[1 - \left(\frac{E_F + \Phi}{E_f}\right)^{1/2}\right], \tag{2.19}$$

where E_F is the Fermi energy of the system, Φ is the work function of the solid, and E_f is the kinetic energy of the photoelectron. $T(E_f, h\nu)$ and $D(E_f)$ are slowly varying as a function of energy, and so the spectrum is dominated by the initial structure of the occupied electronic states. The rate of transition is given by Fermi's golden rule in the dipole approximation as:

$$W_{fi} = \frac{2\pi}{\hbar^2} \left| -\frac{e}{mc} \mathbf{A} \cdot \langle f | \, \mathbf{p} \, | i \rangle \right|^2 \delta(E_f - E_i - h\nu). \tag{2.20}$$

Then the number of electrons detected at an energy E for an excitation energy $h\nu$ is given by:

$$J(E, h\nu) \propto \sum_{i,f} \int |M_{i,f}|^2 \delta(E_f(\mathbf{k}) - E_i(\mathbf{k}) - h\nu)\delta(E_f(\mathbf{k}) - E) d^3\mathbf{k}, \tag{2.21}$$

where the matrix element in equation 2.20 is rewritten as $M_{i,f}$:

$$M_{i,f} = -\frac{e}{mc}\mathbf{A} \cdot \langle f| \mathbf{p} |i\rangle . \tag{2.22}$$

Since $M_{i,f}$ is constant and $h\nu$ is large the final state can be considered as a free electron state, which gives:

$$J(E, h\nu) \propto \sum_{i,f} |M_{i,f}|^2 \rho(E - h\nu), \tag{2.23}$$

where $\rho(E - h\nu)$ is the density of occupied states. If we now neglect the energy dependence of the dipole matrix elements $M_{i,f}$, then the number of electrons detected, $J(E, h\nu)$, is proportional to the density of the states of the system:

$$J(E, h\nu) \propto \rho(E_i), \tag{2.24}$$

and therefore the measured primary photoemission intensity is also proportional to the density of states of the system:

$$I_p(E, h\nu) \propto DOS(E_i). \tag{2.25}$$

2.3.4 Ultraviolet Photoemission Instrumentation

Ultraviolet photoemission spectroscopy (UPS) is a type of photoemission spectroscopy using ultraviolet light, and is typically used to probe the valence band of the sample surface. For our UPS measurements the UV light source is a Leybold-Heraeus He discharge lamp in which an electrical arc created in the presence of He gas excites electrons inducing transitions to higher energy levels. When excited electrons relax to lower energy states they emit photons of wavelengths that are characteristic of He. The two most prominent He emission lines are He Iα (21.2 eV) and He IIα (40.8 eV), corresponding to electronic decay from the $2p$ level to the $1s$ level in the neutral and singly-ionized He atom, respectively. The ratio of He II to He I increases with decreasing He pressure in the lamp, and is therefore tunable using the He leak valve that supplies He flow through the lamp. Note that both He emission lines have three components, α, β, and γ, corresponding to decay transitions from $2p, 3p$, and $4p$ to $1s$, respectively. With respect to the α transition, the β and γ transitions for He I are $< 2\%$ the intensity of He Iα, whereas for He II the β transition is around 2% and the γ is $< 1\%$. Photons emitted from the He discharge lamp travel through a narrow quartz glass tube to the sample, creating a small spot size of about 1mm^2. The energy widths of the He I and He II emission lines are < 0.1 eV.[56]

Photoelectrons emitted from the sample are collected and energy analyzed using a cylindrical mirror analyzer (CMA), a schematic of which is shown as Figure 2.6. A CMA works by deflecting electrons away from the outer cylinders and toward the inner cylinders through applied voltages that

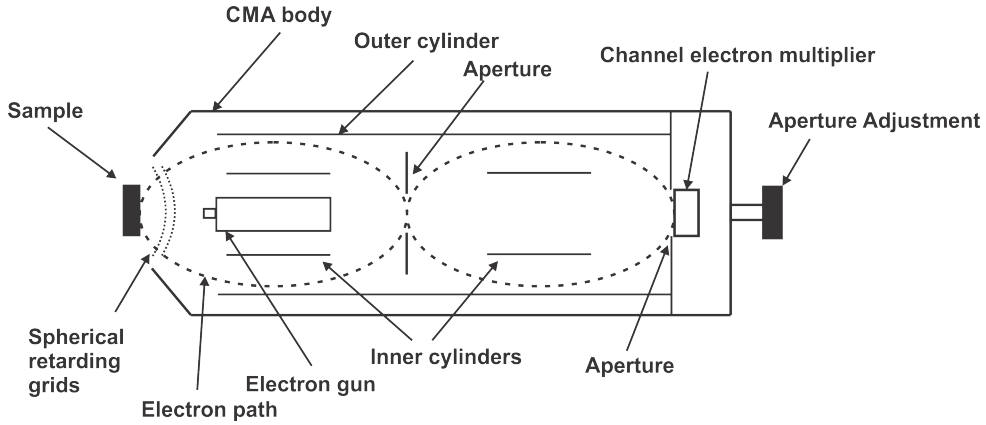

Figure 2.6: Schematic diagram of a double-pass cylindrical mirror analyzer, with the electron path given as dashed lines running from the entrance point near the sample to the electron detector on the far right.

create an electric field between the cylinders, and electrons of a desired kinetic energy then traverse the dashed path to reach the detector. Electrons with too high kinetic energy for a given applied voltage collide with the outer cylinder, and too low kinetic energy collide with the inner cylinder, and are not detected. However a narrow window of kinetic energies pass through, and this energy window is referred to as the pass energy. Electrons that successfully traverse this path collide with the first section of the detection device which is comprised of a highly emissive material that creates showers of electrons for each single electron collision event. Each secondary electron created then collides again with the material to create far more electrons, and this process continues several times with the cascading electrons accelerated toward the detector with an applied high voltage. In this way, a measurable current pulse is created from a single electron event. To create a spectrum, each of these single electron events are counted for a preset period of time at a given electron kinetic energy, and the applied voltages to the CMA cylinders are varied to allow a range of electron kinetic energies to pass. The cylinder voltages are changed so the next value of electron kinetic energies pass through and are counted, and so on, until you have a spectrum of electron intensity as a function of electron kinetic energy.

The electron detector is a type of continuous dynode multiplier known as a single channel electron multiplier, shown in Figure 2.7, which is comprised of a funnel of glass coated on the inside with a semi-conducting material with a negative high voltage applied at the input end and a positive voltage near ground applied at the narrower output end. A single electron from the sample collides with the funnel interior and creates a shower of secondary electrons, and electrons emitted at any point on the funnel interior are accelerated a distance down the funnel before impacting the surface. Upon impacting the surface each secondary electron creates its own shower of secondary electrons.

These showers of electrons are accelerated toward the detector at the narrow end of the funnel by an applied voltage, colliding with the surface on the way and creating larger showers of electrons causing a cascading effect. A large number of electrons generated by a single-electron event ($> 10^7$) reach the end of the tube and form a current pulse through a wire, which is then converted to a voltage pulse measurable by the electrical components and is finally counted by the computer as one event.

The CMA is typically operated in one of two modes: non-retarding mode or retarding mode. In non-retarding mode, electrons pass through the analyser with their initial kinetic energy, and the energy range of desired electrons is swept by varying the outer cylinder potential. In retarding mode, the first spherical grid at the CMA entrance is held at the sample potential of the sample (grounded in this case), and the second grid is held at a negative potential of a few volts less than the energy of the electrons. The second grid energy is known as the pass energy, and effectively reduces the kinetic energy of the photoelectrons to typically 5-15 eV for UPS. Retarding mode is generally used where fine resolution is desired but the number of available counts is limited.

The resolving power resolution of the CMA can be written as $E_P/\Delta E$ and has a fixed value defined by the geometry of the CMA, where E_P is the kinetic energy of the electrons reaching the detector (i.e., the pass energy), and ΔE is the range of electron kinetic energies about the pass energy that reach the detector. Therefore, decreasing the pass energy then decreases the range of kinetic energies that reach the detector and as a result increases the energy resolution. However, decreasing the pass energy also decreases the count rate and therefore the collection time must be increased to maintain an acceptable signal-to-noise ratio.

Spectra of the intensity of photoelectrons as a function of electron kinetic energies are obtained by counting electron events for a preset amount of time for a range of electron kinetic energies. To obtain binding energies rather than kinetic energies, the kinetic energy value corresponding to the Fermi level of a Au sample in contact with the system is measured. Photoelectrons emitted from the Fermi level of the system have the highest kinetic energy and are easily identified in the spectra as a sharp decrease in intensity. The overall resolution of our UPS measurements can be obtained by measuring the full width at half-maximum (FWHM) of the detected Fermi level, and is approximately 0.3 eV. Recall that the energy widths of the He I and He II lines used are about 0.1 eV, which implies that the energy resolution of the CMA is limiting the overall energy resolution of the system. Furthermore work functions and ionization potentials are readily measured using UPS to permit the creation of electronic energy level alignment diagrams scaled to the Fermi level of the system. Details of this process of obtaining binding energies and creating energy alignment diagrams are discussed in Appendix B.

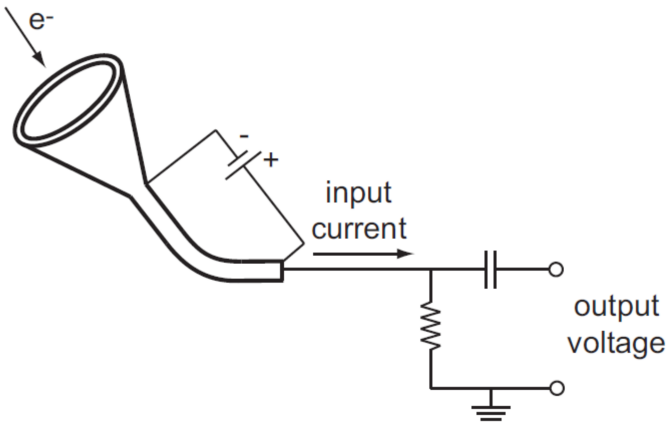

Figure 2.7: Schematic diagram of a channel electron multiplier. Incident photons collide with a highly emissive semiconducting surface creating a shower of secondary electrons which collides again with the tube creating another greater shower, and so on. In this way, a detectable electronic pulse is created from one incident event.

2.3.5 X-Ray Photoemission Instrumentation

X-ray photoemission spectroscopy (XPS) follows the same physical process of photoexcitation discussed above and typically uses Al Kα X-ray photons with 1486.7eV energy. This photon energy is great enough to excite core electrons out of the sample which are inaccessible by UPS, which uses lower energy UV photons (21.2-40.8eV). Since core electrons are only slightly effected by the local chemical environment of the atom being probed, core electrons provide a useful marker of the chemical content of the sample being probed. In particular, one can determine the atomic composition of the sample from high resolution spectra of core levels. Furthermore, the valence band of a sample can be measured using XPS, albeit with a lower cross section than with UPS.

X-rays are generated from the Al Kα line of a SPECS XR50 dual anode source. The dual anode is a copper tube with a wedge-shaped end that has two flat faces, one of which is coated with aluminum and the other with magnesium. Typically the surrounding shields and casings are grounded and the anode is held at high positive voltage (>10 kV). Filaments next to the anodes are heated to induce thermionic emission of electrons that are accelerated toward the anode surface by the high voltage and collide, bombarding the anode. Soft X-rays (1253.6 eV for Mg Kα and 1486.6 eV for Al Kα) are generated and pass through an aperture covered by a thin (about 2μm) Al foil that screens the sample from stray electrons from the filament, heating effects, and any contamination from the source. Note that bombarding the anode with highly accelerated electrons causes the anode to quickly heat up, and so to mitigate overheating effects cooling water flows through the inside of the anode.

In the measurements described in this thesis, Al Kα photons incident on the sample excite core electrons that are analyzed and detected by the CMA in the same manner described above for UPS. Pass energies for XPS range from 50-150 eV, with lower pass energy used for measuring a particular core level of interest and higher pass energy used for a faster, lower-resolution scan spanning a large range of kinetic energies. The latter high pass energy scans are used to quickly measure the chemical composition of the sample with low resolution and, while they do contain quantitative information, more rigorous analyses of relative core intensities is typically done using higher-resolution low pass energy scans of individual core levels.

UPS and XPS are complementary techniques; XPS provides high resolution core level information as well as valence band information, whereas UPS inherently has a higher cross section for probing the valence band and therefore can provide higher resolution data, however core levels are inaccessible to UPS. Core levels contain clear information of the atomic composition of the sample and if the resolution is high enough, they can even elucidate the type of bonding present in the sample (e.g., sp^2, sp^3 C-C bonding, C-O single or double bonds). Additionally, the valence band directly reflects the local chemistry and density of occupied electronic states which provides crucial information regarding electronic structure and bonding. When combined, XPS and UPS permit a greater probing of the electronic structure information. In the measurements described in this thesis, UPS and XPS are housed in the same UHV chamber that also contains equipment for sample preparation and cleaning such as an argon-ion sputter source and sample heater, in addition to removable sublimation sources for *in situ* molecular deposition.

2.4 Inverse Photoemission Spectroscopy

2.4.1 Inverse Photoemission Process

Inverse photoemission is a technique that uses the optical decay process by which monoenergetic electrons incident on a sample have a finite probability to couple to high-lying unoccupied states of the sample and decay to lower-lying unoccupied states by emitting a photon. This process is illustrated schematically for a metal sample in Figure 2.8. The energy of the emitted photon is equal to the difference in the initial energy of the electron and the final energy of the previously unoccupied state the electron relaxes into, $h\nu = E_i - E_f$. Since the initial energy of the electron is a known and tunable value, measuring the energy of the photon permits the determination of the final state energy of the electron. Measuring the number of photons as a function of energy then gives information about the unoccupied density of states of the sample. IMFP describes inverse photoemission just as well as direct photoemission since the incident particles are electrons. The

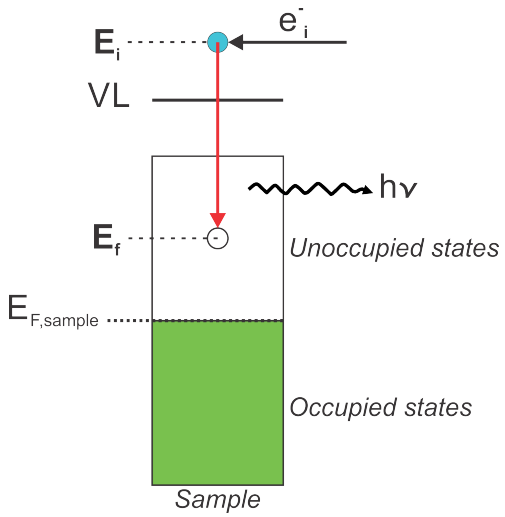

Figure 2.8: Energy diagram illustrating the inverse photoemission process by which an electron of known energy couples to unoccupied states of the sample and releases a photon in the process. This photon is then energetically analyzed by a spherical diffraction grating and detector to yield information about the unoccupied states in the sample.

electron energies typically used are 15-20 eV which corresponds to an IMFP of about 10 Å, similar to the IMFP found in UPS.

Photoemission and inverse photoemission involve the interaction between a photon and an electron, and so they share the same interaction hamiltonian from equation 2.12. For photoemission **A** can be treated as a classical time-dependent perturbation and will have the same results as in a proper quantum mechanical treatment. From this approach[90], one can obtain the differential cross section, $\frac{d\sigma}{d\Omega}$, from Fermi's golden rule similar to what was described above in equations 2.13-2.15:

$$\frac{d\sigma}{d\Omega} = \frac{\alpha\omega}{mc^2hk} |\langle \Psi_f | \hat{\epsilon} \cdot \mathbf{p} | \Psi_i \rangle|^2. \tag{2.26}$$

Here, α is the fine structure constant, ω is the angular frequency of the electromagnetic radiation, m is the mass of the electron, c is the speed of light, k is the magnitude of the electron wave vector, and $\mathbf{p}$ is the momentum of the electron. It is insightful to compare the cross section obtained here with that from direct photoemission in equation 2.15:

$$R = \left[\frac{d\sigma}{d\Omega}\right]_{inv} / \left[\frac{d\sigma}{d\Omega}\right]_{dir} = \frac{\omega^2}{c^2k^2} = \frac{q^2}{k^2}, \tag{2.27}$$

where q is the magnitude of the photon wave vector, and k is the magnitude of the electron wave vector. Simplifying this gives:

$$R = \left(\frac{\lambda_{elec}}{\lambda_{photon}}\right)^2. \tag{2.28}$$

Therefore, the ratio of inverse to direct photoemission cross sections is simply the square of the ratio of the wavelength of the electron to that of the photon. At energies in the range of UV, for

example 10 eV, the inverse photoemission cross section is smaller by a factor of about 10^5. This relationship manifests experimentally through a lower sample current generated in IPS compared to UPS for equivalent incident particle fluxes. In practice, to obtain an inverse photoemission spectrum with good signal-to-noise ratio the acquisition time must be significantly longer than for direct photoemission spectra.

2.4.2 Inverse Photoemission Instrumentation

Inverse photoemission spectroscopy (IPS) involves incident electrons interacting with a sample and producing photons through the process of optical decay, and the generated photons are detected. A schematic diagram of the inverse photoemission experimental setup is shown as 2.9. Incident electrons of a predetermined but fixed energy (10-20eV) are produced from an electron source aimed at the sample. Electrons incident on the sample have a finite probability of being captured by the sample unoccupied states, and can decay to lower energy unoccupied states and release a photon in the process through optical decay. Photons generated in this way travel through a spherical diffraction grating to separate the photons by energy along the horizontal direction, which then collide with a detector. The position on the detector along the horizontal direction (the direction of photon dispersion) indicates the energy of each photon, and the photon counts are summed along the vertical direction for each horizontal position to give a spectrum of photon counts versus photon energy. In this way, photons of many energies are detected simultaneously for a fixed incident electron energy. This type of detection system is known as a grating spectrometer system, and is used in the IPS measurements presented in this thesis. An alternate method of collecting photons is the isochromatic mode in which photons of one specific energy are collected and the incident electron energies are varied to probe a range of unoccupied states.

Following figure 2.9, incident electrons strike the sample with a spot size of about 1mm^2 causing photon emission along a line R'. The photons strike the diffraction grating and disperse. The dispersed photons with a range of energies then reach the detector along a path R. The detector can be moved along the Rowland circle to change the energy range of detected photons. The diffraction grating is at the heart of this detection system as it performs the photon energy separation. The grating equation describes the relationship between the grating spacing and the angles of both the incident and diffracted beams of light, and is written as follows:

$$m\lambda = d(sin\alpha + sin\beta). \tag{2.29}$$

Here, m is the diffraction order, λ is the wavelength of incident light, d is the line spacing of the diffraction grating, α and β are angles of the incident and refracted beams of light with respect to

the surface normal, n in figure 2.9, respectively.

The theoretical energy resolution of the spherical diffraction grating spectrometer system can be estimated using an expression for the light dispersion by the grating in its focal plane, given by[91]:

$$\frac{d\lambda}{dl} = \frac{sin\beta}{2mR_c n cos\beta}\left(10^4 \frac{\mathring{A}}{mm}\right), \tag{2.30}$$

where m is the order of diffraction, R_c the radius of the Rowland circle, n the number of grooves per millimeter, and β is the angle of reflection of the light with respect to the grating surface normal, shown in Figure 2.10. In our experimental equipment, R_c = 750 mm, n = 1200 lines/mm, and β=25°, giving a theoretical grating resolution of 0.06 eV for a photon energy of 19 eV and 0.04 eV for a photon energy of 15 eV.

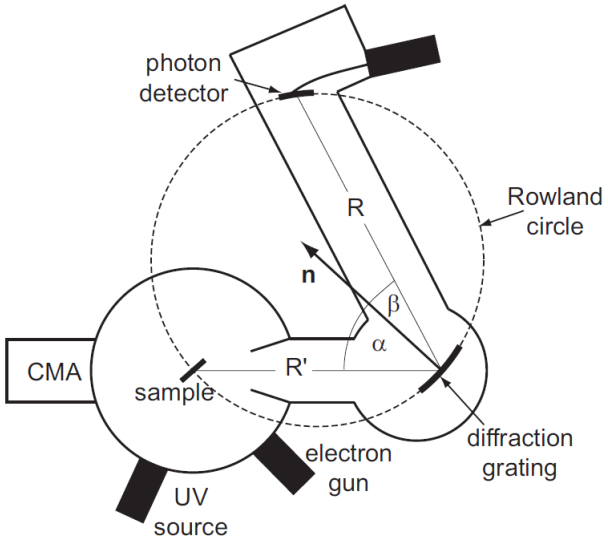

Figure 2.9: Schematic diagram of the diffraction grating vacuum chamber setup.

The inverse photoemission detection system is based on the principle of the Rowland circle, shown as the dashed circle in figure 2.9. A more detailed schematic diagram of the Rowland circle is shown in Figure 2.10a and b for a three-dimensional and two-dimensional perspective, respectively. This system uses a concave spherical mirror diffraction grating to disperse the photons. The Rowland circle limits the loss of light that arises when lenses are used to focus diffracted rays[31]. Let the radius of the spherical grating be R_m, then if the photon source is anywhere on the Rowland circle of radius $R_c = R_m/2$ which contacts the center of the grating the specular beam and all orders of the dispersed beam will be focused at other points on the same Rowland circle. Thus, the Rowland circle is used to identify where the detector must be located with respect to the photon source. Figure 2.10 shows an example of the focusing and dispersing of a light beam incident at point A in the xy plane, on the Rowland circle. Light with wavelength λ_1 strikes the grating and focuses

on the Rowland circle at point B, whereas light with wavelength λ_2, focuses at point C. In this case $\lambda_2 > \lambda_1$, and indeed light with shorter wavelengths originating from point A will focus on the Rowland circle at points farther down the y-axis, with decreased angle β.

Astigmatism is a property of some optical systems in which light propagating in two perpendicular planes have different foci. For example, in such an astigmatic system, if one attempts to form the image of a cross, the vertical and horizontal lines will be in focus at two different distances. An example of this is shown in Figure 2.10a for light rays emanating from point A but with components in the z-direction, illustrated with dashed lines. Although these light rays have the same wavelength λ_1 as other rays that are focused at point B on the Rowland circle, astigmatism results in a different focal distance than rays of the same energy that remain within the xy plane which is shown as point D. Additionally, all rays of the same wavelength emanating from point A will focus on a line in the z-direction (perpendicular to the xy plane) passing through point B, i.e., passing through the Rowland circle. This same set of rays will also focus on a line within the xy plane but perpendicular to the y-axis that passes through point D. The Rowland circle is then called the horizontal focus, and the line tangent to the Rowland circle and perpendicular to the y-axis is called the vertical focus. As the distance from the y-axis increases, the separation of the horizontal and vertical foci increase.

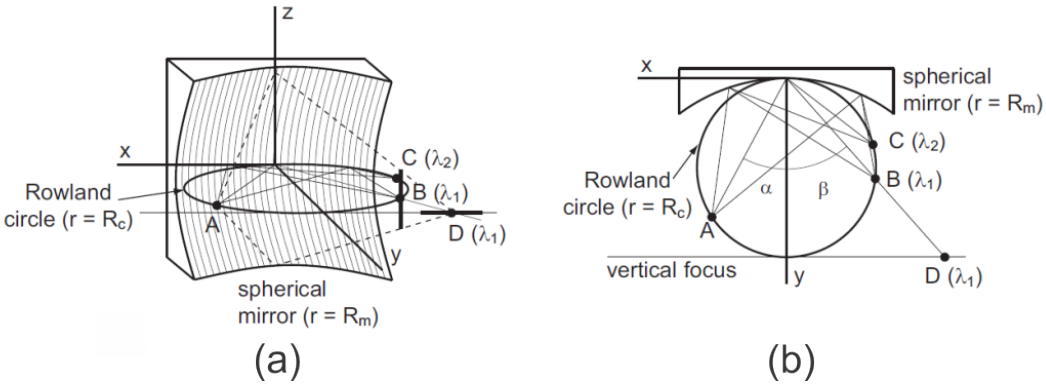

Figure 2.10: Schematic diagram illustrating a spherical diffraction grating and the principle of the rowland circle.

A schematic of the photon detection system is shown as Figure 2.11, which makes use of microchannel plates and a resistive anode encoder. The microchannel plates amplify incident photon events by creating a shower of electrons, however, the regular array of microchannels yield information about the location of the event on the plate. Due to the channeling and applied voltages, the electron cloud will accelerate toward the resistive anode encoder along the channel of the initial photon event, preserving the location.

The resistive anode encoder is a sheet of uniform resistance, and when an electron cloud collides with the encoder a current is generated across the sheet. This current is detected at each of the four corners, A, B, C, and D. Then the position of the event on the encoder is deduced from the following equations:

$$X = \frac{I_A + I_B}{I_A + I_B + I_C + I_D}, \tag{2.31}$$

$$Y = \frac{I_B + I_C}{I_A + I_B + I_C + I_D}, \tag{2.32}$$

where X is the direction of photon dispersion and Y is the perpendicular direction. The X and Y values are converted into two 8-bit digital signals, creating a 256 by 256 matrix of points, where one pair of X and Y coordinates corresponds to one particular point, shown as Figure 2.12. Every detected photon event outputs a digital X and Y coordinate sent to the external computer, which increments that particular matrix element by 1, and in this way builds a two-dimensional matrix of events. To create a spectrum, the program sums along the Y direction for a given X point to obtain the total number of events at the photon energy corresponding to that X coordinate. The total number of events for a given X coordinate are plotted as a function of X coordinate, creating the spectrum of photon counts versus X coordinate.

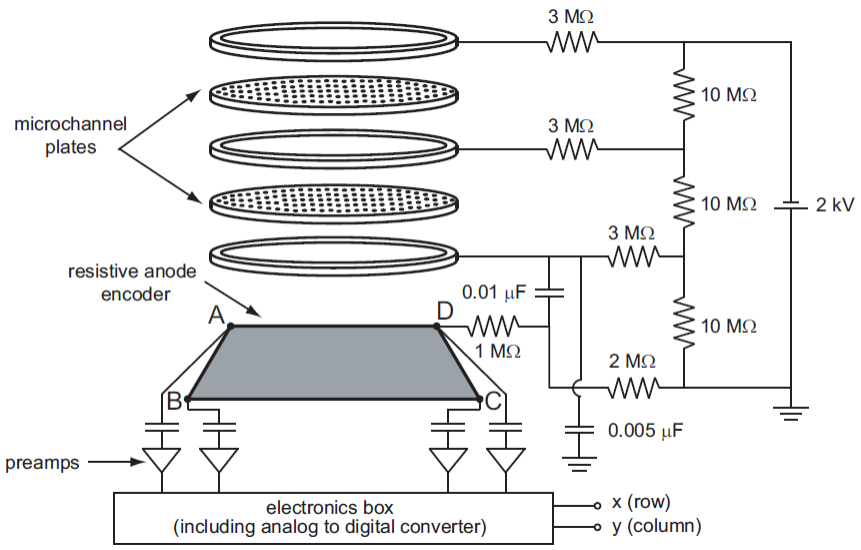

Figure 2.11: Schematic diagram illustrating the working principle of a two-dimensional photon detection system used in IPS.

Prior to taking IPS measurements, the detector sensitivity must be mapped as a function of detector X coordinate. Furthermore, the measured spectra represent photon counts as a function of X coordinate on the detector and must be converted to a binding energy scale with respect to the measured Fermi energy of the system. Briefly, this is accomplished by taking IPS spectra of an

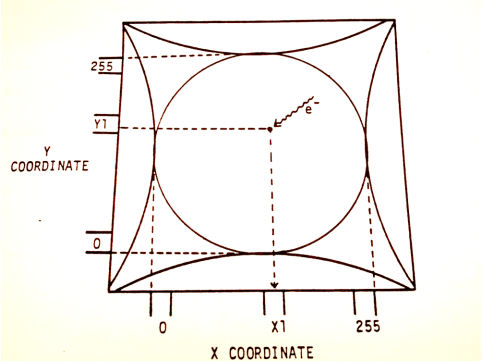

Figure 2.12: Illustration of the active area of the detector, in which an electron pulse hits the detector at point X1,Y1 ($0 \leq X1 \leq 255$, $0 \leq Y1 \leq 255$). The detector then outputs this event as two 8-bit digital signals, corresponding to the X and Y coordinates. These coordinates are read by a computer program which increments that position (X1,Y1) by 1 for every instance that particular set of coordinates is detected.

Au sample for a range of incident electron energies and performing a calibration using the channel position of the Fermi level. Au is used because of its relatively flat density of unoccupied states, that is, it has no strong features in the range of energies probed. Details of these processes are given in Appendix C. The IPS system is housed in the same UHV chamber as both the UPS and XPS systems, permitting an extensive analysis of the electronic structure without ever exposing the sample to ambient conditions.

2.5 Scanning Tunneling Microscopy

The scanning tunneling microscope was invented at IBM Zürich by Gerd Binnig and Heinrich Rohrer in 1981 who earned a Nobel Prize in Physics in 1986 for this development.[26] It is used to study local surface topography of conducting samples with atomic resolution, and is typically operated in UHV with samples at low temperature, room temperature, or elevated temperatures of a few hundred degrees Celsius, and thus is extremely versatile.

Scanning tunneling microscopy (STM) uses the quantum mechanical principle of electron tunneling, by which electrons have a finite probability of tunneling across a potential barrier. Detailed discussions of the microscope's operation are found elsewhere.[25, 43, 172] Briefly, an atomically sharp tip of tungsten wire (though some use Pt-Ir alloys) is brought within a nanometer of the conducting surface in a controlled manner, such that the tip does not collide with the surface. A bias is applied between the tip and the surface, called the tunneling bias, which establishes a tunneling current that may flow from the tip to sample or vice versa depending on the polarity of the bias. Once established, the current can be measured typically in the pA-nA range which is a variable tunneling parameter chosen by the operator. In classical physics, an electron is unable to penetrate

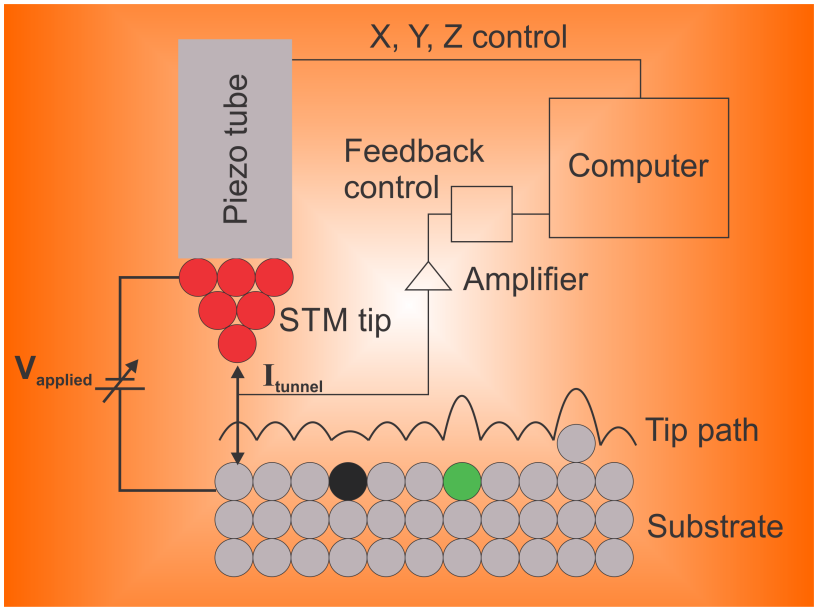

Figure 2.13: Diagram illustrating the STM/Computer interface setup and the path an STM tip takes across a surface that has various adsorbates, defects, and atomic steps.

a potential barrier Φ that is higher than the electron energy E. A quantum mechanical treatment predicts an exponentially decaying electron wave function within the potential barrier of width d as follows:

$$\Psi(d) = \Psi(0)e^{-\kappa d}. \tag{2.33}$$

Here, $\Psi(d)$ is the exponentially decaying wave function of the electron of mass m within the potential barrier, $\Psi(0)$ is the oscillatory wave function of the electron outside of the barrier, d is the spatial width of the potential barrier, and κ is defined as:

$$\kappa = \frac{\sqrt{2m(\Phi - E)}}{\hbar}. \tag{2.34}$$

The tunneling current is proportional to the probability of electrons to tunnel through the potential barrier:

$$I \propto |\Psi(d)|^2 = |\Psi(0)|^2 e^{-2\kappa d}, \tag{2.35}$$

where it is clear that the tunneling current depends exponentially on the width of the potential barrier, which in STM represents the tip-sample separation. This exponential dependence of the tunneling current on the tip-sample separation makes STM extremely sensitive to surface topography. A typical STM has ~ 0.1 Å height resolution and ~ 1 Å lateral resolution permitting the imaging of individual atoms and molecules. The tunneling current is not only representative of the tip-sample separation, but also the local density of electronic states of the sample. For example, for a given tip-sample separation and tunneling bias, an atom or molecule with a high density of states will

establish a larger tunneling current than one with a lower density of states. Thus STM also provides information about the local density of states of the surface.

Figure 2.13 depicts a typical STM experimental setup. The STM tip translates in sub-angstrom steps in a controlled manner using piezoelectric actuators for full three-dimensional control. The applied bias may be varied in magnitude and polarity, and therefore one can choose to tunnel into the sample unoccupied states or tunnel from the occupied states. The tip raster-scans across the surface at adjustable scan speeds and, for the images produced here, can produce a two-dimensional image in about five minutes. STM measurements are typically performed in one of two modes, constant current or constant height modes. In constant current mode, the tunneling current is fixed and the tip-surface separation is adjusted in real time in response to the surface topography as the tip raster scans across the surface by way of a feedback loop. In constant height mode, the tip-sample separation is fixed and the changes in tunneling current are measured. The STM measurements presented here are done in constant current mode.

STM is sensitive to external vibrations and therefore must be isolated from the UHV chamber by floating on springs as well as magnetic damping. Drift is an artifact of the STM equipment that causes the images to appear distorted, but typically diminishes after scanning a given area for some time. Drift may result from piezoelectric creep and also from thermal effects, with higher temperatures inducing more drift than lower temperatures. STM measurements presented are performed using an Omicron variable temperature STM at room temperature, housed in a UHV chamber separate from the UPS and IPS chamber. The STM chamber also contains sample preparation and cleaning equipment such as an argon-ion sputter source and a sample heater for annealing, in addition to XPS to confirm the chemical composition of the surface as well as removable sublimation sources for *in situ* molecular deposition. STM images presented here were processed using the WSxM 5.0 develop 6.4 software.[84] Due to a combination of noise and thermal drift, the uncertainties in the STM measurements are conservatively estimated to be ± 0.1 Å for heights, ± 1 Å for lateral distances, and $\sim 3^\circ$ for angles.

2.6 Computational Methods

2.6.1 GAMESS

Calculational methods were used in this work to aid in the interpretation of photoemission and inverse photoemission spectra, specifically to identify molecular contributions to the spectra. Density of states (DOS) calculations were performed for all isolated molecules (i.e., in the gas-phase) using the General Atomic and Molecular Electronic Structure System (GAMESS) software package

which is discussed further below. In general, for weakly-interacting systems, electronic structure calculations for isolated molecules (i.e., gas-phase molecules) match UPS and IPS results and allow the assignment of spectral features in the occupied and unoccupied states to one or more molecular orbitals. However, in systems where strong chemical interaction is present the molecular spectral features may deviate from gas-phase and the calculations must be modified to improve interpretation of experimental results.

Ab-initio quantum chemistry calculations are performed for isolated molecular species in density functional theory (DFT) formalism using a combination of the Becke three-parameter exchange functional [19] (B3) with the Lee-Yang-Parr correlation energy functional [106] (LYP). Together these form the semi-empirical B3LYP exchange-correlation functional to describe electron-electron interaction. Additionally, the 6-31G basis set was used for all molecules in this work. Details of the DFT formalism and the implementation of B3LYP are discussed in Appendix A.

We use the GAMESS ab-initio quantum chemistry package with the aforementioned DFT method to calculate equilibrium isolated molecular geometries, and density of electronic states, as well as the shapes of occupied and unoccupied molecular orbitals.[154] Models of isolated molecules with calculated equilibrium geometries as well as contour images of molecular orbitals are then produced from the GAMESS calculations by importing the results into Molden, a processing program for molecular and electronic structures. [152]

Several necessary adjustments to the GAMESS results must be applied to properly compare theoretical calculations to experimental spectra. First, GAMESS outputs discrete electronic states as a function of energy which we transform by fitting each state with a Gaussian curve with 1 eV FWHM to simulate broadening. All Gaussians are then summed to create a theoretical spectrum representing the calculated DOS for the isolated molecule. Second, the energy separation between the highest occupied molecular orbital (HOMO) and lowest unoccupied molecular orbital (LUMO) is typically underestimated in DFT calculations and is remedied by rigidly separating the occupied and unoccupied states using the so-called scissor operation. That is, the energy gap is artificially increased while maintaining the relative energy separation between all occupied states and all unoccupied states. The gap is increased by an amount that results in good matching of key features such as the HOMO, LUMO, or other prominent orbitals with the experimental results for multilayers of molecular species on surfaces. A comparison to multilayers of molecules, rather than a monolayer, is performed because the substrate surface contribution is effectively negligible since the probed molecular layer is sufficiently spatially separated from the substrate surface. Finally, the calculations produce electronic states as a function of energy, however this energy must be rigidly shifted such that the zero of energy matches the Fermi energy of the experimental system.

Care must be taken when comparing theoretical DOS to experimental spectra as the calculations neglect several important experimental effects. The cross-section of interaction is not taken into account in the calculations which may result in drastically different intensities for a given state. Additionally, the calculations are done for isolated molecules, that is, in the absence of any substrate, therefore this method is best suited for systems with weak chemical interaction.

2.6.2 FIREBALL and QUANTUM ESPRESSO

Briefly, for ZnTPP and TCNQ on TiO_2(110) our collaborators perform density functional theory calculations using the FIREBALL[48, 89, 107, 108] code and QUANTUM ESPRESSO[66] code suite to establish the molecular binding geometry on a substrate slab using dynamical relaxation methods. Furthermore, by tracking charge transfer and electronic density changes, as well as incorporating intermolecular interactions, the interfacial dipole and electronic energy level alignment can be theoretically reproduced to match experiment within our error bars. The theoretical analysis proceeded in four steps: (1) binding geometry of the molecule on the substrate is determined via dynamical relaxation procedures and energy minimization, (2) electronic energy level alignment and charge transfer for the T=0K case is considered for a single molecule with the calculated adsorption geometry on the substrate surface; this is done through appropriate corrections in the DFT calculation such as the "shift and stretch" procedures[157] (i.e., rigid energy shift and scissor operation discussed earlier), (3) intermolecular effects are introduced and energy alignment is recalculated, (4) T>0K case is considered and energy alignment is recalculated. Details of these calculations as applied to ZnTPP and TCNQ molecules on TiO_2(110) are found in their respective sections as well as references [142] and [119], respectively. Details of the physical principles behind the FIREBALL code are found in Appendix A, and information regarding Quantum ESPRESSO is found in Appendix A and reference [142].

Chapter 3

Molecular Self-Assembly on Noble Metals

3.1 Introduction

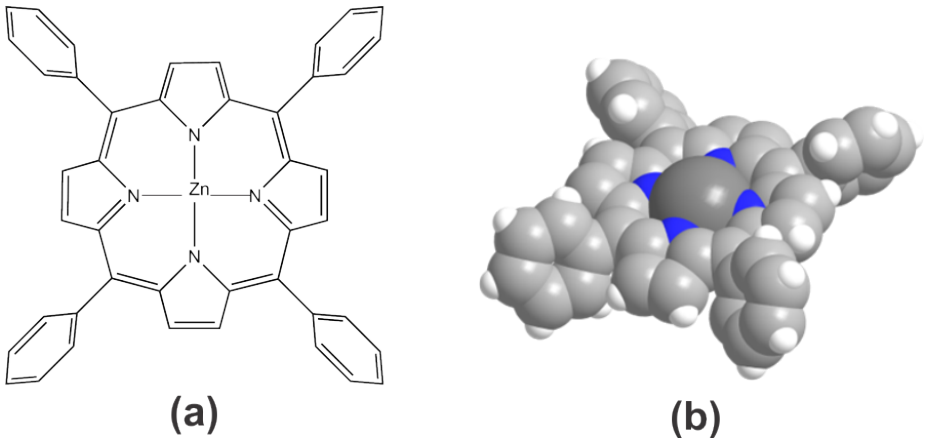

Figure 3.1: (a) Skeleton model of a ZnTPP molecule, comprised of a zinc-centered porphyrin macrocycle and four phenyl moieties. (b) Space-filling model of ZnTPP elucidating the saddle conformation as well as the phenyl rotation with respect to the porphyrin macrocycle typically seen upon adsorption to metal substrates.

Tetraphenylporphyrin (TPP) consists of a porphyrin macrocycle with four phenyl moieties bound to the carbon bridge between adjacent pyrrole groups, as shown in Figure 3.1a. For TPPs in the gas phase, the phenyls are oriented nearly perpendicular to the porphyrin macrocycle[145] and are effectively electronically decoupled[139] permitting many phenyl functionalization possibilities that maintain the electronic and structural integrity of the porphyrin core. The center of the porphyrin core may be free-base (i.e., no metal in the center) or substituted with a metal atom allowing for even greater chemical versatility. An interesting property of TPPs is their ability to self-assemble on noble metal surfaces into highly-ordered nearly-square arrays at room temperature, extending over many tens or hundreds of nanometers. A deep understanding of self-assembly processes and relevant physical and chemical interactions would facilitate the ability to direct the assembly of functionalized molecules for particular purposes. For example, using the detailed knowledge of self-assembly processes one could take advantage of the long-range self-assembled order to create

low-defect functional 2D polymers.[68, 74, 75, 105, 169]

Many studies have been done to characterize the self-assembly process and the stability of the self-assembled geometry of TPPs at surfaces. A variety of techniques were used such as scanning tunneling microscopy (STM) to gain insight into adsorption geometries[13, 20, 33, 35–38, 52, 74, 128, 143, 144, 146, 156, 160, 163, 173, 186, 187, 194, 197, 199], near edge X-ray absorption fine structure (NEXAFS) to elucidate intramolecular features such as the relative orientation of the phenyl groups with respect to the macrocycle[13, 41, 44, 49, 51–53, 140, 186], X-ray[20, 41, 44, 49, 51, 53, 80, 114, 128, 139, 143, 156, 160, 194], ultraviolet[80, 114, 139, 140, 144, 194], and inverse[139, 140, 144] photoemission spectroscopy (XPS, UPS, and IPS) to probe directly the electronic structure and chemistry, and temperature programmed desorption (TPD) to track molecular desorption and hydrogen evolution with temperature[36, 75, 143]. On metal surfaces, due to a strong porphyrin core iminic nitrogen interaction with the substrate, the mesophenyls are typically rotated and can even become coplanar with the porphyrin core.[41, 49, 52, 53]. It has been shown that altering the phenyl groups has a profound impact on the self-assembly behavior and results in deviations from the nearly-square organization observed for TPPs[33, 75, 87, 114, 200]. However substituting various metal centers of TPPs at noble metal surfaces does not typically impact self-assembly, indicating that the final geometry is primarily influenced by intermolecular phenyl-phenyl interactions[5, 35, 36, 156]. Additionally metallation of free-base TPPs (2HTPPs), which involves the acceptance of a single metal ion into the porphyrin core and the release of two hydrogen atoms per molecule, has been studied widely for the potential advantages gained in the flexibility of chemical processes that depend on the metal center[49, 51, 53, 75, 128, 143, 160, 194].While the porphyrin core is planar in the gas phase, upon adsorption onto a metal substrate the core deforms into a saddle-like conformation that is understood as opposing pyrrole groups bending toward and away from the substrate[13, 124] as shown in Figure 3.1b. The energetic barrier leading to saddling, intimately linked to the rotation of phenyl groups with respect to the porphyrin core, is sufficiently low (20 kcal/mol or 0.86 eV/molecule) for molecular distortion to occur after adsorption on surfaces[145].

Highly-ordered self-assembled TPP monolayers on metal substrates typically are obtained using two methods: (i) direct deposition, which is inherently difficult due to the low level of control in UHV sublimation sources, and (ii) multilayer desorption, in which a multilayer is deposited and the sample is subsequently annealed to 400-500K to desorb all but the last layer. In practice, method (ii) has proven more reliable than method (i)[49, 114]. However, methods (i) and (ii) are inherently different, as method (ii) involves the addition of thermal energy to the system which can result in molecular reorganization.

In this chapter, we discuss ZnTPP monolayers prepared via direct deposition and multilayer

desorption on Au(111), Ag(111), and Ag(100) using STM. In particular, we focus on the differences in the monolayers obtained from the two distinct methods, and also on changes in adsorption geometry and binding behavior after subsequent annealing of the monolayer. Studying these three surfaces permits a comparison of the ZnTPP adsorption behavior on two different noble metals with the same surface symmetry, as well as on two different surface symmetries of the same metal.

3.2 ZnTPP on Au(111)

The following discussion ZnTPP on the Au(111) surface is based on work I have done that has been published[146]. In this study, the adsorption of ZnTPP on the Au (111) surface is investigated with scanning tunneling microscopy with a particular emphasis on the relationship between molecular adsorption and modifications to the atomic arrangement of the substrate surface. The clean Au(111) surface exhibits a well-known herringbone (HB) reconstruction, an STM image of which is shown as Figure 3.2, whose orientation has a well-defined relationship with the high symmetry directions of the (111) surface.[17, 125, 168] Moreover, the origin of the HB reconstruction is well understood in terms of anisotropic surface stress, so that modifications of the HB features can provide information on the adsorbate-substrate interaction.[164] The binding behavior of the ZnTPP molecules and the accompanying modification of the substrate are studied for surface coverages from the sub-monolayer to monolayer regime. Both room temperature as-deposited molecular formations and the molecular/substrate registry after *in-situ* thermal treatments are explored. In all cases, the HB reconstruction is still observed when the molecular overlayer is present. However, under certain preparation conditions, the HB reconstruction assumes a reconstruction with a periodicity that is different from that of the clean surface, likely due to modification of the anisotropy in the surface stress. Our findings suggest that for this weakly-interacting system, the binding geometry assumed by the adsorbate is a delicate balance among molecule-molecule interactions, molecule-substrate interactions, and surface stress, indicating that all of these effects are of comparable energy and act in concert to produce the resulting overlayer/substrate morphology.

3.2.1 ZnTPP Ordering as a Function of Coverage and Au Morphology

Coverage Dependent Adsorption Behavior

Before addressing the adsorption of ZnTPP molecules on the Au(111) surface, a characterization of the pristine surface is necessary. The Au(111) surface used in this study possessed large terraces (100-200 nm wide) separated by steps with apparent heights of 2.2 Å, consistent with reported values for monoatomic steps on Au(111) single crystals.[17] The bright bands observed on the terraces are

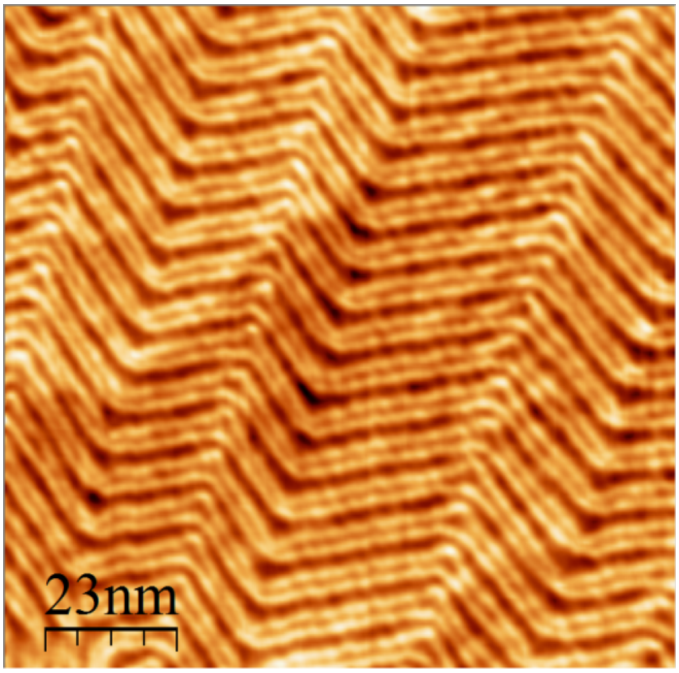

Figure 3.2: STM image of the clean Au(111) surface showing the herringbone pattern.

associated with the so-called soliton walls of the HB reconstruction characteristic of the clean Au(111) surface.[17, 125, 168] The periodicity of the HB reconstruction, perpendicular to the soliton walls (i.e., in the Au $[\bar{1}10]$ direction), matches well with the value of 63 Å found for clean gold.[17] The HB reconstruction unit cell is shown schematically in Figure 3.3, and is understood to be a smooth transition from regions of face centered cubic (fcc) stacking (...ABCABC) to regions of hexagonal close packed (hcp) stacking (...ABCABA), separated by transition zones called soliton walls[125]. In STM, the soliton walls appear as bright stripes that typically extend for a distance of approximately 20 nm and then bend periodically by an angle of $\pm 120°$, creating so-called elbow sites. The regions that contain parallel, straight soliton walls are considered domains, and lines connecting rows of elbows are considered the domain walls.

Figure 3.4 shows an STM image of the Au(111) surface after a low-dose ($\sim$0.1 ML coverage) exposure to ZnTPP molecules. The image shows two large terraces, on which there is no evidence of the presence of molecules, separated by a monatomic step. Observation of the HB reconstruction on the terraces of Figure 3.4 suggest that if any ZnTPP molecules are present on the surface, they are weakly interacting (i.e., do not affect the HB reconstruction) and highly mobile (i.e., are not imaged in STM). In contrast, a significant modulation of intensity, which is not present on the clean Au(111) surface, is observed parallel to the monoatomic step. We interpret this modulation as evidence for ZnTPP molecules bound to the step edge. The preferential bonding is most likely

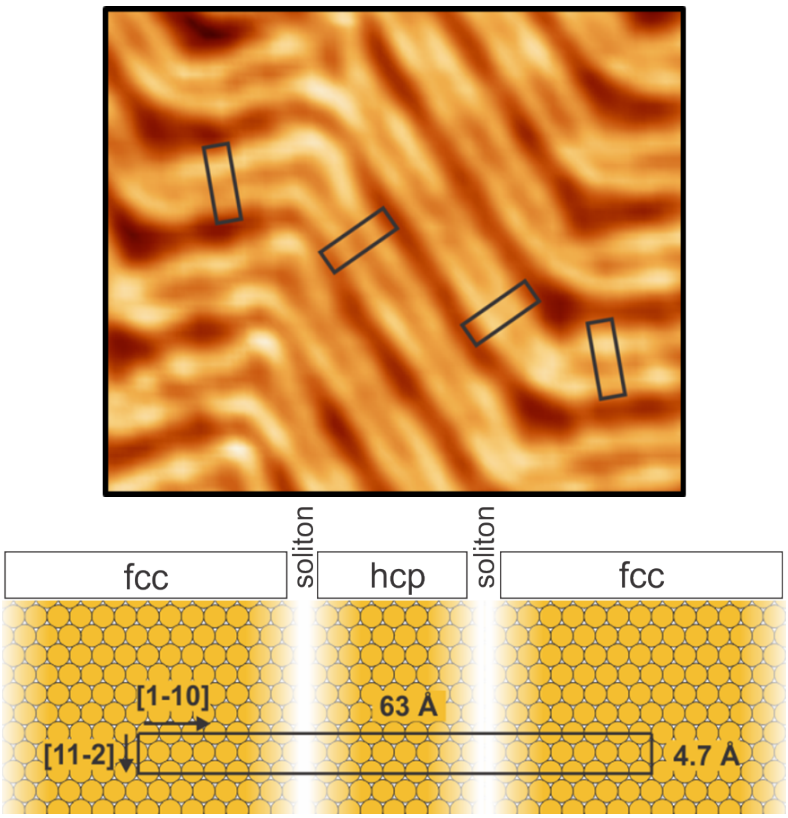

Figure 3.3: STM image of the clean Au(111) surface showing the herringbone pattern unit cell as a black rectangle, as well as the same unit cell on a model fcc(111) surface elucidating fcc and hcp domains separated by soliton walls.

because the ZnTPP molecule can be more highly coordinated at the step edge.[36, 38, 144]

Figure 3.5 shows an STM image from a Au(111) surface exposed to additional molecules for a total coverage of ∼0.4 ML, obtained using tunneling conditions similar to those of Figure 3.4. The image shows a portion of a single terrace which consists of a contiguous region containing a highly-ordered rectangular array of small bright features surrounded by large regions of clean Au that continue to exhibit the HB reconstruction. The rectangular array is attributed to an ordered molecular island, and is typical of what is observed at this coverage. These islands were only observed after the steps were completely decorated with ZnTPP molecules, reminiscent of what has previously been observed in similar systems[144]. Note that not only is the HB reconstruction visible on the bare Au surface, but also superposed with the molecular features. This suggests that the interaction of the molecules with the Au(111) surface is not strong enough to lift the HB reconstruction. Moreover, note that the molecular island forms within a single HB domain (i.e., between rows of elbows). Preferential nucleation of similar organic molecules at Au(111) elbow sites has been reported at low temperatures and is explained by stronger bonding to a particular dislocation at this point.[29, 112, 201]

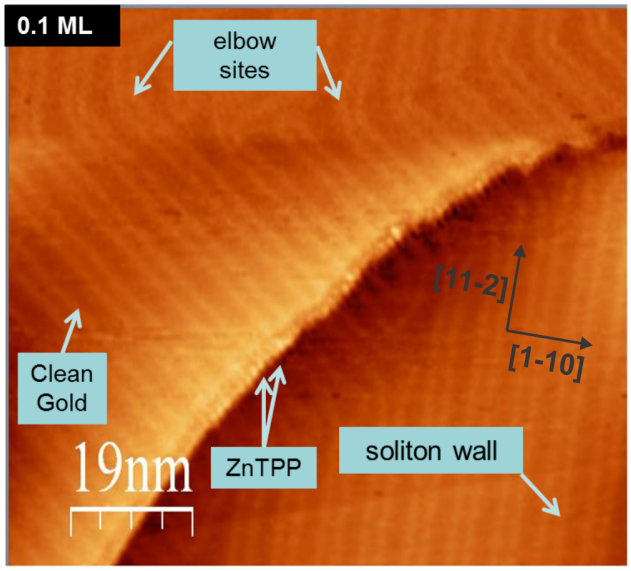

Figure 3.4: Room temperature STM image of ZnTPP on Au(111) at low coverage. Image dimensions are 100×100 nm, taken at V = -1.0 V and I = 0.5 nA.

Figure 3.6 shows a typical STM image containing two terraces separated by a monoatomic step, obtained from the Au(111) surface after further exposure to ZnTPP yielding a coverage of ∼0.8 ML. The image shows larger islands of rectangular molecular arrays forming on different HB domains, as well as small regions of clean gold. Note that the principal symmetry axis of each rectangular molecular lattice is rotated with respect to the underlying soliton wall (i.e., the Au $[11\bar{2}]$ direction) by 17°. This is similar to what has been found for related systems [197]. The individual molecular islands remain within a particular domain of the underlying HB reconstruction, and, just as with intermediate coverages, the periodicity of the HB reconstruction along the $[\bar{1}10]$ direction is unaltered.

From the observations described above, an adsorption sequence with increasing coverage can be outlined for room temperature deposition of ZnTPP on Au(111). When first deposited onto a clean Au(111) surface, ZnTPP molecules decorate the high coordination step edge sites. For higher coverage, although nucleation of individual molecules is not observed at elbow sites of the HB features, islands of ordered molecules stabilize in between the domain walls of the HB reconstruction. The underlying HB solition walls are still visible, indicating that the molecule-substrate interaction is not strong enough to disturb the reconstruction. Furthermore, the ZnTPPs are always observed in groups on terraces or as chains on step edges, and never as isolated molecules, implying that the molecule-molecule stabilization is stronger than the diffusion barrier at the surface. Finally, the strict alignment of the molecular self-assembly with respect to preferential directions of the Au(111) surface as seen in Figure 3.6, indicates that the interaction between the molecular-array and the Au

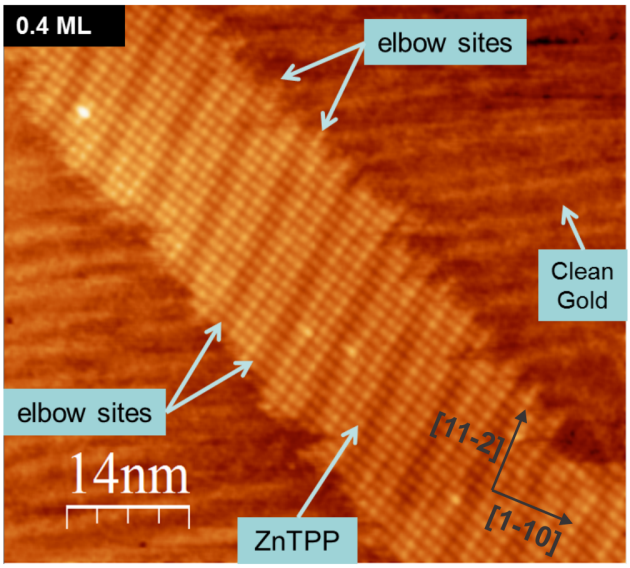

Figure 3.5: Room temperature STM image of ZnTPP on Au(111) at intermediate sub-monolayer coverage. Image dimensions are 75×75 nm, taken at V = -1.0 V and I = 0.35 nA.

substrate plays an important role in establishing the equilibrium surface morphology.

Au atom mobility at step edges

The STM images of Figs. 3.7a and b represent characteristic aspects of the Au step edges of a pristine surface and of a surface exposed to ZnTPP at room temperature, respectively. In Figure 3.7a, the step edges of the clean Au(111) surface appear typically smooth and rounded, indicating a very small anisotropy in the energy of step formation for different edge orientations. Upon exposure to ZnTPP at room temperature, even for a coverage close to a monolayer, the step edge morphology is unmodified (as seen in Figure 3.7b) and it is clear that no correlation exists between the molecules at step edges and the molecular array on the terraces. Thus, the Au substrate morphology appears relatively unperturbed by the presence of the ZnTPP adsorbates.

This is no longer true when energy is added to the system through mild annealing of the substrate. Figure 3.7c represents the typical aspect of Au step edges either after annealing (between 250°C and 265°C) a room temperature-deposited monolayer, or when reaching a monolayer coverage from multilayer desorption at 250°C. In this case, although the characteristic rectangular molecular array found on terraces is preserved, the step edge now conforms to the boundary of the molecular island. This is a clear indication that a cooperative interaction between the molecule and the surface Au atoms, particularly at steps, drives the system to this more stable configuration.

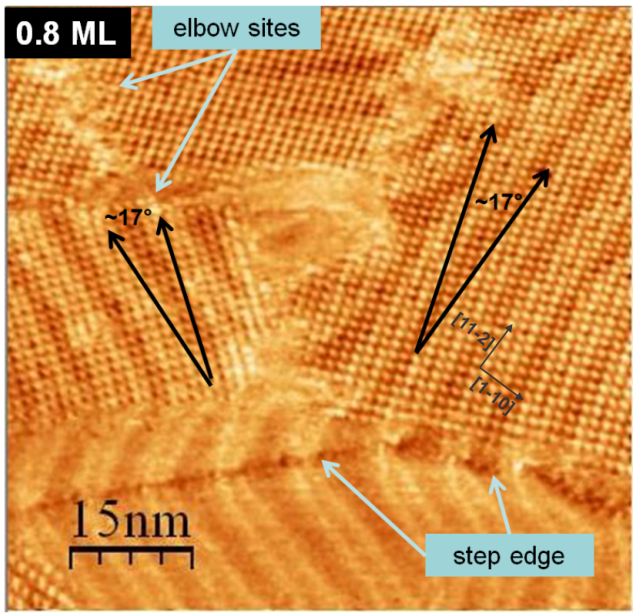

Figure 3.6: Room temperature STM image of ZnTPP on Au(111) at near-monolayer coverage. Image dimensions are 75×75 nm, taken at V = -1.0 V and I = 0.6 nA.

3.2.2 Molecular arrangement in the monolayer regime and surface stress effects

Monolayer regime of ZnTPP on Au(111) at room temperature

Figure 3.8 shows a high resolution STM image of a typical molecular array of rectangular symmetry formed by ZnTPP deposition on Au(111) at room temperature for a coverage near one ML. The larger portion of the figure was obtained with positive bias (i.e., tunneling into the unoccupied states). In this image, sub-molecular features and the HB soliton walls are simultaneously observed. The molecular array is composed of a repeating pattern of a large bright ring, attributed to the main Zn porphyrin macrocycle, surrounded by four small protrusions, associated with the four meso-phenyl groups of the ZnTPP molecule. The low tunneling intensity at the center of the porphyrin rings, i.e., at the location of the Zn ions, can be tentatively explained by considering the electronic configuration of the central Zn ion and the tunneling parameters (+1 V) used to acquire the image. Zn has a filled d orbital ($3d^{10}$), thus it is expected that the contribution of the Zn atom to the tunneling current would be small, resulting in a dark spot at the center of the Zn porphyrin macrocycle in the STM image.[2]

As the position of the ZnTPP phenyl groups and the orientation of the Au(111) HB soliton rows can be determined simultaneously from STM images similar to that of Figure 3.8, the periodicity and relative orientation of the molecular lattice with respect to the high symmetry directions of the Au(111) substrate, as well as the azimuthal orientation of the ZnTPP molecules, can be directly

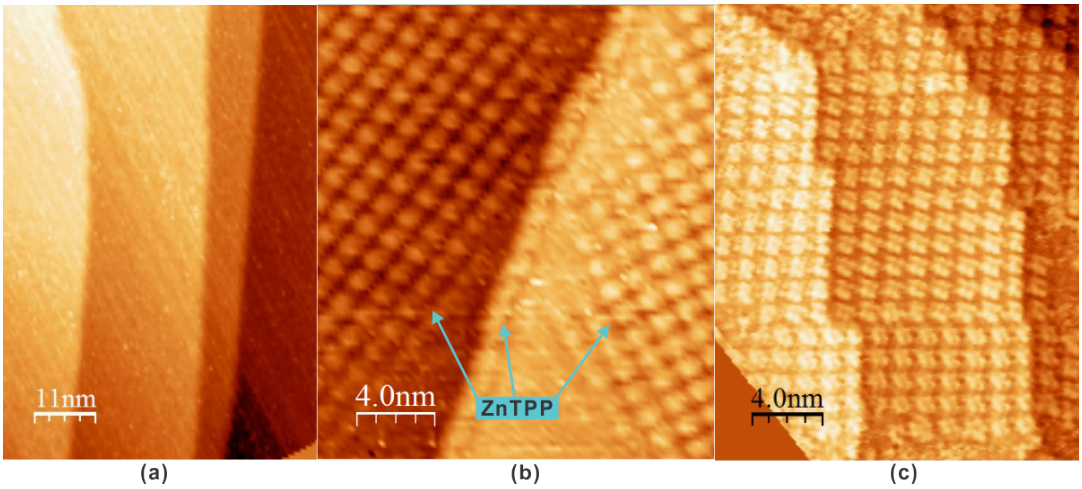

Figure 3.7: (a) Clean Au(111) with large flat terraces and well-defined step edges smoothly running over long distances. (b) Sub-monolayer coverage (directly deposited) with ZnTPP molecules, showing molecular step edge decoration and ZnTPP islands. Molecules trace the existing step edges, and step edges appear unmodified. (c) Monolayer coverage obtained using the annealed multilayer preparation method. The step edges strictly align with ZnTPP molecular rows. Image information: (a) 20×25 nm, V = 2.0 V , I = 1.0 nA; (b) 20×23 nm, V = 1.0 V, I = 0.5 nA; (c) 20×25 nm, V = -0.8 V, I = 0.3 nA.

established. First, however, we discuss the relative molecular arrangement within the array. In the right portion of Figure 3.8, space-filling models of the ZnTPP molecule are superimposed on the STM image to illustrate the overall binding geometry. The molecule is represented with the porphyrin macrocycle parallel to the surface and the phenyl groups rotated so that they are no longer nearly perpendicular to the macrocycle, as they were in Figure 3.1. Although not determined directly from the STM measurements, this adsorption geometry follows reports from near-edge X-ray absorption fine structure (NEXAFS) studies indicating that the phenyl groups of free-base or substituted TPP rotate upon adsorption on metallic surfaces[52, 186].

In Figure 3.8, it is clear that pairs of nearest-neighbor phenyl groups are oriented perpendicular to one another, in a geometry typically called T-stacking. Similar packing geometries have been observed for CoTPP, FeTPP, and H_2TPP on Ag(111)[36] and CuTPP on Au(111)[33], as well as for ZnTPP on Au(111) in solution using electrochemical STM[199]. Although a precise understanding of the energetics favoring this ordering is lacking, the presence and identity of the central 3d transition metal ion do not seem to alter this ordering in comparable systems[13, 33, 34, 36, 38, 41, 52, 144, 163, 173, 187, 194, 199], suggesting that the phenyl groups dominate the molecule-molecule interaction. DFT calculations attempting to describe proper van der Waals interactions between benzene molecules with different relative orientations do not seem to strongly favor pure perpendicular or pure parallel stacking.[69] However, assuming an interaction energy for the phenyl groups relatively

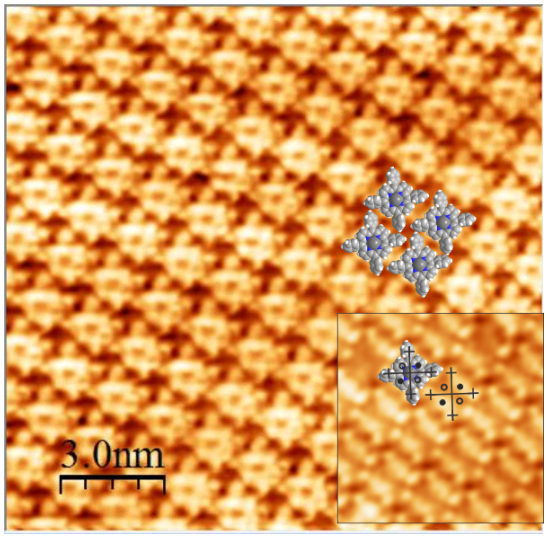

Figure 3.8: High resolution room temperature STM image of ZnTPP on Au(111) directly deposited, taken at V = +1.0 V and (inset) -1.7 V. At greater bias the two-fold symmetry of the ZnTPP molecules becomes visible. Bright lobes (dark lobes) are interpreted as pyrrole groups farther from (closer to) the surface and are denoted with a filled (empty) circle. Large image: 15×15 nm, I = 0.5 nA. Inset image: 9×10 nm, I = 0.5 nA

invariant with stacking geometry [69], in the T-stacking arrangement each phenyl is stabilized by two other neighbors rather than just one in the parallel configuration.

STM images obtained under different tunneling conditions indicate that deformation of the porphyrin macrocycle occurs upon adsorption. The inset STM image in Figure 3.8, taken at a tunneling bias of -1.7 V, clearly shows that the molecules exhibit a two-fold symmetry, as opposed to the four-fold symmetry observed at the other bias. This symmetry breaking has been observed on similar systems and is the result of a change in the position of the opposing pyrrole groups bending either toward or away from the substrate.[13, 33–38, 144, 163, 173, 186, 187, 194] Thus, although the four meso-phenyl groups are still visible as small bright protrusions, only the two opposing pyrrole groups bent upward are seen as bright lobes. A schematic diagram of the molecule, comprised of a large decorated cross, is shown in the inset of Figure 3.8. The centermost point of the schematic represents the location of the Zn ion, and the outer crosses represent the approximate location and width of the phenyl groups. In addition, pairs of filled and empty circles represent the location of the upward and downward oriented pyrrolic groups, respectively. It is important to note that all the molecules in this image are distorted in the same way, that is, all pairs of bright lobes are oriented in the same direction (from lower right to upper left in the figure).

Having established the relative molecular orientation within the islands, we now address alignment of the molecular lattice and the molecular orientation with respect to the high symmetry

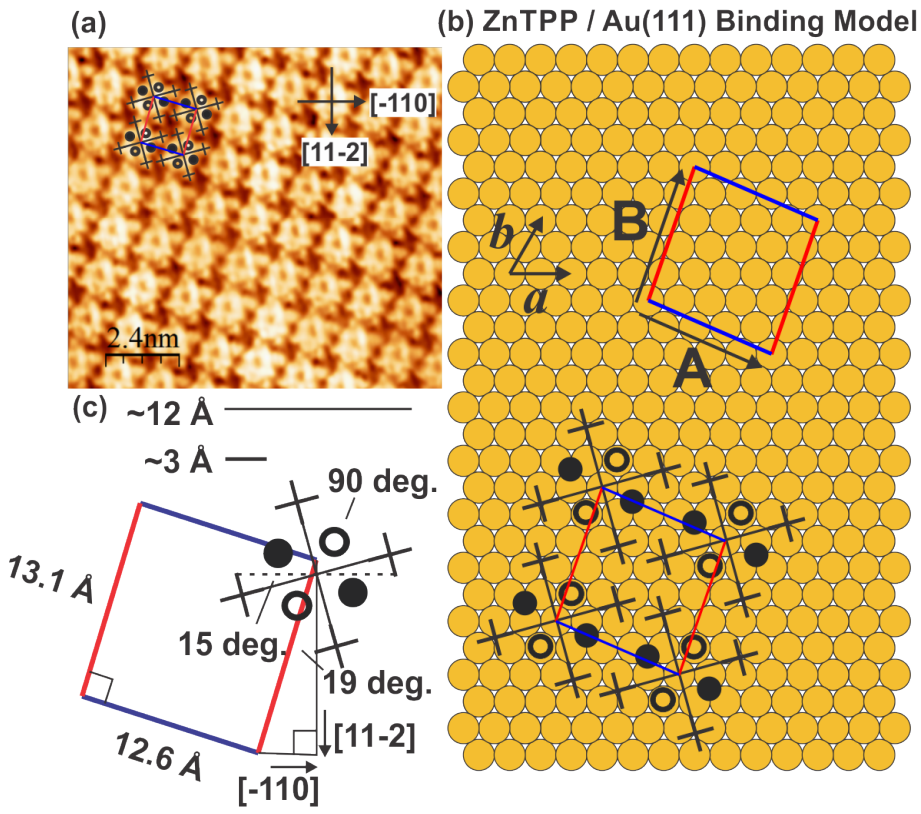

Figure 3.9: Binding model for room temperature deposited ZnTPP on Au(111). (a) STM image on which this model is based. (b) Schematic ZnTPP packing model on a fcc (111) surface. The HB soliton walls run parallel to the [11$\bar{2}$] (vertical) direction. (c) Unit cell of the molecular array, where the large black cross represents the ZnTPP molecule, the small crosses the center of the phenyl groups and the open (filled) circles the position of the downward (upward) pyrrole groups.

directions of the Au(111) surface. Although present in Figure 3.8, the underlying HB structure cannot be clearly seen. However, via Fourier transform analysis, the HB soliton walls can be enhanced and used as a reference in order to place the molecular array within the Au(111) atomic structure. Figure 3.9b shows a model of the Au(111) surface where the HB soliton walls are oriented parallel to the [11$\bar{2}$] direction. Within the error bar of our measurements, each ZnTPP molecule can be centered on a top site of a Au surface atom, consistent with what has been observed for most transition metal TPP molecules[13, 33, 34, 36, 38, 41, 52, 144, 163, 173, 187, 194, 199]. Assuming the molecular dimensions of the free molecule, the adsorption site of one atom of the molecule establishes the registry of the molecular lattice with respect to the underlying Au lattice. Using this assumption, a two dimensional lattice is defined for the molecular overlayer: a 13.1 Å (represented by a red line) by 12.6 Å (represented by a blue line) rectangular unit cell. The molecular lattice is rotated by an angle of 19° with respect to the [11$\bar{2}$] direction of the Au(111) surface, value in good agreement with the experimental angle of 17°$\pm$3° shown in Figure 3.6. The azimuthal orientation of the molecule

with respect to the substrate is indicated by the schematic molecular diagram in Figure 3.9. The major axes of the molecule are experimentally found rotated ∼15° counterclockwise from the $[11\overline{2}]$ and $[\overline{1}10]$ directions of the Au(111) surface. This places the upwardly distorted pyrrolic groups oriented 30° with respect to the $[\overline{1}10]$ direction, and the downward distorted pyrrolic group rotated 30° from the $[11\overline{2}]$ direction. The downward distorted pyrrole groups are thus found on a top site of the Au lattice, whereas the upward bent pyrrole groups are found at hollow sites. This is in good agreement with previous low temperature STM measurements of single AuTPP molecules adsorbed on Au(111).[124] In this geometry, the phenyl groups are located roughly above hollow sites, with one pair of phenyls at hcp sites and the other pair at fcc sites. The corresponding molecular array can be described in terms of matrix notation:

$$\begin{pmatrix} A \\ B \end{pmatrix} = \begin{pmatrix} 5 & -2 \\ -1 & 5 \end{pmatrix} \begin{pmatrix} a \\ b \end{pmatrix}, \tag{3.1}$$

where $\left(\begin{smallmatrix} A \\ B \end{smallmatrix}\right)$ are the unit cell vectors of the molecular overlayer and $\left(\begin{smallmatrix} a \\ b \end{smallmatrix}\right)$ the unit cell vectors of the Au(111) surface along the $[\overline{1}10]$ and $[\overline{1}01]$ directions, respectively. With this binding geometry, the resulting molecular density is 5.7×10^{13} molecules/cm^2, which agrees well with previous investigations of MTPPs on Au(111)[33, 197, 199] and Ag(111)[13].

Monolayer regime of ZnTPP on Au(111) from multilayer sublimation

In contrast to what is found when molecules are deposited at room temperature to build up a monolayer, when a monolayer of ZnTPPs is produced by thermal desorption of a multilayer, the molecular organization described above is not guaranteed anymore as shown in the STM image of Figure 3.10. When compared to Figure 3.8, it is clear that the symmetry of the molecular lattice, the relative orientation of neighboring molecules and the registry of the molecules with respect to the Au(111) surface are different from what was found for a monolayer built-up at room temperature. A monolayer obtained from the thermal desorption of a multilayer results in a molecular layer consisting of rows rotated slightly less than 30° from the soliton walls (i.e., the $[11\overline{2}]$ direction), with molecules in adjacent rows offset by roughly a half-molecule dimension and rotated by 60°. The inset image of Figure 3.10 (taken at -2 V) shows that the molecules exhibit the two-fold symmetry indicative of inequivalent pyrrole groups, as was found in the case of room temperature deposition in Figure 3.8. However, now the orientation of the upper and lower pyrrole groups is rotated from one row to the next. We note that, in some locations on the surface, islands of the nearly-square lattice coexisted within this new geometry, however the latter geometry was the dominant structure. It is possible that the relative amount of these two phases is temperature dependent, however no

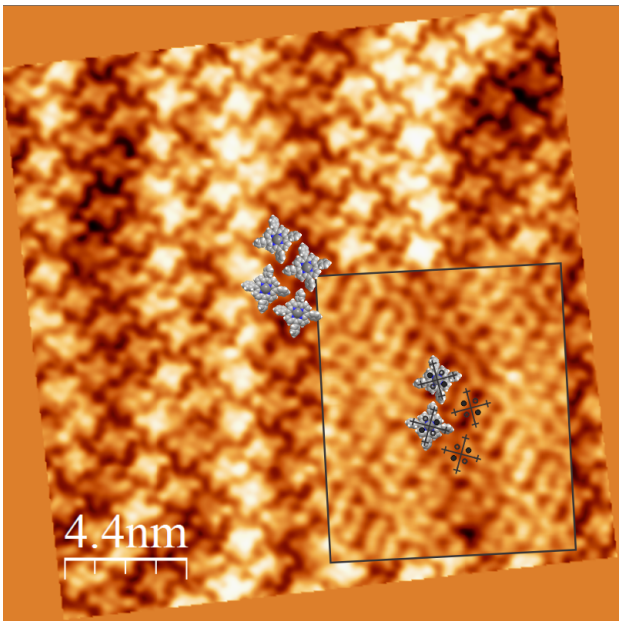

Figure 3.10: High resolution room temperature STM image of ZnTPP on Au(111) prepared from a multilayer, taken at V = -1.4 V and (inset) -2.0 V. Two orientations of ZnTPP molecules are present, each differing by a 60° rotation. At higher bias the two-fold symmetry of the ZnTPP molecules becomes visible. Bright lobes (dark lobes) are interpreted as pyrrole groups farther from (closer to) the surface and are denoted with a filled circle (empty circle). Large image: 22×22 nm, I = 0.5 nA. Inset image: 9×10 nm, I = 0.5 nA

systematic investigation of this question was conducted in this study.

Similar to what had been observed for a room temperature deposited monolayer, an underlying HB reconstruction coexists with the ZnTPP molecular array, and the dimensions of the HB pattern in the $[\bar{1}10]$ direction are identical to those measured on a pristine Au(111) surface. The HB pattern can thus be used for the determination of the molecular lattice in registry with the substrate surface directions as shown in Figure 3.11. Assuming that the ZnTPPs are centered on a top site atom of the Au surface, the unit cell can be defined as a parallelogram that contains two ZnTPP molecules. The longer side of the unit cell measures 32Å (red lines) and is rotated clockwise 20° with respect to the $[11\bar{2}]$ direction, while the smaller side of 13.2Å (blue lines) is rotated anticlockwise 42° with respect to the $[11\bar{2}]$ direction. Within the array, each molecule is rotated by 60° from one row to another in the largest direction of the unit cell, and oriented so as to place the downward bent pyrrole groups on top sites of the Au surface and the upward pyrrole groups on hollow sites. In this geometry, the phenyl groups are all found in hollow sites. Thus, although the molecular array obtained from an annealed multilayer is different from the one observed for room temperature deposition, the local adsorption sites of each individual molecule are identical. This information is summarized in Figure 3.11 using the same notation as in Figure 3.9.

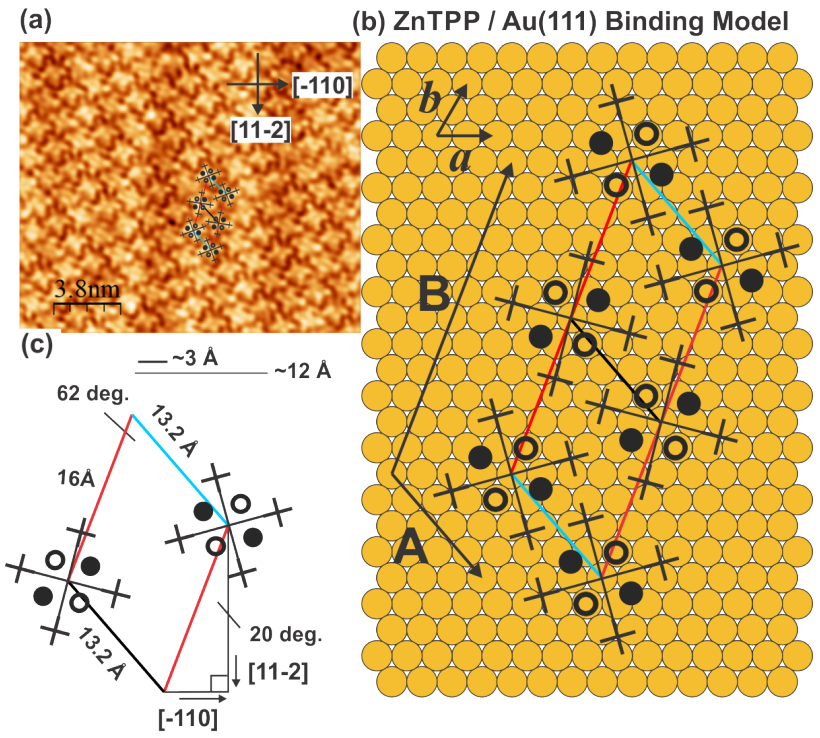

Figure 3.11: Binding model for a monolayer of ZnTPP on Au(111), obtained from multilayer desorption. (a) STM image from which the model is based. (b) Schematic packing model on a fcc (111) surface. The binding geometry of a monolayer resulting from multilayer desorption is notably different from the nearly-square lattice seen from direct deposition in that two molecular phases coexist, one rotated 60° with respect to the other. The HB soliton walls run parallel to the $[11\bar{2}]$ (vertical) direction. (c) Unit cell of the molecular array, where the large black cross represents the ZnTPP molecule, the small crosses the center of the phenyl groups and the open (filled) circles the position of the downward (upward) pyrrole groups.

Within this geometry, the packing density is about 5.4×10^{13} molecules/cm^2, which is slightly less densely packed than the rectangular geometry (5.7×10^{13} molecules/cm^2). The corresponding molecular array can be described in matrix notation as follows:

$$\begin{pmatrix} A \\ B \end{pmatrix} = \begin{pmatrix} 5 & -4 \\ -2 & 12 \end{pmatrix} \begin{pmatrix} a \\ b \end{pmatrix}, \tag{3.2}$$

where $\left(\begin{smallmatrix} A \\ B \end{smallmatrix}\right)$ are the unit cell vectors of the molecular overlayer and $\left(\begin{smallmatrix} a \\ b \end{smallmatrix}\right)$ the unit cell vectors of the Au(111) surface along the $[\bar{1}10]$ and $[\bar{1}01]$ directions, respectively.

This new molecular overlayer could be the result of several possible factors. First, a reorganization of the Au surface upon annealing could favor a new local geometry for the ZnTPPs. However, this explanation is unlikely as the HB reconstruction, apparently undisturbed, is still visible in Figure 3.10. Second, assuming that the packing geometry at the surface is dominated by interactions of the phenyl groups, a new molecular lattice could imply a thermally-induced intramolecular alteration has

occurred. However, the commonly observed structures formed by TPPs upon dehydrogenation and rehybridization result in a planar molecular geometry which, as seen in Figure 3.10, is not the case here.[52, 194] For these reasons we conclude that the molecules remain intact. A possible mechanism giving rise to the molecular ordering found for the annealed multilayer approach is discussed in the next section.

Surface stress effects

Figure 3.12 contains three STM images obtained from (a) a clean Au(111) surface, (b) a near-monolayer room temperature deposited ZnTPP/Au(111), and (c) a near-monolayer obtained from desorption of a ZnTPP multilayer. In these three STM images, the typical HB soliton walls are clearly visible and their separation in the $[\bar{1}10]$ direction is identical. In Fig.3.12a, the domain length of the HB reconstruction, in other words the length of the straight regions of the soliton walls, is nominally ∼20 nm. However, when a ZnTPP monolayer is prepared at room temperature, the domain length is vastly increased to ∼ 100 nm in Figure 3.12b. When the monolayer is prepared from the desorption of a multilayer as shown in Figure 3.12c, the domain length is the same as the one measured on a clean Au(111) surface.

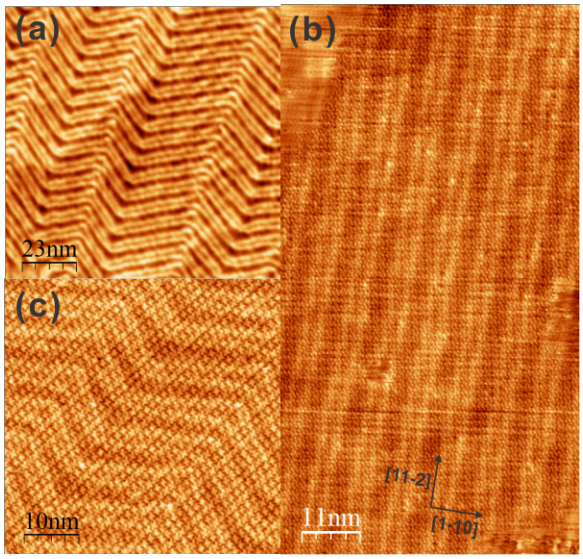

Figure 3.12: Typical HB structure aspect for different surface preparation: (a) Clean Au(111), (b) near-monolayer of room temperature deposited ZnTPP molecules and (c) monolayer coverage obtained using the annealed multilayer preparation method.

The HB reconstruction arises on the clean Au(111) surface as the result of anisotropic tensile surface stress, with tensile stress along the $[11\bar{2}]$ direction (i.e., parallel to the soliton walls) exceeding that along the $[\bar{1}10]$ direction (i.e., perpendicular to the soliton walls)[125]. From fundamental

principles, a surface which possesses an orientational degeneracy of reconstructed phases (such as the 3-fold degeneracy of Au(111)) and an anisotropic stress tensor will spontaneously form elastic stress domains [9, 71, 125]. Furthermore, an increase in surface stress anisotropy leads to decreased domain size [9, 125]. This behavior was shown experimentally through the direct application of mechanical stress on a Au(111) surface[151] and indirectly by inducing stress through adsorption of iron phthalocyanine and perylene on Au(111)[164]. We thus attribute the extended domains observed for the as-deposited ML of ZnTPP on Au(111), in Figure 3.12b, to a decrease of the in-plane surface stress anisotropy felt by the Au(111) surface.

Substrate surface reorganization in the presence of a molecular adsorbate is typically attributed to a combination of several effects: i) charge transfer between the molecular adsorbate and the substrate upon chemical hybridization[164]; ii) charge redistribution within the adsorbate and within the substrate surface without explicit hybridization across the interface[164]; iii) purely mechanical stress applied by the adsorbate on the Au surface atoms[151]. In reality, the boundaries between these three effects are quite blurred, as any mechanical effect will be translated into electronic charge redistribution as well. A weakly interacting adsorbate, such as ZnTPP, is not expected to undergo significant hybridization with the Au(111) surface atoms, suggesting that hybridization may be the weakest of all contributions.

In the adsorption model presented in Figure 3.9, ZnTPPs adsorb with a two-fold rather than a four-fold symmetry. In particular, the upward pyrrole groups have the same orientation parallel to the long-dimension of the molecular unit cell (i.e., the red line of Fig.3.9). To a first order, there is thus an inherent anisotropy due to pyrrole groups bent toward or away from the surface. Given the observation that the HB domain length increases with this adsorption scheme, it can be deduced that the molecular adsorbates reduce the surface stress anisotropy between the $[11\overline{2}]$ and $[\overline{1}10]$ directions. In contrast, in the adsorption model of Figure 3.11, the rotation of the ZnTPPs in alternated rows and the resulting orientation of the inequivalent pyrrole group, removes the strong anisotropy observed in Figure 3.9, resulting in a quasi-isotropic contribution to the stress of the pristine Au(111) surface. Thus the HB domain length of Figure 3.12 is found to be close to that of the clean surface.

Although the exact origin of the anisotropic surface stress is difficult to establish, it is most likely linked to the inequivalent pyrrole orientation. Thus, it could be proposed that pyrrole groups closer to the surface Au atoms exert a force on these atoms, altering the pristine surface energetics. Recall that in Figure 3.9, the HB runs parallel to the vertical $[11\overline{2}]$ direction. Drawing a line connecting two downward pyrroles through the Zn atom of a given ZnTPP results in a line rotated by 30° with respect to the vertical. Thinking of this as a surface stress vector, then its largest component is in the

vertical direction, and smaller component along the horizontal within the binding model of Figure 3.9. If the downward pyrroles apply compressive stress, this stress is preferentially applied along the $[11\bar{2}]$ direction (i.e., the molecules decrease the tensile stress along the $[11\bar{2}]$ direction), which results in overall decreased surface stress anisotropy and larger HB domains. Alternatively, phenyl group rotations with respect to the macrocycle also introduce a two-fold symmetry as the phenyl orientations are intimately linked to pyrrole saddling[145], and likely play a role in the observed stress effects.

An estimation of the applied stress in Figure 3.9 is possible from earlier studies. Theoretical estimates of the surface stress anisotropy in the Au(111) surface atomic layer are approximately 100 ± 20 meV/Å^2.[125] Compressive surface stress anisotropy estimates for perylene and iron phthalocyanine on Au(111) are 6 meV/Å^2 and 164 meV/Å^2, respectively[164]. The large stress difference between the two species is due to the particular nature of the adsorbates bonding to the surface: weak adsorption in the case of perylene versus important Fe 3d states hybridization to Au surface atoms in the case of FePC. We estimate the surface stress anisotropy required to form 100 nm domains to be approximately 45 meV/Å^2.[1] This value being significantly lower than that for FePC seems reasonable considering the weaker interaction expected between ZnTPPs and Au(111).

3.2.3 ZnTPP on Au(111) Summary

In this work, a comprehensive study of the adsorption of ZnTPP molecules on a Au(111) surface using STM is presented, with a particular emphasis on the molecular geometry with respect to the atomic structure of the underlying Au substrate and on the consequences of thermal contribution on the overall system reorganization.

In the case of room temperature deposition, ZnTPP molecules adsorb first at the high coordination step edge sites of the surface, and subsequent nucleation of molecular islands is observed between domain walls of the HB reconstruction. No isolated molecule is observed on terraces at room temperature indicating a weak surface-molecule interaction and favoring a large molecular mobility.

For near-monolayer coverage, an adsorption model is proposed, where the ZnTPP molecules form a rectangular array in registry with the Au surface atoms. Within this model, each ZnTPP is submitted to the same local environment of the Au surface atoms: the molecules are centered on the top site of the Au surface, downward and upward bent pyrroles are found on top- and hollow-sites, respectively, leaving the phenyl groups in hollow sites. For this system, occurrences of unusually long HB domains were observed, that are explained in terms of reduction of the surface stress anisotropy by the adsorbate.

Obtaining a surface via desorption of a ZnTPP multilayer at 265°C enables a new molecular packing, where the molecular array is described by a larger parallelogram lattice, but still allowing for ZnTPP molecules to assume a local environment on the Au surface that is similar to the one observed for room temperature deposition: the molecules are centered on the top site of the Au surface, downward and upward bent pyrroles are found on top- and hollow-sites, respectively, allowing the phenyl groups in hollow sites. However, the symmetry of this molecular arrangement resulting in quasi-isotropic surface stress, the typical domain size of the HBs is found close to the domain size measured on a clean Au surface. Annealing the system to higher temperatures results in molecular desorption from the surface.

This study finds that in the ZnTPP on Au(111) system, adsorption is characterized by a fine interplay between molecule-surface adsorption energy, molecule-molecule interactions and Au surface stress, with none of the energetics dominating another one. Finally the HB reconstruction appears as a valuable source of information to understand adsorption properties of a self-assembled monolayer.

3.3 ZnTPP on Ag(111)

3.3.1 Self-Assembled ZnTPP Monolayer on Ag(111): Direct Deposition

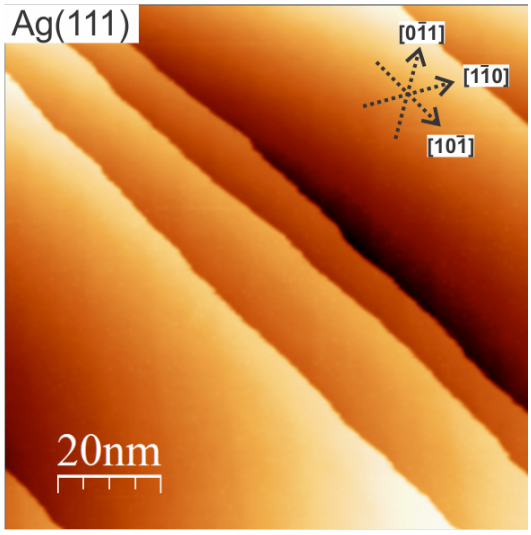

Figure 3.13: Clean Ag(111) surface showing large terraces. Image scanning parameters: 100×100nm, -2.0V, 1.0nA.

Ag(111) presents an opportunity to explore the effects of a different noble metal with the same symmetry as Au(111) on the ZnTPP self-assembly. An STM image of clean Ag(111) prepared prior to *in situ* ZnTPP deposition is shown as Figure 3.13. After sublimation deposition of a approximately 0.1 ML of ZnTPPs onto the room-temperature Ag(111) surface, ZnTPPs organize along step edges

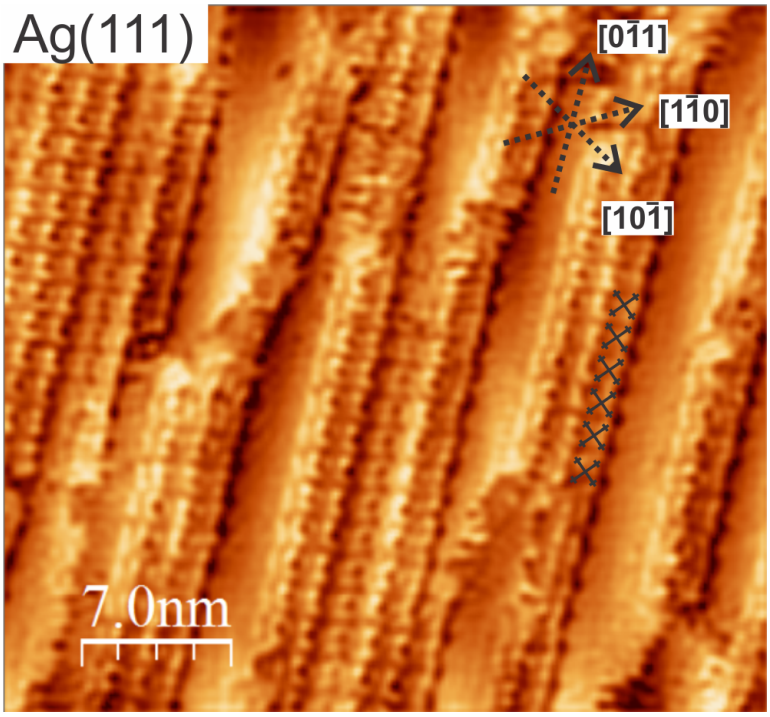

Figure 3.14: Direct-deposited low coverage showing ZnTPP molecules tracing step edges, however not enough to populate terraces. Image scanning parameters: 35 × 35nm, -1.5V, 0.5nA.

as shown in Figure 3.14. Note also that the step edges align with ZnTPPs and create straight stretches of step edge, implying possible Ag surface atom reorganization just as in the Au(111) case, however in this image the system has not been annealed. The room temperature reorganization of substrate surface atoms to align with ZnTPPs possibly indicates a stronger molecule-substrate interaction than ZnTPP on Au(111).

Directly depositing a near-monolayer of ZnTPPs on Ag(111) results in the formation of multiple domains on a given terrace, as shown in Figure 3.15. Three domains labelled I, II, and III correspond to ZnTPP organization with respect to the three high symmetry directions of the Ag(111) surface. A row of ZnTPPs in domain I aligns with the [1$\bar{1}$0] direction, domain II with the [0$\bar{1}$1] direction, and domain III with the [10$\bar{1}$] direction. In addition to the three domains, three additional domains exist that are mirrored with respect to the substrate surface atom high symmetry directions. These additional domains are shown as II$'$ and III$'$, delineated by dashed black lines. Note that while I$'$ is not visible in this frame, it is observed in other images. To map from III to III$'$, mirror the molecule about the Ag [1$\bar{1}$0] direction, and to map from II to II$'$ mirror about the [10$\bar{1}$] direction. This is similar to the three ZnTPP domains observed on Au(111) in Figure 3.6.

A high resolution STM image of this organization near a series of step edges is shown as Figure 3.16. The domain on the large terrace lines up with the step edge near the upper right corner,

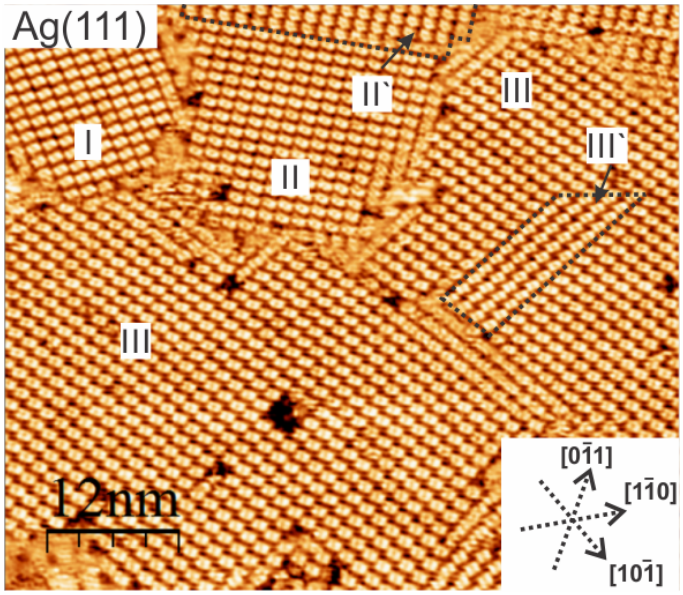

Figure 3.15: Direct-deposited near-monolayer showing ZnTPPs self-assembled into domains I, II, and III. Molecules appear with the saddle conformation at this tunneling bias. A row of ZnTPPs in Domain I aligns with the $[1\bar{1}0]$ direction, II with $[0\bar{1}1]$, and III with $[10\bar{1}]$. Also shown are mirrored domains of II and III labelled II′ and III′, respectively. The mirror plane, i.e., the plane across which a mirror operation is performed on the individual molecules to map to the adjacent domain, for II and II′ is the $[10\bar{1}]$ direction, and for III and III′ is the $[1\bar{1}0]$ direction. Image scanning parameters: 60×50nm, +1.7V, 0.5nA.

however the step edges in the upper left corner seed a domain of another orientation, which is evidenced by three rows of ZnTPPs extending from the step edge into the large terrace. The ZnTPPs in each domain arrange in a nearly-square unit cell. This image also shows that ZnTPPs straddle step edges with two phenyl groups and roughly half of the molecule hanging over the step edge. In this way, ZnTPP phenyl groups behave similar to a grappling hook, enabling higher coordination and in turn stronger molecule-substrate interaction at step edges. The inset image is taken at a bias that reveals the ZnTPP saddle-conformation, with bright lobes corresponding to upward pointing pyrroles (filled circles). Though not shown here, annealing this direct-deposited system to 260°C does not alter the binding geometries; only nearly-square organizations are observed, indicating that the nearly-square organization is a stable configuration or an energetic minimum. In contrast, annealing ZnTPP/Au(111) in the multilayer-desorbed monolayer preparation resulted in a reconfiguration of both ZnTPPs and the substrate surface atoms to minimize the surface stress of the system. Therefore, surface stress likely has a lesser impact on this system compared to Au(111). The nearly-square unit cell observed in this image is described by the binding model shown in Figure 3.18 that will be discussed below for the multilayer-desorption case.

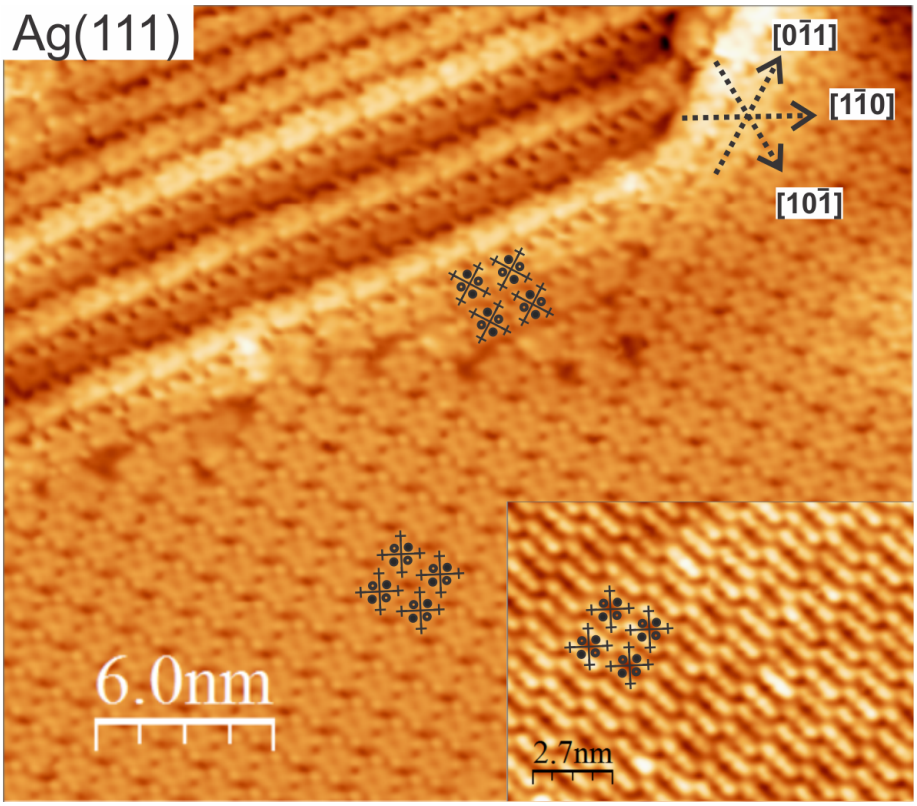

Figure 3.16: High resolution STM image of a direct-deposited near-monolayer of ZnTPPs on Ag(111). The inset is taken at a tunneling bias that reveals the ZnTPP saddle conformation. Schematic ZnTPPs are overlaid to elucidate the adsorption geometry. Image scanning parameters: 30×26nm, -1.0V, 0.5nA; (Inset) 13×10nm, +1.5V, 0.5nA.

3.3.2 Self-Assembled ZnTPP Monolayer on Ag(111): Multilayer Desorption

A representative STM image showing monolayer coverage of ZnTPPs on Ag(111) obtained via multilayer desorption is shown as Figure 3.17. The larger portion of Figure 3.17 was obtained with negative sample bias (i.e., tunneling from the occupied states). The striking long range self-assembled order is characterized by a repeating pattern of a large bright ring, interpreted as the Zn-porphyrin macrocycle, surrounded by four small protrusions, associated with the four meso-phenyl groups of the ZnTPP molecule, just as with Au(111) and the direct-deposited monolayer of Ag(111). Again, the low tunneling intensity at the center of the porphyrin rings, at the location of the Zn ions, can be tentatively explained by considering that the Zn ion has a filled d orbital ($3d^{10}$) with states that are too deep to be probed by the tunneling biases used (-2V to +2V), thus its expected contribution to the tunneling current is small.[6] The inset in Figure 3.17 is obtained using a tunneling bias that reveals the saddling conformation for each ZnTPP molecule, rather than the four-fold symmetry observed at other biases.

It is evident from this image that the ZnTPPs adsorb with the porphyrin macrocycle parallel to

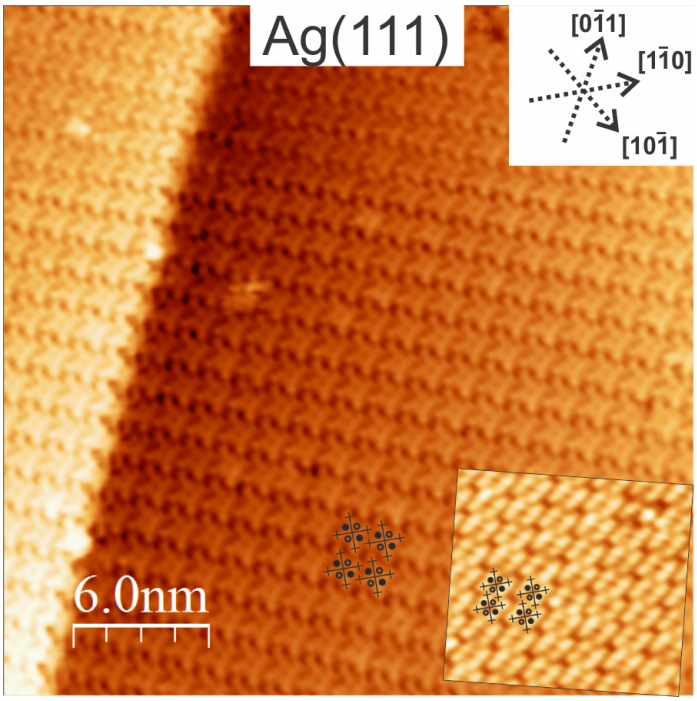

Figure 3.17: Monolayer coverage of ZnTPP on Ag(111) achieved by annealing multilayer coverage to 500K, with schematic ZnTPPs shown as black crosses. The inset images are taken at a bias which reveals the two-fold conformation of the ZnTPPs, interpreted as the pyrrole groups bending toward (open circles) or away from (filled circles) the substrate surface. Primary image scanning parameters: 30×30nm, -1.2V, 0.3nA. Inset image scanning parameters: 10×10nm, +1.5V, 0.5nA.

the substrate surface, just as with Au(111) and the direct-deposited case for Ag(111). Furthermore, the ZnTPPs self-organize into a nearly-square lattice of 15.0×14.5Å, which is the same ordering as that of the direct-deposited monolayer. Similar ordering has been found for TPPs on metal surfaces, and is primarily driven by the intermolecular phenyl-phenyl interactions[13, 20, 33–38, 124, 144, 146, 163, 173, 186, 194]. NEXAFS measurements performed by other groups indicate that the phenyl groups are typically oriented approximately 60° with respect to the porphyrin macrocycle when bound to the substrate in a densely-packed monolayer, rather than nearly perpendicular as in the gas phase[52, 186]. The phenyl groups of neighboring molecules may take the form of so-called T-stacking, i.e., perpendicular to one another, or $\pi - \pi$ stacking, i.e., parallel to one another. On noble metal (111) surfaces T-stacking is primarily observed [33, 36, 146, 199], however DFT calculations attempting to describe proper van der Waals interactions between benzene molecules with varied relative orientations do not strongly favor pure T-stacking over pure $\pi - \pi$ stacking[69].

Having established the geometry of the molecular unit cells, as well as the azimuthal orientation of the ZnTPPs within the unit cell, and knowing the orientation of the high-symmetry directions of the underlying metal substrate from low-energy electron diffraction (LEED) measurements, we can

now align the ZnTPPs to the lattice of the Ag(111) substrate surface. Figure 3.18 shows the binding model for ZnTPPs on Ag(111), in which we use the molecular dimensions of the free molecule and apply the ZnTPP unit cell measurements obtained using STM.

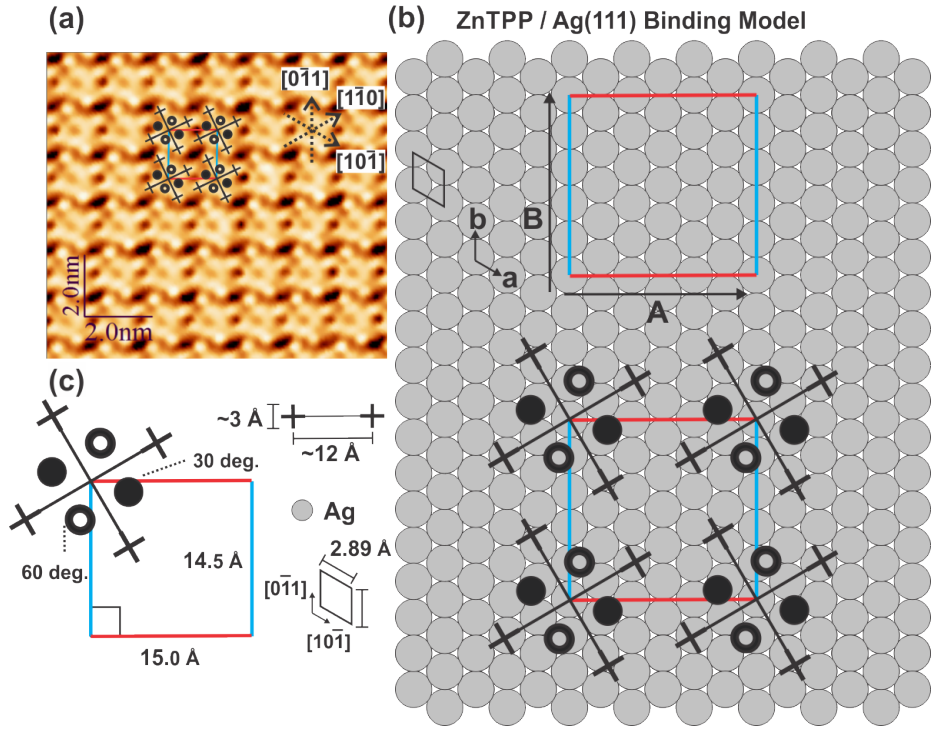

Figure 3.18: (a) Representative STM image on which this model is based. (b) Binding model of schematic ZnTPP molecules with open (filled) circles representing downward (upward) bending pyrrole groups. (c) Unit cell of ZnTPP organization on Ag(111) for a monolayer obtained by multilayer desorption via annealing to 470K. Note that if we fix the central Zn ion to an Ag top site, all molecules adsorb in the same way: downward (upward) pyrroles bind to top (3-fold hollow) sites, and all phenyls bind to 3-fold hollow sites. Image scanning parameters: 19 × 19nm, -1.0V, 0.5nA.

A model for the adsorption of ZnTPPs on the Ag(111) surface is presented in Figure 3.18. A typical STM image used to determine the unit cell of the molecular overlayer and its azimuthal orientation is shown in Figure 3.18a, while the corresponding model is schematically represented in Figure 3.18b. A model for the adsorption of ZnTPP is given in Figure 3.18b and characteristic distances are shown in Figure 3.18c. It is assumed that the ZnTPP is centered on top of an underlying Ag atom, consistent with what has been observed for most transition metal TPP molecules on noble metal surfaces[13, 33, 34, 36, 38, 41, 52, 144, 146, 163, 173, 187, 194, 199]. Using the experimental nearly-square unit cell of 15.0 × 14.5Å and measured azimuthal orientation, all the significant components of the ZnTPPs molecules are in registry with substrate atoms; phenyls are above threefold hollow and atop sites, and downward and upward pyrroles are above atop sites. The corresponding molecular array can be described in matrix notation:

$$\begin{pmatrix} A \\ B \end{pmatrix} = \begin{pmatrix} 6 & 3 \\ 0 & 5 \end{pmatrix} \begin{pmatrix} a \\ b \end{pmatrix} \tag{3.3}$$

where (***AB***) are the unit cell vectors of the molecular overlayer, and (***ab***) the unit cell vectors of the Ag(111) surface along the $[10\bar{1}]$ and $[0\bar{1}1]$ directions, respectively. The packing density for this organization is 4.6×10^{13} molecules/cm^2.

3.3.3 ZnTPP on Ag(111) Summary

In this section, ZnTPPs on the Ag(111) surface are investigated for both direct-deposited and multilayer desorbed monolayers. Direct-deposited low-coverage ZnTPPs first adsorb to Ag(111) step edges, with Ag step edges conforming to the molecular organization. With greater ZnTPP coverage, islands nucleate from step edges onto terraces. ZnTPPs organize into a nearly-square unit cell in domains that are in registry with the high symmetry substrate directions. Additionally, a binding model is proposed in which all molecules bind to the substrate surface in the same way. This binding model describes both the direct-deposited and the multilayer-desorbed monolayers. Annealing the system, either to obtain a monolayer via multilayer desorption or to test the stability of a direct-deposited monolayer, does not alter the ZnTPP organization, in stark contrast to what is observed on Au(111). A detailed comparison of ZnTPP/Ag(111) compared to Au(111) is found in the conclusions of this chapter.

3.4 ZnTPP on Ag(100)

3.4.1 Self-Assembled ZnTPP Monolayer on Ag(100): Direct Deposition

To further probe the adsorption behavior of ZnTPPs on noble metals, we study ZnTPPs on the Ag(100) surface to compare how different surface symmetries of the same metal effect the adsorption geometry. Figure 3.19 shows an STM image of the clean Ag(100) surface. Atomic resolution imaging of the Ag(100) surface is shown as Figure 3.20. Directly depositing a sub-monolayer of ZnTPPs results in the formation of islands near step-edges, as shown in Figure 3.21. The streaky imaging is the result of the STM tip interacting with molecules moving too quickly to be imaged on the terraces. Note also that the Ag step edges appear aligned with the ZnTPP overlayer, even though this system has not been annealed in the presence of molecules. This suggests room-temperature Ag surface atomic reorganization due to the presence of ZnTPPs. Additionally, since the ZnTPPs first adsorb to Ag step edges due to higher coordination with Ag surface atoms, the island then grows outward from the step edge onto the terrace.

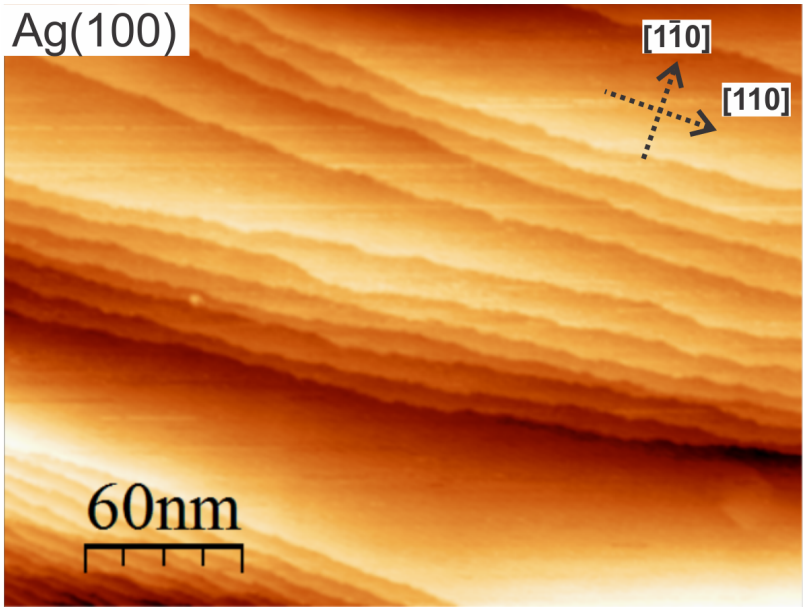

Figure 3.19: STM image of the clean Ag(100) surface, with step edges parallel to the Ag [110] direction. Image scanning parameters: 300 × 230nm, -2.0V, 1.0nA.

Figure 3.22 shows a near-monolayer of ZnTPPs on Ag(100) exhibiting self-assembled order described by two rows in a roughly-square arrangement adjacent to one row that is offset by a half-molecule distance. This creates a striking pattern that extends nearly perfectly along each row for hundreds of nanometers (limited by terrace size), and with very few mistakes perpendicular to the rows. A high-resolution STM image of a direct-deposited near-monolayer of ZnTPPs is shown as Figure 3.23, with schematic ZnTPPs overlaid showing the centers of phenyl rings as small crosses, and upward (downward) bent pyrroles as filled (open) circles. The schematic ZnTPPs outline the rectangular unit cell of the pattern, containing three molecules per unit cell. It is clear that this "2+1" pattern exhibits a 45° azimuthal rotation between the different rows, in addition to a half-molecule offset. Henceforth, the more frequently occurring ZnTPPs that make up the "2" of the "2+1" pattern will be referred to as majority rows, and the "1" will be referred to as minority rows. Obtaining an image at a tunneling bias that reveals the saddle-conformation of the ZnTPPs, shown as the inset of Figure 3.23, reveals the orientation of upward and downward bent pyrroles with respect to the ZnTPP unit cell and elucidates the azimuthal rotation from the majority to minority rows.

Figure 3.24a shows a portion of the STM image from Figure 3.23 with the ZnTPP unit cell overlaid, from which the unit cell dimensions and azimuthal orientations are measured. Assuming the dimensions of the gas-phase ZnTPP molecule, ZnTPP schematic molecules and unit cell dimensions are overlaid on a model Ag(100) surface, shown as Figure 3.24b. Figure 3.24c elucidates

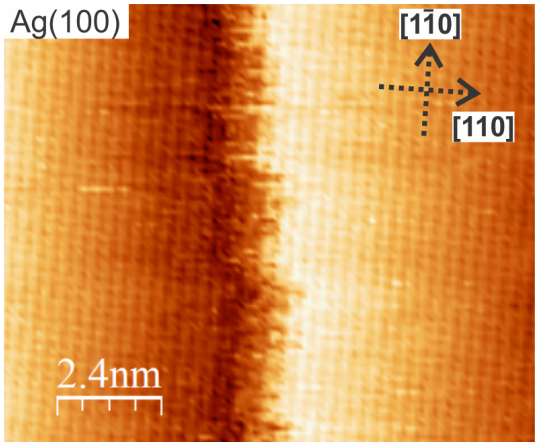

Figure 3.20: Atomic resolution STM image of the clean Ag(100) surface. Image scanning parameters: 12 × 10nm, -1.0V, 0.5nA.

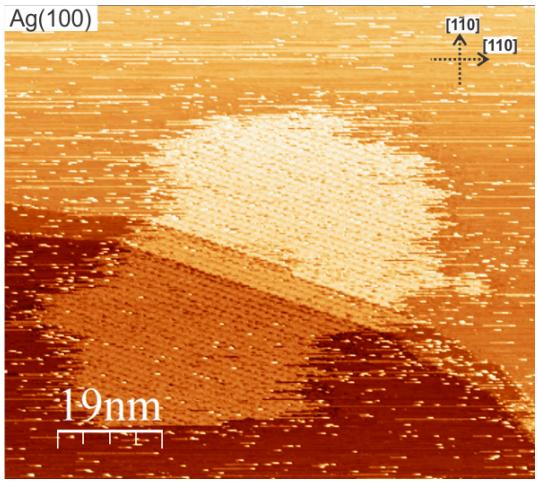

Figure 3.21: Direct-deposited low coverage of ZnTPPs on Ag(100). ZnTPP islands form outward from step edges, and step edges align with ZnTPP overlayer. Image scanning parameters: 100 × 100nm, -1.0V, 0.5nA.

the dimensions and azimuthal orientations within the unit cell. Placing the Zn atoms on a top site, the ZnTPPs in the square portion of the unit cell all reside above the same Ag sites; phenyls centered above top sites, and pyrroles centered between four fold hollow and top sites. The azimuthally rotated molecule has phenyl rings centered above four fold hollow sites, with both upward and downward pyrroles above top sites. This unit cell consists of three molecules and is a rectangle with dimensions of 38.7×12.9Å, which results in a packing density of 6.01 × 10^{13}molecules/cm^2. Expressing the overlayer in terms of the Ag(100) high symmetry directions gives the following,

$$\begin{pmatrix} A \\ B \end{pmatrix} = \begin{pmatrix} 12 & 6 \\ -2 & 4 \end{pmatrix} \begin{pmatrix} a \\ b \end{pmatrix} \tag{3.4}$$

where (**AB**) are the ZnTPP unit cell vectors, and (**ab**) are the [110] and [1$\bar{1}$0] high symmetry

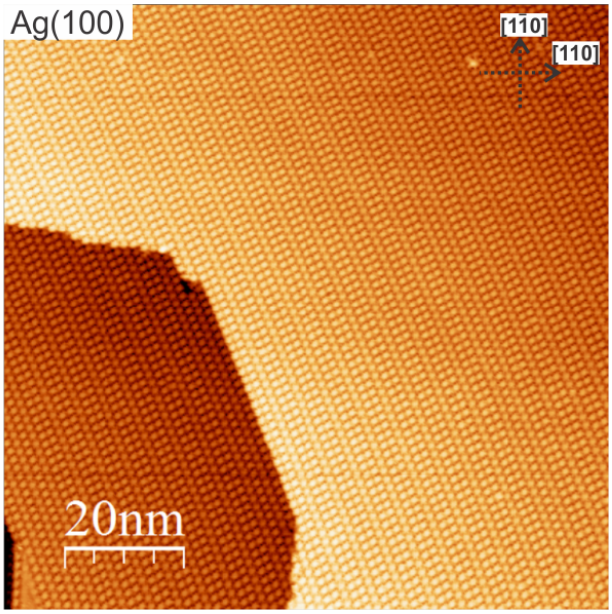

Figure 3.22: Direct-deposited near-monolayer of ZnTPPs on Ag(100) showing striking low-defect large scale order. This "2+1" pattern continues nearly perfectly with one defect row near the right of the image. Note the step edge tracing the pattern as well as defect rows in the pattern on the lower terrace possibly induced by the step edge. Image scanning parameters: 100 × 100nm, -1.2V, 0.5nA.

directions of the Ag(100) surface, respectively.

To test the stability of the monolayer, the system is annealed to 240°C and allowed to come to room temperature before imaging. The STM image of Figure 3.25 shows the result of annealing the near-monolayer from Figure 3.23. Two domains are visible, both of which are square, however the larger domain matches the orientation of the majority ZnTPPs in the "2+1" pattern, whereas the smaller domain corresponds to the minority orientation seen earlier (i.e., 45° rotated ZnTPPs). In this case, both domains form square unit cells. In the as-deposited monolayer, the "2+1" pattern consisted of double rows forming squares combined with single rows of 45° rotated ZnTPPs in between. The formation of two adjacent or consecutive minority rows occurred in the as-deposited monolayer, albeit sparsely, however in this annealed case domains several minority rows wide have formed. This marks the beginning of a thermal-induced transition seemingly toward large square domains rather than the "2+1" pattern.

Further annealing the system to 260°C results in completely square domains, as shown in Figure 3.26. Two domains shown in this image appear rotated with respect to the Ag(100) surface, however they are equivalent domains of the same registry with the Ag(100) substrate except for a mirror operation. This mirroring does not change the registry with the substrate, it simply results from a different direction of growth of the ZnTPP island with respect to the substrate. These domains

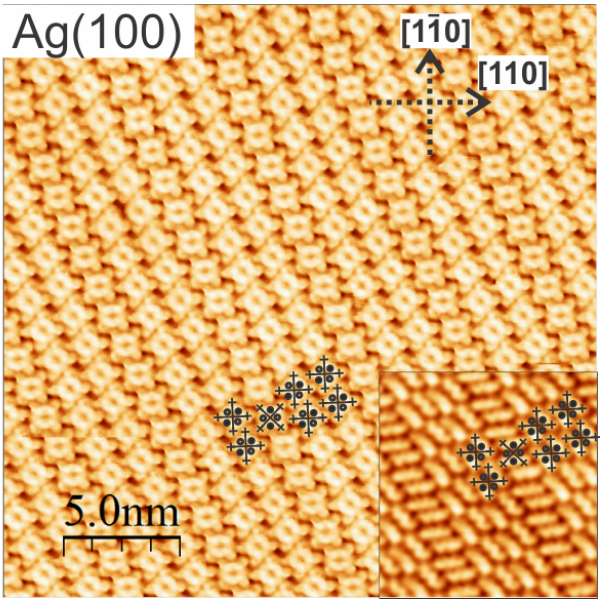

Figure 3.23: Direct-deposited near-monolayer of ZnTPPs on Ag(100). ZnTPPs organize into a highly-ordered array described by two adjacent rows with a square unit cell next to one row of ZnTPPs rotated by 45°. The inset shows the saddle conformation of ZnTPPs upon adsorption and elucidates exactly how the pyrrole groups rotate azimuthally. Schematic molecules are shown as large black crosses, with small crosses indicating the centers of phenyl groups, and open (filled) circles representing downward (upward) pyrroles. Image scanning parameters: 25 × 25nm, -1.0V, 0.3nA; Inset 10 × 10nm, +1.2V, 0.3nA.

match the majority ZnTPP configuration from the "2+1" pattern. The presence of rotated ZnTPP rows or two adjacent domains with a half-molecule offset (as seen in Figure 3.25) were not observed within a given island after this anneal. Thus the thermodynamically favored nearly-square unit cell is achieved by annealing the "2+1" direct-deposited monolayer to 260°C.

3.4.2 Self-Assembled ZnTPP Monolayer on Ag(100): Multilayer Desorption

Recall that annealing the direct-deposited monolayer between 510K and 530K resulted in a gradual transformation from "2+1", to two square domains (510K, Figure 3.25), to one dominant square domain (530K, Figure 3.26). A monolayer obtained via multilayer desorption at 470K, shown as Figure 3.27 reveals two alternating square domains. The domains outlined by black molecules are the same as the majority domains of the "2+1" pattern, whereas the domain outlined by green molecules is the same as the minority domains of the direct-deposited monolayer. Thus, it seems the first layer of molecules for multilayer coverage may organize similarly to the direct-deposited case, even though there are many extra layers of molecules above the first layer during the anneal. Perhaps the overlayers of molecules do not significantly influence the binding geometry of the first layer as the first layer interacts more strongly with the substrate than with other molecular layers.

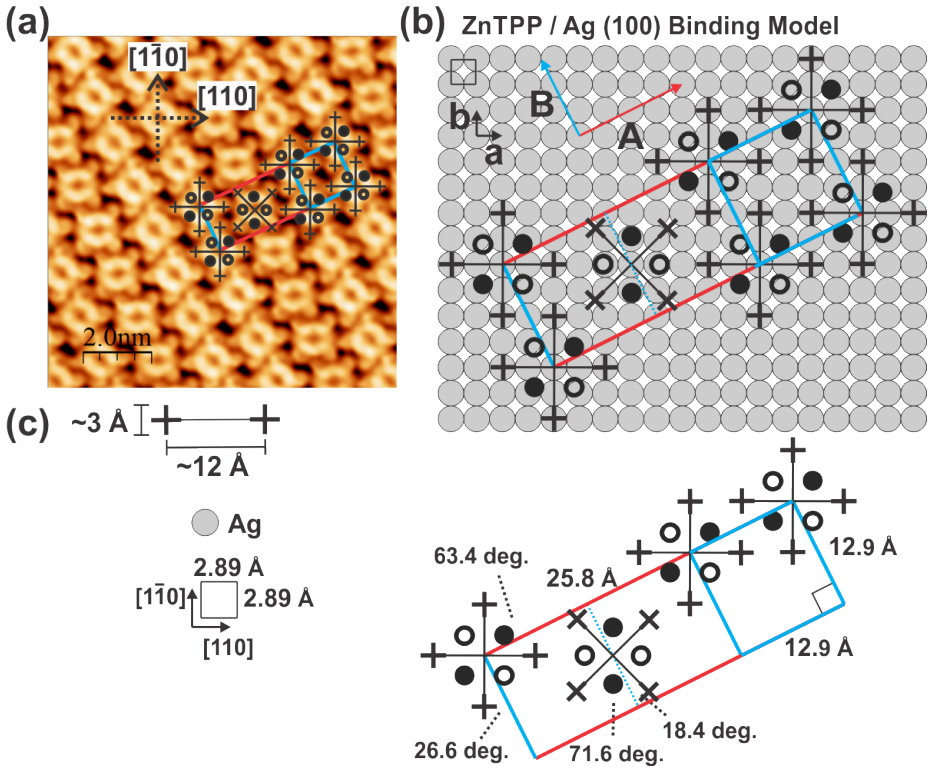

Figure 3.24: (a) Representative STM image on which this model is based. (b) Binding model of schematic ZnTPP molecules with open (filled) circles representing downward (upward) bending pyrrole groups. (c) Unit cell of ZnTPP organization on Ag(100) for a monolayer obtained by direct deposition with sample at room temperature. Image scanning parameters: 10×10nm, -1.0V, 0.5nA.

A higher resolution STM image after annealing this system to 500K is shown as Figure 3.28. The larger portion of Figure 3.28 was obtained with negative sample bias (i.e., tunneling from the occupied states). It is evident from this image that the ZnTPPs adsorb with the porphyrin macrocycle parallel to the substrate surface. Furthermore, the ZnTPPs self-organize into a nearly-square lattice of 12.9×12.9Å. The brighter molecules could be related to metal-free ZnTPPs or to different substrate-molecule interaction due to a localized surface impurity. The inset of Figure 3.28 is obtained using a tunneling bias that reveals the saddling conformation for each ZnTPP molecule, rather than the four-fold symmetry observed at other biases. The upward bent pyrroles are observed as two bright lobes, with the dark lobe in between them connecting the downward pyrroles through the Zn ion. This is represented schematically by superimposed ZnTPP frameworks, with outermost crosses indicating the width and extent of the phenyl groups and the open (filled) circles representing pyrrole groups bending toward (away from) the substrate surface.

Having established the geometry of the molecular unit cells, as well as the azimuthal orientation of the ZnTPPs within the unit cell, and knowing the orientation of the high-symmetry directions of the underlying metal substrate from low-energy electron diffraction (LEED) measurements, we

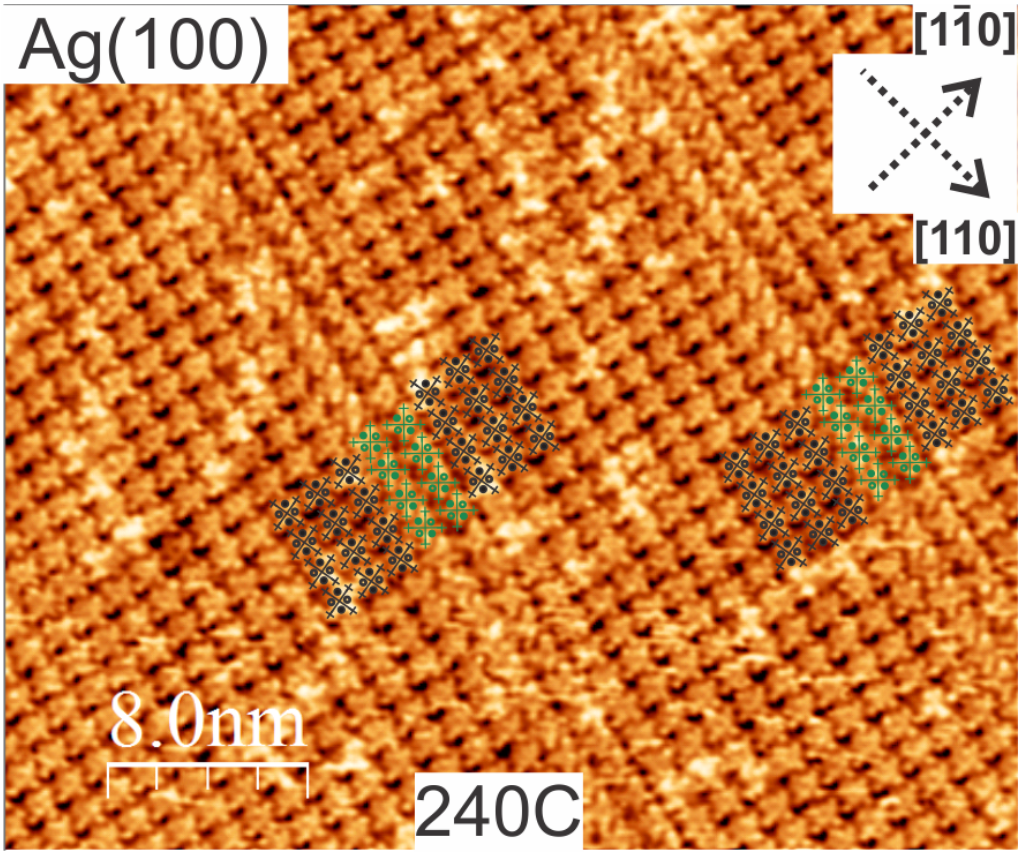

Figure 3.25: This image shows a direct-deposition near-monolayer of ZnTPPs that has been annealed to 240°C, after which one square domain (black molecules; the majority domain in the as-deposited monolayer case) begins to dominate over another square domain (green). Image scanning parameters: 40 × 40nm, -1.0V, 0.5nA.

can now align the ZnTPPs to the lattice of the Ag(100) substrate surface. Figures 3.29 shows the binding model for a monolayer of ZnTPPs on Ag(100) obtained via multilayer desorption, in which we use the molecular dimensions of the free molecule and apply the ZnTPP unit cell measurements obtained using STM.

Figure 3.29a shows an example STM image from which we extract the ZnTPP unit cell dimensions and azimuthal orientations within the unit cell. Figure 3.29b shows a model Ag(100) surface where each gray circle represents a Ag atom, with the ZnTPP unit cell overlaid. Figure 3.29c shows the measured 12.9×12.9Å square unit cell with phenyls axis rotated by 26.6° counterclockwise from the unit cell directions. Centering each ZnTPP on a Ag top site, the resulting arrangement is obtained using the measured ZnTPP unit cell dimensions. In this organization, each ZnTPP molecule has identical binding geometry; the phenyls and pyrroles are located at atop sites of the Ag(100) surface.

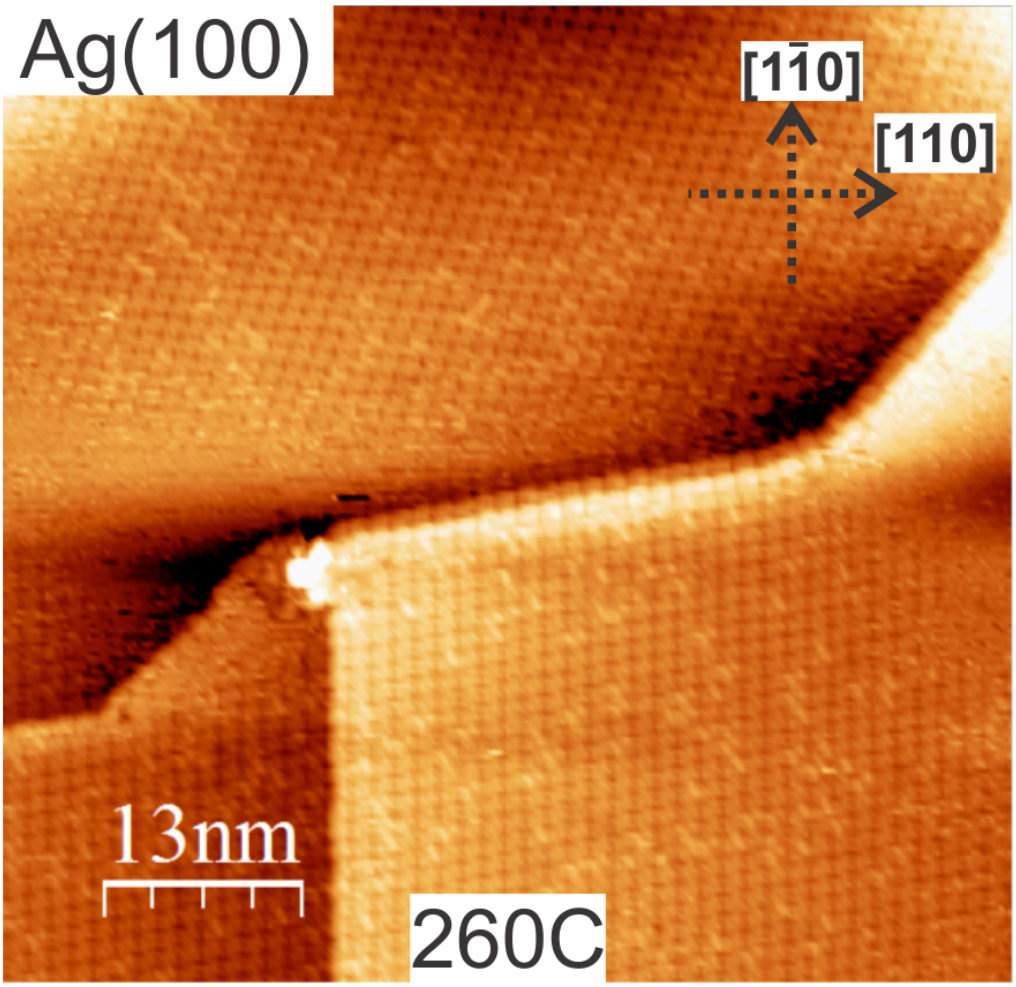

Figure 3.26: This image shows a direct-deposition near-monolayer of ZnTPPs that has been annealed to 260°C. Only one square domain is observed on a given terrace which matches the square pattern (i.e., the "2" of the 2+1 pattern) of the as-deposited system. Image scanning parameters: 65×65nm, -1.2V, 0.5nA.

The corresponding molecular array can be described in matrix notation:

$$\begin{pmatrix} A \\ B \end{pmatrix} = \begin{pmatrix} 4 & -2 \\ 2 & 4 \end{pmatrix} \begin{pmatrix} a \\ b \end{pmatrix} \tag{3.5}$$

where ($\boldsymbol{AB}$) are the unit cell vectors of the molecular overlayer, and ($\boldsymbol{ab}$) the unit cell vectors of the Ag(100) surface along the [110] and [1$\bar{1}$0] directions, respectively. This unit cell matches the square portion of the as-deposited unit cell shown in Figure 3.24 except for a mirror operation across the vertical. The packing density for this organization is 5.9×10^{13} molecules/cm^2, which agrees quite well with previous studies on similar systems[13, 33, 146, 197, 199].

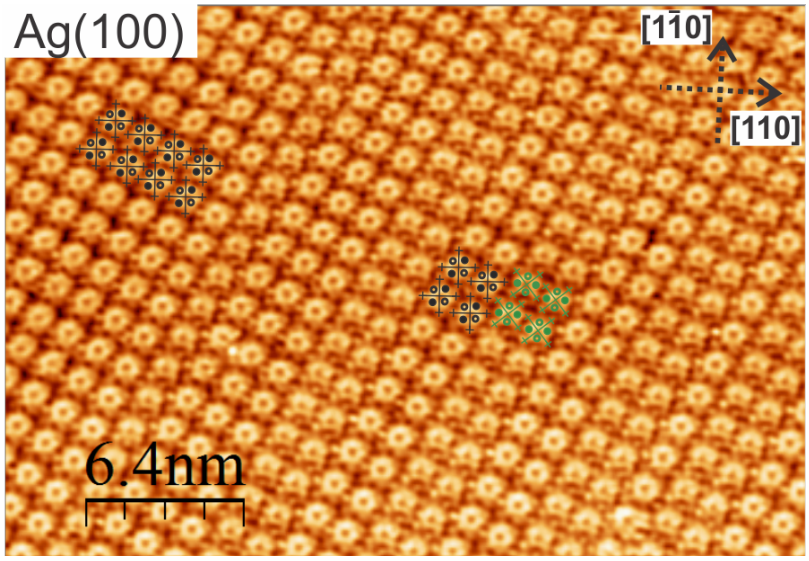

Figure 3.27: Monolayer coverage of ZnTPP on Ag(100) achieved by annealing multilayer coverage to 470K, with schematic ZnTPPs shown as black crosses. Two domains are visible, the more prominent domain is outlined by black schematic molecules, while the smaller domains are outlined by green molecules. Black molecules match the majority domain (the 2 of the "2+1" pattern) observed in the direct-deposited Ag(100) images, while green molecules match the minority domain. Image scanning parameters: 32 × 22nm, -1.0V, 0.3nA.

3.4.3 ZnTPP on Ag(100) Summary

A direct-deposited ZnTPP monolayer on Ag(100) exhibits a striking "2+1" pattern not observed on either of the (111) surfaces discussed earlier. Upon annealing the system, this pattern gradually transforms to one square domain of ZnTPPs. This behavior combined with the observations that Ag step edges align with ZnTPPs possibly indicate that the Ag surface atoms and ZnTPPs reorganize as the system is annealed. Furthermore, the multilayer-desorbed monolayer shows similar organization to the direct-deposited monolayer that was annealed to 510K; two square domains coexisting, with one more prominent than the other. This implies that the organization of the first layer of molecules is not significantly influenced by the other layers of molecules above it. Just as in the direct-deposited monolayer case, further annealing of this coverage to higher temperatures results in just one square domain throughout which matches the majority domain in the "2+1" pattern.

3.5 Conclusions

From the ZnTPP/Au(111) system, the impact of the molecular monolayer on the surface stress anisotropy is evident through the increase of HB domain size after adsorbing a monolayer of ZnTPPs. This observation combined with knowledge of 2-fold saddling conformation and associated phenyl rotation implies that the ZnTPPs contribute an anisotropic surface stress to the Au(111) surface

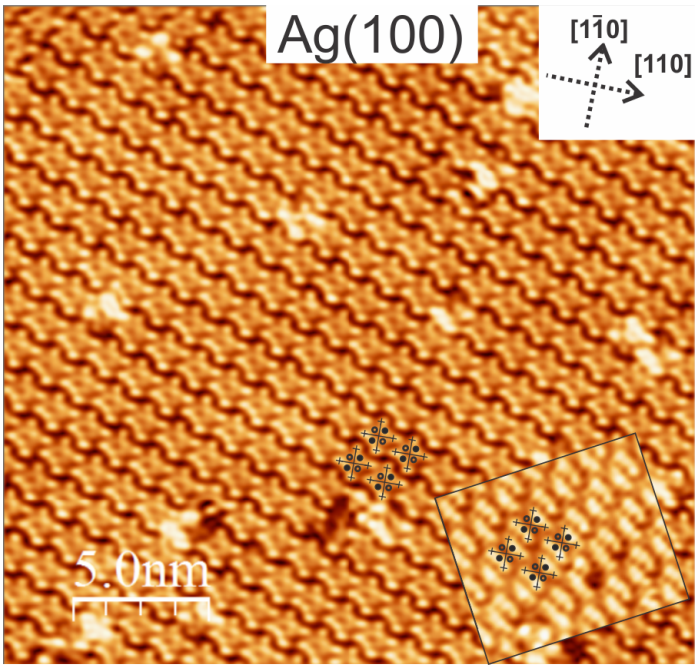

Figure 3.28: Monolayer coverage of ZnTPP on Ag(100) achieved by annealing multilayer coverage to 500K, with schematic ZnTPPs shown as black crosses. The inset image is taken at a bias which reveals the two-fold conformation of the ZnTPPs, interpreted as the pyrrole groups bending toward (open circles) or away from (filled circles) the substrate surface. Primary image scanning parameters: 25 × 25nm, -1.0V, 0.3nA. Inset image scanning parameters: 8 × 6nm, +1.0V, 0.5nA.

through a combination of pyrrole saddling and phenyl orientations. In this argument the downward pyrroles, which are closest to the substrate surface, exert a net compressive force along the Au [11$\bar{2}$] direction, thus decreasing the surface stress anisotropy and increasing HB domain sizes. Upon annealing the system, ZnTPPs reconfigure such that pyrrole saddling alternates between adjacent ZnTPP rows and reduces the net surface stress anisotropy imparted to the Au surface. This reconfiguration allows the substrate surface atoms to revert back to pristine surface stress values.

ZnTPPs adsorbed onto Ag(111) proves to be a useful system to compare with Au(111). The qualitative ZnTPP direct-deposited adsorption behavior is similar for both systems in that nearly-square domains form aligning with the three high symmetry directions of the substrate surfaces. However, at step edges, Ag atoms align with ZnTPPs prior to any annealing, and ZnTPP islands extend outward from step edges. Recall that on Au(111) islands formed on terraces via HB elbow sites. Additionally, high resolution imaging reveals that ZnTPPs organize with a slightly larger unit cell and different azimuthal orientation within the unit cell on Ag(111) compared to Au(111). This results in a lower packing density on Ag(111) (4.6×10^{13} molecules/cm^2) compared with Au(111) (5.7×10^{13} molecules/cm^2). Annealing the ZnTPP/Ag(111) system ultimately results in molecular decomposition rather than desorption seen on Au(111), indicating a stronger molecule-substrate

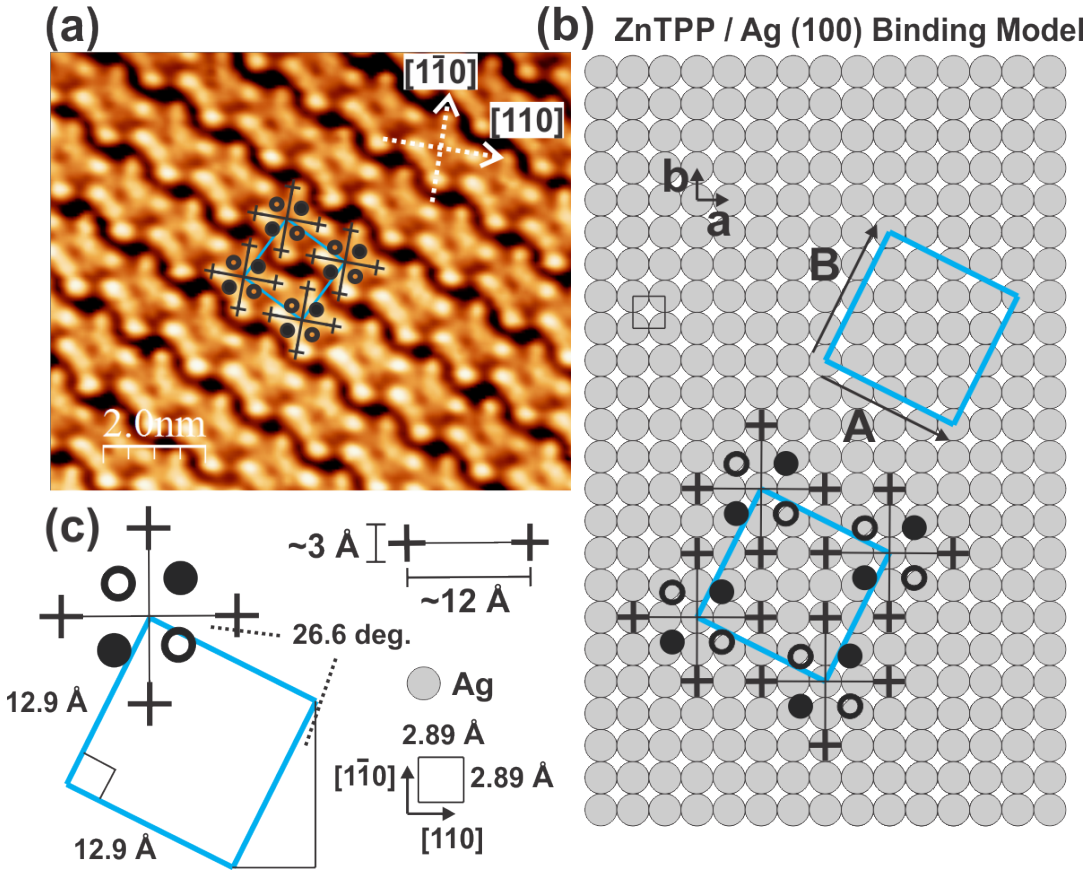

Figure 3.29: (a) Representative STM image on which this model is based. (b) Binding model of schematic ZnTPP molecules with open (filled) circles representing downward (upward) bending pyrrole groups. (c) Unit cell of ZnTPP organization on Ag(100) for a monolayer obtained by multilayer desorption via annealing to 500K. Note that if we fix the central Zn atom to an Ag top site, all molecules adsorb in the same way: pyrroles and phenyls above top sites. Image scanning parameters: 10×10nm, -1.0V, 0.5A.

interaction in this system. It is likely that the stronger Ag-ZnTPP interaction, specifically the Ag-Zn and Ag-N interactions, inhibits the formation of packing as tight as seen on Au(111) due to molecule-molecule phenyl interactions competing with maintaining molecule-substrate registry.

ZnTPP monolayers obtained via multilayer desorption on Ag(111) exhibit a different organization compared to Au(111). A nearly-square organization is observed which shares the same organization as the direct-deposited monolayer. Recall that ZnTPPs in a square configuration impart a net anisotropic surface stress, in this case to the Ag(111) surface, due to the saddling conformation. However, on Ag(111) the nearly-square organization persists after annealing both a direct-deposited monolayer and for a multilayer-desorbed monolayer. This implies that surface stress plays less of a role in the ZnTPP/Ag(111) system compared to ZnTPP/Au(111). Indeed, the surface energy, surface stress, and surface relaxation (i.e., the decrease in separation of the first and second layer of

surface atoms to attain equilibrium charge distribution) calculated for Ag(111) are typically lower than Au(111) and most 4d transition metals[101, 103, 159, 181].

While there are differences between the ZnTPP overlayer models for the Ag(100) and Ag(111) surfaces, it is clear that the ZnTPP molecules adsorb in registry with the surface atoms. On both surfaces, each phenyl group is subjected to T-type interactions with neighboring molecules, but with slightly different phenyl-phenyl distances due to the different surface symmetry. The pyrrole and phenyl groups have different local environments with respect to the Ag atoms on each surface, indicating that their local interaction with the surface could have a lesser impact on the total energy than the phenyl interactions. On the Ag surfaces, molecular registry with the surface appears to be governed by a subtle equilibrium between interactions with Ag surface atoms at different positions and the T-type interphenyl stacking in order to minimize the total energy of the system.

On Ag(100), the gradual transition from the "2+1" pattern to one dominant domain (i.e., the majority domain from the "2+1") by way of thermal annealing suggests there exists a delicate balance between molecule-molecule and molecule-substrate interactions for this system. We can better understand the behavior of ZnTPPs on Ag(100) from the observations on Au(111), since the Au(111) HB provides insight into surface stress anisotropy. Recall that the downward pyrroles (i.e., the pyrroles closest to the substrate surface) supply a compressive stress along a line connecting two downward pyrroles through the Zn atom of a given ZnTPP. Looking at the binding model for ZnTPP/Ag(100) shown in Figure 3.24, two ZnTPP orientations exist: the minority orientation with pyrroles along high-symmetry nearest-neighbor directions, and the majority orientation with pyrroles along next-nearest-neighbor directions. Using the same argument as for Au(111) surface stress effects, let a line drawn connecting two downward pyrroles through the Zn atom of a given ZnTPP molecule represent the compressive surface stress vector that the pyrroles apply to the substrate surface. For the minority ZnTPPs on Ag(100), this line is parallel to the [110] high-symmetry direction, however for the majority ZnTPPs this vector has equal components along both the [110] and $[1\bar{1}0]$ directions. It follows then that the downward pyrroles of the minority ZnTPPs induce a greater surface stress anisotropy than the majority ZnTPPs, assuming each ZnTPP supplies the same magnitude of compressive stress. This could explain the preferential orientation of the majority ZnTPPs over the minority ZnTPPs; the majority ZnTPPs induce smaller surface stress anisotropy per molecule than the minority ZnTPPs. Furthermore, upon annealing the system the majority ZnTPP conformation dominates, with minority ZnTPPs diminishing as annealing temperature is increased. As with Au(111), due to an intimate link between pyrrole saddling and phenyl orientation[145], phenyl groups likely contribute to the surface stress as they too bind close to the substrate surface.

To further investigate the transformation from "2+1" to square patterning via annealing, we are collaborating with theorists who perform DFT calculations of the ZnTPP unit cell adsorption geometry and binding energy on a Ag(100) surface to help determine realistic (i.e., energy-minimized) pathways through which the transformation can progress. By approaching this STM evidence with DFT, we can learn more about the fundamental interactions at organic/noble metal interfaces; in particular the relative strengths of molecule-molecule and molecule-substrate interactions, as well as the effects of thermal annealing on the ZnTPPs and Ag(100) surface atoms. The fundamental interactions and principles studied for this system can then be compared to Au(111) and Ag(111) and eventually extended to other organic/metal systems. In this way, we hope to obtain general principles governing the organization of molecules at weakly-interacting organic/metal interfaces.

Chapter 4

Molecular Dehydrogenation on Ag(100) and Ag(111)

4.1 Introduction

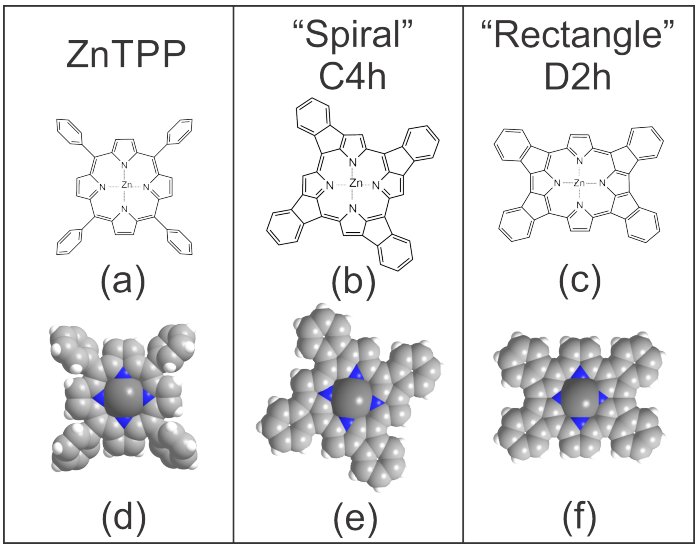

Figure 4.1: Skeleton models of (a) the intact ZnTPP molecule, comprised of a zinc-centered porphyrin macrocycle and four phenyl moieties, as well as (b) the "spiral" C4h and (c) "rectangle" D2h dehydrogenated ZnTPPs in which meso-phenyls and pyrroles lose hydrogen atoms and subsequently form C-C bonds. Also shown as (d) is the space-filling model of the intact ZnTPP elucidating the saddle conformation as well as the phenyl rotation with respect to the porphyrin macrocycle typically seen upon adsorption to metal substrates. Additionally, (e) and (f) show space-filling models of the spiral and rectangle molecules, respectively.

The following discussion is based in part on work I performed that is already published[147]. As mentioned in the previous chapter, multilayer desorption is a typical method of obtaining monolayer coverage, but care must be taken when considering annealing temperatures. Annealing above 600K can desorb the monolayer or chemically alter the molecules and destroy the long-range order[52]. Investigating the evolution with temperature of TPPs on metal substrates for multilayer coverages down to a monolayer has therefore been a topic of recent interest. For free-base TPPs (2HTPPs) on metal substrates, annealing a monolayer above 450K may result in dehydrogenation of the two hydrogen atoms in the porphyrin core and subsequent metallation by abstraction of an atom from

the substrate surface[49, 51, 53, 75, 128, 143, 160, 194]. For both 2HTPPs and metal-centered TPPs (MTPPs), annealing the intact monolayer above 550K results in dehydrogenation of meso-phenyl and pyrrole groups and subsequent C-C bond formation between the two[49, 52, 53, 143, 194]. This intramolecular rehybridization forces both the phenyls and the pyrroles to be coplanar with the porphyrin core, flattening the molecule. In earlier studies of this process, two types of dehydrogenation products were postulated, each with different symmetry. One dehydrogenated TPP exhibits C4h symmetry, often referred to as "spiral", and involves one phenyl bonding to an adjacent pyrrole with no two phenyls bonded to the same pyrrole, shown as Figure 4.1b. The other exhibits D2h symmetry, often referred to as "rectangle", and involves two adjacent phenyls bonding to the same pyrrole, leaving two pyrroles devoid of phenyl bonding shown as Figure 4.1c.[52]

Although not reported for 2HTPP on Ag(111)[52], intermolecular bonding upon dehydrogenation should also be possible for high molecular coverage. The formation of covalent bonds upon annealing intact TPP molecules is a relatively new frontier and has broad implications on the creation of highly ordered 1D or 2D structures through direct chemical reactions at the surface. Self-assembled TPP monolayers exhibit extremely low defect densities and high order over many tens or hundreds of nanometers with their intermolecular interactions dictated by phenyl-phenyl van der Waals forces. However van der Waals interactions lead to fragile structures with weak intermolecular attraction. The formation of covalent bonding could in principle alleviate these drawbacks, and ideally one could take the long-range self-assembled structure created via weaker interactions and lock it in place using covalent bonding, resulting in a rigidly-connected 2D structure.[68, 105, 169] Although some evidence of intramolecular dehydrogenation of TPPs on metal substrates has been proposed from STM imaging,[52, 143] a complete description of the dehydrogenation processes, from a highly-ordered monolayer of intact ZnTPPs to final rehybridized species is highly desirable, in particular for 2D-polymeric growth. Furthermore, the subsequent alteration of the adsorbate electronic structure upon dehydrogenation needs to be fully explored.

In this chapter, we study the progression with annealing temperature of an intact ZnTPP monolayer to a dehydrogenated layer, exhibiting novel intra- and inter-molecular rehybridization, on both the Ag(100) and Ag(111) surfaces. To investigate this progression further, we perform the same procedure using the zinc phthalocyanine (ZnPC) molecule which is similar in structure to the ZnTPP however it is completely planar in the gas phase and upon adsorption. Additionally, for ZnPC there are no obvious intramolecular bonding pathways that can occur upon dehydrogenation akin to the D2h and C4h symmetries of the ZnTPP. In this way, we hope to isolate which features of the ZnTPP and the ZnPC are most influential in the final organization of the dehydrogenated molecular layer. Finally, since STM does not supply chemical sensitivity, we use photoemission spectroscopy and gas

phase density of states calculations to investigate the dehydrogenation process for similar sample treatment from an electronic structure perspective.

4.2 ZnTPP Dehydrogenation on Ag(100) and Ag(111)

After characterizing the monolayer coverages of ZnTPP on Ag(100) and Ag(111), further annealing was done to probe the stability of the monolayer as a function of temperature. Recall that 500K anneals were done to obtain the monolayers from multilayer desorption. Upon annealing to 550K, STM imaging becomes unstable and streaky. When brief episodes of stability occur, a loss of long range order is observed. Further annealing to 600-640K results in a stable, highly-disordered layer of molecules.

Figure 4.2 shows an STM image of a monolayer of ZnTPPs on Ag(100) annealed to 610 K. An interesting feature is the persistence of short range order in the presence of long range disorder. Note that these molecules do not appear covalently bonded to each other and are likely interacting via van der Waals forces. The measured unit cell of this array is 1.47nm×1.41nm, significantly larger than for the intact ZnTPP layer (1.29×1.29nm) due to the increased footprint of the dehydrogenated ZnTPP molecule. The overall molecular coverage for this image is about 0.7 ML, indicating that about 0.3 ML desorbed due to the anneal. Additionally, when annealed at 610K, several bright molecules exhibiting a saddle conformation are observed, reminiscent of the intact ZnTPP at room temperature. These features are indicated with black circles in Figure 4.2. After annealing at 640K, these intact molecules are no longer observed at the surface of the Ag(100) crystal.

Figures 4.3a and b show examples of ZnTPPs on Ag(100) and Ag(111), respectively, after annealing to 640K. Individual molecules are observed in both images, however the shape of the molecules is very different, the molecular array is highly disordered, and the overlayer has a much lower density of molecules than was found for the self-assembled monolayers of ZnTPP molecules found in the STM images of Figures 3.17 and 3.28. This suggests that, in addition to a loss of order in the overlayer, molecular rehybridization has occurred. To further investigate the nature of this new molecular overlayer system, STM images were acquired using a variety of tunneling conditions.

The STM images of Figures 4.3a and b were taken under the same tunneling conditions as the insets of Figures 3.17 and 3.28, i.e., conditions under which the intact molecule exhibits the saddle conformation. However the molecules in these images, and other images taken with biases ranging from -2.0V to +2.0V, appear planar. At annealing temperatures greater than 550K, previous work has shown that the meso-phenyls and pyrroles could dehydrogenate and form C-C bonds [49, 52, 53, 143, 194]. This C-C bond formation forces the phenyl and pyrrole to be coplanar,

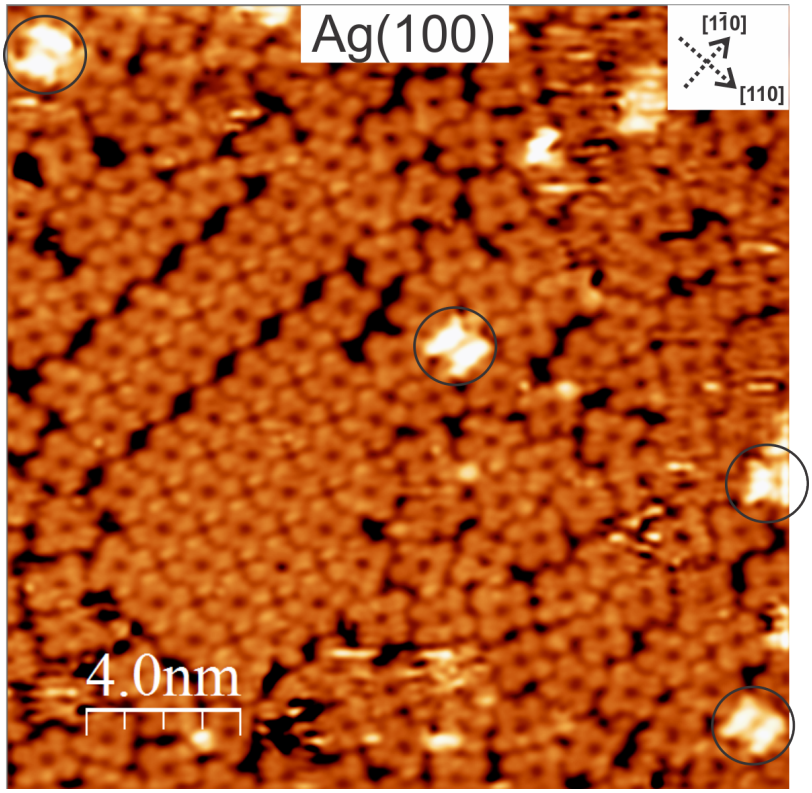

Figure 4.2: STM image of a ZnTPP monolayer on Ag(100) annealed to 610K. Note the striking persistence of order amongst the dominant disorder in the layer. Image parameters: 20 × 20nm, +1.5V, 0.7nA.

consistent with our STM observations.

The low density of molecules remaining on the surface in Figures 4.2 (about 0.7 ML) and 4.3 (about 0.5 ML) is likely a result of the larger molecular footprint of the dehydrogenated ZnTPP molecule, forcing some molecules to leave the surface. Additionally, note that annealing at 640K results in a lower density of molecules than at 610K shown in Figure 4.2, indicating thermal desorption of molecules even after dehydrogenation. The striking lack of translational order observed for this system can be a consequence of the planar conformation assumed by the dehydrogenated molecules. As the phenyls are no longer upright, they can no longer achieve the attractive T- or π-type stacking over long distances as they did prior to dehydrogenation. However, Figure 4.2 clearly shows short range order over the distance of several molecules, indicating there still exists an attractive intermolecular interaction in the absence of T-type phenyl stacking. This ordered area is likely a remnant of order from the intact ML and possibly dehydrogenated at a later time when there is more space to accommodate the larger unit cell. Annealing at 640 K eliminates any instances of order seen in Figure 4.2.

Although the dehydrogenated ZnTPPs appear randomly ordered in the large scale images of

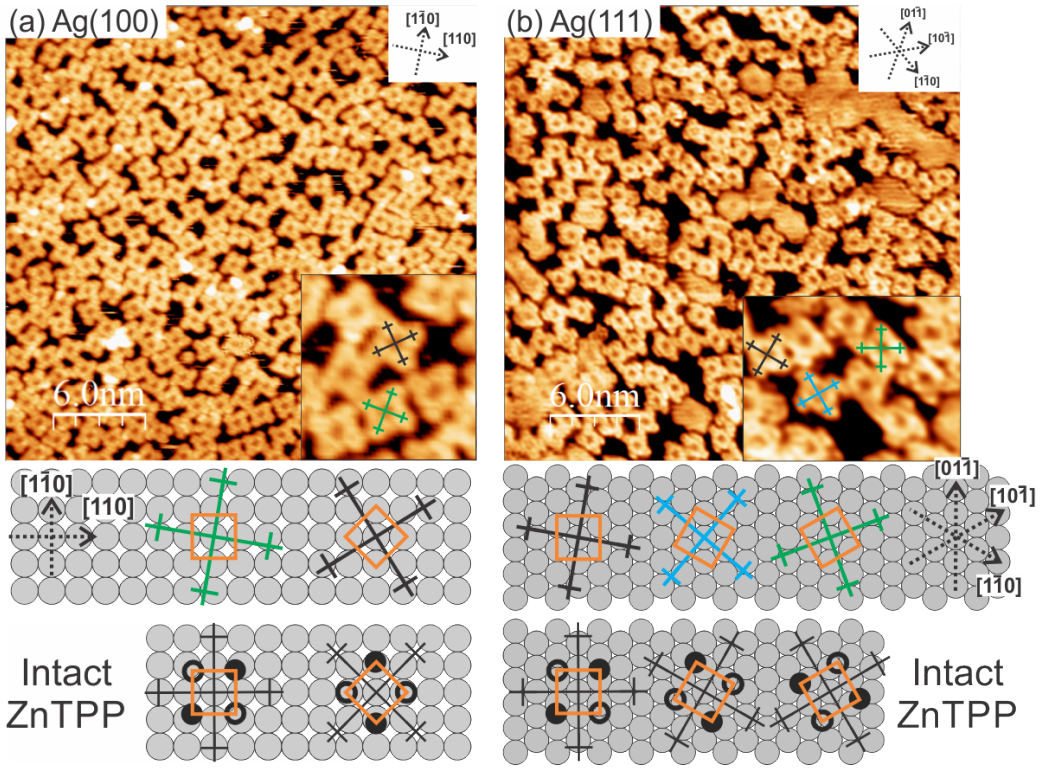

Figure 4.3: Dehydrogenated ZnTPPs on (a) Ag(100) and (b) Ag(111) after a 640K anneal, showing a disordered layer of molecules. The tunneling bias at which these images were taken is the same as the previously shown images with two-fold ZnTPPs. Insets show zoomed in areas of the larger images, with framework ZnTPP molecules of C4h symmetry (defined below) overlaid on selected spiral molecules elucidating different adsorption orientation with respect to the substrate high symmetry directions. The relative orientation of the porphyrin core is not altered upon dehydrogenation. Image parameters: (a) 30 × 30nm, +1.5V, 0.7nA, (b) 30 × 30nm, +1.5V, 0.5nA.

Figure 4.3a and 4.3b, the insets reveal that the dehydrogenated ZnTPPs adopt preferred orientations with respect to the high symmetry directions of the substrate surfaces. In this case, we have only used spiral molecules of C4h symmetry, as it is easier to represent their orientation using a large cross, terminated by four smaller crosses representing the center of the fused phenyl groups. In order to compare these adsorbates to the intact ZnTPP molecules, an orange square (linking the four pyrrole groups) represents the relative orientation of the porphyrin core at the bottom of Figure 4.3a and 4.3b. On both surfaces, the porphyrin core is not altered upon dehydrogenation. From this observation we conclude that, for the dehydrogenated ZnTPPs, molecule-molecule interactions are too weak to give rise to a translationally ordered overlayer. However, the molecule-surface interaction is strong enough to establish a preferred molecular orientation with respect to the lattice of the substrate.

A theoretical description for the formation of dehydrogenated 2HTPPs was developed by Di Santo et al. in an effort to explain NEXAFS measurements indicating phenyls becoming coplanar with

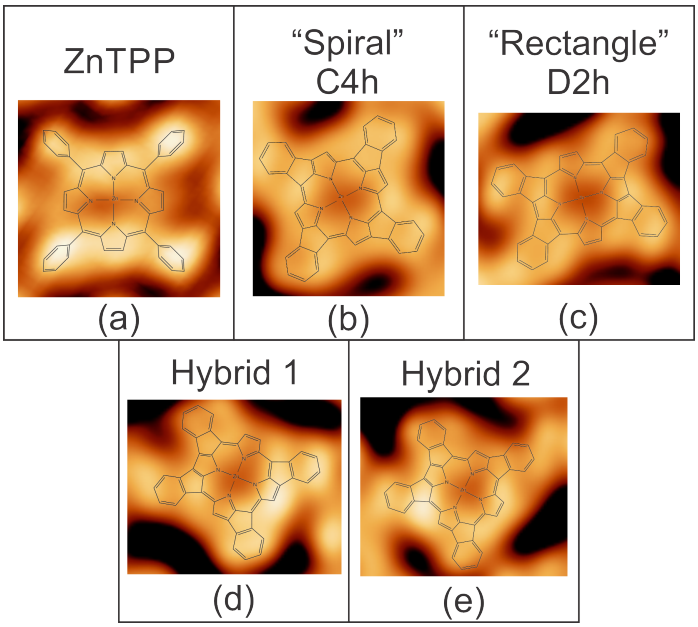

Figure 4.4: Representative STM images of (a) intact ZnTPP, (b) spiral, and (c) rectangle dehydrogenated ZnTPPs with framework models overlaid. Other structures were observed with bonding characteristics different from purely spiral or rectangle, shown as (d) hybrid 1 and (e) hybrid 2, also with framework models overlaid to indicate the proposed bonding. All images shown were taken on Ag(100), with (a) for the intact monolayer case and (b)-(e) after a 640K anneal. Image parameters: (a) +1.5V, 0.5nA, (b)-(e) -0.3V, 0.7nA.

the porphyrin macrocycle after annealing a multilayer to 550K on Ag(111)[52]. Subsequent studies of TPPs on several noble metal surfaces using NEXAFS confirmed those observations[41, 49, 53]. Furthermore TPD has been used to characterize dehydrogenation rates as a function of coverage and showed that the rate of dehydrogenation is lower at higher coverages due to the stabilizing effect of higher intermolecular coordination[75, 143, 194, 200].

While dehydrogenated TPPs have been studied using NEXAFS and TPD, only limited STM evidence for the nature of the product molecules exists. Röckert et al.[143] and Xiao et al.[194] show single molecule dehydrogenation of 2HTPP on Cu(111), with the molecule dehydrogenating in a two-step process by which half of the molecule dehydrogenates and appears dark in STM due to reduced substrate-molecule separation, followed by the other half at a higher temperature anneal. However, the formation of long-range order of 2HTPPs on Cu(111) is inhibited due to the strong interaction between the porphyrin core iminic nitrogen atoms and the Cu surface, and thus their work focuses on the single-molecule regime.

Figures 4.4a, b, and c respectively show high-resolution STM images of adsorbed intact ZnTPP as well as spiral and rectangle dehydrogenated ZnTPPs after annealing to 640K on Ag(100). In addition, Figures 4.4d and 4.4e show two new dehydrogenation products called hybrid 1 and hybrid

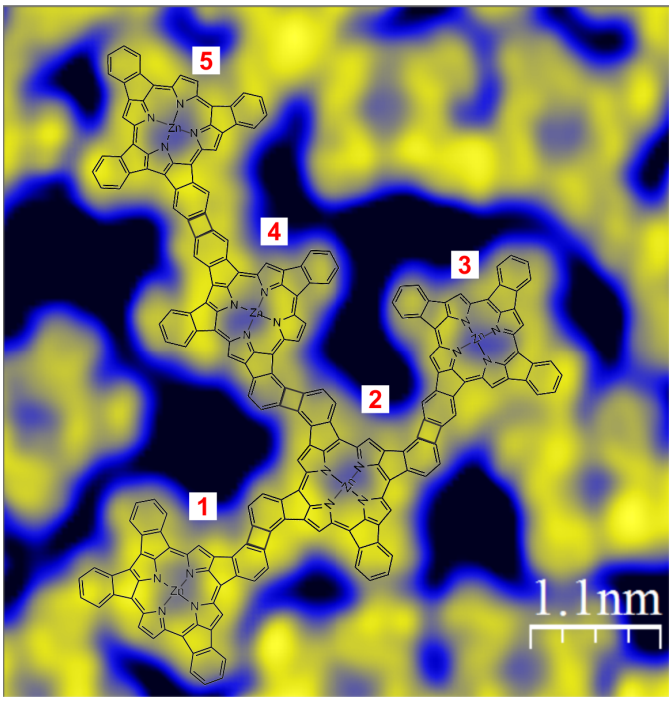

Figure 4.5: STM image of dehydrogenated ZnTPPs on Ag(100) after a 640K anneal. A chain of covalently bonded dehydrogenated ZnTPPs is shown, comprised of 5 molecules labeled in red. A framework bonding model of the ZnTPP chain is overlaid elucidating the C-C bond formation due to intermolecular hybridization. Note the presence of spiral C4h dehydrogenated species with counterclockwise and clockwise symmetry (molecules 2 and 3, respectively) as well as hybrid 1 (molecule 1) and hybrid 2 (molecules 4 and 5) types. Image parameters: 5.5 × 6nm, -0.3V, 0.7nA.

2, respectively, due to their inclusion of features from both spiral and rectangle symmetries. The submolecular resolution obtained is sufficient to propose intramolecular bonding models for each structure, shown as overlaid framework models. The spiral molecule exhibits clockwise C-C bonding between phenyls and pyrroles. The chiral counterpart of this molecule (i.e., counterclockwise C-C bonding) was also observed. On the other hand, the rectangle molecule shows two phenyls bonding to the same pyrrole, with two pyrroles devoid of phenyl bonding. Hybrid 1 has the two leftmost phenyls bonding to the same pyrrole, similar to the rectangle molecule, whereas the two rightmost pyrroles bond clockwise to adjacent pyrroles, similar to the clockwise spiral. In hybrid 2, the leftmost phenyls share the same characteristics as rectangle and hybrid 1, however on the right side one phenyl bonds to a counterclockwise pyrrole whereas the other phenyl bonds to a clockwise pyrrole. The higher symmetry spiral and rectangle molecules were predicted and calculated assuming the dehydrogenation of a single TPP molecule, however hybrids 1 and 2 show dehydrogenation characteristics with lower symmetry. Thus, dehydrogenated close-packed molecular layers exhibit distinct features possibly arising from intermolecular interactions that are not present in the single-molecule regime. A comparison of ground-state energies of the four dehydrogenated TPP structures

has been calculated using DFT for gas phase 2HTPPs[188]. The rectangle is the lowest energy configuration ($\Delta E = 0$ eV), followed by hybrid 1 ($\Delta E = 0.176$ eV), then spiral ($\Delta E = 0.263$ eV), and finally hybrid 2 ($\Delta E = 0.420$ eV). However, gas-phase TPP conformation is markedly different from saddled TPPs on a noble metal substrate such as Ag; the substrate surface should be taken into account to obtain more accurate ground state energies.

Figure 4.5 shows a high-resolution STM image of dehydrogenated ZnTPPs on Ag(100) after annealing to 640K. In this figure, adjacent molecules appear connected via phenyl group covalent bonding, forming a chain of dehydrogenated ZnTPPs. These dehydrogenated ZnTPP chains were also observed on Ag(111) for similar annealing temperatures, and can be seen in Figure 4.3b. A bonding scheme is overlaid with five labeled molecules that are covalently bonded via (dehydrogenated) phenyl C-C bonds. Note the presence of spiral dehydrogenation products with counterclockwise and clockwise symmetry (molecules 2 and 3, respectively) as well as hybrid 1 (molecule 1) and hybrid 2 (molecules 4 and 5) types. The intermolecular bonding scheme shown is similar to that of the biphenylene molecule, which is comprised of two benzene rings connected by way of a strained but stable square bonding configuration.[57, 113, 135, 136] To establish the validity of this model, we compare the idealized structural model with the measured distances in STM. For example, for molecules 4 and 5 the calculated Zn-Zn distance in this configuration, with the square C-C bond length of 1.5Å[135], is 16.5Å. The measured STM Zn-Zn distance of 17.1Å is consistent with this model. Repeating this process for all molecules shown gives similar results. Additionally, the bond dissociation energy of biphenylene, i.e., the amount of energy required to cleave one of the two C-C bonds, is approximately 2.84 eV or 65.4 kcal/mol, and the additional energy required to cleave the last C-C bond is 5.13 eV or 118.4 kcal/mol, suggesting these structures are stable configurations at room temperature.[136] The formation of porphyrin chains upon annealing is similar to the observations of Haq et al., who examined dehydrogenation of porphyrins and diphenylporphyrins on Cu(110) and showed the formation of macromolecular chains by way of C-C and C-Cu-C bonding[75]. However, in our case the inclusion of an Ag atom into the C-C bonding shown in Figure 4.5 is inconsistent with our observations, as the inclusion of a C-Ag bond length of 2.0Å would increase the theoretical Zn-Zn distance to 18.5Å, a value much larger than what is observed.[131]. Furthermore the presence of Ag atoms would be evident by their bright appearance at low tunneling biases (<0.5 V, i.e., in the HOMO-LUMO gap of the molecule), which was not observed.

In summary, this STM study has shown that an intact monolayer is obtained after annealing a multilayer to 500K. Dehydrogenated ZnTPPs form after annealing above 550K, and above 600-640K ZnTPPs interact with one another to form covalent molecular chains described by the formation

of C-C bonds between neighboring dehydrogenated phenyl groups. Further annealing above 650-700K decomposes the molecules and the ZnTPP signature geometries are lost, confirming that the monolayer of TPP molecules do not desorb intact, but dehydrogenate or decompose before desorbing as was observed in similar systems[49, 114].

4.3 ZnPC on Ag(100)

4.3.1 Monolayer Adsorption Geometry via Multilayer Desorption

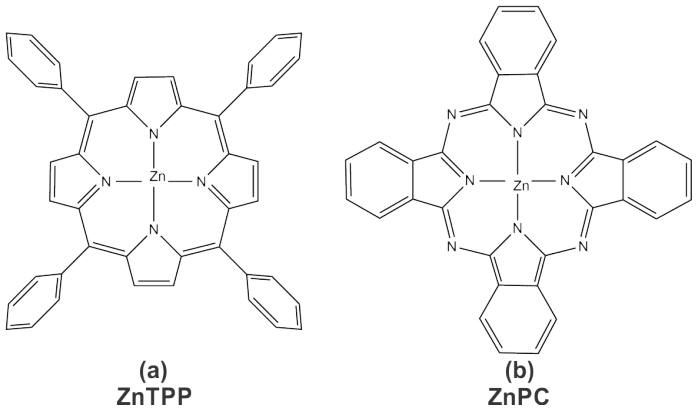

Figure 4.6: Skeleton models of (a) ZnTPP and (b) ZnPC.

The progression of ZnTPP binding behavior with annealing temperature on Ag(100) and Ag(111) showed that annealing above 280°C resulted in the loss of large scale order. Additionally, annealing above 280°C induced dehydrogenation of the mesophenyls and pyrroles accompanied by intramolecular rehybridization resulting in several rehybridization products. All of these products have a larger footprint than the intact ZnTPPs due to phenyl rotation parallel to the porphyrin plane. This increased footprint forces molecules out of the tightly packed monolayer, causing difficult imaging in STM as well as disruption of the large scale order. To investigate this idea, ZnPC molecules are used, shown as Figure 4.6b, which have a planar configuration that is more likely to remain intact in the event of dehydrogenation. These molecules have fewer parameters influencing the adsorption behavior upon dehydrogenation since all molecules likely retain four-fold geometries after dehydrogenation, rather than ZnTPPs which can rehybridize several ways. In this way, we hope to learn more about the progression of self-assembled monolayers with annealing temperature, specifically the transition from intermolecular van der Waals interactions to dehydrogenation and subsequent intermolecular rehybridization.

PCs have been studied using STM and have proven to be highly stable molecules in UHV capable of withstanding UHV sublimation deposition methods. Metal PCs adsorbed to noble metal

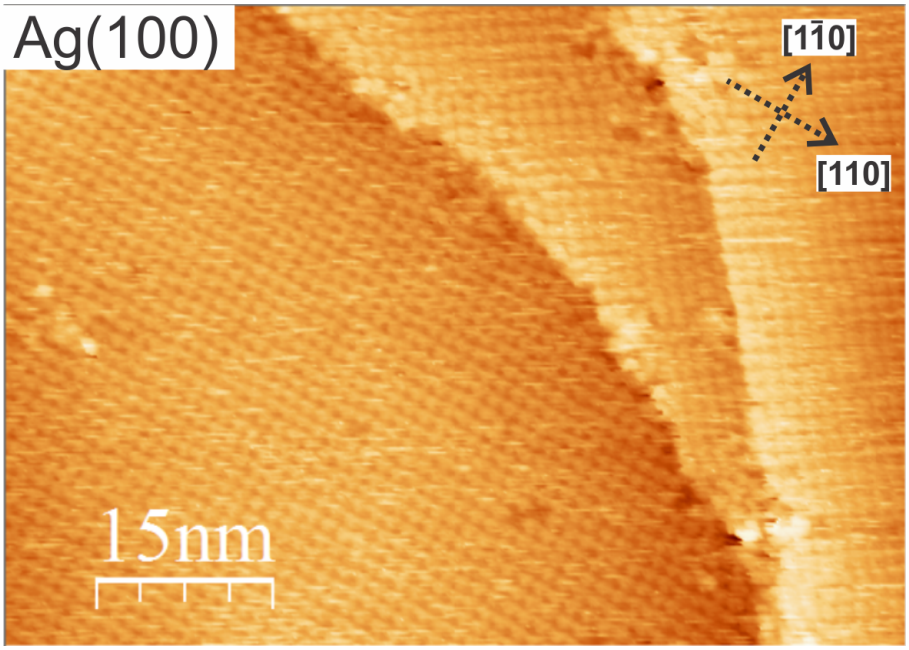

Figure 4.7: STM image of a ZnPC monolayer on Ag(100) after annealing to 300°C showing several domains. Image parameters: 75×53nm, -1.0V, 0.3nA.

surfaces from sub-ML to multilayers have been studied with both STM and spectroscopic techniques, supplemented with DFT electronic structure calculations.[16, 28, 104, 115, 123, 166, 167] PCs are found to form disordered monolayers in cases with strong substrate-molecule interaction, however they can also organize into a variety of patterns depending on the crystallographic orientation of the substrate surface as well as the strength of the metal-center interaction with the substrate.

We followed the same sample preparation that was done for ZnTPPs; depositing a multilayer onto clean Ag(100) and annealing to desorb all but the monolayer. Figure 4.7 shows an STM image of a monolayer of ZnPC on Ag(100) with several domains and significant disorder near the step edge bends. ZnPC molecules arrange to fit the curvature of the step edge, whereas step edges regularly conformed to ZnTPP organizations for similar preparations. This is likely due to the planarity of the ZnPC molecules. In contrast, ZnTPP phenyl groups act as a grappling hook to interact more strongly with substrate step edges as evidenced by ZnTPPs straddling the step edge between two terraces, as shown in Figure 3.16. Additionally, the annealing temperature required to reach a stable ZnPC monolayer was approximately 50°C greater than that for ZnTPPs. This is likely due to the reduced substrate-molecule separation since ZnPCs are planar; this planarity results in the ZnPC macrocycle adsorbing closer to the substrate surface compared to that of the ZnTPP with its protruding phenyl legs. That is, ZnTPP phenyl groups are typically rotated with respect to the porphyrin macrocycle in such a way to increase the separation of the ZnTPP macrocycle from the

substrate surface, possibly resulting in decreased macrocycle-substrate interaction and therefore less temperature required to desorb overlayers.

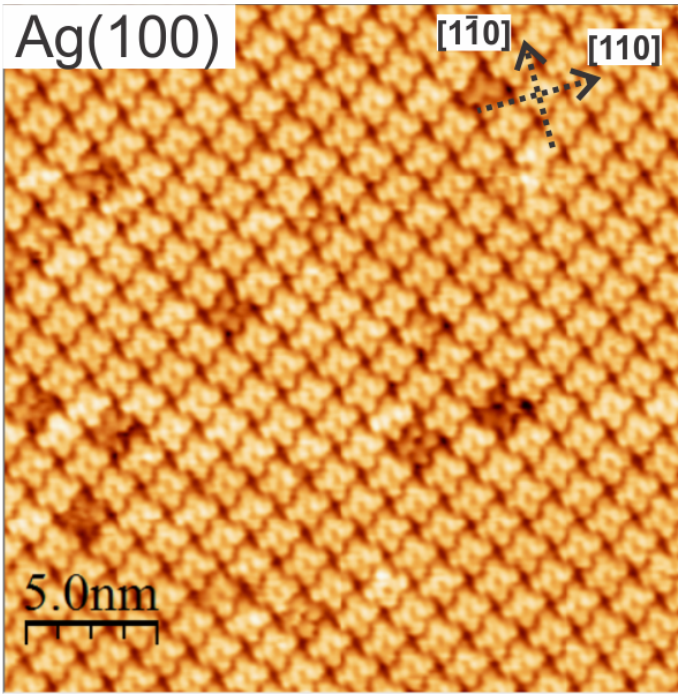

Figure 4.8: High resolution STM image of a ZnPC monolayer on Ag(100) after annealing to 320°C. Image parameters: 25×25nm, -1.0V, 0.3nA.

Figure 4.8 shows a high resolution STM image of a ZnPC monolayer after annealing a multilayer to 320°C. The adsorption geometry is described by long range self-assembled square order, with each ZnPC imaged as a cross with a dark center at the location of the Zn ion. Scanning with a range of tunneling biases consistently reveals crosses with dark centers, whereas for ZnTPPs a 2-fold saddling conformation was observed at certain biases. Metal-centered PCs tend to conform to Ag substrates with either a D_{4h} symmetry or a so-called "shuttlecock" shape, with the metal center closer to the surface than the rest of the molecule.[16, 123] Due to the relatively weak nature of the Zn-Ag interaction, a planar D_{4h} symmetry likely describes ZnPC adsorption to Ag(100). Just as with ZnTPP, the Zn ion states are not accessible by the tunneling biases used here (-1.5V to +1.5V) so the dark appearance of the Zn ion persists for this preparation and these tunneling conditions. The measured unit cell for this organization is 13.9×13.9Å, similar to that found in comparable systems.[115, 167]

Figure 4.9a shows a high resolution STM image with a schematic ZnPC unit cell overlaid, in which large black crosses represent the ZnPC molecule and smaller crosses identify the centers and width of the benzene-like rings. Figure 4.9b shows a model Ag(100) surface with the ZnPC unit cell

overlaid. In this model, Zn ions are placed above Ag top sites, and the measured unit cell dimensions are applied to create the final organization shown. The unit cell of 12.9×12.9Å is identical to that found for ZnTPPs (Figure 3.29) and is described in matrix notation as follows:

$$\begin{pmatrix} A \\ B \end{pmatrix} = \begin{pmatrix} 4 & 2 \\ -2 & 4 \end{pmatrix} \begin{pmatrix} a \\ b \end{pmatrix} \tag{4.1}$$

where (**AB**) are the unit cell vectors of the molecular overlayer, and (**ab**) the unit cell vectors of the Ag(100) surface along the [110] and [1$\bar{1}$0] directions, respectively. The packing density for this organization is 5.9×10^{13} molecules/cm^2.

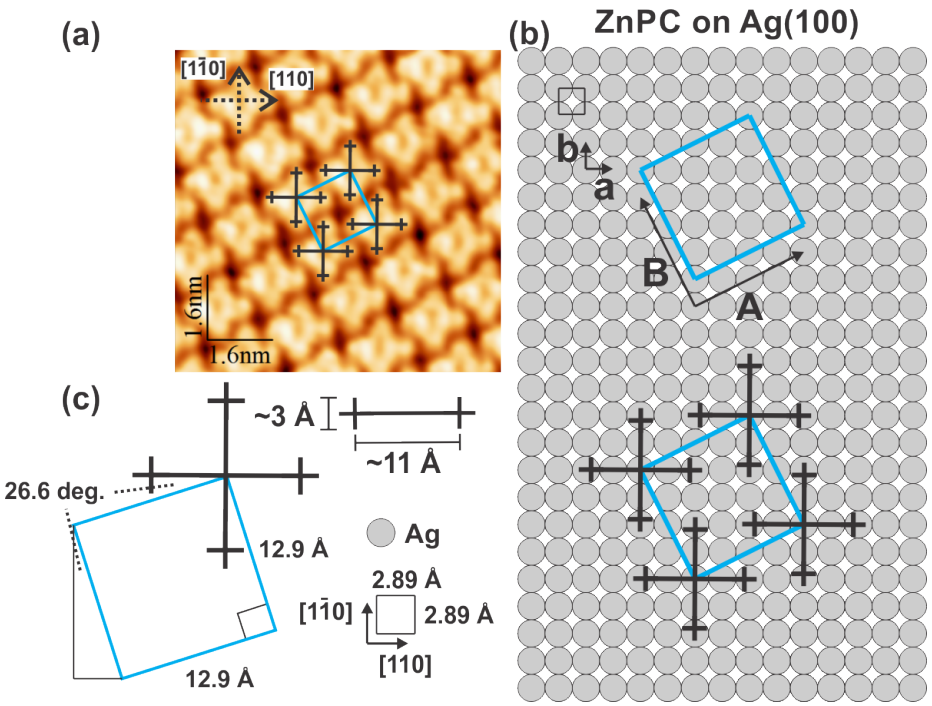

Figure 4.9: (a) High resolution STM image of a ZnPC monolayer on Ag(100) after annealing to 320°C. (b) Binding model of schematic ZnPC molecules on a model Ag(100) surface. (c) ZnPC unit cell geometry showing the 12.9×12.9Å square unit cell. Image parameters: 8×8nm, -1.0V, 0.3nA.

4.3.2 ZnPC Monolayer Evolution via Annealing

Further annealing to 350°C results in a loss of long range order and difficult STM imaging, similar to what was observed for ZnTPPs annealed above 280°C. Just as with ZnTPPs, higher annealing was required to obtain high resolution images. In this case, 380°C was sufficient to obtain high resolution STM images of ZnPCs, such as that shown in Figure 4.10. It is clear that ZnPCs do not maintain long range order upon annealing to such high temperatures, however they do appear to form intermolecular bonds just as ZnTPPs did. ZnPC chains in Figure 4.10 appear connected

in several ways. First is by way of benzene groups of adjacent molecules that connect at positions along the benzene ring forming either a straight or bent chain. Second, in some cases the molecules appear connected between a benzene ring and the ZnPC macrocycle, possibly through the formation of a C-N bond with a nitrogen atom on the macrocycle perimeter.

Even though ZnPCs reduce the possible intramolecular changes due to dehydrogenation compared to ZnTPPs, there is an important issue that arises: how does one conclusively distinguish a dehydrogenated ZnTPP or ZnPC molecule from its intact counterpart using STM? Recall that for ZnTPPs a 2-fold saddling conformation identified intact ZnTPPs, whereas planar ZnTPPs identified dehydrogenated (and rehybridized) ZnTPPs. Phenyl dehydrogenation and rehybridization with pyrrole groups flattens the molecule, changing its conformation from saddled to planar. However, ZnPCs are planar molecules without any obvious intramolecular rehybridization pathways that would cause the ZnPCs to appear as anything but crosses. So, while the number of rehybridization products has been reduced compared to ZnTPP, so too has our ability to infer the onset of dehydrogenation. Therefore, the best we can do with STM is deduce that dehydrogenation occurred by observing either intramolecular changes or intermolecular bond formation in the absence of intramolecular rehybridization.

STM provides invaluable information regarding the adsorption behavior of molecular monolayers, however it does not supply chemical sensitivity. In the example of dehydrogenation above, changes in the electronic structure of the molecule can provide conclusive evidence of the onset of dehydrogenation, rather than inferring the onset by intra- and inter-molecular behaviors. To gain further insight into the dehydrogenation behavior of ZnTPP monolayers, electronic structure information is obtained via UPS, IPS, and XPS performed on samples prepared in the same way as for the STM dehydrogenation study.

4.4 Photoemission and Electronic Structure Calculations

4.4.1 ZnTPP on Noble Metals

Before studying ZnTPP dehydrogenation on Ag(100) and Ag(111) in the context of electronic structure, it is beneficial to first understand the electronic structure of intact ZnTPP as a function of coverage and annealing temperature on noble metal substrates. Recall from STM observations that ZnTPP on Au(111), Ag(111), and Ag(100) proved to be relatively weakly interacting systems with no significant alteration of the molecular structure upon adsorption, such as decomposition or extreme bending or twisting. Additionally, little charge transfer is expected between the organic and metals. Therefore, we can expect that the ZnTPP gas phase density of states should sufficiently

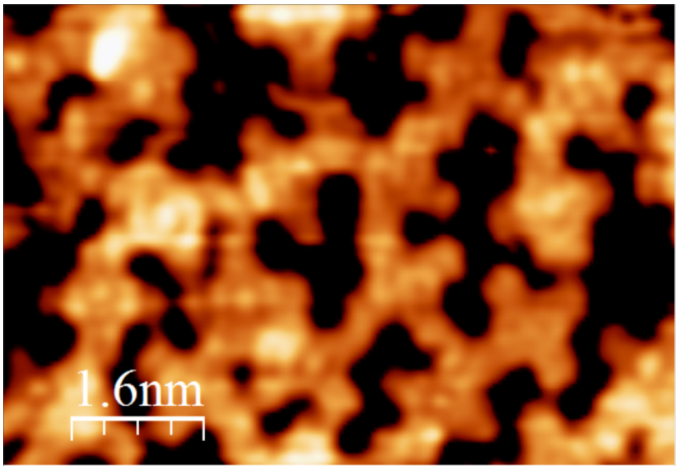

Figure 4.10: High resolution STM image of ZnPC on Ag(100) after annealing a monolayer to 380°C. Annealing at these temperatures induces intermolecular bonding as well as a loss of long range self-assembled order. Image parameters: 8×6nm, -0.5V, 0.7nA.

describe the measured occupied and unoccupied states.

Figure 4.11 shows a summary of UPS and IPS measurements of ZnTPP on Au(111) for multilayer and subsequent anneals to reach a monolayer. In these spectra, the Au surface contribution has been subtracted following the procedure described in Appendix B, leaving only the experimentally measured molecular states. These spectra can therefore be directly compared to DOS spectra calculated for molecular species, which is shown as the top curve in Figure 4.11. In Figure 4.12 is a graph that represents the calculated density of states (DOS) of the ZnTPP molecule, obtained as a convolution of the DOS with a 1 eV FWHM gaussian function. Individual states are indicated as vertical bars below the DOS curve, and representative molecular orbitals are shown above the DOS curve. Examples of the nearly-degenerate or degenerate HOMOs and LUMOs are presented, as well as typical phenyl-bearing states such as the HOMO-5 and LUMO+2 states. For the intact ZnTPP molecule, the HOMOs and LUMOs primarily reside on the macrocycle and are decoupled from phenyl states. Strong phenyl-localized states are found around -6.5 eV in occupied states and around 0 eV in unoccupied states. A multilayer matches the DOS quite well, with the HOMOs located around -2.0V and LUMOs around +2.4V, as well as occupied and unoccupied phenyl states around -4V and +4.5V, respectively. Annealing from multilayer to monolayer causes the HOMO-LUMO gap to decrease, as well as significant broadening of the HOMOs and LUMOs. In the monolayer, the HOMOs are located -1.7V below the Fermi level, and LUMOs +1.9V above the Fermi level. Secondary electron cutoff measurements were also performed to measure the vacuum level and interfacial dipole of the system.

By combining these measurements we create a complete electronic energy level diagram for

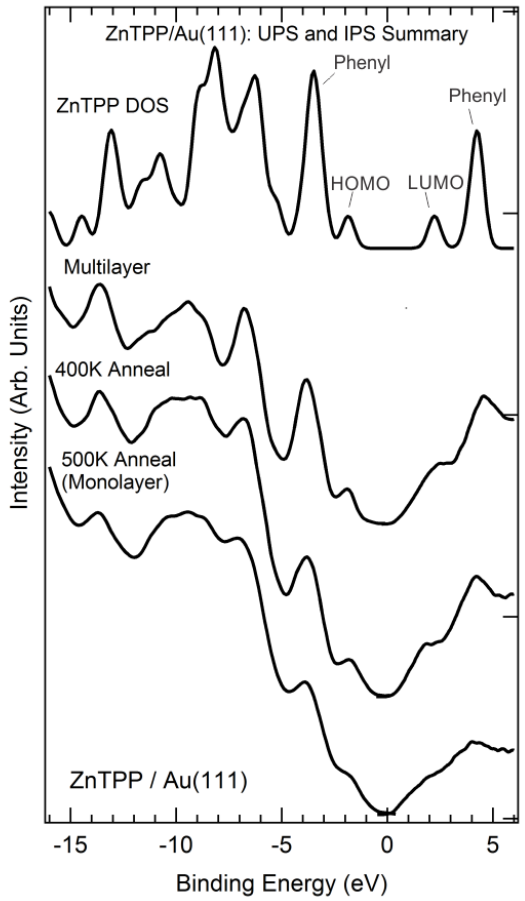

Figure 4.11: Combined UPS (negative binding energy) and IPS (positive binding energy) spectra for a ZnTPP multilayer on Au(111), followed by anneals at 400K and 500K (monolayer).

ZnTPP/Au(111), as shown in Figure 4.13, from which trends can be extracted. First, the interfacial dipole upon adsorbing a multilayer is 0.8 eV due to the pillow effect[32, 98]. Annealing to reach a monolayer decreases the dipole by 0.2 eV. Additionally, the HOMO-LUMO gap decreases going from multilayer to monolayer in a nearly-symmetric way.

The decreasing HOMO-LUMO gap in going from multilayer to monolayer can be explained using a substrate screening model[126]. When a molecule is brought within the vicinity of a metal surface, several effects influence the HOMOs and LUMOs. The self-consistent molecule-surface interaction rearranges electron densities and alters the alignment of the HOMOs and LUMOs energies. Then, electronic coupling to metallic states will broaden discrete molecular orbitals into resonances, as well as further shift orbital energies. Lastly, which is depicted in Figure 4.14, Coulombic interactions between the substrate and either the electron added to the LUMO or the hole added to the HOMO (generated via IPS or UPS, respectively), results in a polarization of the metal substrate. Additionally, neighboring molecules can also contribute to the polarization of the system. Note

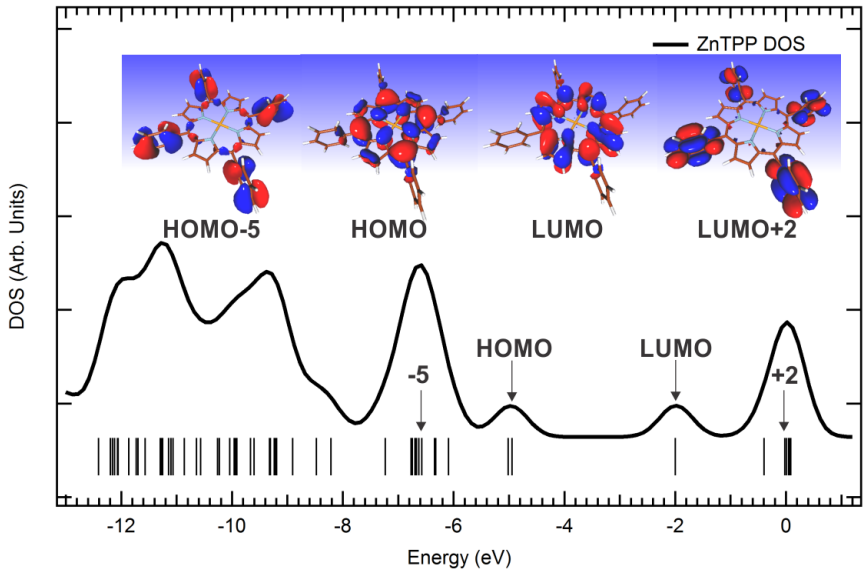

Figure 4.12: Electronic structure of the ZnTPP molecule: DOS and chosen molecular orbitals.

that the transport gap, E_t, is distinct from the optical gap, E_{opt}. The transport gap is measured in photoemission experiments and is the energetic threshold for creating an unbound electron-hole pair. In contrast, the optical gap is the threshold for the creation of a bound electron-hole pair, for example, by optical excitation of an electron from the valence band to conduction band, and is lower energy than the transport gap. This process of creating a bound electron-hole pair maintains a neutral charge state for the system. Consequently, the energy difference between the transport gap and optical gap is known as the binding energy of the exciton created upon optical absorption, E_{exc}.

While the qualitative trends seem to match the experimental summary, in practice it is difficult to quantitatively fit this model to the experimental trends. The main issue is the uncertainty in the number of molecular layers present in the multilayer as well as in intermediate states in obtaining the monolayer. Approximating the number of layers in a given multilayer preparation is difficult due to the inherent instability of the sublimation deposition source. This results in a very high uncertainty in the separation between the substrate surface and the outermost molecular layer. The most accurate data point is therefore the monolayer, as the molecule-substrate separation can be approximated with some certainty, however the molecule-substrate separation for all other data points is difficult to determine. Additionally, for multilayers, measurements integrate over several molecular layers effectively averaging over gradual changes that may be present in different layers.

To summarize, photoemission measurements indicate that the ZnTPP/Au(111) system is weakly

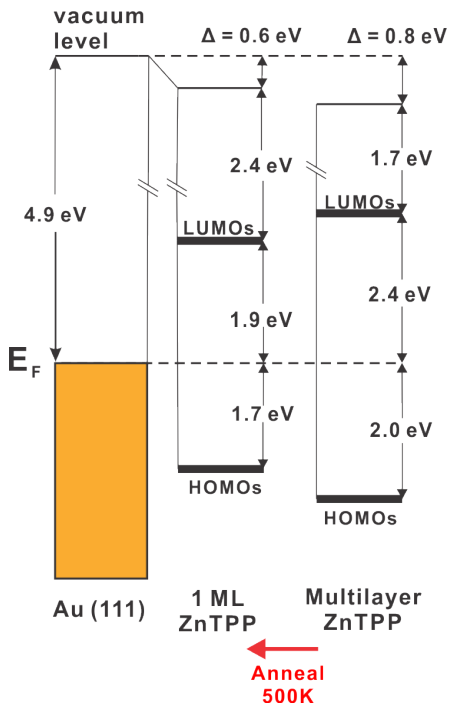

Figure 4.13: Electronic energy level alignment diagram for ZnTPP on Au(111), with respect to the Fermi level of the system.

interacting. The molecular contribution to the experimental spectra is accurately described by gas-phase DOS calculations, indicating, for example, that ZnTPPs do not form strong chemical bonds with Au, nor do they transfer significant amounts of charge. Substrate polarization screens the singly-ionized HOMO and LUMO resulting in a decreased HOMO-LUMO gap as the thickness progresses from multilayer to monolayer. Furthermore a 0.8 eV interfacial dipole develops primarily due to the pillow-effect, commonly observed for weakly interacting molecular layers on noble metal surfaces.

4.4.2 ZnTPP Dehydrogenation

Spectroscopic techniques probing the density of occupied and unoccupied electronic states can provide a way to distinguish intact and dehydrogenated molecules, provided the dehydrogenated molecules exhibit strong changes in the DOS. For example, ZnTPP phenyl groups drastically alter their orientation with respect to the porphyrin macrocycle from being nearly perpendicular with decoupled electronic states to being coplanar. Such a large change in molecular structure is accompanied by a large change in electronic structure. Thus, while the STM study provides valuable topographical information and helps in defining local order as well as some aspects of the molecular transformations upon dehydrogenation, access to the electronic structure is limited. In particular the

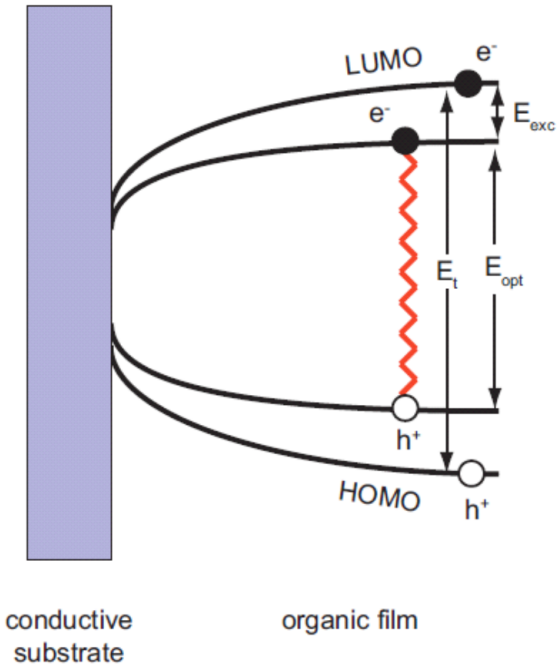

Figure 4.14: Electronic energy level alignment diagram depicting the HOMO-LUMO energy separation decreasing with distance to the substrate surface for an organic multilayer down to monolayer due to more efficient substrate screening.

nature of the molecule-surface interaction and resulting interface dipole are not directly accessible. Therefore XPS, UPS and IPS have been used in parallel to investigate the electronic structure of ZnTPPs on Ag(100) and Ag(111), starting from a ZnTPP multilayer and following by its subsequent anneals at 500K, 550K, and 600K.

Figure 4.15 is of the same construction as Figure 4.12 but for the spiral (top) and rectangle (bottom) dehydrogenated ZnTPPs. For both C4h and D2h symmetries, the phenyls and porphyrin core are coplanar and the HOMOs and LUMOs are now delocalized over the entire π-system, leading to a reduction of the HOMO-LUMO gap. Intramolecular hybridization leads to a splitting of the initially degenerate and localized phenyl states of the intact ZnTPP molecule resulting in a broadening and intensity reduction of the spectral features found experimentally around -4 eV. In Figure 4.15, remaining phenyl states are still found peaking around -6.5 eV and 0 eV in occupied and unoccupied states, respectively, but appear attenuated in intensity, as their contribution is now spread across a large energy range (from -7.5 eV to -5 eV). As the DOS calculated for both C4h and D2h symmetries are similar in nature, we have chosen to visually compare the experimental spectra to an average spectrum of these two DOS shown in Figure 4.15.

Figures 4.16a and b show the combined experimental molecular occupied (E<0) and unoccupied

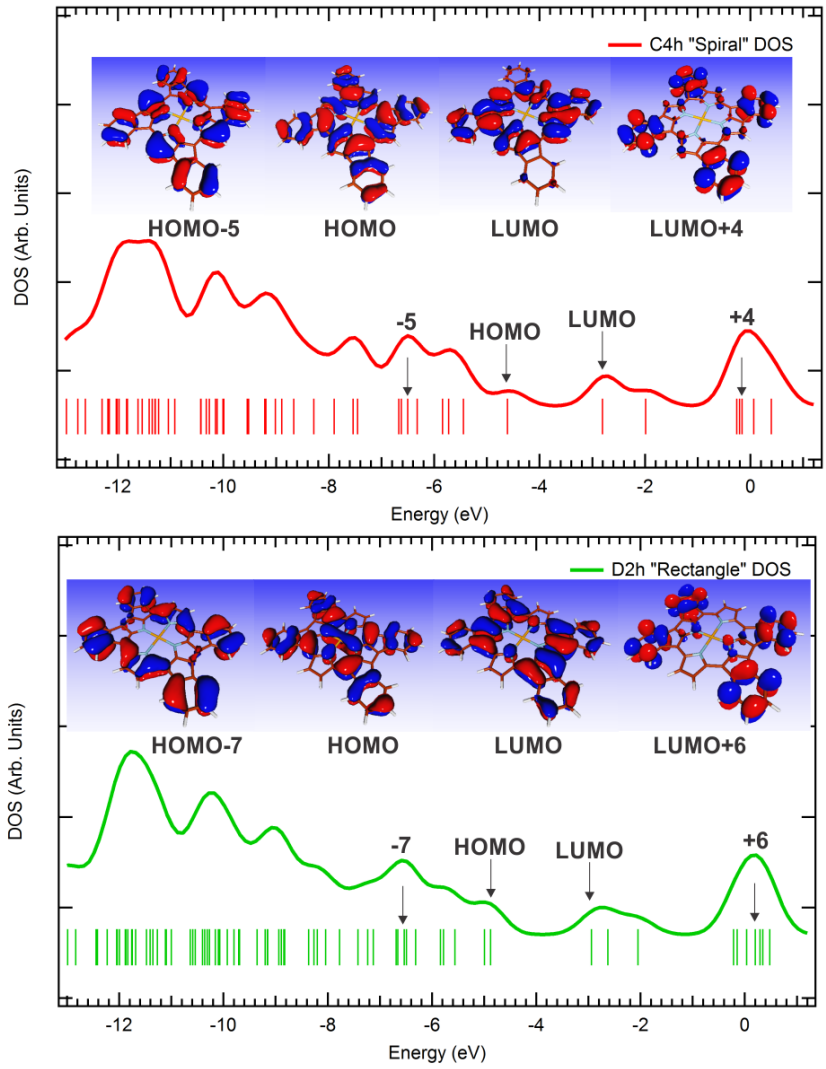

Figure 4.15: Electronic structure of two models for the dehydrogenated ZnTPP molecule: spiral (top) and rectangle (bottom) products DOS and chosen molecular orbitals.

(E>0) states spectra measured on Ag(100) and Ag(111), respectively. In these spectra, the Ag surface contribution has been subtracted following the procedure described in Appendix B, leaving only the experimentally measured molecular states. These spectra can therefore be directly compared to DOS spectra calculated for molecular species. The occupied and unoccupied states spectra measured on the ZnTPP multilayer on both Ag surfaces are, as expected, similar and compare well to the DOS calculated for a ZnTPP molecule shown at the top of Figures 4.16a and b. The ZnTPP HOMOs and LUMOs states found at -2.3 eV and +1.7 eV, respectively, are confined to the porphyrin macrocycle of the molecule, whereas the strong states found at -4.3 eV and +4.0 eV are phenyl-related.

After annealing to 500K, a temperature for which the STM images of Figures 3.28 and 3.17

indicate that an ordered monolayer of intact ZnTPP is obtained, the occupied and unoccupied states spectra of the monolayer possess all the characteristic features measured previously on the multilayer, therefore indicating a weak interaction between ZnTPPs and the Ag surfaces, as postulated from STM imaging. Aside from minor broadening, a shift of the HOMOs-related feature and of the occupied phenyl states toward the Fermi energy by 0.1eV on Ag(100) and 0.2eV on Ag(111) is measured, with respect to their positions for the multilayer, likely due to more efficient screening from the substrate[126] as explained above. Indeed, while the occupied states features are shifted, the unoccupied states remain at the multilayer positions, indicating that band bending is not occurring.[98]

Further annealing to 550 K and 600 K results in a significant increase in broadening of the HOMOs region and of the region between -5 eV and -11 eV of the UPS spectra for both substrates. The unoccupied molecular states are not strongly altered upon annealing, although a broadening of the LUMOs states is visible. Again, the relatively good agreement between experimental spectra and calculated DOS indicates a weak interaction between the dehydrogenated molecules and the Ag surfaces.

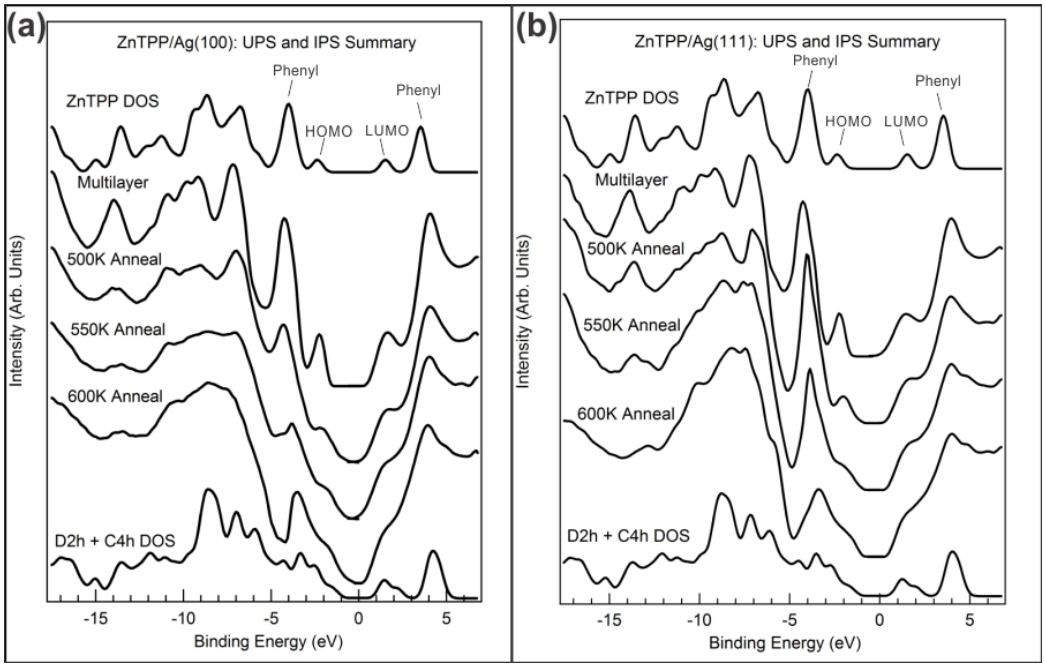

Figure 4.16: Combined ultraviolet photoemission (negative binding energy) and inverse photoemission (positive binding energy) spectra of ZnTPP on (a) Ag(100) and (b) Ag(111) for multilayer coverage, and after annealing to 500K, 550K, and 600K, with the zero of energy defined as the Fermi energy of the system. Also shown are the calculated density of states of both gas phase ZnTPPs (top curve) and the sum of spiral (C4h) and rectangle (D2h) dehydrogenated species (bottom curve).

To gain further insight into the electronic structure changes upon dehydrogenation, the C1s core

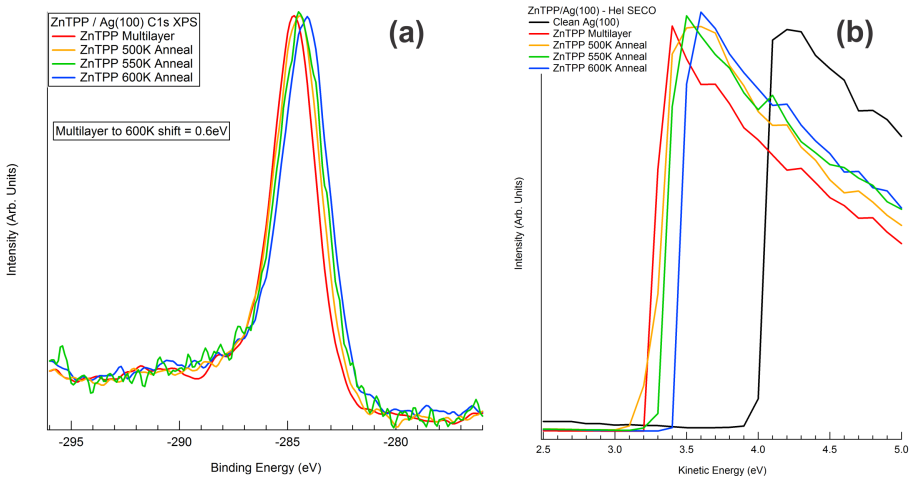

Figure 4.17: (a) XPS C1s core level spectra for ZnTPP on Ag(100) multilayer, and 500K, 550K, and 600K anneals. (b) Secondary electron cutoff (SECO) measured using HeI UPS for clean Ag(100), ZnTPP multilayer on Ag(100), and 500K, 550K, and 600K anneals.

levels are measured using XPS. The C 1s core level spectra, shown in Figures 4.17a and 4.18a for Ag(100) and Ag(111) respectively, shift progressively to lower binding energies from an as-deposited multilayer and through subsequent anneals at 500 K, 550 K, and 600 K. From the multilayer to 550 K anneals, the system progressively reaches a monolayer coverage, therefore the 0.5 eV shift is explained by an improved screening of the core hole in the presence of the substrate when the thickness of the molecular layer decreases. Beyond 550 K, dehydrogenation occurs and alters both the local chemistry and likely the molecule-surface distance[143, 194]. Therefore the 0.1 eV shift cannot be explained only as a screening effect.[114, 143, 194]

As a supplement to the previous occupied and unoccupied states measurements, the secondary electron cutoff (SECO) is measured for the same surface preparations and are shown as Figures 4.17b and 4.18b, for the Ag(100) and Ag(111) surfaces, respectively. Upon deposition of the ZnTPP multilayer on the clean Ag surfaces, the SECO shifts by 0.8 eV toward lower electron kinetic energies. This shift has been described for similar weakly-interacting adsorbates on metal surfaces in terms of the pillow-effect.[93, 178] Annealing to 500K, i.e., desorbing the multilayer, results in little or no shift in the SECO, however the 550K anneal shifts the SECO by 0.1 eV toward the Fermi level. After annealing to 600K, the SECO shifts toward higher kinetic energy by 0.2 eV on Ag(100) and 0.4 eV on Ag(111).

Combining UPS and IPS measurements with measurement of the SECO using HeI UPS, we can create a complete electronic energy level alignment diagram for ZnTPP on Ag(100) and Ag(111) as shown in Figures 4.19a and 4.19b, respectively. Specifically, the relative energy separations of the ZnTPP HOMO and LUMO with respect to the Fermi energy of the system (E_F) as well as the

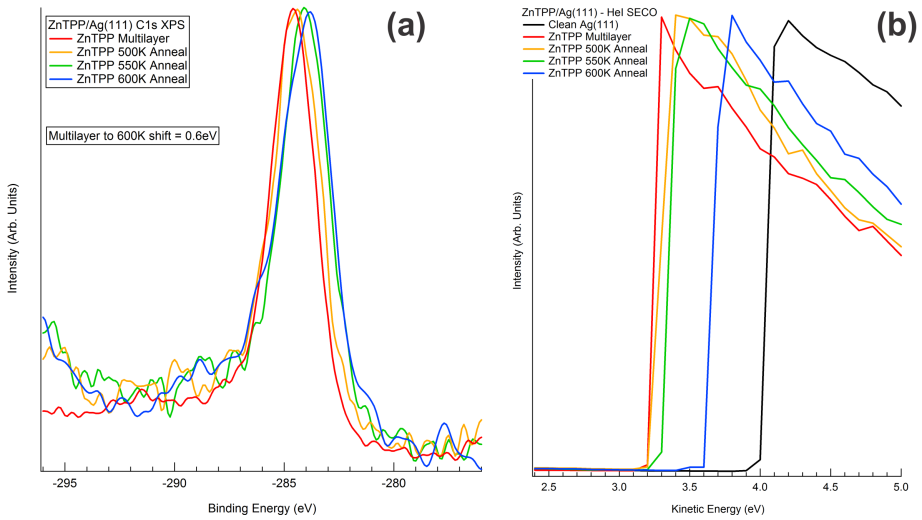

Figure 4.18: (a) XPS C1s core level spectra for ZnTPP on Ag(111) multilayer, and 500K, 550K, and 600K anneals. (b) Secondary electron cutoff (SECO) measured using HeI UPS for clean Ag(111), ZnTPP multilayer on Ag(111), and 500K, 550K, and 600K anneals.

vacuum level shift, or interfacial dipole (Δ), are depicted.

Upon adsorption of either the multilayer ZnTPP or the monolayer ZnTPP onto clean Ag, there is a pronounced decrease in the vacuum level (Δ=0.8 eV) due to the push-back or pillow effect.[32, 98] As mentioned earlier, from a multilayer to a monolayer configuration, a subtle HOMO-LUMO gap narrowing is measured, attributed to a more efficient screening from the substrate when all the molecules are in direct contact with the Ag surface.[126] Additionally, no change in the interfacial dipole is measured in going from multilayer to monolayer for either surface.

Upon dehydrogenation, the HOMO-LUMO gap is further reduced due to the increased delocalization of the HOMOs and LUMOs enabled by the planar geometry of the new species at the surface. Moreover, Δ is further reduced by 0.2eV for Ag(100) and 0.4eV for Ag(111). Recall that from STM observations molecular coverage decreased from 1 ML to 0.7 ML after a 610K anneal and 0.5 ML after a 640K anneal. Such decreases in molecular coverage could result in a reduction of the pillow effect compared to 1 ML, and therefore a decrease of Δ. Additionally, recall that upon dehydrogenation the molecules flatten, significantly altering their conformation to the substrate surface. The phenyls and pyrroles are closest to the substrate for the intact molecule, however after dehydrogenation they are coplanar with the porphyrin core. This could have one of two effects: the porphyrin core remains fixed as the phenyls and pyrroles flatten resulting in a net increase in molecule-substrate separation, or the porphyrin core settles closer to the substrate surface after the phenyls and pyrroles flatten which results in a decreased molecule-substrate separation. In the latter case, a decreased molecule-substrate distance results in greater electron density pushed back

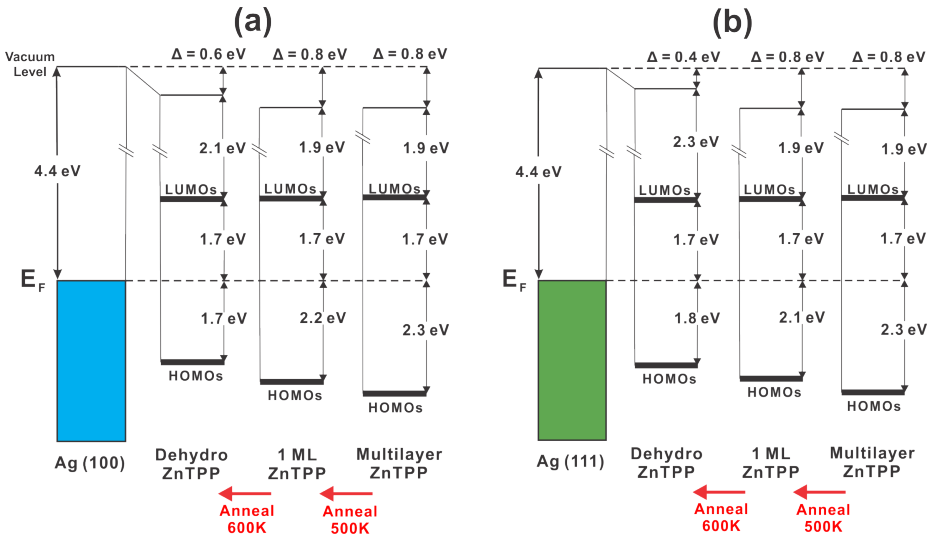

Figure 4.19: Electronic energy level alignment diagram for ZnTPP multilayer, monolayer, and dehydrogenation on (a) Ag(100) and (b) Ag(111). Δ represents the change in vacuum level from that of the clean Ag(100) or Ag(111) substrate. LUMOs were inferred from inverse photoemission spectroscopy, and HOMOs from ultraviolet photoemission spectroscopy, both of which are in reference to the Fermi level of the system (E_F), shown as the horizontal dashed line.

into the metal surface and an increase in the pillow-effect dipole, which is opposite to what is observed. However in the former case, an increase in molecule-substrate separation would reduce the pillow dipole. Alternatively, as we will note in the next chapter for ZnTPP/TiO_2(110), a reduced molecule-substrate separation increases the probability of electron transfer between the molecule and substrate, which would also effect the interfacial dipole in a way that depends on the direction of electron transfer. The interfacial dipole consists of a combination of charge redistribution and charge transfer effects that is complicated to interpret, and we cannot conclusively say which of the aforementioned situations best represents our system.

Note that we have only performed spectroscopic measurements on ZnTPP, and not ZnPC. This is because dehydrogenated ZnTPPs are significantly different than intact ZnTPPs in that the phenyl states are no longer decoupled from the macrocycle states, resulting in large changes of electronic structure. ZnPCs are not likely to reconfigure intramolecularly upon dehydrogenation and instead remain planar. Given that the majority of measurable DOS differences between intact ZnTPPs and dehydrogenated ZnTPPs were related to significant changes of molecular geometry, and assuming ZnPCs are unlikely to alter their structure upon dehydrogenation besides the removal of H atoms, it is unlikely that UPS and IPS will distinguish intact ZnPCs from dehydrogenated ZnPCs. As of this writing, no such DOS comparison has been performed, and so we leave the DOS comparison and subsequent spectroscopic investigation for future study.

4.5 Conclusions

The progression of an intact ZnTPP monolayer, obtained via multilayer desorption, to a dehydrogenated layer upon annealing was described using STM. It was shown that an intact monolayer is achieved by annealing a multilayer to 500K. Further annealing to 550K induces dehydrogenation which flattens the molecules, increasing their footprint and forcing them out of the densely-packed monolayer. Annealing to 600-640K dehydrogenates the remaining ZnTPPs and desorbs any molecules in the second layer, leaving a stable dehydrogenated layer on the surface that is easily imaged but has lost long range order. High resolution imaging elucidates intramolecular dehydrogenation processes leading not only to spiral or rectangular rehybridizations but also to an array of hybrid dehydrogenation products. Intermolecular bonding through hydrogen loss was also observed and indicates a possible route for long-range 2D polymer growth.

To test the hypothesis that the flattening of ZnTPP molecules upon dehydrogenation primarily disrupted the self-assembled order, ZnPC was studied. Since ZnPC self-assembles and is a planar molecule, its footprint should not change upon dehydrogenation. Furthermore, there are no obvious intramolecular rehybridization pathways that are likely to occur upon dehydrogenation of ZnPC, providing a better chance to maintain the intact ZnPC self-assembled organization. The qualitative STM progression with temperature was similar to that for ZnTPP; annealing the monolayer to subsequently higher temperatures resulted in large scale disorder and difficult imaging, followed by the desorption of molecules as well as intermolecular bonding forming ZnPC chains. Additionally, identifying the onset of dehydrogenation in ZnPC is more difficult than for ZnTPP, and can only be inferred by observing intermolecular bonding.

Spectroscopic measurements of the occupied and unoccupied molecular states, using UPS and IPS respectively, provide valuable and conclusive chemical information of the dehydrogenation evolution of the ZnTPP molecules with temperature. The results show gradual evolution from intact ZnTPP states to dehydrogenated states as a function of annealing temperatures that agree well with the progression seen in STM. The HOMOs and phenyl states shift toward the Fermi energy from multilayer to monolayer coverage after a 500K anneal due to enhanced substrate screening compared to the multilayer. Annealing to 550K and 600K broadens the HOMO and occupied phenyl states and decreases the intensity of the phenyl-derived state. The spectra obtained after annealing to 600K agree well with the C4h + D2h calculated DOS and no longer show contribution from the intact ZnTPP calculated DOS, which is consistent with the STM results.

In summary, this work provides a unique perspective on dehydrogenated TPPs on noble metal surfaces by confirming the existence of spiral or rectangle dehydrogenation products, as well as

hybrid symmetries and intermolecular bond formations. Furthermore, in an attempt to simplify the system using ZnPC, a molecule whose structure does not significantly change upon dehydrogenation, we showed that the dehydrogenation process is more intricate than originally thought. Indeed, the planar ZnPC molecule exhibits loss of long range order upon dehydrogenation just as ZnTPPs do. Additionally, electronic structure information obtained with UPS and IPS confirms the progression of an intact ZnTPP monolayer to a dehydrogenated ZnTPP layer by way of a direct comparison with electronic structural calculations.

Chapter 5

Organic/Oxide Interfaces: Adsorption Geometry and Electronic Energy Level Alignment

5.1 Introduction

Characterizing self-assembly is a crucial step in understanding the organic/metal interface and gives insight into molecule-substrate and molecule-molecule interactions. It is also beneficial to study the chemistry at the surface using a combination of theoretical and experimental methods that, when combined, provide valuable insights and interpretation of the interactions at the interface. Then, taking results from adsorption geometry measurements and applying them to theoretical models of electronic structure at the interface greatly aids in accurate interpretation of the occupied and unoccupied states measurements. For example, constraints placed on the organic conformation and organization at the substrate surface from STM provide a foundation for theoretical modeling of adsorption geometry and subsequent electronic structure calculations, which, in principle, should more accurately reflect the measured occupied and unoccupied states from XPS, UPS, and IPS. Combining these three methods improves the confidence of energy level alignment models for a given molecular adsorption geometry on the substrate of interest.

In the previous chapter, we introduced how electronic structure measurements are obtained and interpreted using gas-phase molecular DOS calculations. To briefly review, the clean substrate surface occupied and unoccupied states are fully characterized prior to deposition of molecules to test that the surface is properly prepared. The clean substrate spectra is also subtracted from the combined molecule/substrate spectra to give the molecular contribution. After subtraction of the substrate contribution from the total molecule/substrate spectra, we compare the remaining molecular contribution to gas phase molecular DOS calculations to aid in interpretation of the experimental spectra (see Appendix B). If the molecule-substrate interaction is sufficiently weak that the spectra is well-described by gas phase molecular DOS (e.g., ZnTPP on Ag(111), Ag(100)), the binding energies of molecular HOMOs, LUMOs, and other prominent orbitals are extracted from experimental spectra. Furthermore, the secondary electron cutoff of the clean substrate and molecule-covered substrate are measured to give the substrate vacuum level and work function, as

well as the change in vacuum level due to the presence of the molecule. The change in vacuum level is directly linked to the interfacial dipole at the surface in the presence of molecules and provides insight into the charge redistribution upon molecule adsorption. In this way, we can create complete electronic energy level alignment diagrams of the clean substrate as well as the multilayer- and monolayer-covered substrate with respect to the Fermi level of the system, with substrate band edges and organic HOMOs and LUMOs measured directly.

As was shown in the previous chapter for ZnTPPs on noble metal surfaces, gas phase molecular DOS sufficiently describes weakly interacting systems to match experimental results. However, to better understand charge transfer and charge reorganization at the interface, molecular conformation to the surface, and interpretation of the interfacial dipole, more sophisticated theoretical methods are used that include the substrate. The approach used is as follows. The adsorption geometry of a single molecule on the surface of a substrate slab is first calculated at zero temperature and compared with STM measurements. Then, energy alignment of the molecule with the substrate surface is calculated for zero temperature and room temperature, with intermolecular effects on the molecule of interest included. In this chapter, we compare experimental energy alignment to theoretical models of the electronic structure at the interface based on the adsorption geometry taken from STM, for both ZnTPP/TiO_2(110) and TCNQ/TiO_2(110). As each molecule/TiO_2 system is unique, the exact applied calculational method varies from case to case. Thus, details for the ZnTPP and TCNQ systems can be found in references [142] and [119], respectively.

Hybrid materials that contain interfaces between transition-metal oxides and organic species exhibit very promising properties for applications in devices like solar cells, light-emitting diodes, fuel cells, and thin-film transistors. In particular, the easy injection of charge between the oxide and the organic, which depends critically on the barriers formed at the interface between the materials, plays a very important role in the good efficiency of those devices.[60, 92, 109, 121, 130, 158]

A large amount of work has been undertaken in an effort to understand the energy level alignment between different metal/organic and organic/organic interfaces.[39, 59, 98] In contrast, very few studies have analyzed the energy level alignment at the interface between transition-metal oxides and organic semiconductors. In a recent work, Greiner et al.[67] analyzed a variety of nonreactive oxide/organic interfaces and concluded that the energy level alignment is determined mainly by one driving force: the electron chemical potential equilibration between the oxide Fermi level and the organic ionization energy. On the other hand, Xu et al.[195] have conclusively shown that a second driving force is the oxide doping and the concomitant formation of a space-charge layer upon the interaction with the organic material; for strongly n-doped oxides, such as ZnO or TiO_2, this mechanism is particularly important when the organic affinity level is located below the oxide Fermi

level, as is the case of F4TCNQ physisorbed on a H-saturated ZnO(000$\bar{1}$) surface.[195] Recently, other groups have also shown the important role that the oxide/organic interface chemistry has in the barrier formation.[109, 189] This suggests that the injection of charge between transition-metal oxides and organic materials depends crucially on the interface barrier that is determined mainly by the relative electronegativity of both materials, the possible space-charge layer formed in the oxide, and the chemical interaction between the oxide and the organic.

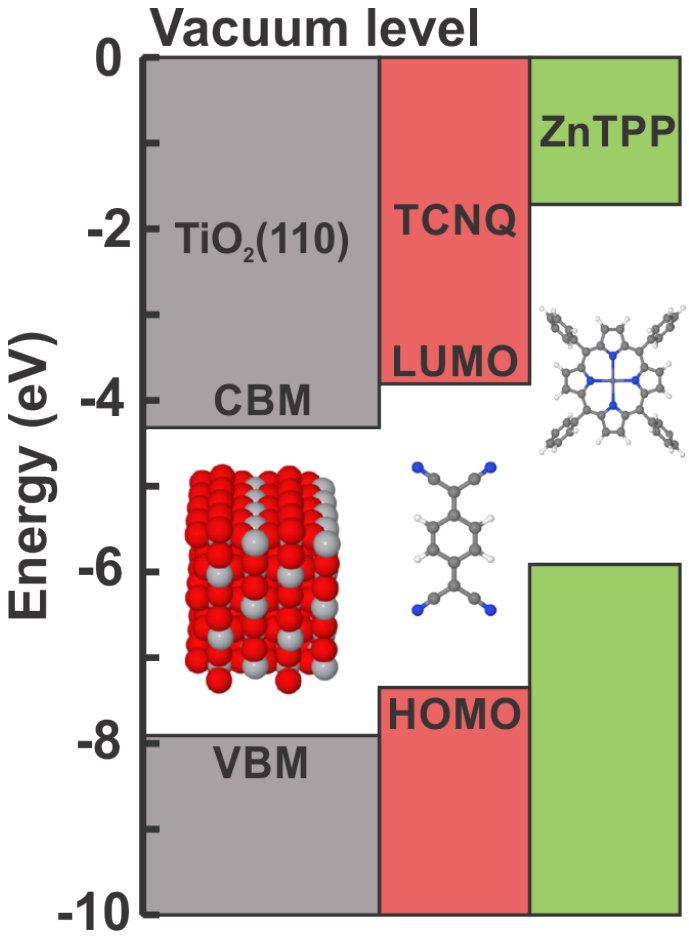

Figure 5.1: Relative energy level alignment diagram showing TiO_2(110) CBM and VBM, and the HOMOs and LUMOs of isolated TCNQ and ZnTPP defined with respect to the vacuum level (a large distance from the substrate surface).

Figure 5.1 shows the relative energy level alignment of the TiO_2(110) conduction band minimum (CBM) and valence band maximum (VBM) with the HOMOs and LUMOs of TCNQ and ZnTPP with respect to the vacuum level far from the substrate surface. The large electron affinity of TCNQ makes it a strong electron acceptor, whereas ZnTPP HOMOs and LUMOs are relatively far from the TiO_2 band edges, thus it is not expected to interact as strongly. Monolayers of each of these molecules on the TiO_2(110) surface are studied using photoemission spectroscopy and DFT electronic structure

calculations, as well as STM for ZnTPP. The experimental approach to each system is similar; molecules are sublimated in UHV onto a clean $TiO_2(110)$ surface, and photoemission measurements are taken *in situ*. However, due to the wide range of chemical composition and electronic structure of each molecule and the resulting differences in molecule-substrate interactions, the electronic structure calculations and theoretical energy level alignment are unique for each system.

In this chapter, we start with ZnTPP on the wide bandgap oxide semiconductor, $TiO_2(110)$, using the same multilayer and monolayer preparation method as on the noble metals, i.e., multilayer desorption. Next we study a TCNQ monolayer on $TiO_2(110)$. Recall that TCNQ is a relatively small molecule with significantly larger electron affinity than ZnTPP, and represents an organic/oxide interface with relatively strong interactions compared to ZnTPP/TiO_2. We will show that the gas phase molecular DOS is not sufficient to describe the system, necessitating a more sophisticated theoretical approach. From this approach, we elucidate the fundamental physical interactions that contribute to the electronic energy level alignment at the interface, including an interpretation of the interfacial dipole.

5.2 ZnTPP on $TiO_2(110)$

5.2.1 Introduction

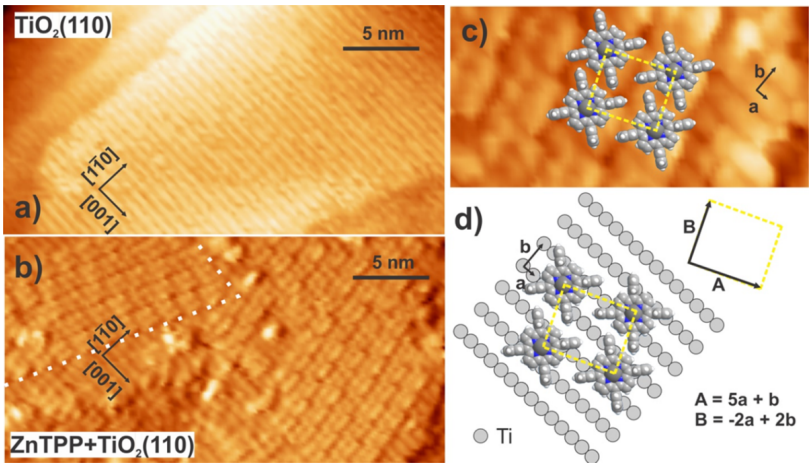

Figure 5.2: STM images of (a) a clean $TiO_2(110)$ surface before and (b) after ZnTPP adsorption. Both images were taken at $V_s = +2$V and are thus mapping unoccupied states. (c) Zoomed-in area of (b) that contains both a ZnTPP-covered region and a clean surface region, allowing determination of the molecular adsorption scheme in (d).

The following discussion of ZnTPP on the $TiO_2(110)$ surface is based on work I have done in collaboration with theoretical physicists that has been published[142]. For details on the calculational methods used in this work, please see reference [142].

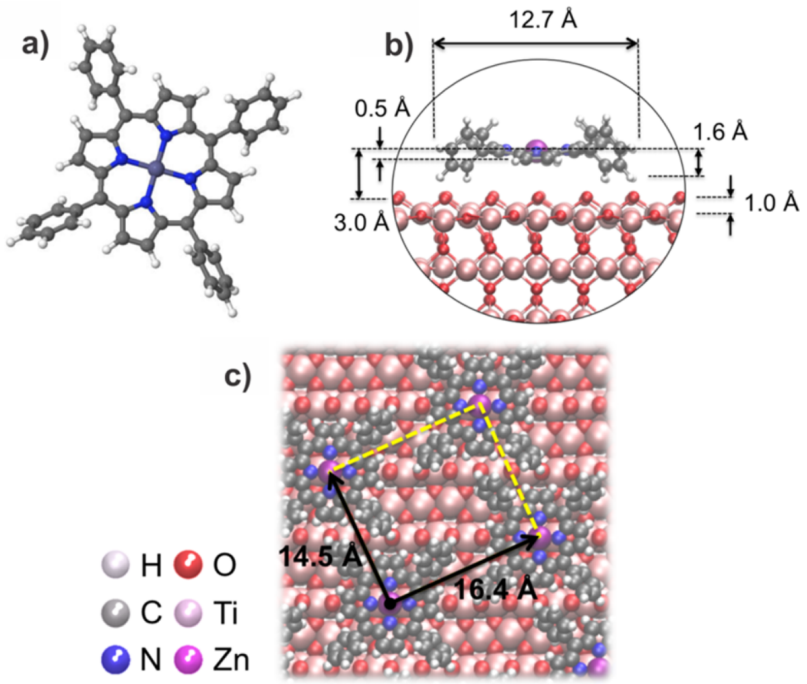

Figure 5.3: Surface geometry for the densely packed ZnTPP/TiO_2(110) interface. (a) Gas-phase molecule. (b) Geometry of the molecule on TiO_2(110). (c) Close-packed geometry of the ZnTPP monolayer.

Owing to their strong light absorption properties, interfaces between metalloporphyrins and wide band gap semiconductors have been natural candidate systems for photovoltaic and photochemical applications.[40, 86, 140, 176, 185, 198] For such applications, the efficiency of photoexcited charge transfer processes depends on the relative energy alignment of the molecular orbitals involved in light absorption (typically HOMO-LUMO transitions) with respect to the band edges of the surface onto which they are adsorbed. Molecule-substrate energy level alignment at interfaces cannot be readily predicted using, for example, the individual properties of the molecule and of the surface,[39, 59, 98] as upon contact complex charge rearrangement occurs, leading to the creation of an interface dipole.

To date, experimental energy alignment studies of porphyrin derivatives on TiO_2 have been limited to solution-sensitized films or single-crystal surfaces where molecular adsorbates are covalently bound to the surface via carboxylic acid anchor groups. These methods, although representative of real-life devices, can obscure the intrinsic properties of the molecule/oxide interface owing to disorder arising from multiple bonding geometries and from exposure to the ambient as well as charge exchange associated with the carboxylic acid anchor groups.[139–141]

In this work, we performed a combined experimental and theoretical study of a paradigmatic model interface: a ZnTPP monolayer deposited via sublimation onto a well-characterized TiO_2(110) surface in a controlled UHV environment. The result is a well-ordered ZnTPP/TiO_2(110) interface

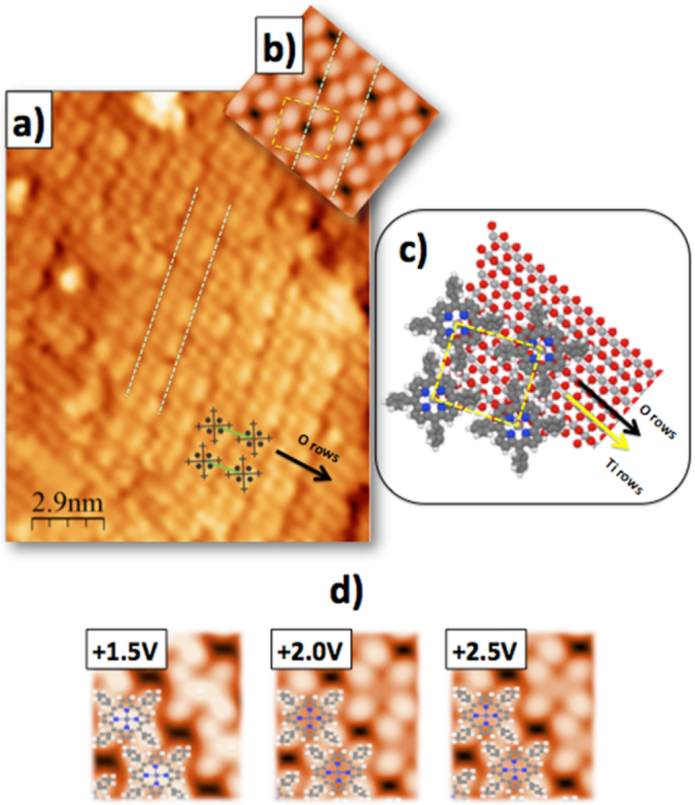

Figure 5.4: Comparison between (a) experimental and (b) simulated STM images at $V_s = +2.0$V for the ZnTPP/TiO_2(110) interface model represented in (c). For comparison, (d) shows a series of computed STM images for $V_s = +1.5$, +2.0, and +2.5V.

that is highly suited for study using a joint experimental-theoretical approach. The geometry, relative on-surface orientation, periodicity, and registry of the ZnTPP molecular array with the TiO_2(110) substrate have been studied using STM, and a detailed adsorption model has been proposed, based on a DFT energy minimization approach and supported by simulations of the STM images. Moreover, the energy level alignment has been determined experimentally using a combination of XPS, UPS, and IPS. The nature of the charge rearrangement at the interface has been explored using a DFT approach introducing appropriate corrections. Excellent agreement between experiment and theory, in both the geometric structure and the energy level alignment, is found for this system at monolayer coverage. The calculated interface dipole for a different ZnTPP monolayer, taking for each ZnTPP molecule the geometry of an isolated molecule interacting with the oxide, differs substantially from the experimental findings, illustrating the importance of intermolecular effects in establishing the ZnTPP geometry and the interface dipole of the molecular monolayer.

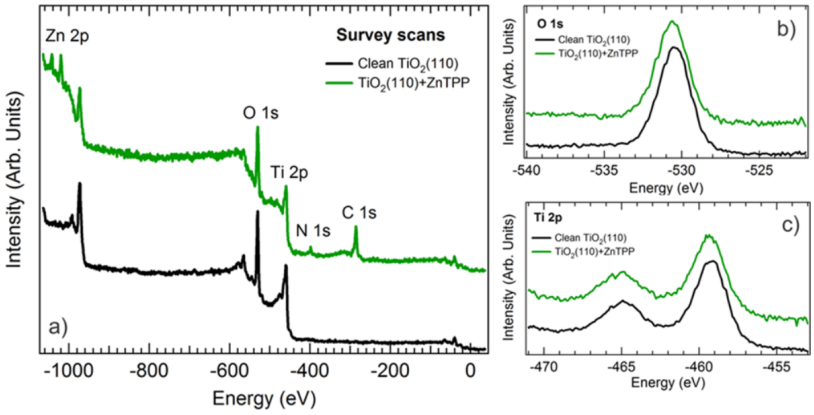

Figure 5.5: (a) XPS survey scans measured on the clean TiO_2(110) surface and covered with a monolayer of ZnTPP molecules. No band bending was observed upon ZnTPP adsorption as observed from (b) the O1s and (c) Ti2p core levels of the TiO_2 substrate before and after ZnTPP monolayer formation.

5.2.2 Surface Preparation

The rutile TiO_2(110) sample was a commercially produced single crystal from MTI corporation, cut to within 0.5° of the (110) plane. The surface was degassed and prepared in an ultrahigh vacuum using several cycles of 1 keV Ar+ ion sputtering (while maintaining a maximum sample current of 2 μA) and annealing in UHV at 600°C. The cleanliness of the surface was checked using XPS, and the surface termination was assessed either by low-energy electron diffraction (LEED) or by STM.

ZnTPP molecules [Frontier Scientific, >95% purity] were deposited by way of sublimation deposition in the same UHV environment using a thoroughly degassed Knudsen cell held between 250 and 280°C. The deposition rate was measured using a quartz crystal monitor.

5.2.3 Results and Discussion

Adsorption Geometry

When cut along the (110) plane, rutile TiO_2 crystals expose a surface with 2-fold symmetry, comprised of alternated O and Ti rows running along the [001] crystallographic direction. STM images of the clean and ZnTPP-covered TiO_2(110) surface, measured by tunneling into the unoccupied states (+2V), are shown in Figure 5.2. Figure 5.2a is an STM image of the clean surface. Although the O rows are protruding above the plane containing the first exposed Ti atoms, the latter appear as bright rows in STM images obtained at this bias owing to the unoccupied Ti 3d states of the conduction band, and the former as darker lines between those rows.[50] A detailed analysis of Figure 5.2a gives a measured row separation of 6.3 ± 0.2 Å, which is in good agreement with the value of 6.5 Å expected based on the bulk lattice parameters.

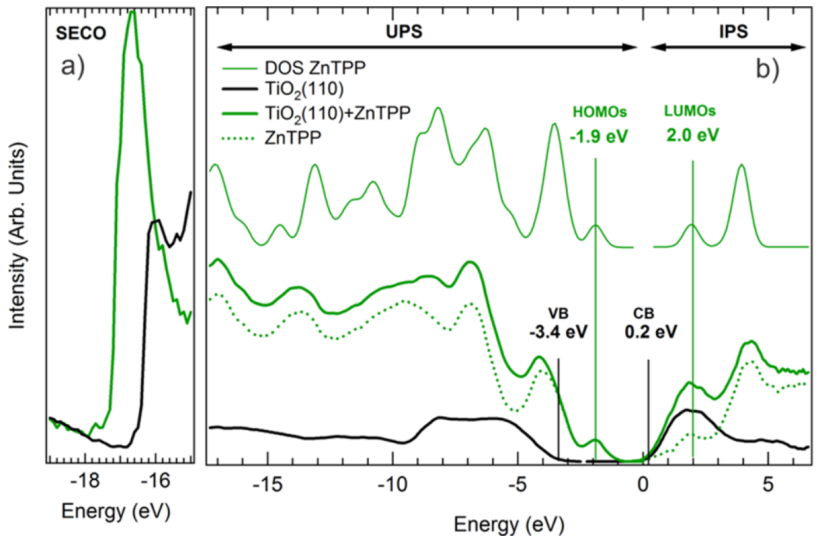

Figure 5.6: (a) Secondary electron cutoff (SECO); (b) UPS and IPS spectra of the clean (heavy black curve) and ZnTPP-covered (heavy green curve) $TiO_2(110)$ surface. The difference spectrum (dotted green curve) is to be compared to the calculated DOS (thin green curve).

Studies of the ZnTPP molecule deposited by sublimation onto single-crystal surfaces in ultrahigh vacuum have used two different methods to achieve monolayer coverage: (*i*) molecular deposition with increasing exposure until the surface is fully covered by a monolayer of molecules or (*ii*) deposition of a molecular multilayer followed by low-temperature (150-200°C) annealing to desorb weakly bound molecules and leave a monolayer on the surface.[52, 114, 146] Recently, method *i* has been used to study adsorption of a ZnTPP derivative on $TiO_2(110)$ and led to a somewhat disordered monolayer with no clear evidence of preferred adsorption sites.[129] In the study described here, we have chosen method *ii*: desorption of a multilayer at room temperature followed by annealing at 150°C. An STM image of a surface prepared in this way is shown in Figure 5.2b. This method of preparation leads to large terraces that are nearly completely covered by ordered molecular features. The molecular array is comprised of a rectangular lattice with measured dimensions of 16.3Å×14.3Å. Figure 5.2c is a close up of the lower right corner of Figure 5.2b showing adjacent regions with and without ZnTPP molecules. The smaller repeating unit, which is composed of four bright lobes arranged in a square configuration, is characteristic of ZnTPP and associated with the four mesophenyls of the molecule. The center of ZnTPP typically appears as a depression owing to the absence of unoccupied Zn states at this bias.[140, 146]

Using the adjacent clean and molecule-covered regions of the surface, the registry of the molecular array with respect to the surface lattice of the substrate can be determined. Extrapolating the oxygen rows in Figure 5.2c toward the molecule-covered area shows that the Zn center of each molecule as well as opposite pyrroles of the porphyrin macrocycle lie along an oxygen row. As a result, the

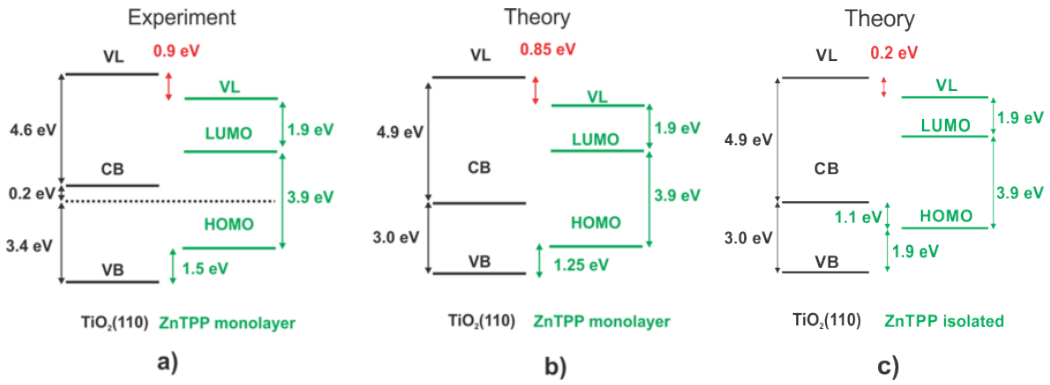

Figure 5.7: Energy alignment. Comparison: (a) Experiment for a monolayer, (b) theory for the ZnTPP monolayer, and (c) theory for a ZnTPP monolayer with the molecular adsorption geometry corresponding to an isolated ZnTPP molecule on $TiO_2(110)$ (see text).

phenyls are aligned with the Ti rows adjacent to the oxygen row on which the molecule is centered. While it is not possible to determine the precise location of the ZnTPP molecules along the oxygen row, it is clear that the primitive vectors of the molecular lattice (A and B) are not aligned with those of the underlying surface (a and b). Figure 5.2d shows an adsorption geometry that is consistent with the STM images of Figure 5.2b and 5.2c. For simplicity, only the Ti rows are represented here. Using a notation where a is the unit vector along the [001] direction with a Ti-Ti distance of 3Å and b the unit vector in the $[1\bar{1}0]$ direction with a Ti-Ti distance between two rows of 6.5Å, the ZnTPP lattice vectors A and B can be expressed in terms of the substrate lattice vectors as $A = 5a + b$ and $B = 2a + 2b$. Additionally, Figure 5.2b shows that two different domains are visible on the surface, indicating that the ZnTPP molecules can organize themselves in two equivalent ways, which are reflected about a $1\bar{1}0$ mirror plane.

The overlayer geometry deduced from our STM measurements is both confirmed and refined by our theoretical calculations, the details of which can be found in reference [142]. Using the Quantum Espresso code, as described briefly in Appendix A and in detail in reference [142], we find that the lowest energy configuration corresponds to a geometry in which the central Zn atom is placed 3.0Å directly above an oxygen atom of the O row, as shown Figure 5.3b. In this model geometry the ZnTPP molecules form a monolayer with one molecule per unit cell with dimensions 16.4Å×14.5Å (see Figure 5.3c), quite close to the experimentally measured values. For reference, the calculated geometry of the gas-phase ZnTPP molecule is shown in Figure 5.3a. We should stress that in our calculations the final molecule geometry depends crucially on the repulsive interaction between the mesophenyl rings of adjacent molecules; calculations for an isolated molecule on the oxide surface yield a distinct molecular conformation, and if this geometry is used in the monolayer case, we obtain a smaller charge transfer to the oxide. We will see later that accounting for the adsorption geometry

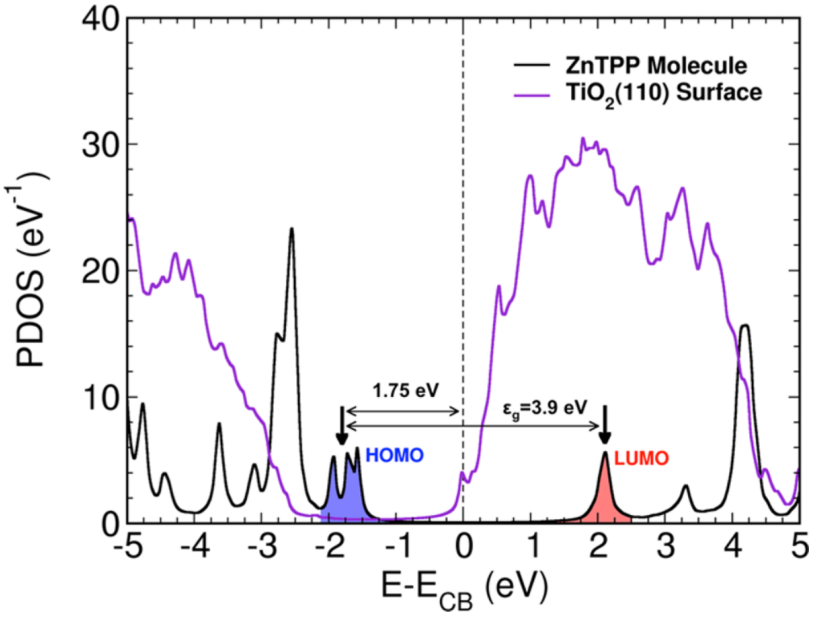

Figure 5.8: DOS projected on the molecule and oxide orbitals.

of the full monolayer is critical for obtaining the correct energy alignment at the interface. Upon adsorption, the ZnTPP molecules become distorted as shown in Figure 5.3c. The ZnTPP porphyrin ring is adsorbed at a distance of 2.5-3.0Å above the TiO_2(110) O row, with the mesophenyl rings keeping a rotation with respect to the flat ZnTPP molecular skeleton similar to the one found for the gas-phase geometry. In particular, the mesophenyl rings of the molecule rotate by an angle between 2.5° and 6.5° with respect to the gas-phase geometry, so that those rings form an angle of 50 ± 2° with the flat porphyrin molecular skeleton, instead of 54.5° in the gas phase; these rotations enable some of the H atoms of the mesophenyl rings to form weak bonds with the O atoms of the surface, such that the H-O distances are between 2.2 and 2.4Å.

Using this relaxed geometry summarized in Figure 5.3, we also calculated the theoretical STM image for the ZnTPP monolayer on TiO_2(110) using a combination of a Greens function formalism and local-orbital DFT, described in detail in reference [142]. Figure 5.4a reports the experimental STM image measured at $V_s = +2$V. Figure 5.4b shows the theoretical STM image for a tunneling bias of $V_s = +2.0$ V, and Figure 5.4d shows a series of computed STM images for $V_s = +1.5$, +2.0, and +2.5 V. For comparison, the adsorption geometry of the ZnTPPs on the TiO_2(110) surface is also reported in Figure 5.4c. The details of the "shift and stretch" corrections[157] introduced in the local-orbital DFT electronic structure calculation are discussed in reference [142], and these corrections to the energy alignment are taken into account in the theoretical STM images. At these tunneling conditions the mesophenyls appear as bright lobes arranged in a square, while the central Zn atom is not contributing to the image, in good agreement with the experimental STM image.

Notice that in the STM image of Figure 5.4b, two out of four mesophenyl rings show, due to their rotation, some non-negligible overlap with the corresponding mesophenyls of neighboring molecules. This suggests the possibility of probing different surface geometries depending on the alternative rotation of those ZnTPP mesophenyls.

The good agreement between the experimentally determined molecular bonding geometry and that found by a DFT energy minimization approach combined with simulations of the STM images strongly suggests that this theoretical interface geometry is an appropriate structural model for our combined theoretical and experimental analysis of the interface electronic structure and energy level alignment.

Energy Alignment

In order to fully characterize the energy alignment of the TiO_2(110)/ZnTPP monolayer interface, XPS, UPS, and IPS spectra of the core levels, valence band, and conduction band, respectively, were measured before and after the ZnTPP monolayer was established. A survey scan of the TiO_2(110) surface before and after molecular deposition is shown in Figure 5.5a. The XPS spectrum of the clean surface (black curve) indicates the presence of only Ti 2p and O 1s core levels, whereas the spectrum after ZnTPP monolayer formation (green curve) contains peaks associated with the Zn 2p, C 1s, and N 1s core levels. Figure 5.5b and 5.5c contains high-resolution O 1s and Ti 2p core level spectra. The absence of any appreciable shift in these core levels after ZnTPP deposition indicates that adsorption of this molecule does not induce band bending, which suggests that there is relatively little charge transfer between the surface and the ZnTPP overlayer.[119] This is not surprising given that the molecule is weakly bound to the TiO_2 surface.

UPS spectra of the valence band and secondary electron cutoff as well as IPS spectra of the conduction band region for the clean TiO_2(110) and ZnTPP monolayer covered surfaces are shown in Figure 5.6. All spectra have been referenced to a common Fermi level set at 0 eV, so that occupied states occur at negative energy and unoccupied states at positive energy. The VB and CB of clean TiO_2(110) (black curve) shown in Figure 5.6b are characteristic of that surface. The VB is mainly composed of O 2p states with a sharp high-energy edge that when extrapolated yields a valence band maximum at 3.4 eV. The CB possesses strong Ti 3d features, whose edge when extrapolated puts the conduction band minimum at 0.2 eV. Thus, the band gap measured on this TiO_2(110) surface is 3.6 eV, consistent with that reported in the literature.[139–141] As expected, the TiO_2(110) surface appears strongly n-doped with the Fermi energy near the conduction band minimum. The electron affinity of the pristine surface is estimated to be 4.6 eV, based on the SECO edge of Figure 5.6a.

The spectra of Figure 5.6b that were obtained from the ZnTPP monolayer-covered TiO_2(110)

surface (thick green curve) exhibit strong molecular features both in the occupied and in the unoccupied states. By subtracting appropriately scaled UPS and IPS spectra of the clean surface from the spectra of the ZnTPP-covered surface, features associated with the molecular layer can be isolated. The background-subtracted curves, representing the molecular contribution to the spectra, are shown as green dotted lines in Figure 5.6b. This experimentally measured electronic structure can be directly compared to the DOS calculated (GAMESS-US,[154] B3LYP,[18, 19, 106] 6-31G*[155] adjusted to fit the experimental HOMO-LUMO gap) for a ZnTPP gas-phase molecule shown on top of Figure 5.6b as a thin green line.

It is clear that there is a good correspondence between the measured occupied and unoccupied states and the calculated ZnTPP molecule electronic structure. In particular, molecular states that are found in the TiO_2(110) band gap region around 1.9 eV can be attributed to the ZnTPP HOMOs, while the first unoccupied states measured around 2 eV in IPS correspond to the ZnTPPs LUMOs. Additionally, both the theoretical and the experimental curves exhibit strong mesophenyl-related features in both the occupied and the unoccupied states, centered at 3.0 and 4.0 eV, respectively. The good agreement between the difference spectra and the molecular calculation provides further evidence that there is relatively little charge transfer between the surface and the molecular layer.[119] Finally, using the SECO measured on the ZnTPP monolayer shown in Figure 5.6a, an effective electron affinity of 1.9 eV is calculated for the ZnTPP monolayer. These results are very similar to those found in earlier studies of TiO_2(110) surfaces sensitized with ZnTPP derivatives in solution.[139–141]

Figure 5.7a shows the full energy diagram for the monolayer ZnTPP/TiO_2(110) system that is drawn from the experimental measurements. The shift in the vacuum levels of the clean and ZnTPP-covered TiO_2(110) surfaces indicates that there is an interface dipole of 0.9 eV.

We analyzed theoretically the interface energy level alignment by means of the local-orbital (FIREBALL) DFT code using the geometry provided by our plane-waves (QUANTUM ESPRESSO) DFT calculations (see Figure 5.3). In our local-orbital Hamiltonian we introduced the scissor and shift operators with the values U and ε chosen to yield initially the values of the molecular levels as shown by the experimental data of Figure 5.7a. In particular, the HOMO/LUMO energy gap for the (deformed) organic molecule is set to 3.9 eV using the scissor operator; also, the initial affinity level is set to 1.9 eV (energy difference from the LUMO level to the initial vacuum level) using the shift operator. Figure 5.7b shows the final position for the different energy levels at the organic/oxide interface (i.e., after self-consistency), and Figure 5.8 shows our calculated DOS projected on the molecule and on the oxide orbitals. We should mention that our LDA calculations for TiO_2 yield an energy gap for the oxide of 3.0 eV instead of the 3.6 eV measured experimentally; we minimized the

effects of this energy difference, assuming that the CB and VB edges of the oxide are 4.9 and 7.9 eV, respectively, instead of 4.6 and 8.2 eV. From Figure 5.8 we see that the HOMO level (taken as an average of the different levels of the HOMO broken symmetry) is located around 1.25 eV above the oxide valence band edge, while the LUMO level is 2.15 eV above the oxide conduction band edge. This indicates, as shown in Figure 5.7b, that in our calculations the interface dipole is around 0.85 eV, in excellent agreement with the experimental evidence (0.9 eV, see Figure 5.7a). This dipole is mostly due to the electron charge transfer from the molecule to the oxide, which we find to be around 0.28 electrons per molecule. The electron transfer alone yields an interface dipole of around 0.8 eV. An additional 0.05 eV is associated with the intrinsic dipole of the slightly deformed molecule. It is also worth mentioning that in the calculated DOS shown in Figure 5.8 the occupied and unoccupied mesophenyl-related states already mentioned above (see Figure 5.6) are found around 3 and 4 eV, respectively, in reasonable agreement with the results shown in that figure.

As a final note we point out that in performing these theoretical calculations it was important to consider full monolayer coverage in order to accurately represent the experiments. When calculations were performed for the case of an isolated ZnTPP molecule on the TiO_2(110) surface it was found that the ZnTPP molecule acquired a saddle-shaped porphyrin ring and rotated mesophenyls: an adsorption geometry similar to the one obtained for ZnTPP embedded in a monolayer. However, the molecule-surface distance is significantly larger for the isolated molecule case: the zinc-terminal oxygen distance is found to be 3.9Å, which is 0.9Å larger than the same distance calculated for the monolayer. This has non-negligible effects on the energy alignment at the interface. The calculated energy alignment for a monolayer, taking for each molecule the geometry of the isolated case, is shown in Figure 5.7c. Although the HOMO and LUMO positions are not markedly different from the ones calculated for the monolayer, the interface dipole is reduced by 0.7 eV to a value of 0.15 eV. This change is the result of less charge transfer from the molecule to the oxide, a consequence of the larger molecule-surface separation. In other words, the repulsive interaction between the mesophenyl rings of adjacent molecules stabilizes a densely packed monolayer with a reduced molecule-surface distance, resulting in greater molecule-surface charge transfer and a larger interface dipole.

5.2.4 Summary

The adsorption geometry and the energy level alignment of a ZnTPP monolayer on the rutile TiO_2(110) surface, a model weakly bound organic monolayer/oxide semiconductor interface, has been studied using a combination of STM, XPS, UPS, IPS, and DFT calculations.

It is found that for the ZnTPP monolayer obtained by desorption of a multilayer grown on a TiO_2(110) surface, ZnTPPs forms a dense and highly ordered array in registry with the underlying

TiO_2(110) surface. In particular, each ZnTPP molecule is centered on top of an oxygen atom of a bridging oxygen row and that the molecule is distorted upon adsorption. In this configuration, rotated phenyls accommodate weak hydrogen bonds to the surface oxygen atoms.

Theoretical exploration indicates that the energy alignment of the ZnTPP molecular levels with respect to the TiO_2(110) band edges is highly sensitive to the molecular coverage and subsequent adsorption configurations. Only a densely packed monolayer model, accounting for molecular distortions and molecule-molecule interactions, led to the correct interface dipole. These results point to the fact that it is crucial for organic/oxide interfaces, even for weakly bonded adsorbates, to properly take into account the short- and long-range interactions of the system as whole.

5.3 TCNQ on TiO_2(110)

5.3.1 Introduction

The following discussion of TCNQ on the TiO_2(110) surface is based on work I have done in collaboration with theoretical physicists that has been published[119]. As mentioned in the introduction to this chapter, organic/oxide interfaces exhibit a variety of effects such as electron chemical equilibration between the oxide Fermi level and organic ionization energy, oxide doping and subsequent formation of a space-charge layer, and organic/oxide interface chemistry and its effect on barrier formation. To understand how the combination of all these effects operates in the formation of the oxide/organic level alignment, we have analyzed in this work the particular case of the TiO_2/TCNQ interface; TiO_2 is one of the most extensively studied substrates for organic devices,[148, 149] while TCNQ is an organic molecule frequently used because of its very electronegative properties,[10, 22, 58, 118] showing a strong chemical interaction with the substrate. We can expect that an important chemical interaction and charge transfer should appear between the two materials, which should affect the interface barrier formation as well as the creation of a metal oxide space charge layer. In the following we shall show experimentally and theoretically that this charge transfer is significant with one electron being transferred from the oxide to the $LUMO_{TCNQ}$ level which is located below the oxide conduction band edge; our results are also compatible with an important increase in the metal oxide work function. We shall also show that the chemical interaction between the oxide and this very electronegative organic material plays an important role in the creation of that charge transfer and in the formation of an oxide space charge layer.

In our approach, we first use UPS, IPS, and XPS to characterize the electronic properties of the TCNQ/TiO_2 interface. A theoretical analysis of these data is a delicate task[195] because of the different length scales associated with the oxide space charge layer or with the intimate contact

between the organic and the oxide. In our analysis we combine a DFT-LDA calculation of that contact with a classical description of the space charge layer; the connection between these two different regimes is provided by the charging energy of the molecule, which is associated with the charge transfer from the oxide space charge layer to the LUMO_{TCNQ} level.

5.3.2 Experimental Results

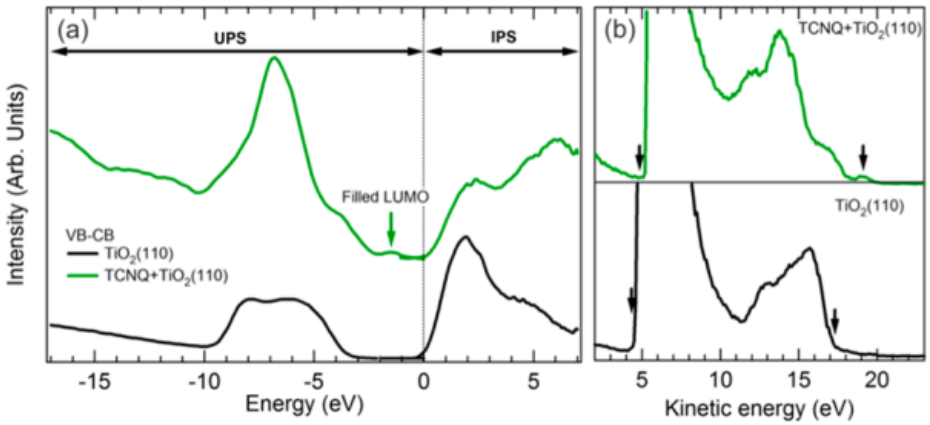

Figure 5.9: (a) Valence and conduction band spectra measured using UPS (He II, $h\nu = 40.8$ eV) and IPS (E = 20.3 eV), respectively, of the clean $TiO_2(110)$ surface and of the same surface saturated with TCNQ. The zero of energy is chosen as the position of the Fermi level. (b) Secondary electron cutoff determination using the full width of the emitted photoelectrons (He I, $h\nu = 21.2$ eV).

A $TiO_2(110)$ single-crystal surface prepared in UHV and exposed to TCNQ was found to saturate at room temperature to a coverage referred to as monolayer coverage (ML) in the following. The valence and conduction band spectra of the clean and TCNQ-exposed TiO_2, measured using ultraviolet and inverse photoemission spectroscopies, respectively, are displayed in Figure 5.9a. In this figure, the zero of energy is defined as the Fermi level, so that the occupied states are characterized with a negative energy and the unoccupied state with a positive energy. The VB of the pristine $TiO_2(110)$ surface originates mainly from O 2p states, while the CB is composed of Ti 3d states. A linear fit of the sharp band edges to the background of the spectra indicates a valence band maximum at -3.5 eV and a conduction band minimum at 0.1 eV, resulting in a 3.6 eV gap for TiO_2. The position of the Fermi level, only 0.1 eV below the conduction band, is indicative of the strong n-doped nature of the TiO_2 crystal (see the supporting information below for the details of band edges measurements). Upon TCNQ adsorption, molecular states appear in both occupied and unoccupied states, as seen in Figure 5.9a. These molecular states cannot be interpreted in terms of the molecular signature of an intact TCNQ molecule. (In contrast, the VB and CB spectra of a TCNQ multilayer grown at 230 K on a metal substrate, shown in the supporting information below, can be directly compared

to the DOS calculated for a TCNQ molecule.) This indicates that TCNQ is strongly affected by the presence of the TiO_2 surface. Particularly important for this study, the first occupied molecular states are found in the gap of TiO_2, 1.5 eV below the measured Fermi level, as indicated by the arrow in Figure 5.9a. In the unoccupied states, broad molecular features, superimposed upon the contribution of the strong Ti 3d state of the TiO_2 substrate CB, prevent a clear determination of the unoccupied frontier molecular states. The position of the VL of the system has also been measured

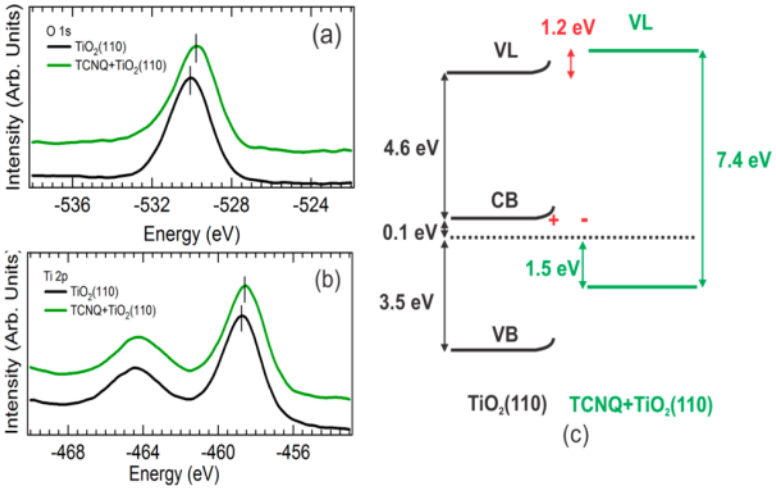

Figure 5.10: (a) O 1s and (b) Ti 2p core levels of the substrate before and after TCNQ adsorption. A clear peak displacement is observed for both core levels and attributed to upward band bending. (c) Energy diagram obtained from the experimental data shown in Figures 5.9 and 5.10.

for the clean and TCNQ-exposed $TiO_2(110)$ surface, using the position of the SECO of the total spectra of emitted photoelectrons shown in Figure 5.9b. An energy separation of 13 eV (delimited by the arrows) is measured between the VB edge and the SECO of the clean $TiO_2(110)$ surface. With a photon excitation energy of 21.2 eV and a measured gap of 3.6 eV, the electron affinity for the $TiO_2(110)$ surface is found to be 4.6 eV. For the TCNQ-saturated TiO_2 surface, the distance between the first occupied molecular state and the SECO (delimited by the arrows) is measured to be 13.8 eV, giving a distance of 7.4 eV between that first occupied molecular state and the VL of the molecule (see Figure 5.10c).

Figure 5.10 shows X-ray photoemission spectra measured on the clean and on the subsequently saturated $TiO_2(110)$ surface. In Figure 5.13 (see supporting information below), large-scale survey scans indicate that, as expected, only C 1s and N 1s core levels are added to the initial Ti 2p and O 1s core levels belonging to the surface. The molecular coverage can be evaluated by comparing the relative ratio of C 1s and Ti 2p core levels to no more than a monolayer. Upon TCNQ adsorption, a noticeable shift of the TiO_2 surface core levels is observed, as shown in panels a and b of Figure 5.10. Both the O 1s and Ti 2p core level spectra are found shifted toward the Fermi level by about

0.2 eV after TCNQ adsorption. Such behavior is interpreted as an upward band bending at the surface of the TiO_2 substrate, due to charge reorganization at the TCNQ/TiO_2 interface. This band bending and the VL (of the TiO_2 and 1 ML TCNQ system) shift, shown in panel c of Figure 5.10, are indicative of a strong negative charge transfer from the oxide to the molecule. This is analyzed theoretically in the following.

5.3.3 Theoretical Analysis and Discussion

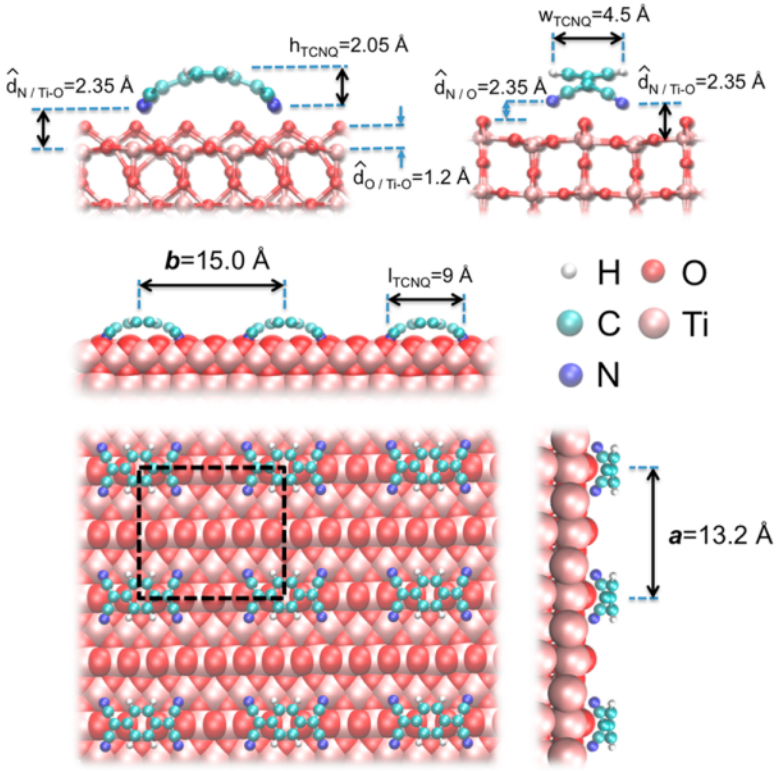

Figure 5.11: Surface geometry for the TiO_2/TCNQ interface. Notice the pronounced on-surface molecule bending of 2.05 Å, which is the height of the molecule, h_{TCNQ}. Width and length of the molecule, w_{TCNQ} and l_{TCNQ}, respectively, are also indicated, as well as the average distances between N atoms and the oxide O-rows, $\hat{d}_{N/O}$; between the N atoms and the topmost oxide Ti-O plane, $\hat{d}_{N/Ti-O}$; and between the oxide O-rows and the topmost oxide Ti-O plane, $\hat{d}_{O/Ti-O}$. The blackdashed square of size (13.2×15.0) Å^2 shows the unit cell used in the calculations.

The TCNQ/TiO_2 interface was analyzed by means of an accurate and efficient local-orbital DFT approach (see reference [119] for further details). In a first step, we consider the T = 0 K case and analyze the interface geometry neglecting van der Waals interactions due to the strong chemical bonds between the molecules and the oxide surface, which are partially ionic. In a second step, the electronic properties of the interface, including the TiO_2/TCNQ level alignment and charge transfer, are calculated introducing appropriate corrections in the DFT calculation.[22, 118] Although

the intermolecular distance is long, there is an important interaction between molecules related to the electrostatic potential induced by the molecule/oxide charge transfer. Finally, we introduce temperature effects and analyze the space charge layer formation and the charge transfer from the oxide to the LUMO_{TCNQ} level.

For a careful discussion of the organic/oxide interface electronic properties, one has to introduce some corrections to the standard DFT calculations because of limitations of this approach: (a) the Kohn-Sham energy levels yield transport gaps that are usually too small;[22, 59, 118] (b) although the local-orbital basis set has been optimized in each material to give a reasonable description of the electronic properties of either the oxide or the organic (except for their energy gaps), their initial relative level alignment is not correctly described, a general problem that appears for even well-converged LDA calculations.[102]

The energy gap for a TCNQ molecule in the gas phase, E_g^{gas}, (measured as the energy difference between its electron affinity and ionization potential) is about 5.3 eV, whereas the energy gap between the Kohn-Sham HOMO and LUMO levels in LDA (or in generalized gradient approximation) calculations, E_g^{LDA}, is 1.7 eV.[95, 117, 120, 122] This difference is related to the self-interaction energy and is described by the molecular charging energy term, U^{mol}, with $U^{mol} = E_g^{gas} - E_g^{LDA} = 3.6$ eV for TCNQ in the gas phase.[59]

In the case of the organic/oxide interface, additional electron correlation effects reduce the gas phase charging energy, U^{mol}, to U and, consequently, the energy gap of the adsorbed TCNQ molecule. These effects are associated with the image potential induced by the oxide and the other molecules on the electron (LUMO) or the hole (HOMO) of the molecule under consideration. Similar to what has been reported before for organic adsorbates on metal surfaces, U is calculated by analyzing the case of an isolated molecule on the oxide[7] (neglecting in this way the effects of the other molecules) and relating U to the electrostatic energy shift introduced in the frontier orbitals of the molecule, eV^{charge}, by the charge transfer, n (expressed in electron units), between the oxide and the single molecule: $eV^{charge} = nU$. In our calculation, we find $U = 1.9$ eV leading to a TCNQ energy gap of 1.7 eV +1.9 eV = 3.6 eV. We stress that this is the energy gap for any TCNQ molecule of the organic monolayer, even though we have calculated it for an isolated one; the rationale behind this is that the image potential effects, which are mainly controlled by the effects of the oxide on a single molecule, determine the organic energy gap. Accordingly, we account for those polarization effects on the energy gap by introducing the scissor operator in the DFT-LDA calculation.[7, 8, 21] We stress that once U is determined from the single-molecule case, the corresponding scissor operator is applied for all the molecules of the monolayer; this implies, as already mentioned, neglecting other molecules contributions to the dynamical polarization effects of the system on the organic energy

levels.

The misalignment between the initial levels of the oxide and the organic is corrected by introducing the shift operator mentioned earlier.[7, 8, 21] In our calculations, the initial LUMO_{TCNQ} level is chosen 5.0 eV below the vacuum level, a value close to the ones reported for TCNQ multilayers (and by this work within our error bars as shown in Figure 5.14) if the energy gap is reduced symmetrically around the midgap to 3.6 eV.[21] For the oxide, the conduction band edge, E_C, is located 4.6 eV below the vacuum level (as shown in Figure 5.10c). Although in our calculations the oxide energy gap is only 3.0 eV, we expect a good description of the most important charge transfer that takes place at the TCNQ/TiO_2(110) interface: the charge transfer from the conduction band of the strongly n-doped oxide to the LUMO_{TCNQ} level.

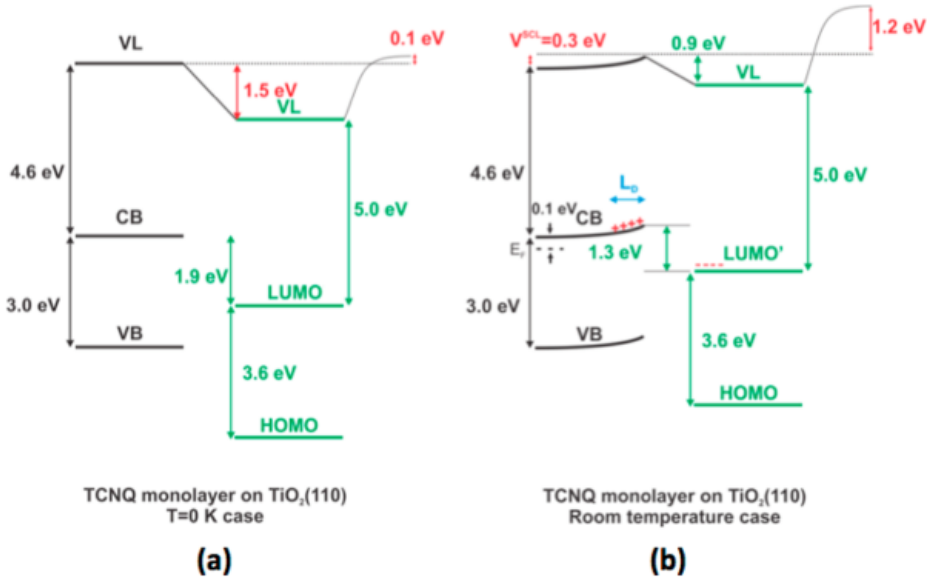

Figure 5.12: Energy alignment calculated for the TCNQ/TiO_2(110) interface at (a) T = 0 K and (b) room temperature. A 0.30 eV band bending is estimated at room temperature for n-doped TiO_2.

Figure 5.12a shows the energy level alignment obtained at T = 0 K for a TCNQ monolayer on TiO_2(110). Although before contact (i.e., with vacuum levels aligned), the LUMO_{TCNQ} level was initially located 0.4 eV below the oxide CB edge, its final position is now 1.9 eV below the CB. This shift originates from two effects: (a) a strong oxide-molecule hybridization resulting in a 1.6 eV shift of the LUMO_{TCNQ} toward higher binding energies, competing with (b) an electrostatic dipole of 0.1 eV moving the LUMO level toward lower binding energies due to charge rearrangement upon hybridization. This electrostatic dipole has two contributions: V^{mol}, a dipole induced by the distortion of the molecule upon adsorption on the surface (eV^{mol} = 0.50 eV) and V^{charge} from charge transfer (eV^{charge} = 0.60 eV). The result of the hybridization and the total electrostatic dipole is a downward displacement of the LUMO level with respect to its initial position by 1.50 eV,

yielding a LUMO that is now found 1.9 eV below the CB.

Given the highly n-doped nature of the TiO_2 substrate (for our doping level, the Fermi level is found 0.1 eV below the conduction band edge), this energy alignment suggests that, at room temperature, there should be a strong thermally excited charge transfer from the oxide to the $LUMO_{TCNQ}$. This populated LUMO will be referred to as LUMO$'$ in the following as it is not formally the lowest unoccupied state of the system anymore. This transfer of charge should create an important electrostatic potential at the interface with two contributions: a surface potential V^{SCL} due to the space charge layer in the oxide extending a distance of a Debye length, L_D, into the crystal (as shown in Figure 5.12b) and an interface potential due to the negative charge (Q in electron unit) in the LUMO$'$ level and the corresponding opposite positive charge in the oxide ($-Q$, also in electron unit).[3]

The space-charge (or boundary layer) potential, $V(z)$, can be analyzed using the Poisson equation:

$$L_D^2 \frac{d^2}{dz^2}\left(\frac{eV}{k_BT}\right) = -[e^{-eV/k_BT} - 1], \tag{5.1}$$

where $L_D^2 = \varepsilon kT/4\pi e n_e$ (n_e being the electron charge density for the n-doped oxide material) and z is the direction normal to the interface.[62] In our calculations, we consider $n_e \approx 10^{19} cm^{-3}$ and $\varepsilon \approx 120$ for the oxide (110) direction resulting in $L_D \approx 40$ Å at room temperature. At the surface of the oxide, the surface potential V^{SCL} can be approximated to $V^{SCL} \approx 4\pi Q e L_D/\varepsilon A$, A being the surface area per molecule (around 200 Å^2), resulting in an energy shift of $eV^{SCL}/Q \approx 0.30$ eV. Assuming $Q = 1$, this value is compatible with the 0.2 eV O 1s and Ti 2p core levels shifts measured in photoemission upon TCNQ adsorption (as shown in Figure 5.10). Consequently, the effect of the space charge layer on the oxide-organic alignment is to displace both the oxide surface layers and the organic levels to lower binding energies.

The strong charge transfer Q from the oxide toward the LUMO$'$ level that results in the formation of the space charge layer also induces a shift of the molecular levels. We denote this shift by eV^S, and its value is given by $eV^S = U^{eff}Q$, where U^{eff} incorporates not only the charging energy of the molecule but also the interaction between molecules; this means that U^{eff} collects the electrostatic effects created by the monolayer on a single molecule. Similarly to what is done for an isolated molecule, for the monolayer case, U^{eff} is calculated from the equation $eV_{ML}^{charge} = U^{eff} n_{ML}$, where V_{ML}^{charge} is the electrostatic potential induced on the frontier orbitals of the molecule by the charges of the system (including all the molecules) and n_{ML} the oxide-to-TCNQ charge transfer per molecule expressed in electron units. It is convenient to calculate V_{ML}^{charge} and n_{ML} as incremental quantities

introducing a fictitious shift, Δ, to the TCNQ molecular levels. Then, $e\delta V_{ML}^{charge}$ is obtained from the atomic charges induced in the molecules by the energy shift Δ, and U^{eff} is calculated from $e\delta V_{ML}^{charge} = U^{eff}\delta n_{ML}$; our calculations yield $U^{eff} = 2.2$ eV, a value slightly larger than $U = 1.9$ eV (calculated in a similar way for an isolated molecule). The value of U for the single molecule was used to incorporate the dynamical polarization processes (image potential effects) in the organic energy gap,[7] while U^{eff} is introduced to incorporate the induced electrostatic potential on the organic molecular levels due to the charge transfer from TiO_2 to the TCNQ monolayer.

Once U^{eff} is established, we analyze how that induced potential, eV^S, modifies the oxide-organic alignment by making use of the previous monolayer calculations for T = 0 K. The idea is to introduce an external shift Δ_0 to the TCNQ-levels to simulate the effect of that charge transfer induced shift, eV^S. Assuming $Q = 1$, then $eV^S = U^{eff}$, which implies that one has to apply a shift of $\Delta = \Delta_0 = 2.2$ eV to the TCNQ molecular levels and recalculate the resulting oxide-organic realignment.[4, 153] The result of this process is shown in Figure 5.12b. In the energy diagram, the LUMO′ of TCNQ is found 1.3 eV below the oxides conduction band edge, to be compared to the experimental value of 1.80 eV, indicating that the charge transfer to TCNQ is about 1 electron. A shift from $\Delta = 0$ to $\Delta = 2.2$ eV induces a change in the charge transfer of about 0.5 electrons from TCNQ to the oxide, which creates a potential shift of 0.5×2.2 eV = 1.1 eV that opposes the original displacement. Therefore, the room-temperature realignment of the LUMO′ level with respect to the oxide band edges is the result of two effects: (a) a strong oxide-molecule hybridization shift of 2.1 eV (toward higher binding energies), 0.5 eV larger than the value found for T = 0 K; and (b) a new interface electrostatic dipole of $2.2 - 1.1 = 1.1$ eV (toward lower binding energies), yielding a total interface electrostatic dipole of 1.2 eV (see Figure 5.12b).

It is important to point out that all these effects also alter the work function of the surface by 1.50 eV, when taking into account the mentioned total interface electrostatic dipole of 1.2 eV and the space charge layer shift of 0.30 eV. This value is in good agreement with the experimentally measured 1.2 eV work function increase upon TCNQ adsorption on the TiO_2(110) surface (as shown in Figure 5.10c). We stress that the main contribution to this work function shift comes from the transfer of charge to the LUMO′ level.

Finally, it is worth mentioning that a second TCNQ layer (or a multilayer) physisorbed on-top of this first monolayer would feel an important realignment with respect to the oxide because the chemical shift of 2.1 eV, associated with the interaction between the oxide and the TCNQ first layer, should disappear. At the same time, we can expect an increase of the TCNQ energy gap to around 5.2 eV, which should also shift the LUMO′ level by 0.8 eV (1/2 of the change in the energy gap) to higher energies. These two effects should dramatically displace the LUMO′ level from 1.3 eV below

to 1.6 eV above the conduction band. As a consequence, only the first TCNQ layer would be able to develop a strong accumulation of charge incoming from the oxide.

5.3.4 Summary

We have shown that there is an important charge transfer between TiO_2 and a TCNQ monolayer, with one electron filling the LUMO level of the organic molecule. This is strongly suggested by the experimental evidence showing that, upon the deposition of a TCNQ-monolayer on TiO_2, a space charge in the oxide is formed and that an important increase in the work function of the TiO_2 and 1 ML TCNQ system appears. Our theoretical analysis based on a combination of a DFT approach and a calculation of the space charge potential, as provided by the molecule charging energy, supports this interpretation and shows the important role that the oxide/organic interface chemistry as well as their electron-chemical equilibration and the oxide space charge have in the barrier formation. Our results are tantamount to the formation of an electron accumulation layer in the first organic layer; although this strong accumulation of charge can be expected to disappear for successive layers, this effect should be considered as an important ingredient for tuning devices having those components.

5.3.5 Supplementary Information

Surface Characterization

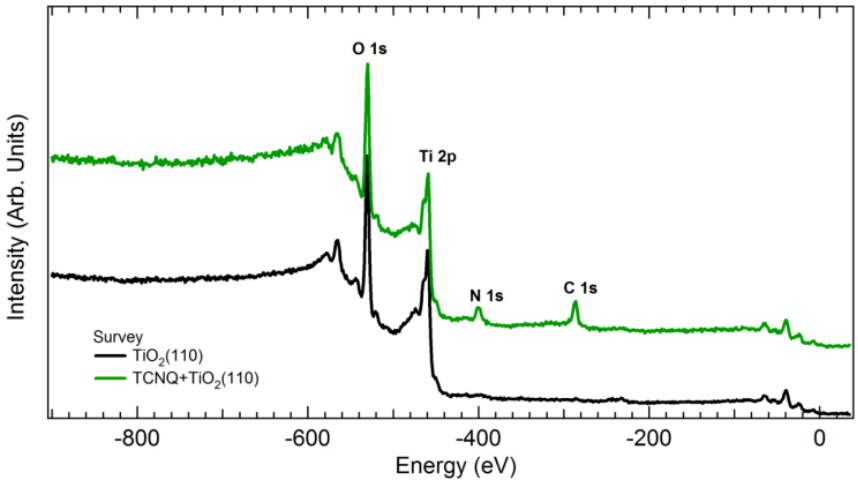

Figure 5.13: Survey scans of the $TiO_2(110)$ surface before and after saturation with TCNQ at room temperature. The main core levels are labeled and used for coverage determination.

Figure 5.13 shows large scale survey scans before and after saturation with TCNQ at RT. These data indicate that, as expected, after a monolayer saturation, only C 1s and N 1s core levels are added to the initial Ti 2p and O 1s core levels belonging to the surface. The molecular coverage

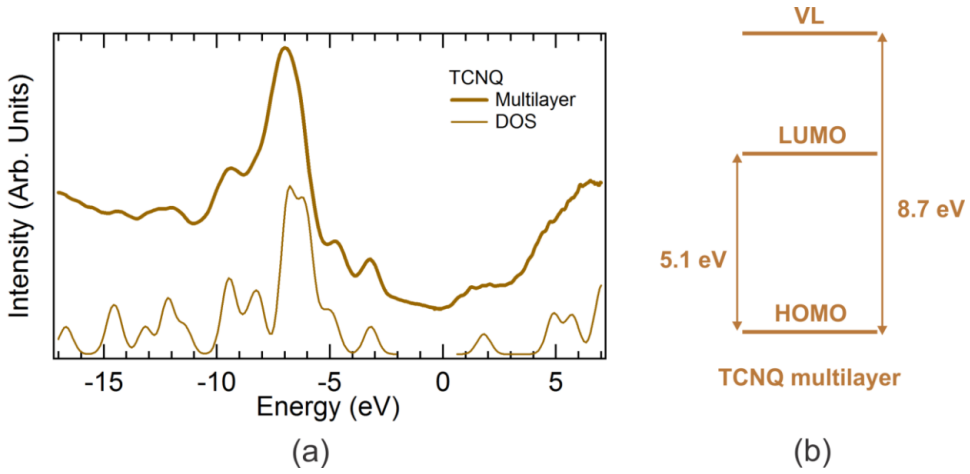

Figure 5.14: (a) Valence and conduction band spectra measured using UPS and IPS respectively, of a TCNQ multilayer on Cu at 230K compared to a calculated TCNQ gas phase DOS, and (b) corresponding energy diagram. The zero of energy is chosen as the position of the Fermi level.

can be evaluated by comparing the relative ratio of C 1s and Ti 2p core levels to no more than a monolayer.

Figure 5.14 shows the valence and conduction spectra for a TCNQ multilayer on Cu at 230K as well as the DOS for the gas phase molecule calculated[154] using the B3LYP exchange-correlation functional and a 6-31G basis set, with a scissor operator applied to align to experimental features. The DOS was calculated by performing a sum of the individual electronic states convoluted with a 1 eV full width half maximum gaussian function. The energy diagram, Figure 5.14b, can be expected to be similar for other multilayer cases. However, for a TCNQ monolayer on TiO_2 the energy gap is reduced to 3.6 eV; assuming this narrowing of the gap to be symmetric around the mid-gap, we find the LUMO level at 4.4 eV from vacuum. Notice that this energy has a resolution of around 0.6 eV.

TiO_2(110) Band Gap Determination

Figure 5.15 shows the valence and conduction band edges measured using UPS and IPS, respectively. Linear extrapolation is used to determine band onsets, giving a gap of 3.6 eV. Note that another common method used to determine the band gap is to consider the band edge as the onset of signal, which gives a narrower gap than what is used in this work. For example, using the latter method this data gives a gap of about 2.8 eV.

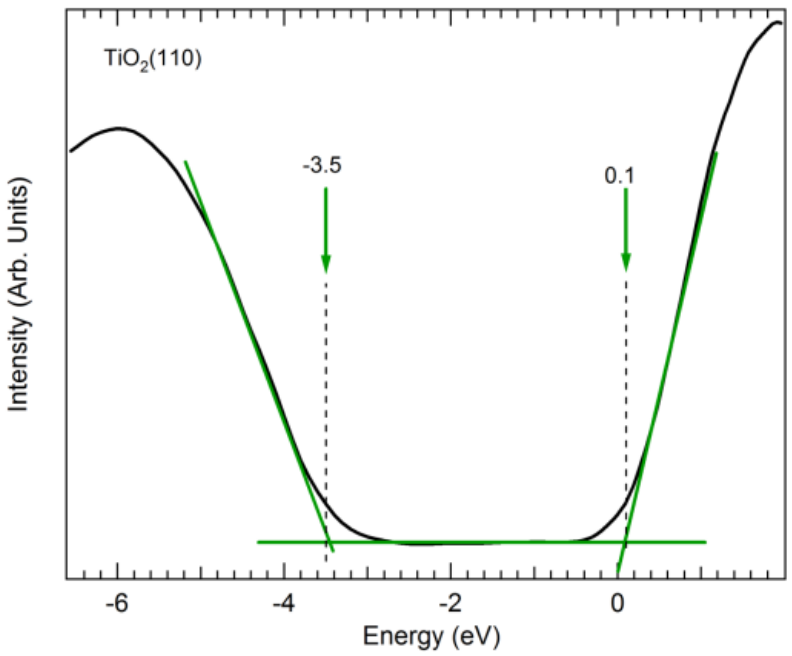

Figure 5.15: Details of the pristine $TiO_2(110)$ band edges. The edges are determined as the intersection of the linearly fitted band edges with the flat spectral background. The VB edge is estimated at -3.5 eV and the CB edge at 0.1 eV.

Theoretical Details

Figure 5.16 shows the projected DOS onto TCNQ and a layer of TiO_2 after introducing the Δ_0-shift in the molecular levels. At RT a space charge is created in the oxide due to the electron transfer to the LUMO level; this charge transfer is simulated in our calculations introducing that Δ_0-shift in the molecular levels.

5.4 Conclusions

ZnTPP and TCNQ on $TiO_2(110)$ are examples of two organic/oxide interfaces spanning a large range of interaction strengths and, as a result, different phenomena influencing the electronic energy level alignment. In the weakly-interacting ZnTPP/$TiO_2(110)$ system, molecular conformation to the substrate and molecular coverage significantly impact the energy level alignment and interfacial dipole. Monolayer coverage stabilizes individual molecules, altering their local conformation to the TiO_2 surface such that the Zn-O distance is 0.9Å shorter than for a single ZnTPP. Thus, for such a weakly interacting system the molecular conformation and bonding upon adsorption to the surface as well as the intermolecular interactions strongly influence energy level alignment.

In the TCNQ/$TiO_2(110)$ system, molecular distortion and chemical bonding upon adsorption

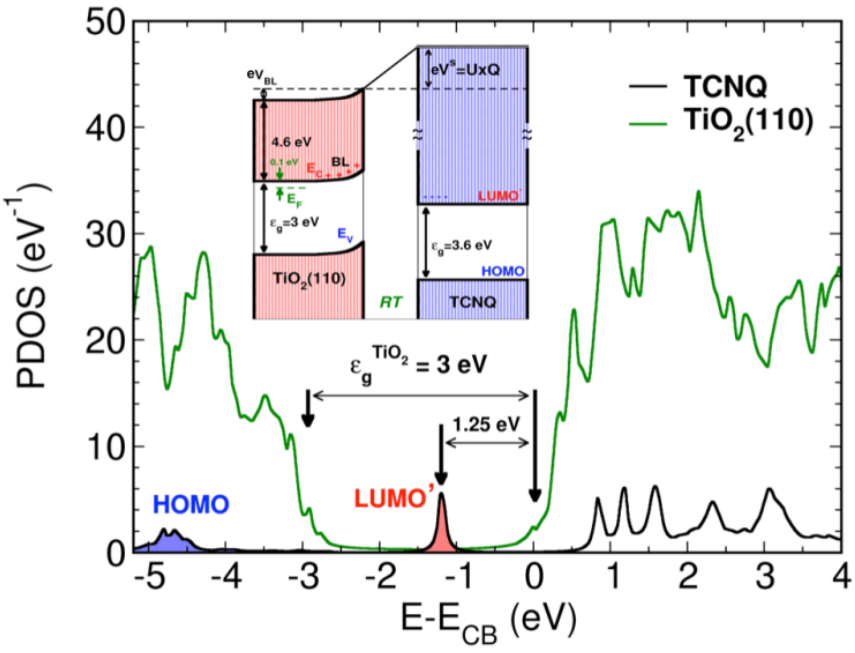

Figure 5.16: Projected DOS onto the TCNQ molecule and the TiO_2 first layer, for the TCNQ/TiO_2 interface (1 ML) at RT. The inset shows the space charge potential and the molecule charging energy induced by the electron transfer to the LUMO level.

at zero temperature are more extreme than for ZnTPPs. At room temperature, electron transfer from the TiO_2 CB to the TCNQ LUMO and the subsequent development of a space charge layer in the oxide emerge as significant effects in addition to the zero temperature interactions. Furthermore, molecular charging and intermolecular electrostatic effects as a result of filling the LUMO in the TCNQ monolayer contribute to the energy alignment. For strongly interacting systems, understanding the individual chemistry of the organic with the oxide is crucial to modeling energy level alignment. The relative strength of the effects listed above, as well as the possible emergence of other effects not seen here, likely vary for different strongly-interacting organic/oxide interfaces. However, this work provides insight on fundamental interactions that exist at both weakly- and strongly-interacting organic/oxide interfaces from which future organic/oxide interface studies will benefit.

Bibliography

[1] . Starting with the theoretical calculation for clean Au(111)[125], inserting 100 nm for the desired domain size yields a surface stress anisotropy of approximately 45 meV/Å^2.

[2] . Different central metal ions may appear as bright spots under certain tunneling conditions, as shown by Scudiero and coauthors, who observed a bright center for CoTPP and a dark center for NiTPP for -1.0 V applied bias on Au(111), permitting a differentiation of the two molecules[156]. The 3d orbital energy of the Zn ion is low compared to Ni, Co, Fe, and Cu[44], however, to gain a more complete understanding of the central metal ion contrast one must take into consideration the interaction of the central metal ion with the porphyrin macrocycle and the substrate. For example, bias-dependent contrast of the Co ion in CoTPP on Ag(111) cannot be described by considering the Co ion and Ag substrate alone, the macrocycle effects must be included[13, 35].

[3] . Fitting the initial LUMO level to 4.4 eV, at a position slightly above E_C, would shift the final LUMO or LUMO′ levels by around 0.3 eV closer to E_C (see Figure 5.12).

[4] . In our theoretical approximation we neglect the spin-dependent solution for the organic energy levels (a reasonable approximation for a nonmagnetic material) and the new geometry that the corresponding charge transfer might induce in the system. This effect should probably increase the oxideorganic interaction and should modify slightly[195] the results of this work without changing its main conclusions.

[5] . A notable exception to the observation that substituting different metal centers does not alter the intermolecular organization is on the Cu(111) substrate. 2HTPP does not aggregate due to strong interactions between the iminic nitrogens and the Cu(111) surface, but CuTPP and CoTPP do self-organize.[37, 38, 144, 194].

[6] . In gas-phase DOS calculations of the ZnTPP molecule, occupied states with weighting on the Zn atom first appear 1.2eV below the HOMO, with the HOMO itself about 1.8-2.0eV below the fermi level. Roughly speaking, it would then require greater than 3V tunneling bias to extract electrons from the Zn occupied states, and so at the biases used in these images (1.5V being the greatest) the center appears dark, i.e., with low tunneling current. Of course, this crude approximation ignores molecule-substrate interactions and any effects of the STM tip on the imaging. Different central metal ions may appear as bright spots under certain tunneling conditions[156], however, to gain a more complete understanding of the central metal ion

contrast one must take into account the interaction of the metal ion with both the substrate and the porphyrin macrocycle[14, 35].

[7] E. Abad, C. González, J. Ortega, and F. Flores. Charging energy, self-interaction correction and transport energy gap for a nanogap organic molecular junction. *Organic Electronics*, 11 (2):332–337, 2010.

[8] E. Abad, Y. J. Dappe, J. I. Martínez, F. Flores, and J. Ortega. C_6h_6/au (111): interface dipoles, band alignment, charging energy, and van der waals interaction. *The Journal of chemical physics*, 134(4):044701, 2011.

[9] O. L. Alerhand, D. Vanderbilt, R. D. Meade, and J. D. Joannopoulos. Spontaneous formation of stress domains on crystal surfaces. *Phys. Rev. Lett.*, 61:1973–1976, Oct 1988.

[10] H. Alves, A. S. Molinari, H. Xie, and A. F. Morpurgo. Metallic conduction at organic charge-transfer interfaces. *Nature materials*, 7(7):574–580, 2008.

[11] S. Anderson, H. L. Anderson, and J. K. M. Sanders. Assembly and crystal structure of a photoactive array of five porphyrins. *Angew. Chem. Int. Ed. Engl.*, 34(10), 1995.

[12] S. Aramaki, Y. Sakai, and N. Ono. Solution-processible organic semiconductor for transistor applications: Tetrabenzoporphyrin. *Applied Physics Letters*, 84(12):2085–2087, 2004.

[13] W. Auwärter, K. Seufert, F. Klappenberger, J. Reichert, A. Weber-Bargioni, A. Verdini, D. Cvetko, M. Dell'Angela, L. Floreano, A. Cossaro, G. Bavdek, A. Morgante, A. P. Seitsonen, and J. V. Barth. Site-specific electronic and geometric interface structure of co-tetraphenylorphyrin layers on ag(111). *Phys. Rev. B*, 81:245403, 2010.

[14] W. Auwarter, K. Suefert, F. Bischoff, D. Ecija, S. Vijayaraghavan, S. Joshi, F. Klappenberger, N. Samudrala, and J. V. Barth. A surface-anchored molecular four-level conductance switch based on single proton transfer. *Nat Nano*, 7(1):41–46, 2012. doi: 10.1038/NNANO.2011.211.

[15] G. Bachelet, D. Hamann, and M. Schlüter. Pseudopotentials that work: From h to pu. *Physical Review B*, 26(8):4199, 1982.

[16] J. Baran, J. Larsson, R. Woolley, Y. Cong, P. Moriarty, A. Cafolla, K. Schulte, and V. Dhanak. Theoretical and experimental comparison of snpc, pbpc, and copc adsorption on ag (111). *Physical Review B*, 81(7):075413, 2010.

[17] J. V. Barth, H. Brune, G. Ertl, and R. J. Behm. Scanning tunneling microscopy observations on the reconstructed au(111) surface: Atomic structure, long-range superstructure, rotational domains, and surface defects. *Phys. Rev. B*, 42:9307–9318, 1990.

[18] A. D. Becke. Density-functional exchange-energy approximation with correct asymptotic-behavior. *Physical Review A*, 38(6):3098–3100, 1988. ISSN 1050-2947. doi: DOI 10.1103/PhysRevA.38.3098. URL <Go to ISI>://WOS:A1988Q146900044.

[19] A. D. Becke. Density-functional thermochemistry .3. the role of exact exchange. *Journal of Chemical Physics*, 98(7):5648–5652, 1993. ISSN 0021-9606. doi: Doi 10.1063/1.464913. URL <Go to ISI>://WOS:A1993KV99700048.

[20] J. P. Beggan, S. A. Krasnikov, N. N. Sergeeva, M. O. Senge, and A. A. Cafolla. Control of the axial coordination of a surface-confined manganese(iii) porphyrin complex. *Nanotechnology*, 23(23):235606, 2012. URL http://stacks.iop.org/0957-4484/23/i=23/a=235606.

[21] J. Beltrán, F. Flores, and J. Ortega. The role of charge transfer in the energy level alignment at the pentacene/c_60 interface. *Physical Chemistry Chemical Physics*, 16(9):4268–4274, 2014.

[22] J. I. Beltrán, F. Flores, J. I. Martínez, and J. Ortega. Energy level alignment in organic-organic heterojunctions: The ttf/tcnq interface. *The Journal of Physical Chemistry C*, 117(8): 3888–3894, 2013.

[23] C. N. Berglund and W. Spicer. Photoemission studies of copper and silver: theory. *Physical Review*, 136(4A):A1030, 1964.

[24] R. Bielefeld. rotary vane pump, 2006. URL https://commons.wikimedia.org/wiki/File:Rotaryvanepump.svg.

[25] G. Binnig and H. Rohrer. Scanning tunneling microscopyfrom birth to adolescence. *reviews of modern physics*, 59(3):615, 1987.

[26] G. Binnig, H. Rohrer, C. Gerber, and E. Weibel. Surface studies by scanning tunneling microscopy. *Physical review letters*, 49(1):57, 1982.

[27] J. M. Blanco, C. Gonzalez, P. Jelinek, J. Ortega, F. Flores, and R. Perez. First-principles simulations of stm images: From tunneling to the contact regime. *Physical Review B*, 70(8), 2004. ISSN 1098-0121. URL <Go to ISI>://WOS:000223716700079.

[28] M. Böhringer, R. Berndt, and W.-D. Schneider. Transition from three-dimensional to two-dimensional faceting of ag (110) induced by cu-phthalocyanine. *Physical Review B*, 55(3):1384, 1997.

[29] M. Böhringer, K. Morgenstern, W.-D. Schneider, M. Wühn, C. Wöll, and R. Berndt. Self-assembly of 1-nitronaphthalene on au(111). *Surf. Sci.*, 444(13):199 – 210, 2000.

[30] H. L. Bonkovsky, J.-T. Guo, W. Hou, T. Li, T. Narang, and M. Thapar. Porphyrin and heme metabolism and the porphyrias. 2013. doi: 10.1002/cphy.c120006. URL `http://dx.doi.org/10.1002/cphy.c120006`.

[31] M. Born, E. Wolf, A. Bhatia, D. Gabor, A. Stokes, A. Taylor, P. Wayman, and W. Wilcock. *Principles of Optics: Electromagnetic Theory of Propagation, Interference and Diffraction of Light*. Cambridge University Press, 2000.

[32] S. Braun, W. R. Salaneck, and M. Fahlman. Energy-level alignment at organic/metal and organic/organic interfaces. *Advanced Materials*, 21(14-15):1450–1472, 2009.

[33] J. Brede, M. Linares, S. Kuck, J. Schwbel, A. Scarfato, S.-H. Chang, G. Hoffmann, R. Wiesendanger, R. Lensen, P. H. J. Kouwer, J. Hoogboom, A. E. Rowan, M. Brring, M. Funk, S. Stafstrm, F. Zerbetto, and R. Lazzaroni. Dynamics of molecular self-ordering in tetraphenyl-porphyrin monolayers on metallic substrates. *Nanotechnology*, 20(27):275602, 2009.

[34] J. Brede, M. Linares, R. Lensen, A. E. Rowan, M. Funk, M. Broring, G. Hoffmann, and R. Wiesendanger. Adsorption and conformation of porphyrins on metallic surfaces. *J. Vac. Sci. Technol. B*, 27(2):799–804, 2009.

[35] F. Buchner, K.-G. Warnick, T. Wölfle, A. Görling, H.-P. Steinrück, W. Hieringer, and H. Marbach. Chemical fingerprints of large organic molecules in scanning tunneling microscopy: Imaging adsorbate-substrate coupling of metalloporphyrins. *J. Phys. Chem. C*, 113(37):16450–16457, 2009.

[36] F. Buchner, I. Kellner, W. Hieringer, A. Görling, H.-P. Steinrück, and H. Marbach. Ordering aspects and intramolecular conformation of tetraphenylporphyrins on ag(111). *Phys. Chem. Chem. Phys.*, 12:13082–13090, 2010.

[37] F. Buchner, J. Xiao, E. Zillner, M. Chen, M. Röckert, S. Ditze, M. Stark, H.-P. Steinrück, J. M. Gottfried, and H. Marbach. Diffusion, rotation, and surface chemical bond of individual 2h-tetraphenylporphyrin molecules on cu(111). *J. Phys. Chem. C*, 115(49):24172–24177, 2011.

[38] F. Buchner, E. Zillner, M. Röckert, S. Gläβel, H.-P. Steinrück, and H. Marbach. Substrate-mediated phase separation of two porphyrin derivatives on cu(111). *Chem.-Eur. J.*, 17(37): 10226–10229, 2011.

[39] D. Cahen, A. Kahn, and E. Umbach. Energetics of molecular interfaces. *Materials Today*, 8 (7):32–41, 2005.

[40] W. M. Campbell, A. K. Burrell, D. L. Officer, and K. W. Jolley. Porphyrins as light harvesters in the dye-sensitised tio2 solar cell. *Coordination Chemistry Reviews*, 248(13-14):1363–1379, 2004. ISSN 0010-8545. doi: DOI 10.1016/j.ccr.2004.01.007. URL `<Go to ISI>://WOS:000224473900017`.

[41] C. Castellarin-Cudia, P. Borghetti, G. Di Santo, M. Fanetti, R. Larciprete, C. Cepek, P. Vilmercati, L. Sangaletti, A. Verdini, A. Cossaro, L. Floreano, A. Morgante, and A. Goldoni. Substrate influence for the zn-tetraphenyl-porphyrin adsorption geometry and the interface-induced electron transfer. *ChemPhysChem*, 11(10):2248–2255, 2010.

[42] C.-M. Che, H.-F. Xiang, S.-Y. Chui, Z.-X. Xu, V. Roy, J. Yan, W.-F. Fu, P. Lai, and I. D. Williams. A high-performance organic field-effect transistor based on platinum(ii) porphyrin: Peripheral substituents on porphyrin ligand significantly affect film structure and charge mobility. *Chemistry - An Asian Journal*, 3(7):1092–1103, 2008.

[43] C. J. Chen. *Introduction to scanning tunneling microscopy*. Oxford University Press, 2008.

[44] M. Chen, X. Feng, L. Zhang, H. Ju, Q. Xu, J. Zhu, J. M. Gottfried, K. Ibrahim, H. Qian, and J. Wang. Direct synthesis of nickel(ii) tetraphenylporphyrin and its interaction with a au(111) surface: A comprehensive study. *J. Phys. Chem. C*, 114(21):9908–9916, 2010.

[45] C. J. Cramer. *Essentials of computational chemistry: theories and models*. John Wiley and Sons, 2013.

[46] X. Crispin, V. Geskin, A. Crispin, J. Cornil, R. Lazzaroni, W. R. Salaneck, and J.-L. Bredas. Characterization of the interface dipole at organic/metal interfaces. *Journal of the American Chemical Society*, 124(27):8131–8141, 2002.

[47] B. Czech and B. Stankiewicz. The na-adsorbed ge (001) surface: Structure and stm image simulations. *Applied Surface Science*, 254(14):4279–4285, 2008.

[48] A. A. Demkov, J. Ortega, O. F. Sankey, and M. P. Grumbach. Electronic structure approach for complex silicas. *Physical Review B*, 52(3):1618, 1995.

[49] G. Di Santo, C. Castellarin-Cudia, M. Fanetti, B. Taleatu, P. Borghetti, L. Sangaletti, L. Floreano, E. Magnano, F. Bondino, and A. Goldoni. Conformational adaptation and electronic structure of 2h-tetraphenylporphyrin on ag(111) during fe metalation. *The Journal of Physical Chemistry C*, 115(10):4155–4162, 2011. doi: 10.1021/jp111151n. URL http://dx.doi.org/10.1021/jp111151n.

[50] U. Diebold. The surface science of titanium dioxide. *Surface Science Reports*, 48(58):53–229, 2003. ISSN 0167-5729. doi: http://dx.doi.org/10.1016/S0167-5729(02)00100-0. URL http://www.sciencedirect.com/science/article/pii/S0167572902001000.

[51] K. Diller, F. Klappenberger, M. Marschall, K. Hermann, A. Nefedov, C. Wll, and J. V. Barth. Self-metalation of 2h-tetraphenylporphyrin on cu(111): An x-ray spectroscopy study. *The Journal of Chemical Physics*, 136(1):–, 2012. doi: http://dx.doi.org/10.1063/1.3674165. URL http://scitation.aip.org/content/aip/journal/jcp/136/1/10.1063/1.3674165.

[52] G. DiSanto, S. Blankenburg, C. Castellarin-Cudia, M. Fanetti, P. Borghetti, L. Sangaletti, L. Floreano, A. Verdini, E. Magnano, F. Bondino, C. A. Pignedoli, M.-T. Nguyen, R. Gaspari, D. Passerone, and A. Goldoni. Supramolecular engineering through temperature-induced chemical modification of 2h-tetraphenylporphyrin on ag(111): Flat phenyl conformation and possible dehydrogenation reactions. *Chem.-Eur. J.*, 17(51):14354–14359, 2011.

[53] G. DiSanto, C. Sfiligoj, C. Castellarin-Cudia, A. Verdini, A. Cossaro, A. Morgante, L. Floreano, and A. Goldoni. Changes of the moleculesubstrate interaction upon metal inclusion into a porphyrin. *Chemistry A European Journal*, 18(40):12619–12623, 2012. ISSN 1521-3765. doi: 10.1002/chem.201201640. URL http://dx.doi.org/10.1002/chem.201201640.

[54] R. Ditchfield, W. J. Hehre, and J. A. Pople. Self-consistent molecular-orbital methods. ix. an extended gaussian-type basis for molecular-orbital studies of organic molecules. *The Journal of Chemical Physics*, 54(2):724–728, 1971.

[55] M. Ernzerhof and G. E. Scuseria. Assessment of the perdew–burke–ernzerhof exchange-correlation functional. *The Journal of chemical physics*, 110(11):5029–5036, 1999.

[56] G. Ertl and J. Küppers. *Low Energy Electrons and Surface Chemistry*. Vch Pub, 1985.

[57] J. K. Fawcett and J. Trotter. A refinement of the structure of biphenylene. *Acta Crystallographica*, 20(1):87–93, Jan 1966.

[58] J. Ferraris, D. Cowan, V. t. Walatka, and J. Perlstein. Electron transfer in a new highly conducting donor-acceptor complex. *Journal of the American Chemical Society*, 95(3):948–949, 1973.

[59] F. Flores, J. Ortega, and H. Vazquez. Modelling energy level alignment at organic interfaces and density functional theory. *Physical Chemistry Chemical Physics*, 11(39):8658–8675, 2009.

[60] S. R. Forrest. Ultrathin organic films grown by organic molecular beam deposition and related techniques. *Chemical Reviews*, 97(6):1793–1896, 1997.

[61] W. M. C. Foulkes and R. Haydock. Tight-binding models and density-functional theory. *Physical review B*, 39(17):12520, 1989.

[62] D. R. Frankl. Electrical properties of semiconductor surfaces. 1967.

[63] R. Friend, R. Gymer, A. Holmes, J. Burroughes, R. Marks, C. Taliani, D. Bradley, D. Dos Santos, J. Bredas, and M. Lögdlund. Electroluminescence in conjugated polymers. *Nature*, 397 (6715):121–128, 1999.

[64] M. Fuchs and M. Scheffler. Ab initio pseudopotentials for electronic structure calculations of poly-atomic systems using density-functional theory. *Computer Physics Communications*, 119 (1):67–98, 1999.

[65] H. Gao, H. Zhang, Z. Xue, and S. Pang. Scanning tunneling microscopy and atomic force microscopy investigation of organic tetracyanoquinodimethane thin films. *Journal of materials research*, 12(08):1942–1945, 1997.

[66] P. Giannozzi, S. Baroni, N. Bonini, M. Calandra, R. Car, C. Cavazzoni, D. Ceresoli, G. L. Chiarotti, M. Cococcioni, I. Dabo, A. Dal Corso, S. de Gironcoli, S. Fabris, G. Fratesi, R. Gebauer, U. Gerstmann, C. Gougoussis, A. Kokalj, M. Lazzeri, L. Martin-Samos, N. Marzari, F. Mauri, R. Mazzarello, S. Paolini, A. Pasquarello, L. Paulatto, C. Sbraccia, S. Scandolo, G. Sclauzero, A. P. Seitsonen, A. Smogunov, P. Umari, and R. M. Wentzcovitch. Quantum espresso: a modular and open-source software project for quantum simulations of materials. *Journal of Physics-Condensed Matter*, 21(39), 2009. ISSN 0953-8984.

[67] M. T. Greiner, M. G. Helander, W.-M. Tang, Z.-B. Wang, J. Qiu, and Z.-H. Lu. Universal energy-level alignment of molecules on metal oxides. *Nature materials*, 11(1):76–81, 2012.

[68] L. Grill, M. Dyer, L. Lafferentz, M. Persson, M. Peters, and S. Hecht. Nanoarchitectures by covalent assembly of molecular building blocks. *Nature Nanotech.*, 2, 2007.

[69] S. Grimme. Do special noncovalent $\pi - \pi$ stacking interactions really exist? *Angew. Chem., Int. Edit.*, 47(18), 2008.

[70] A. Hagfeldt, G. Boschloo, L. Sun, L. Kloo, and H. Pettersson. Dye-sensitized solar cells. *Chem. Rev.*, 110:6595 – 6663, 2010.

[71] W. Haiss. Surface stress of clean and adsorbate covered solids. *Rep. Prog. Phys.*, 64(5):591, 2001.

[72] D. Hamann. Generalized norm-conserving pseudopotentials. *Physical Review B*, 40(5):2980, 1989.

[73] D. Hamann, M. Schlüter, and C. Chiang. Norm-conserving pseudopotentials. *Physical Review Letters*, 43(20):1494, 1979.

[74] F. Hanke, S. Haq, R. Raval, and M. Persson. Heat-to-connect: Surface commensurability directs organometallic one-dimensional self-assembly. *ACS Nano*, 5(11):9093–9103, 2011. doi: 10.1021/nn203337v. URL `http://dx.doi.org/10.1021/nn203337v`. PMID: 22003852.

[75] S. Haq, F. Hanke, M. S. Dyer, M. Persson, P. Iavicoli, D. B. Amabilino, and R. Raval. Clean coupling of unfunctionalized porphyrins at surfaces to give highly oriented organometallic oligomers. *Journal of the American Chemical Society*, 133(31):12031–12039, 2011. doi: 10.1021/ja201389u. URL `http://dx.doi.org/10.1021/ja201389u`. PMID: 21707113.

[76] J. Harris. Simplified method for calculating the energy of weakly interacting fragments. *Physical Review B*, 31(4):1770, 1985.

[77] W. A. Harrison. *Solid state theory*. Courier Corporation, 1970.

[78] D. S. Hecht, R. J. A. Ramirez, M. Briman, E. Artukovic, K. S. Chichak, J. F. Stoddart, and G. Grner. Bioinspired detection of light using a porphyrin-sensitized single-wall nanotube field effect transistor. *Nano Letters*, 6(9):2031–2036, 2006.

[79] W. J. Hehre, R. Ditchfield, and J. A. Pople. Selfconsistent molecular orbital methods. xii. further extensions of gaussiantype basis sets for use in molecular orbital studies of organic molecules. *The Journal of Chemical Physics*, 56(5):2257–2261, 1972.

[80] W. Hieringer, K. Flechtner, A. Kretschmann, K. Seufert, W. Auwrter, J. V. Barth, A. Grling, H.-P. Steinrück, and J. M. Gottfried. The surface trans effect: Influence of axial ligands on the surface chemical bonds of adsorbed metalloporphyrins. *Journal of*

the American Chemical Society, 133(16):6206–6222, 2011. doi: 10.1021/ja1093502. URL http://dx.doi.org/10.1021/ja1093502. PMID: 21462965.

[81] I. Hill, A. Rajagopal, A. Kahn, and Y. Hu. Molecular level alignment at organic semiconductor-metal interfaces. *Applied Physics Letters*, 73(5):662–664, 1998.

[82] M. H. Hoang, Y. Kim, S.-J. Kim, D. H. Choi, and S. J. Lee. High-performance single-crystal-based organic field-effect transistors from -extended porphyrin derivatives. *Chemistry - A European Journal*, 17(28):7772–7776, 2011.

[83] P. Hohenberg and W. Kohn. Inhomogeneous electron gas. *Physical review*, 136(3B):B864, 1964.

[84] I. Horcas, R. Fernandez, J. M. Gomez-Rodriguez, J. Colchero, J. Gomez-Herrero, and A. M. Baro. Wsxm: A software for scanning probe microscopy and a tool for nanotechnology. *Review of Scientific Instruments*, 78(1), 2007. ISSN 0034-6748.

[85] S. Hüfner. *Photoelectron Spectroscopy: Principles and Applications*. Springer Science & Business Media, 2013.

[86] H. Imahori, T. Umeyama, K. Kurotobi, and Y. Takano. Self-assembling porphyrins and phthalocyanines for photoinduced charge separation and charge transport. *Chemical Communications*, 48(34):4032–4045, 2012.

[87] M. In't Veld, P. Iavicoli, S. Haq, D. B. Amabilino, and R. Raval. Unique intermolecular reaction of simple porphyrins at a metal surface gives covalent nanostructures. *Chem. Commun.*, pages 1536–1538, 2008. doi: 10.1039/B718865J. URL http://dx.doi.org/10.1039/B718865J.

[88] H. Ishii and K. Seki. Energy level alignment at organic/metal interfaces studied by uv photoemission: Breakdown of traditional assumption of a common vacuum level at the interface. *Electron Devices, IEEE Transactions on*, 44(8):1295–1301, 1997.

[89] P. Jelínek, H. Wang, J. P. Lewis, O. F. Sankey, and J. Ortega. Multicenter approach to the exchange-correlation interactions in ab initio tight-binding methods. *Physical Review B*, 71 (23):235101, 2005.

[90] P. Johnson and J. Davenport. Calculated inverse photoemission cross sections from adsorbed molecules. *Physical Review B*, 31(12):7521, 1985.

[91] P. Johnson, S. Hulbert, R. Garrett, and M. Howells. Normal incidence grating spectrometer designed for inverse photoemission studies in the range 10–30 ev. *Review of scientific instruments*, 57(7):1324–1328, 1986.

[92] D. Kabra, L. P. Lu, M. H. Song, H. J. Snaith, and R. H. Friend. Efficient single-layer polymer light-emitting diodes. *Advanced Materials*, 22(29):3194–3198, 2010.

[93] A. Kahn, N. Koch, and W. Gao. Electronic structure and electrical properties of interfaces between metals and -conjugated molecular films. *Journal of Polymer Science Part B: Polymer Physics*, 41(21):2529–2548, 2003. ISSN 1099-0488. doi: 10.1002/polb.10642. URL `http://dx.doi.org/10.1002/polb.10642`.

[94] W. Kaminski, P. Jelinek, R. Pérez, F. Flores, and J. Ortega. Si-substitutional defects on the α-sn/si (111)-(3$\times$ 3) surface. *Applied surface science*, 234(1):286–291, 2004.

[95] K. Kanai, K. Akaike, K. Koyasu, K. Sakai, T. Nishi, Y. Kamizuru, T. Nishi, Y. Ouchi, and K. Seki. Determination of electron affinity of electron accepting molecules. *Applied Physics A*, 95(1):309–313, 2009.

[96] E. Kaxiras. *Atomic and electronic structure of solids*. Cambridge University Press, 2003.

[97] J. R. Kirtley and J. Mannhart. Organic electronics: When ttf met tcnq. *Nature materials*, 7 (7):520–521, 2008.

[98] N. Koch. Energy levels at interfaces between metals and conjugated organic molecules. *Journal of Physics: Condensed Matter*, 20(18):184008, 2008.

[99] W. Koch, M. C. Holthausen, and M. C. Holthausen. *A chemist's guide to density functional theory*, volume 2. Wiley-Vch Weinheim, 2001.

[100] W. Kohn and L. J. Sham. Self-consistent equations including exchange and correlation effects. *Physical Review*, 140(4A):A1133, 1965.

[101] J. Kollár, L. Vitos, J. M. Osorio-Guillén, and R. Ahuja. Calculation of surface stress for fcc transition metals. *Phys. Rev. B*, 68:245417, 2003.

[102] L. Kronik, R. Fromherz, E. Ko, G. Ganteför, and J. R. Chelikowsky. Highest electron affinity as a predictor of cluster anion structures. *Nature materials*, 1(1):49–53, 2002.

[103] S. Kwon, Z. Nabi, K. Kádas, L. Vitos, J. Kollár, B. Johansson, and R. Ahuja. Surface energy and stress release by layer relaxation. *Physical Review B*, 72(23):235423, 2005.

[104] M. Lackinger and M. Hietschold. Determining adsorption geometry of individual tin–phthalocyanine molecules on ag (111)—-a stm study at submonolayer coverage. *Surface science*, 520(1):L619–L624, 2002.

[105] L. Lafferentz, V. Eberhardt, C. Dri, C. Africh, G. Comelli, F. Esch, S. Hecht, and L. Grill. Controlling on surface polymerization by hierarchical and substrate directed growth. *Nature Chem.*, 4, 2012.

[106] C. T. Lee, W. T. Yang, and R. G. Parr. Development of the colle-salvetti correlation-energy formula into a functional of the electron-density. *Physical Review B*, 37(2):785–789, 1988. ISSN 0163-1829.

[107] J. P. Lewis, K. R. Glaesemann, G. A. Voth, J. Fritsch, A. A. Demkov, J. Ortega, and O. F. Sankey. Further developments in the local-orbital density-functional-theory tight-binding method. *Physical Review B*, 64(19):195103, 2001.

[108] J. P. Lewis, P. Jelínek, J. Ortega, A. A. Demkov, D. G. Trabada, B. Haycock, H. Wang, G. Adams, J. K. Tomfohr, E. Abad, et al. Advances and applications in the fireballab initio tight-binding molecular-dynamics formalism. *physica status solidi (b)*, 248(9):1989–2007, 2011.

[109] H. Li, P. Winget, and J.-L. Brédas. Transparent conducting oxides of relevance to organic electronics: Electronic structures of their interfaces with organic layers. *Chemistry of Materials*, 26(1):631–646, 2013.

[110] L.-L. Li and E. W.-G. Diau. Porphyrin-sensitized solar cells. *Chem. Soc. Rev.*, 42:291–304, 2013.

[111] Liquidat. Cut through turbomolecular pump, 2005. URL `https://commons.wikimedia.org/wiki/File:Cutthroughturbomolecularpump.jpg`.

[112] L. W. Liu, K. Yang, W. D. Xiao, Y. H. Jiang, B. Q. Song, S. X. Du, and H. Gao. Selective adsorption of metal-phthalocyanine on au(111) surface with hydrogen atoms. *Appl. Phys. Lett.*, 103(2), 2013.

[113] W. C. Lothrop. Biphenylene. *Journal of the American Chemical Society*, 63(5):1187–1191, 1941.

[114] T. Lukasczyk, K. Flechtner, L. R. Merte, N. Jux, F. Maier, J. M. Gottfried, and H.-P. Steinrück. Interaction of cobalt(ii) tetraarylporphyrins with a ag(111) surface studied with photoelectron spectroscopy. *J. Phys. Chem. C*, 111(7):3090–3098, 2007.

[115] K. Manandhar, T. Ellis, K. Park, T. Cai, Z. Song, and J. Hrbek. A scanning tunneling microscopy study on the effect of post-deposition annealing of copper phthalocyanine thin films. *Surface Science*, 601(17):3623–3631, 2007.

[116] R. M. Martin. *Electronic structure: basic theory and practical methods*. Cambridge university press, 2004.

[117] J. I. Martínez, E. Abad, F. Flores, and J. Ortega. Simulating the organic-molecule/metal interface tcnq/au (111). *physica status solidi (b)*, 248(9):2044–2049, 2011.

[118] J. I. Martínez, E. Abad, J. I. Beltrán, F. Flores, and J. Ortega. Barrier height formation in organic blends/metal interfaces: Case of tetrathiafulvalene-tetracyanoquinodimethane/au (111). *The Journal of chemical physics*, 139(21):214706, 2013.

[119] J. I. Martnez, F. Flores, J. Ortega, S. Rangan, C. Ruggieri, and R. Bartynski. Chemical interaction, space-charge layer, and molecule charging energy for a tio2/tcnq interface. *The Journal of Physical Chemistry C*, 119(38):22086–22091, 2015. ISSN 1932-7447.

[120] K. Medjanik, S. Perkert, S. Naghavi, M. Rudloff, V. Solovyeva, D. Chercka, M. Huth, S. Nepijko, T. Methfessel, C. Felser, et al. Formation of an intermolecular charge-transfer compound in uhv codeposited tetramethoxypyrene and tetracyanoquinodimethane. *Physical Review B*, 82(24):245419, 2010.

[121] J. Meyer, S. Hamwi, M. Kröger, W. Kowalsky, T. Riedl, and A. Kahn. Transition metal oxides for organic electronics: energetics, device physics and applications. *Advanced Materials*, 24 (40):5408–5427, 2012.

[122] B. Milián, R. Pou-Amérigo, R. Viruela, and E. Ortı. On the electron affinity of tcnq. *Chemical physics letters*, 391(1):148–151, 2004.

[123] A. Mugarza, R. Robles, C. Krull, R. Korytár, N. Lorente, and P. Gambardella. Electronic and magnetic properties of molecule-metal interfaces: Transition-metal phthalocyanines adsorbed on ag (100). *Physical Review B*, 85(15):155437, 2012.

[124] S. Müllegger, M. Rashidi, T. Lengauer, E. Rauls, W. G. Schmidt, G. Knör, W. Schöfberger, and R. Koch. Asymmetric saddling of single porphyrin molecules on au(111). *Phys. Rev. B*, 83:165416, 2011.

[125] S. Narasimhan and D. Vanderbilt. Elastic stress domains and the herringbone reconstruction on au(111). *Phys. Rev. Lett.*, 69:1564–1567, 1992.

[126] J. B. Neaton, M. S. Hybertsen, and S. G. Louie. Renormalization of molecular electronic levels at metal-molecule interfaces. *Phys. Rev. Lett.*, 97:216405, 2006. doi: 10.1103/PhysRevLett.97.216405. URL `http://link.aps.org/doi/10.1103/PhysRevLett.97.216405`.

[127] Y.-Y. Noh, J.-J. Kim, Y. Yoshida, and K. Yase. Effect of molecular orientation of epitaxially grown platinum(ii) octaethyl porphyrin films on the performance of field-effect transistors. *Advanced Materials*, 15(9):699–702, 2003.

[128] J. Nowakowski, C. Wackerlin, J. Girovsky, D. Siewert, T. A. Jung, and N. Ballav. Porphyrin metalation providing an example of a redox reaction facilitated by a surface reconstruction. *Chem. Commun.*, 49:2347–2349, 2013. doi: 10.1039/C3CC39134E.

[129] P. Olszowski, L. Zajac, S. Godlewski, B. Such, R. Jöhr, T. Glatzel, E. Meyer, and M. Szymonski. Role of a carboxyl group in the adsorption of zn porphyrins on tio2(011)-2×1 surface. *The Journal of Physical Chemistry C*, 119(37):21561–21566, 2015. ISSN 1932-7447.

[130] B. O'Regan and M. Grätzel. A low-cost, high-efficiency solar cell based on dye-sensitized colloidal tio2 films. *nature*, 353(6346):737–740, 1991.

[131] A. G. Orpen, L. Brammer, F. H. Allen, O. Kennard, D. G. Watson, and R. Taylor. Supplement. tables of bond lengths determined by x-ray and neutron diffraction. part 2. organometallic compounds and co-ordination complexes of the d- and f-block metals. *J. Chem. Soc., Dalton Trans.*, pages S1–S83, 1989.

[132] G. Otero, G. Biddau, C. Sánchez-Sánchez, R. Caillard, M. F. López, C. Rogero, F. J. Palomares, N. Cabello, M. A. Basanta, J. Ortega, et al. Fullerenes from aromatic precursors by surface-catalysed cyclodehydrogenation. *Nature*, 454(7206):865–868, 2008.

[133] G. Otero-Irurueta, J. I. Martínez, G. Lovat, V. Lanzilotto, J. Méndez, M. F. López, L. Floreano, and J. A. Martín-Gago. Densely packed perylene layers on the rutile tio2 (110)-(1× 1) surface. *The Journal of Physical Chemistry C*, 119(14):7809–7816, 2015.

[134] M. K. Panda, K. Ladomenou, and A. G. Coutsolelos. Porphyrins in bio-inspired transformations: Light-harvesting to solar cell. *Coordination Chemistry Reviews*, 256(21):2601–2627, 2012.

[135] R. C. Peck, J. M. Schulman, and R. L. Disch. Ab initio heats of formation of medium-sized hydrocarbons. 12. 6-31g* studies of the benzenoid aromatics. *The Journal of Physical Chemistry*, 94(17):6637–6641, 1990.

[136] C. Perthuisot, B. L. Edelbach, D. L. Zubris, N. Simhai, C. N. Iverson, C. Mller, T. Satoh, and W. D. Jones. Cleavage of the carboncarbon bond in biphenylene using transition metals. *Journal of Molecular Catalysis A: Chemical*, 189(1):157 – 168, 2002. ISSN 1381-1169.

[137] J. S. Prauzner-Bechcicki, S. Godlewski, A. Tekiel, P. Cyganik, J. Budzioch, and M. Szymonski. High-resolution stm studies of terephthalic acid molecules on rutile tio2 (110)-(1× 1) surfaces. *The Journal of Physical Chemistry C*, 113(21):9309–9315, 2009.

[138] E. Rabinowitch. Spectra of porphyrins and chlorophyll. *Rev. Mod. Phys.*, 16(4):226–235, 1945.

[139] S. Rangan, S. Katalinic, R. Thorpe, R. A. Bartynski, J. Rochford, and E. Galoppini. Energy level alignment of a zinc(ii) tetraphenylporphyrin dye adsorbed onto tio_2(110) and zno($11\bar{2}0$) surfaces. *J. Phys. Chem. C*, 114(2):1139–1147, 2010.

[140] S. Rangan, S. Coh, R. A. Bartynski, K. P. Chitre, E. Galoppini, C. Jaye, and D. Fischer. Energy alignment, molecular packing, and electronic pathways: Zinc(ii) tetraphenylporphyrin derivatives adsorbed on tio_2(110) and zno($11\bar{2}0$) surfaces. *J. Phys. Chem. C*, 116(45):23921–23930, 2012.

[141] S. Rangan, A. Batarseh, K. P. Chitre, A. Kopecky, E. Galoppini, and R. A. Bartynski. Tuning energy level alignment at organic/semiconductor interfaces using a built-in dipole in chromophore-bridge-anchor compounds. *Journal of Physical Chemistry C*, 118(24):12923–12928, 2014.

[142] S. Rangan, C. Ruggieri, R. Bartynski, J. I. Martnez, F. Flores, and J. Ortega. Densely packed zntpps monolayer on the rutile tio2(110)-(1×1) surface: Adsorption behavior and energy level alignment. *The Journal of Physical Chemistry C*, 120(8):4430–4437, 2016.

[143] M. Röckert, M. Franke, Q. Tariq, S. Ditze, M. Stark, P. Uffinger, D. Wechsler, U. Singh, J. Xiao, H. Marbach, H.-P. Steinrück, and O. Lytken. Coverage- and temperature-dependent metalation and dehydrogenation of tetraphenylporphyrin on cu(111). *Chemistry A European Journal*, 20(29):8948–8953, 2014. ISSN 1521-3765. doi: 10.1002/chem.201402420. URL `http://dx.doi.org/10.1002/chem.201402420`.

[144] G. Rojas, X. Chen, C. Bravo, J.-H. Kim, J.-S. Kim, J. Xiao, P. A. Dowben, Y. Gao, X. C. Zeng, W. Choe, and A. Enders. Self-assembly and properties of nonmetalated tetraphenyl-porphyrin on metal substrates. *J. Phys. Chem. C*, 114(20):9408–9415, 2010.

[145] A. Rosa, G. Ricciardi, , and E. J. Baerends. Synergism of porphyrin-core saddling and twisting of meso-aryl substituents. *The Journal of Physical Chemistry A*, 110(15):5180–5190, 2006. doi: 10.1021/jp060931i.

[146] C. Ruggieri, S. Rangan, R. A. Bartynski, and E. Galoppini. Zinc(ii) tetraphenylporphyrin adsorption on au(111): An interplay between molecular self-assembly and surface stress. *The Journal of Physical Chemistry C*, 119(11):6101–6110, 2015. doi: 10.1021/acs.jpcc.5b00217.

[147] C. Ruggieri, S. Rangan, R. Bartynski, and E. Galoppini. Zinc(ii) tetraphenylporphyrin on ag(100) and ag(111): Multilayer desorption and dehydrogenation. *The Journal of Physical Chemistry C*, 2016.

[148] C. Sánchez-Sánchez, J. I. Martínez, V. Lanzilotto, G. Biddau, B. Gómez-Lor, R. Pérez, L. Floreano, M. F. López, and J. Á. Martín-Gago. Chemistry and temperature-assisted dehydrogenation of c_60 h_30 molecules on tio_2 (110) surfaces. *Nanoscale*, 5(22):11058–11065, 2013.

[149] C. Sánchez-Sánchez, J. I. Martínez, V. Lanzilotto, J. Méndez, J. A. Martín-Gago, and M. F. López. Antiphase boundaries accumulation forming a new c_60 decoupled crystallographic phase on the rutile tio_2 (110)-(1$\times$ 1) surface. *The Journal of Physical Chemistry C*, 118(47): 27318–27324, 2014.

[150] O. F. Sankey and D. J. Niklewski. Ab initio multicenter tight-binding model for molecular-dynamics simulations and other applications in covalent systems. *Physical Review B*, 40(6): 3979, 1989.

[151] O. Schaff, A. K. Schmid, N. C. Bartelt, J. de la Figuera, and R. Q. Hwang. In situ stm studies of strain stabilized thin film dislocation networks under applied stress. *Mat. Sci. Eng. A*, 319-321:914–918, 2001.

[152] G. Schaftenaar and J. H. Noordik. Molden: a pre-and post-processing program for molecular and electronic structures*. *Journal of computer-aided molecular design*, 14(2):123–134, 2000.

[153] R. Schlesinger, Y. Xu, O. T. Hofmann, S. Winkler, J. Frisch, J. Niederhausen, A. Vollmer, S. Blumstengel, F. Henneberger, P. Rinke, et al. Controlling the work function of zno and the energy-level alignment at the interface to organic semiconductors with a molecular electron acceptor. *Physical Review B*, 87(15):155311, 2013.

[154] M. W. Schmidt, K. K. Baldridge, J. A. Boatz, S. T. Elbert, M. S. Gordon, J. H. Jensen, S. Koseki, N. Matsunaga, K. A. Nguyen, S. Su, et al. General atomic and molecular electronic structure system. *Journal of computational chemistry*, 14(11):1347–1363, 1993.

[155] K. L. Schuchardt, B. T. Didier, T. Elsethagen, L. S. Sun, V. Gurumoorthi, J. Chase, J. Li, and T. L. Windus. Basis set exchange: A community database for computational sciences. *Journal of Chemical Information and Modeling*, 47(3):1045–1052, 2007. ISSN 1549-9596.

[156] L. Scudiero, D. E. Barlow, and K. W. Hipps. Physical properties and metal ion specific scanning tunneling microscopy images of metal(ii) tetraphenylporphyrins deposited from vapor onto gold (111). *J. Phys. Chem. B*, 104(50):11899–11905, 2000.

[157] L. Segev, A. Salomon, A. Natan, D. Cahen, L. Kronik, F. Amy, C. K. Chan, and A. Kahn. Electronic structure of si (111)-bound alkyl monolayers: Theory and experiment. *Physical Review B*, 74(16):165323, 2006.

[158] M. Sessolo and H. J. Bolink. Hybrid organic-inorganic light-emitting diodes. *Advanced Materials*, 23(16):1829–1845, 2011.

[159] V. B. Shenoy. Atomistic calculations of elastic properties of metallic fcc crystal surfaces. *Physical Review B*, 71(9):094104, 2005.

[160] T. E. Shubina, H. Marbach, K. Flechtner, A. Kretschmann, N. Jux, F. Buchner, H.-P. Steinrück, T. Clark, and J. M. Gottfried. Principle and mechanism of direct porphyrin metalation: joint experimental and theoretical investigation. *Journal of the American Chemical Society*, 129(30):9476–9483, 2007. doi: 10.1021/ja072360t. URL `http://dx.doi.org/10.1021/ja072360t`. PMID: 17625856.

[161] H. Sirringhaus. Device physics of solution-processed organic field-effect transistors. *Adv. Mater.*, 17(20):2411–2425, 2005.

[162] J. C. Slater. The theory of complex spectra. *Physical Review*, 34(10):1293, 1929.

[163] M. Stark, S. Ditze, M. Drost, F. Buchner, H.-P. Steinrück, and H. Marbach. Coverage dependent-disorder order transition of 2h-tetraphenylporphyrin on cu(111). *Langmuir*, 29 (12):4104–4110, 2013.

[164] J. T. Sun, L. Gao, X. B. He, Z. H. Cheng, Z. T. Deng, X. Lin, H. Hu, S. X. Du, F. Liu, and H. Gao. Surface reconstruction transition of metals induced by molecular adsorption. *Phys. Rev. B*, 83:115419, 2011.

[165] M. Švec, P. Jelínek, P. Shukrynau, C. González, V. Cháb, and V. Drchal. Local atomic and electronic structure of the pb/ si (111) mosaic phase: Stm and ab initio study. *Physical Review B*, 77(12):125104, 2008.

[166] M. Takada and H. Tada. Scanning tunneling microscopy and spectroscopy of phthalocyanine molecules on metal surfaces. *Japanese journal of applied physics*, 44(7S):5332, 2005.

[167] T. Takami, C. Carrizales, and K. Hipps. Commensurate ordering of iron phthalocyanine on ag (111) surface. *Surface Science*, 603(21):3201–3204, 2009.

[168] N. Takeuchi, C. Chan, and K. Ho. Au(111): A theoretical study of the surface reconstruction and the surface electronic structure. *Phys. Rev. B*, 43:13899–13906, 1990.

[169] R. Tanoue, R. Higuchi, K. Ikebe, S. Uemura, N. Kimizuka, A. Z. Stieg, J. K. Gimzewski, and M. Kunitake. Thermodynamic self-assembly of two-dimensional π-conjugated metal-porphyrin covalent organic frameworks by "on-site" equilibrium polymerization. *Journal of Nanoscience and Nanotechnology*, 14(3):2211–2216, 2014. doi: doi:10.1166/jnn.2014.8540.

[170] A. Tekiel, S. Godlewski, J. Budzioch, and M. Szymonski. Nanofabrication of ptcda molecular chains on rutile tio2 (011)-(2$\times$ 1) surfaces. *Nanotechnology*, 19(49):495304, 2008.

[171] C. Tengstedt, W. Osikowicz, W. R. Salaneck, I. D. Parker, C.-H. Hsu, and M. Fahlman. Fermi-level pinning at conjugated polymer interfaces. *Applied Physics Letters*, 88(5):053502, 2006.

[172] J. Tersoff and D. Hamann. Theory of the scanning tunneling microscope. pages 59–67, 1993.

[173] L. G. Teugels, L. G. Avila-Bront, and S. J. Sibener. Chiral domains achieved by surface adsorption of achiral nickel tetraphenyl- or octaethylporphyrin on smooth and locally kinked au(111). *J. Phys. Chem. C*, 115(6):2826–2834, 2011.

[174] S. Tokito, K. Noda, and Y. Taga. Metal oxides as a hole-injecting layer for an organic electroluminescent device. *Journal of Physics D: Applied Physics*, 29(11):2750, 1996.

[175] J. B. Torrance. The difference between metallic and insulating salts of tetracyanoquinodimethone (tcnq): how to design an organic metal. *Accounts of chemical research*, 12(3): 79–86, 1979.

[176] M. Urbani, M. Grtzel, M. K. Nazeeruddin, and T. Torres. Meso-substituted porphyrins for dye-sensitized solar cells. *Chemical Reviews*, 114(24):12330–12396, 2014. ISSN 0009-2665.

[177] H. Vázquez, W. Gao, F. Flores, and A. Kahn. Energy level alignment at organic heterojunctions: Role of the charge neutrality level. *Physical Review B*, 71(4):041306, 2005.

[178] H. Vázquez, Y. J. Dappe, J. Ortega, and F. Flores. Energy level alignment at metal/organic semiconductor interfaces: pillow effect, induced density of interface states, and charge neutrality level. *The Journal of Chemical Physics*, 126(14), 2007. doi: http://dx.doi.org/10.1063/1.2717165. URL `http://scitation.aip.org/content/aip/journal/jcp/126/14/10.1063/1.2717165`.

[179] H. Vázquez, F. Flores, and A. Kahn. Induced density of states model for weakly-interacting organic semiconductor interfaces. *Organic Electronics*, 8(2):241–248, 2007.

[180] S. H. Vosko, L. Wilk, and M. Nusair. Accurate spin-dependent electron liquid correlation energies for local spin density calculations: a critical analysis. *Canadian Journal of Physics*, 58(8):1200–1211, 1980.

[181] J. Wan, Y. Fan, D. Gong, S. Shen, and X. Fan. Surface relaxation and stress of fcc metals: Cu, ag, au, ni, pd, pt, al and pb. *Modelling and Simulation in Materials Science and Engineering*, 7(2):189, 1999.

[182] L. Wan and I. Kingo. Adlayer structure of tcnq molecules on cu (111): Anin situ stm study. *Chinese Science Bulletin*, 46(5):377–379, 2001.

[183] C. Wang, H. Dong, W. Hu, Y. Liu, and D. Zhu. Semiconducting π-conjugated systems in field-effect transistors: a material odyssey of organic electronics. *Chemical reviews*, 112(4): 2208–2267, 2011.

[184] Z. Wang, J. Girard, C. Pasquier, D. Jérome, and K. Bechgaard. Scanning tunneling microscopy in ttf-tcnq: Phase and amplitude modulated charge density waves. *Physical Review B*, 67(12): 121401, 2003.

[185] M. R. Wasielewski. Photoinduced electron-transfer in supramolecular systems for artificial photosynthesis. *Chemical Reviews*, 92(3):435–461, 1992.

[186] A. Weber-Bargioni, W. Auwärter, F. Klappenberger, J. Reichert, S. Lefrancois, T. Strunskus, C. Wöll, A. Schiffrin, Y. Pennec, and J. V. Barth. Visualizing the frontier orbitals of a conformationally adapted metalloporphyrin. *ChemPhysChem*, 9(1):89–94, 2008.

[187] A. Weber-Bargioni, J. Reichert, A. P. Seitsonen, W. Auwarter, A. Schiffrin, and J. V. Barth. Interaction of cerium atoms with surface-anchored porphyrin molecules. *J. Phys. Chem. C*, 112(10):3453–3455, 2008.

[188] A. Wiengarten, J. A. Lloyd, K. Seufert, J. Reichert, W. Auwärter, R. Han, D. A. Duncan, F. Allegretti, S. Fischer, S. C. Oh, et al. Surface-assisted cyclodehydrogenation; break the symmetry, enhance the selectivity. *Chemistry–A European Journal*, 21(35):12285–12290, 2015.

[189] P. Winget, L. K. Schirra, D. Cornil, H. Li, V. Coropceanu, P. F. Ndione, A. K. Sigdel, D. S. Ginley, J. J. Berry, J. Shim, et al. Defect-driven interfacial electronic structures at an organic/metal-oxide semiconductor heterojunction. *Advanced Materials*, 26(27):4711–4716, 2014.

[190] C. B. Winkelmann, I. Ionica, X. Chevalier, G. Royal, C. Bucher, and V. Bouchiat. Optical switching of porphyrin-coated silicon nanowire field effect transistors. *Nano Letters*, 7(6): 1454–1458, 2007.

[191] D. P. Woodruff and T. A. Delchar. *Modern techniques of surface science*. Cambridge university press, 1994.

[192] D. P. Woodruff and T. A. Delchar. *Modern techniques of surface science*. Cambridge university press, 1994.

[193] W. Wu, Y. Liu, and D. Zhu. π-conjugated molecules with fused rings for organic field-effect transistors: Design, synthesis and applications. *Chem. Soc. Rev.*, 39:1489–1502, 2010.

[194] J. Xiao, S. Ditze, M. Chen, F. Buchner, M. Stark, M. Drost, H.-P. Steinrück, J. M. Gottfried, and H. Marbach. Temperature-dependent chemical and structural transformations from 2h-tetraphenylporphyrin to copper(ii)-tetraphenylporphyrin on cu(111). *The Journal of Physical Chemistry C*, 116(22):12275–12282, 2012. doi: 10.1021/jp301757h. URL `http://dx.doi.org/10.1021/jp301757h`.

[195] Y. Xu, O. T. Hofmann, R. Schlesinger, S. Winkler, J. Frisch, J. Niederhausen, A. Vollmer, S. Blumstengel, F. Henneberger, N. Koch, et al. Space-charge transfer in hybrid inorganic-organic systems. *Physical review letters*, 111(22):226802, 2013.

[196] H. Yan, S. Li, C. Yan, Q. Chen, and L. Wan. Adsorption of ttf, tcnq and ttf-tcnq on au (111): An in situ ecstm study. *Science in China Series B: Chemistry*, 52(5):559–565, 2009.

[197] Z.-Y. Yang and C. Durkan. Edge and terrace structure of cotpp on au(111) investigated by ultra-high vacuum scanning tunnelling microscopy at room temperature. *Surf. Sci.*, 604(78): 660 – 665, 2010.

[198] A. Yella, H. W. Lee, H. N. Tsao, C. Y. Yi, A. K. Chandiran, M. K. Nazeeruddin, E. W. G. Diau, C. Y. Yeh, S. M. Zakeeruddin, and M. Gratzel. Porphyrin-sensitized solar cells with cobalt (ii/iii)-based redox electrolyte exceed 12 percent efficiency. *Science*, 334(6056):629–634, 2011. ISSN 0036-8075.

[199] S. Yoshimoto, E. Tsutsumi, K. Suto, Y. Honda, and K. Itaya. Molecular assemblies and redox reactions of zinc(ii) tetraphenylporphyrin and zinc(ii) phthalocyanine on au(111) single crystal surface at electrochemical interface. *Chem. Phys.*, 319(13):147 – 158, 2005.

[200] L. Zhang, M. Lepper, M. Stark, D. Lungerich, N. Jux, W. Hieringer, H.-P. Steinrück, and H. Marbach. Self-assembly and coverage dependent thermally induced conformational changes of ni(ii)-meso-tetrakis (4-tert-butylphenyl) benzoporphyrin on cu(111). *Phys. Chem. Chem. Phys.*, 17:13066–13073, 2015. doi: 10.1039/C5CP01490E. URL `http://dx.doi.org/10.1039/C5CP01490E`.

[201] X. Zhang, L. Tang, and Q. Guo. Low-temperature growth of c_{60} monolayers on au(111): Island orientation control with site-selective nucleation. *J. Phys. Chem. C*, 114(14):6433–6439, 2010.

[202] P. Zucca, A. Rescigno, A. C. Rinaldi, and E. Sanjust. Biomimetic metalloporphines and metalloporphyrins as potential tools for delignification: Molecular mechanisms and application perspectives. *Journal of Molecular Catalysis A: Chemical*, 388389:2 – 34, 2014. ISSN 1381-1169. doi: http://dx.doi.org/10.1016/j.molcata.2013.09.010. URL `http://www.sciencedirect.com/science/article/pii/S138111691300335X`. Special Issue on Biomass Catalysis.

Appendix A

Hartree-Fock and DFT: Formulation and Calculational Insights

A.1 Introduction

A formidable problem in the physics of solids is how to solve the many-body Schrödinger equation (i.e., obtain the many-body wavefunction, $\Psi(\mathbf{r}_i)$) for the complete hamiltonian of the solid, which incorporates electron-ion, electron-electron, and ion-ion interactions. Practical approximations are made that aid in obtaining testable approximate solutions to the problem, and perform reasonably well. Discussed below is a theoretical foundation and framework for obtaining approximate solutions to the many-body Schrödinger equation first by simplifying the hamiltonian of the solid, then by introducing approximations in which we can treat valence electrons with single particles wavefunctions while still capturing the many-body nature of the system.[96]

Then we discuss the theoretical basis and formulation of density functional theory (DFT) in which one deals with the total density of electrons, $n(\mathbf{r})$, rather than the many-body wave function. DFT is one of the most powerful computational methods in physics and chemistry today that produces astonishingly accurate results with relatively little computational fortitude, and its impact, importance, and success is justified by the shared 1998 Nobel price for Chemistry between the main developers of DFT, W. Kohn and J.A. Pople. Finally we will discuss details of the DFT calculations presented in this work, in particular the B3LYP hybrid exchange-correlation functional with the 6-31G basis set, as well as the principles behind the FIREBALL code and a brief summary of the Quantum ESPRESSO code suite.

A.2 The Hamiltonian of a Solid

To obtain an exact theory of the electronic behavior in a solid, one must necessarily deal with the quantum mechanical Schrödinger equation and a hamiltonian that describes all interactions of electrons with electrons, electrons with ions, and ions with ions. The many-body Schrödinger

equation may be written as

$$H\Psi(\mathbf{R}_I;\mathbf{r}_i) = E\Psi(\mathbf{R}_I;\mathbf{r}_i), \tag{A.1}$$

where H is the hamiltonian describing the system, $\Psi(\mathbf{R}_I;\mathbf{r}_i)$ is the wavefunction of the ions and electrons with position vectors $\mathbf{R}_I$ and $\mathbf{r}_i$ respectively, and E is the energy of the system. In the Born-Oppenheimer approximation the motions of electrons and ionic nuclei are separated due to the 3 to 5 orders of magnitude difference in mass, and one may think of the electrons responding instantaneously to any ionic motion. Within this approximation, and assuming the ions are at rest, the hamiltonian describing the interactions mentioned above may be written as

$$H = -\sum_i \frac{\hbar^2}{2m_e}\nabla^2_{\mathbf{r}_i} + \sum_{i,I}\frac{Z_I e^2}{|\mathbf{R}_I - \mathbf{r}_i|} + \frac{1}{2}\sum_{i,j(j\neq i)}\frac{e^2}{|\mathbf{r}_i - \mathbf{r}_j|} + \frac{1}{2}\sum_{I,J(J\neq I)}\frac{Z_I Z_J e^2}{|\mathbf{R}_I - \mathbf{R}_J|}, \tag{A.2}$$

where the first term is the kinetic energy of the electrons, the second term describes ion-electron interaction, the third term electron-electron interaction, and the fourth term ion-ion interaction. Then, if we neglect the ion-ion interaction term, which is simply a constant from the perspective of the electronic degrees of freedom, we have

$$H = -\sum_i \frac{\hbar^2}{2m_e}\nabla^2_{\mathbf{r}_i} + \sum_i V_{ion}(\mathbf{r}_i) + \frac{e^2}{2}\sum_{i,j(j\neq i)}\frac{1}{|\mathbf{r}_i - \mathbf{r}_j|}. \tag{A.3}$$

where

$$V_{ion}(\mathbf{r}_i) = -\sum_{i,I}\frac{Z_I e^2}{|\mathbf{R}_I - \mathbf{r}_i|}. \tag{A.4}$$

Solving for $\Psi(\mathbf{r}_i)$ using this simplified hamiltonian is still extremely difficult due to the electron exchange and correlation properties. The exchange property is another name for the antisymmetric or fermionic nature of electrons, for example, exchanging positions of two electrons with the same spin induces a sign change of Ψ due to the Pauli exclusion principle. The correlation property is that every electron is affected by the motions of every other electron in the system. In the next sections we will discuss how to introduce these properties in an average way through a mean-field approximation starting with simple single-electron equations.

A.3 Hartree Approximation

The Hartree approximation assumes a specific form for the many-body wavefunction, in particular a product of N normalized single-particle states that represent non-interacting electrons, written as

$$\Psi^H(\mathbf{r}_i) = \phi_1(\mathbf{r}_1)\phi_2(\mathbf{r}_2)...\phi_N(\mathbf{r}_N). \tag{A.5}$$

Here, each state $\phi_N(\mathbf{r}_N)$ is the single-electron state of the Nth electron, and the superscript H denotes the Hartree approximation. Then the total energy is,

$$\begin{aligned} E^H &= \langle \Psi^H | \, H \, | \Psi^H \rangle \\ &= \sum_i \langle \phi_i | \, \frac{-\hbar^2 \nabla_{\mathbf{r}}^2}{2m_e} + V_{ion}(\mathbf{r}) \, | \phi_i \rangle + \frac{e^2}{2} \sum_{i,j(j \neq i)} \langle \phi_i \phi_j | \, \frac{1}{|\mathbf{r} - \mathbf{r}'|} \, | \phi_i \phi_j \rangle \end{aligned} \tag{A.6}$$

and from this we obtain the single-particle Hartree equation via a variational argument:

$$\left[\frac{-\hbar^2 \nabla_{\mathbf{r}}^2}{2m_e} + V_{ion}(\mathbf{r}) + e^2 \sum_{(j \neq i)} \langle \phi_j | \, \frac{1}{|\mathbf{r} - \mathbf{r}'|} \, | \phi_j \rangle \right] \phi_i(\mathbf{r}) = \epsilon_i \phi_i(\mathbf{r}), \tag{A.7}$$

where ϵ_i are Lagrange multipliers introduced to take into account the normalization of the single-particle states, ϕ_i. Then ϕ_i can be determined by solving the single-particle Schrödinger equation if all other $\phi_j(\mathbf{r}_j)(j \neq i)$ are known. One accomplishes this iteratively, due to the self-consistency of the problem, by assuming a set of ϕ_i states to construct the single-particle hamiltonian. Then compare the resulting new ϕ_i states with the original ones and modify the original ones such that they resemble the new ϕ_i states and repeat until some tolerance condition is met. However, the Hartree approximation only includes the Coulomb repulsion via a mean-field approximation to the electron-electron interaction, that is, each electron sees all of the others as an average field, and the approximation also does not address the fermionic nature of electrons.

A.4 Hartree-Fock Approximation

To add another level of reality to this approximate system, one must introduce the fermionic nature of electrons into the many-body wavefunction. To do this, we choose a wavefunction that is an antisymmetrized version of that used in the Hartree approximation. That is, the wavefunction which includes the fermionic nature of electrons must change sign upon switching the coordinates of two electrons. In doing this, we obtain the so-called Slater determinant[162]:

$$\Psi^{HF}(\mathbf{r}_i) = \frac{1}{\sqrt{N!}} \begin{vmatrix} \phi_1(\mathbf{r}_1) & \phi_1(\mathbf{r}_2) & \dots & \phi_1(\mathbf{r}_N) \\ \phi_2(\mathbf{r}_1) & \phi_2(\mathbf{r}_2) & \dots & \phi_2(\mathbf{r}_N) \\ \vdots & \vdots & \ddots & \vdots \\ \phi_N(\mathbf{r}_1) & \phi_N(\mathbf{r}_2) & \dots & \phi_N(\mathbf{r}_N) \end{vmatrix} \tag{A.8}$$

where superscript HF denotes the Hartree-Fock approximation, and N is the total number of electrons. The spin components are neglected and may be added later by considering two electrons, one with spin up and one with spin down, located at each position $\mathbf{r}_i$. Then the total energy using the

HF wavefunction is:

$$E^{HF} = \langle \Psi^{HF} | \, H \, | \Psi^{HF} \rangle = \sum_i \langle \phi_i | \, \frac{-\hbar^2 \nabla_{\mathbf{r}}^2}{2m_e} + V_{ion}(\mathbf{r}) \, | \phi_i \rangle + \frac{e^2}{2} \sum_{i,j(j\neq i)} \langle \phi_i \phi_j | \, \frac{1}{|\mathbf{r}-\mathbf{r}'|} \, | \phi_i \phi_j \rangle - \frac{e^2}{2} \sum_{i,j(j\neq i)} \langle \phi_i \phi_j | \, \frac{1}{|\mathbf{r}-\mathbf{r}'|} \, | \phi_j \phi_i \rangle \quad \text{(A.9)}$$

and the single-electron HF equation obtained similarly to equation A.7 is:

$$\left[\frac{-\hbar^2 \nabla_{\mathbf{r}}^2}{2m_e} + V_{ion}(\mathbf{r}) + e^2 \sum_{(j\neq i)} \langle \phi_j | \, \frac{1}{|\mathbf{r}-\mathbf{r}'|} \, | \phi_j \rangle \right] \phi_i(\mathbf{r}) - e^2 \sum_{(j\neq i)} \langle \phi_j | \, \frac{1}{|\mathbf{r}-\mathbf{r}'|} \, | \phi_i \rangle \, \phi_j(\mathbf{r}) = \epsilon_i \phi_i(\mathbf{r}), \quad \text{(A.10)}$$

The extra term in this equation compared to the Hartree equation (A.7) is the exchange term that takes into account the effect of exchanging electrons. We may rewrite this equation in simplified notation as follows:

$$\left[\frac{-\hbar^2 \nabla_{\mathbf{r}}^2}{2m_e} + V_{ion}(\mathbf{r}) + V_i^H(\mathbf{r}) + V_i^X(\mathbf{r}) \right] \phi_i(\mathbf{r}) = \epsilon_i \phi_i(\mathbf{r}), \quad \text{(A.11)}$$

where

$$V_i^H(\mathbf{r}) = e^2 \int \frac{\rho(\mathbf{r}') - \rho_i(\mathbf{r}')}{|\mathbf{r}-\mathbf{r}'|} d\mathbf{r}' \quad \text{(A.12)}$$

$$V_i^X(\mathbf{r}) = -e^2 \int \frac{\rho_i^X(\mathbf{r},\mathbf{r}')}{|\mathbf{r}-\mathbf{r}'|} d\mathbf{r}' \quad \text{(A.13)}$$

and $V_{ion}(\mathbf{r})$ is given in equation A.4. In this simplified notation, we have

$$\rho_i(\mathbf{r}) = |\phi_i(\mathbf{r})|^2 \quad \text{(A.14)}$$

$$\rho(\mathbf{r}) = \sum_i \rho_i(\mathbf{r}) \quad \text{(A.15)}$$

$$\rho_i^X(\mathbf{r},\mathbf{r}') = \sum_{j\neq i} \frac{\phi_i(\mathbf{r}')\phi_i^*(\mathbf{r})\phi_j(\mathbf{r})\phi_j^*(\mathbf{r}')}{\phi_i(\mathbf{r})\phi_i^*(\mathbf{r})} \quad \text{(A.16)}$$

So, in the end, we can write the total electron-electron interaction potential in the HF approximation as:

$$V_i^{HF}(\mathbf{r}) = e^2 \int \frac{\rho(\mathbf{r}')}{|\mathbf{r}-\mathbf{r}'|} d\mathbf{r}' - e^2 \int \frac{\rho_i(\mathbf{r}') + \rho_i^X(\mathbf{r},\mathbf{r}')}{|\mathbf{r}-\mathbf{r}'|} d\mathbf{r}' \quad \text{(A.17)}$$

where the first term represents the total Coulomb repulsion potential felt by all electrons in states $\phi_i(\mathbf{r})$, and the second term represents the effects of fermionic exchange and is different for each state $\phi_i(\mathbf{r})$.

The HF approximation makes five significant simplifications to the many-body Schrödinger equation: the Born-Oppenheimer approximation is assumed valid, the solution is assumed to be a linear

combination of a finite number of typically orthonormal basis functions, each energy eigenfunction is assumed to be properly described by a single Slater determinant, the mean-field approximation is used for the electron-electron interaction, and relativistic effects are entirely neglected. Of these, averaging over the electron-electron interactions can lead to large deviations in the theoretical HF results from experimental results on real systems. There are many post-HF methods that are used to improve the accuracy of this method which will not be discussed here.[45] In general, HF proves to be a useful method for solving the Schrödinger equation for atoms, molecules, and solids. However it is also computationally expensive to approach this problem from the wavefunction perspective. Fortunately another approach was developed, DFT, that revolutionized computational chemistry, which attacks the many-body problem from the perspective of electron densities rather than wave functions.

A.5 Density Functional Theory

Hohenberg, Kohn, and Sham developed DFT between 1964 and 1965 with the basic ideas contained in two original papers.[83, 100] Instead of attempting to extrapolate the physics of many-body electronic systems from the many-body Schrödinger equation involving the many-body wavefunction, $\Psi(\mathbf{r}_i)$, as is done in HF theory, DFT formulates the problem using the total density of electrons, $n(\mathbf{r})$. Note that this formulation is an enormous simplification since the many-body wavefunction need not be specified. Additionally, the approximations listed above for HF theory are no longer needed at the onset, and instead we develop single-particle equations exactly and add approximations as necessary. The relationships established by Hohenberg and Kohn are as follows. First, for any system of interacting particles in an external potential $V(\mathbf{r})$, the external potential is determined uniquely, except for a constant, by the ground state particle density, $n_0(\mathbf{r})$. Since the hamiltonian is fully determined, except for a constant energy shift, it follows that the many-body wavefunctions for all states, ground and excited, are determined. Therefore, all properties of the system are completely determined given only the ground state density, $n_0(\mathbf{r})$. Second, a universal functional for the energy $E[n(\mathbf{r})]$ in terms of the particle density can be defined, valid for any external potential $V(\mathbf{r})$. For any particular external potential the exact ground state energy of the system is the global minimum value of this universal functional, and the density $n(\mathbf{r})$ that minimizes this functional is the exact ground state density, $n_0(\mathbf{r})$. Furthermore, the functional $E[n(\mathbf{r})]$ is sufficient to determine the exact ground state energy and density.[116]

We start by assuming a functional of the total electron density, $n(\mathbf{r})$, may be written as

$$F[n(\mathbf{r})] = \langle \Psi | \, (T + W) \, | \Psi \rangle \,, \tag{A.18}$$

with

$$n(\mathbf{r}) = \sum_i |\phi_i(\mathbf{r})|^2, \tag{A.19}$$

where T and W are the kinetic energy and electron-electron interactions, Ψ is the wavefunction for a system with hamiltonian H, and $\phi_i(\mathbf{r})$ are the single-particle orbitals of the Slater determinant. Since the electron density is determined uniquely by the external potential $V(\mathbf{r})$, and since T and W are common to all solids, we conclude that the total energy of the system is itself a functional of the electron density and may be written as

$$E[n(\mathbf{r})] = \langle \Psi | \, H \, | \Psi \rangle = F[n(\mathbf{r})] + \int V(\mathbf{r}) n(\mathbf{r}) d\mathbf{r}. \tag{A.20}$$

Explicitly writing out the terms in the energy equation gives,

$$F[n(\mathbf{r})] = T^S[n(\mathbf{r})] + \frac{e^2}{2} \int \int \frac{n(\mathbf{r}) n(\mathbf{r}')}{|\mathbf{r} - \mathbf{r}'|} d\mathbf{r} d\mathbf{r}' + E^{XC}[n(\mathbf{r})] \tag{A.21}$$

where the first term is the kinetic energy of the Slater determinant states denoted by superscript S and is given by

$$T^S[n(\mathbf{r})] = \sum_i \langle \phi_i | - \frac{\hbar^2}{2m_e} \nabla^2_{\mathbf{r}} | \phi_i \rangle . \tag{A.22}$$

The second term in equation A.21 is the Coulomb interaction, and the final term is the exchange-correlation term, E^{XC}. This term incorporates all of the many-body characteristics of the real electronic system and will be elaborated on below. First, we apply a variation of the electron density

$$\delta n(\mathbf{r}) = \delta \phi_i^*(\mathbf{r}) \phi_i(\mathbf{r}) \tag{A.23}$$

while enforcing that

$$\int \delta n(\mathbf{r}) d(\mathbf{r}) = \int \delta \phi_i^*(\mathbf{r}) \phi_i(\mathbf{r}) d(\mathbf{r}) = 0 \tag{A.24}$$

which states the the total number of particles does not change. We may then write single-particle equations, with the use of the Lagrange multipliers ϵ_i, as

$$\left[-\frac{\hbar^2}{2m_e} \nabla^2_{\mathbf{r}} + V^{eff}(\mathbf{r}, n(\mathbf{r})) \right] \phi_i(\mathbf{r}) = \epsilon_i \phi_i(\mathbf{r}) \tag{A.25}$$

with the potential, $V^{eff}(\mathbf{r}, n(\mathbf{r}))$, given by

$$V^{eff}(\mathbf{r}, n(\mathbf{r})) = V(\mathbf{r}) + e^2 \int \frac{n(\mathbf{r})'}{|\mathbf{r} - \mathbf{r}'|} d\mathbf{r}' + \frac{\delta E^{XC}[n(\mathbf{r})]}{\delta n(\mathbf{r})} \tag{A.26}$$

where $V(\mathbf{r})$ is the ionic external potential, and the last term is the variational derivative of the exchange-correlation energy functional. The single-particle equations of equation A.25 are known as the Kohn-Sham equations, and their solutions are single-particle orbitals, $\phi_i(\mathbf{r})$, known as Kohn-Sham orbitals. Since the effective potential, $V^{eff}(\mathbf{r}, n(\mathbf{r}))$, depends solely on the electron density,

$n(\mathbf{r})$, we may solve these equations iteratively until a self-consistency condition is reached. However, the exact form of the exchange-correlation energy, E^{XC}, is not known and must first be accounted for.

It is interesting to note that the form of E^{XC} required to capture all many-body effects of a real system is not known, and many models have been developed to approximate this term. It is convenient to write the exchange-correlation energy as

$$E^{XC}[n(\mathbf{r})] = \int (\epsilon^X[n(\mathbf{r})] + \epsilon^{cor}[n(\mathbf{r})])n(\mathbf{r})d\mathbf{r}, \tag{A.27}$$

with $\epsilon^X[n(\mathbf{r})]$ representing the pure exchange energy and $\epsilon^{cor}[n(\mathbf{r})]$ representing the correlation part. The exchange-correlation term then appears in the Kohn-Sham equations as

$$V^{XC}[n(\mathbf{r})] = \frac{\delta E^{XC}[n(\mathbf{r})]}{\delta n(\mathbf{r})}. \tag{A.28}$$

In a uniform system where only the Coulomb repulsion and exchange interaction describe the electron-electron interactions, the exchange energy may be written as

$$E^X = -\frac{3}{4}\frac{e^2}{\pi}k_F N, \tag{A.29}$$

where k_F is the wavenumber of electrons at the Fermi energy, and N is the total number of electrons. If we rewrite the total number of electrons as $N = \int n d\mathbf{r}$, then the energy becomes

$$E^X[n] = -\frac{3}{4}\frac{e^2}{\pi}\int k_F n d\mathbf{r} = -\frac{3}{4}e^2\left(\frac{3}{\pi}\right)^{1/3}\int [n]^{1/3} n d\mathbf{r}. \tag{A.30}$$

Generalizing this equation to situations where the density is not uniform gives

$$E^X[n(\mathbf{r})] = \int \epsilon^X[n(\mathbf{r})]n(\mathbf{r})d\mathbf{r} \tag{A.31}$$

$$\epsilon^X[n(\mathbf{r})] = -\frac{3}{4}e^2\left(\frac{3}{\pi}\right)^{1/3}[n(\mathbf{r})]^{1/3}. \tag{A.32}$$

If electrons only interacted via Pauli exclusion principle, that is, if $\epsilon^{corr} = 0$ then the exchange term $\epsilon^X[n(\mathbf{r})]$ can be used in the Kohn-Sham equations and give an exact solution in terms of the single-particle wavefunctions $\phi_i(\mathbf{r})$. However, in real systems electrons interact via Coulomb repulsion amongst each other as well as attraction to the ions, in addition to the Pauli exclusion principle. The attraction to ion cores is incorporated in the external potential term, $V(\mathbf{r})$, and one part of the electron-electron Coulomb interaction is included in the second term of equation A.26, which leaves the long range interaction felt by every electron that depends on the motions of all other electrons, which is incorporated in the correlation term, $\epsilon^{cor}[n(\mathbf{r})]$.

Approximate functionals developed to deal with the exchange-correlation potential in DFT is an active field of study. For example, in the local density approximation (LDA), the exchange-correlation energy is simply an integral over all space with the exchange-correlation energy density

at each point assumed to be the same as that of a homogenous electron gas with the same density. However, this approximation performs poorly in systems with large electron density gradients, and so the generalized gradient approximations (GGAs) was developed as an improvement. GGAs take a first step beyond LDA by considering the magnitude of the gradient of the density as well as the value of the density at each point. There now exist many GGA functionals that are used in quantitative calculations.

A class of exchange-correlation energy functional is known as the hybrid functional class, which incorporate both an orbital-dependent Hartree-Fock exchange and an explicit density functional. These functionals are the most accurate functionals available for energetics calculations and is the preferred choice for the computational chemistry community[55, 99]. A popular hybrid functional known as the Becke three-parameter Lee-Yang-Parr (B3LYP) functional uses a combination of Becke's three-parameter exchange functional of the form

$$E_{XC} = E_{XC}^{LDA} + a_0(E_X^{HF} - E_X^{DFA}) + a_X E_X^{Becke} + a_C E_C. \tag{A.33}$$

with the Lee-Yang-Parr correlation to give

$$E_{XC}^{B3LYP} = E_{XC}^{LDA} + a_0(E_X^{HF} - E_X^{LDA}) + a_X(E_X^{GGA} - E_X^{LDA}) + E_C^{LDA} + a_C(E_C^{GGA} - E_C^{LDA}), \tag{A.34}$$

where $a_0 = 0.20$, $a_X = 0.72$, $a_C = 0.81$, E_X^{GGA} is the Becke 88 (B88) exchange functional[18], E_C^{GGA} is the Lee-Yang-Parr correlational functional[106], and E_C^{LDA} is the Vosko-Wilk-Nusair (VWN) LDA approximation to the correlation functional[180]. Here, subscript XC means exchange-correlation, subscript X means exchange, and superscript DFA denotes an LDA or GGA functional. The coefficients are typically empirically adjusted to fit atomic and molecular data. The B3LYP hybrid functional is used in this work in gas-phase density of states calculations for the molecules presented.

A.6 Basis Sets

Localized functions provide an intuitive description of electronic structure and bonding. Quantitative methods in which the wavefunction is expanded as a linear combination of atomic-like orbitals, such as Gaussians, Slater-type orbitals, and numerical radial atomic-like orbitals can be very efficient and accurate. In performing DFT calculations for a given system one must specify a basis, and thus efficiency is gained while generality is lost. This is in contrast to plane wave methods where one basis applies more generally but is computationally costly. In choosing localized basis functions for a given calculation, there are two competing considerations: reduction of the number of basis functions and ease of computation. Additionally, functions must be well-chosen to be chemically relevant, that is, to accurately describe a given system.

Pairs of electrons are assigned to molecular orbitals, ψ_i, which are written as a linear combination of atomic orbitals (LCAO) as

$$\psi_i = \sum_\mu c_{\mu i}\phi_\mu, \tag{A.35}$$

where $c_{\mu i}$ are variational coefficients, and ϕ_μ are the one-electron basis functions. The obvious choice for atomic orbital basis functions are the orbitals of the hydrogen atom, which are referred to as Slater-type orbitals (STO), and are written as

$$\phi_\mu(\mathbf{r}) = r^l e^{-\zeta r} Y_l^m(\theta, \phi). \tag{A.36}$$

Here, $Y_l^m(\theta, \phi)$ are spherical harmonics with $-l \leq m \leq l$, and ζ is a constant related to the effective charge of the nucleus due to partial shielding by electrons. The integer l has values of $0, 1, 2, 3...$ corresponding to the $s, p, d, f...$ orbitals. While the STOs describe exactly the H atom and have qualitatively correct asymptotic behavior for $r \to 0$ and $r \to \infty$ in that they decay exponentially away for large r and s-types have a cusp at the nucleus as $r \to 0$, they are also inefficient when computing integrals.

The next class of orbitals are the Gaussian-type orbitals (GTOs), and are given as

$$\phi_\mu(\mathbf{r}) = r^l e^{-\zeta r^2} Y_l^m(\theta, \phi). \tag{A.37}$$

GTOs also decay as $r \to \infty$ however they do so faster than STOs, additionally, s-type GTOs do not have a nuclear cusp and are generally much easier to compute than STOs. STOs are more accurate than GTOs, however they take longer to compute. A solution is to compose a new GTO that mimics an STO by taking a linear combination of GTOs to create so-called contracted Gaussian-type orbitals (CGTOs), which maintain the accuracy of STOs while having the computational efficiency of GTOs.

Basis sets are also classified by the number of basis functions they contain. The minimal basis set has just one basis function (e.g., one STO, GTO, or CGTO), whereas a double-zeta or triple-zeta has two or three basis functions for each atomic orbital. Additionally, there are split-valence basis sets that use only one basis function for each core-level atomic orbital and a larger basis (i.e., two or more basis functions) for the valence atomic orbitals. For example, the H atom has just one atomic orbital, the $1s$, and the minimal basis would be one basis function (STO, GTO, or CGTO). For the C atom, which has an electronic structure of $1s, 2s, 2p_x, 2p_y, 2p_z$ with five atomic orbitals, the minimal basis would have 5 basis functions. A double-zeta basis would have two basis functions per orbital, or ten basis functions total. A split-valence double-zeta basis would have nine basis functions: one basis function for the core $1s$ level, and two basis functions for each of the four valence levels, $2s, 2p_x, 2p_y, 2p_z$.

In dealing with molecular environments, orbitals become distorted from their spherical harmonic shapes due to the presence of other atoms. For example, an s orbital can polarize in one direction if it is mixed with a p orbital, just as p orbitals can polarize if mixed with d orbitals. In general, to polarize a basis function with angular momentum l, mix it with basis functions of angular momentum $l+1$. Furthermore, the use of diffuse functions which have small ζ components (i.e., electrons are held far away from the nucleus) are necessary when dealing with anions and electronegative atoms (e.g., fluorine) with large electron density. Diffuse functions are also necessary for accurate polarizabilities or binding energies of van der Waals complexes.

One of the so-called Pople basis sets, developed by Nobel Laureate, John Pople, is the 6-31G basis set.[54, 79] This is a split-valence double-zeta basis set in which the core orbital is a CGTO made of six Gaussians, and the valence is described by two orbitals, one single Gaussian and one CGTO made of three Gaussians. In basis set naming notation, one denotes a polarization set with an asterisk at the end, for example, 6-31G*, which in this case adds d polarization functions on non-hydrogen atoms and may also be written as 6-31G(d). 6-31G** is simply 6-31G* with the addition of p polarization functions for hydrogen, or 6-31G(d,p). For the DFT calculations presented in this work, the 6-31G basis set is used with the B3LYP hybrid functional and calculations are performed in the GAMESS software package.[154]

A.7 FIREBALL

The FIREBALL method is based on the *ab initio* tight-binding molecular dynamics formalism developed by Sankey and Niklewksi (SN method).[150] The SN method is based on norm-conserving pseudo-potentials[15, 73] and solely uses the LDA approximation limit of DFT, using the Harris-Foulkes functional.[61, 76] The atomic basis set is a minimal non-orthogonal local-orbital basis of so-called fireball orbitals, which are slightly excited pseudo-atomic orbitals that vanish at some radius r_c rather than at infinity for typical orbitals. This boundary condition is equivalent to an atom-in-the-box and has the effect of raising the electronic energy levels due to the confinement of the atom. The radial cutoffs, r_c, are chosen such that these electronic eigenvalues remain negative and are only mildly perturbed from the free-atom case. The electronic eigenstates are expanded as a linear combination of pseudo-atomic orbitals within a localized minimal sp^3 basis for the atoms. In short, FIREBALL is a real-space local-pseudo-atomic-orbital molecular dynamics implementation of DFT, cast in a tight-binding-like form that provides a substantial improvement in computational efficiency and high accuracy. The Kohn-Sham self-consistent density functional is replaced by an approximate self-consistent functional based on atomic occupation numbers.[48]

A.7.1 Orbitals and Basis Sets

To solve the one-electron Schrödinger equation:

$$\left\{-\frac{\hbar^2}{2m_e}\nabla^2 + V(\mathbf{r})\right\}\psi_i(\mathbf{r}) = \varepsilon_i\psi_i(\mathbf{r}), \tag{A.38}$$

where

$$V(\mathbf{r}) = V_{ext}(\mathbf{r}) + \frac{\delta E^{XC}[\rho(\mathbf{r})]}{\delta\rho(\mathbf{r})} + \frac{e^2}{2}\int\frac{\rho_{in}(\mathbf{r})}{|\mathbf{r}-\mathbf{r}'|}d^3\mathbf{r}', \tag{A.39}$$

where $\rho(\mathbf{r})$ are charge densities and a set of numerical atomic-like orbitals is used based on a pseudo-potential formalism. Note that $V(\mathbf{r})$ is similar to equation A.26 above, with slightly different notation, i.e. using $\rho(\mathbf{r})$ rather than $n(\mathbf{r})$ for charge density. Construction of pseudo-potentials starts by solving the Kohn-Sham equations self-consistently for all electrons of the free atom. Then, the pseudo-potential and pseudo-atomic wavefunctions are generated using the fhiPP code, which is freely available[64], via the Hamann-scheme.[72] The pseudo-potentials are then transformed into a fully separable form. The fireball orbitals are expressed in the form $\psi(r) = f(r)Y_{lm}(\theta,\phi)$, where $f(r)$ is a radial component, and $Y_{lm}(\theta,\phi)$ is the angular component made up of spherical harmonic functions. These orbitals vanish at some radius r_c as mentioned above. Interactions are pre-computed using a multi-center expansion. Given any two atomic orbitals, i and j, beyond some cutoff radius $(r_{ci} + r_{cj})$, the matrix elements become exactly zero. That is, if the distance between any two atomic centers is larger than the cutoffs of the two wavefunctions on the centers, then the overlap is zero and the interactions between atomic centers will go to zero. Thus, there is only a prescribed interaction range over which the integrals must be evaluated, which are computed for up to three-centers exactly. In the FIREBALL approach, integrals are pre-calculated on a numerical grid and the specific values required are extracted from the tabulated values via interpolation. Since the integral tables depend only on the atom type, the r_c values of each atom, and the type of DFT exchange-correlation functional used, the integral tables need only be calculated once for a given number of atomic species, rather than calculating them in real time. With this pre-generation of integrals, the integrals may be spread out over multiple processors based on integral types, which is beneficial since the number of integrals for each database grows as N^3, where N is the number of atoms.

A.7.2 Tight-Binding Density Functional Formalism

FIREBALL replaces the Kohn-Sham energy functional with a self-consistent extension of the Harris-Foulkes functional, written as

$$E_{tot}^{Harris} = E^{BS} + \{U^{ion-ion} - U^{ee}[\rho_{in}(\mathbf{r})]\} + \{U^{XC}[\rho_{in}(\mathbf{r})] - V^{XC}[\rho_{in}(\mathbf{r})]\}. \tag{A.40}$$

The primary difference is that the Kohn-Sham equations are defined in terms of both an input and output charge density, whereas the Harris-Foulkes functional is defined only by an input charge density, $\rho_{in}(\mathbf{r})$. The first term, E^{BS}, is the band-structure energy $\sum_{i,occ}\varepsilon_i$, where the eigenvalues ε_i are the eigenvalues of the one-electron Schrödinger equation given by equation A.38 above, and the summation is over all i occupied states. The second term in equation A.40 is the short-range repulsive ion-ion interaction that is offset by the overcounting of Hartree interactions. Written explicitly,

$$U^{short-range}(\mathbf{r}) = \{U^{ion-ion} - U^{ee}[\rho_{in}(\mathbf{r})]\}, \tag{A.41}$$

with

$$U^{ion-ion} = \frac{e^2}{2}\sum_{i,j}\frac{Z_i Z_j}{|\mathbf{R}_i - \mathbf{R}_j|}, \tag{A.42}$$

and

$$U^{ee}[\rho_{in}(\mathbf{r})] = \frac{e^2}{2}\int\frac{\rho_{in}(\mathbf{r})\rho_{in}(\mathbf{r}')}{|\mathbf{r}-\mathbf{r}'|}d^3\mathbf{r}d^3\mathbf{r}'. \tag{A.43}$$

The last term of equation A.40 is a correction of the exchange-correlation energy, given by

$$\{U^{XC}[\rho_{in}(\mathbf{r})] - V^{XC}[\rho_{in}(\mathbf{r})]\} = \int\rho_{in}(\mathbf{r})\{\varepsilon_{XC}[\rho_{in}(\mathbf{r})] - \frac{\delta E^{XC}[\rho(\mathbf{r})]}{\delta\rho(\mathbf{r})}\}. \tag{A.44}$$

In evaluating the total energy of the system from equation A.40, the input density is a sum of confined spherical atomic-like densities,

$$\rho_{in}(\mathbf{r}) = \sum_i n_i|\phi_i(\mathbf{r}-\mathbf{R}_i)|^2, \tag{A.45}$$

where the fireball orbitals $\phi_i(\mathbf{r}-\mathbf{R}_i)$ are used as basis functions for solving the one-electron Schrödinger equation, equation A.38. The self-consistent occupation number, n_i, determines the number of electrons occupying each spherically confined atomic-like density, and is given by $n_i = n_i^0 + \delta n_i$, where n_i^0 is the number of electrons of the neutral atom, and δn_i describes the charge transfer between the atoms of the system.

A.7.3 Exchange-correlation Interactions

Exchange-correlation interactions are evaluated in FIREBALL using the McWEDA method[89], which uses a many-center expansion based on an expansion of the density one site at a time. Note that this is a higher order approximation than the nearly-uniform density approximation used in the original SN method, and it can be used with gradient-corrected functionals. The primary goal here is to calculate the exchange-correlation contributions from precalculated integrals stored in data tables, using a three-center approximation. Let i_μ and i_ν be the atomic sites corresponding to orbital μ and ν respectively, then we consider two cases: on-site matrix elements ($i_\mu = i_\nu$), and off-site matrix

elements ($i_\mu \neq i_\nu$). To improve upon the original SN approach and generalize it beyond the minimal sp^3 basis sets, the exchange-correlation matrix elements are calculated as the sum of a one-center or two-center term plus a correction. The main term (one- or two-center term) is calculated exactly, and the correction is calculated using the many-center expansion of the SN method. To calculate this correction, a generalized SN approximation (GSN) for the exchange-correlation matrix elements is defined as the following,

$$\int \phi_{i\mu}(\mathbf{r}) V_{XC}[\rho;\mathbf{r}]\phi_{i\nu}(\mathbf{r})d\mathbf{r} = V_{XC}[\overline{\rho}_{\mu\nu};\mathbf{r}]S + V'_{XC}[\overline{\rho}_{\mu\nu};\mathbf{r}]\left(\int \phi_{i\mu}(\mathbf{r})\rho(\mathbf{r})\phi_{i\nu}(\mathbf{r})d\mathbf{r} - \overline{\rho}_{\mu\nu}S\right) \quad \text{(A.46)}$$

with

$$S = \int \phi_{i\mu}(\mathbf{r})\phi_{i\nu}(\mathbf{r})d\mathbf{r}. \quad \text{(A.47)}$$

Furthermore,

$$\overline{\rho}_{\mu\nu} = \frac{\langle w_\mu | \, \rho \, | w_\nu \rangle}{\langle w_\mu | w_\nu \rangle}, \quad \text{(A.48)}$$

where w_μ are the weighting functions taken as a spherical average of the pseudo-atomic orbital, i.e., $w_{il} = |R_{il}(r)|Y_{00}(\Omega)$, where $|R_{il}(r)|$ is the absolute value of the radial function $R_{il}(r)$ associated with the particular orbital ϕ_{il}.

Now we address on-site and off-site matrix elements in detail. Starting with the on-site matrix elements $i_\mu = i_\nu$, we have,

$$\begin{aligned}\int \phi_{i\mu}(\mathbf{r}) V_{XC}[\rho;\mathbf{r}]\phi_{i\nu}(\mathbf{r})d\mathbf{r} = &\int \phi_{i\mu}(\mathbf{r}) V_{XC}[\rho_i;\mathbf{r}]\phi_{i\nu}(\mathbf{r})d\mathbf{r} \\ &+ V'_{XC}[\overline{\rho}_{\mu\nu};\mathbf{r}]\left(\int \phi_{i\mu}(\mathbf{r})\rho(\mathbf{r})\phi_{i\nu}(\mathbf{r})d\mathbf{r} - \overline{\rho}_{\mu\nu}S\right) \\ &- V'_{XC}[\overline{\rho}_i;\mathbf{r}]\left(\int \phi_{i\mu}(\mathbf{r})\rho_i(\mathbf{r})\phi_{i\nu}(\mathbf{r})d\mathbf{r} - \overline{\rho}_i S\right) \\ &+ (V_{XC}[\overline{\rho}_{\mu\nu};\mathbf{r}] - V_{XC}[\overline{\rho}_i;\mathbf{r}])S, \quad \text{(A.49)}\end{aligned}$$

with

$$\overline{\rho}_i = \frac{\langle w_\mu | \, \rho_i \, | w_\nu \rangle}{\langle w_\mu | w_\nu \rangle}. \quad \text{(A.50)}$$

In the previous equations, ρ_i, is the density at atomic site i, and the matrix elements are written as a one-center contribution (first term on the right side) plus a correction consisting of several terms based on the functional derivative of the potential (V'_{XC}), and the average density, $\overline{\rho}$. The one-center term is calculated exactly and is much larger than the correction terms.

For off-site matrix elements ($(i_\mu = i) \neq (i_\nu = j)$) we write the matrix element as a two-center main contribution that is exactly calculated ($\rho_{ij} = \rho_i + \rho_j$), plus a correction. Writing this out

explicitly gives,

$$\int \phi_{i\mu}(\mathbf{r})V_{XC}[\rho;\mathbf{r}]\phi_{j\nu}(\mathbf{r})d\mathbf{r} = \int \phi_{i\mu}(\mathbf{r})V_{XC}[\rho_{ij};\mathbf{r}]\phi_{j\nu}(\mathbf{r})d\mathbf{r} + V'_{XC}[\overline{\rho}_{\mu\nu};\mathbf{r}]\left(\int \phi_{i\mu}(\mathbf{r})\rho(\mathbf{r})\phi_{j\nu}(\mathbf{r})d\mathbf{r} - \overline{\rho}_{\mu\nu}S\right) - V'_{XC}[\overline{\rho}_{ij};\mathbf{r}]\left(\int \phi_{i\mu}(\mathbf{r})(\rho_i(\mathbf{r}) + \rho_j(\mathbf{r}))\phi_{j\nu}(\mathbf{r})d\mathbf{r} - \overline{\rho}_{ij}S\right) + (V_{XC}[\overline{\rho}_{\mu\nu};\mathbf{r}] - V_{XC}[\overline{\rho}_{ij};\mathbf{r}])S, \quad \text{(A.51)}$$

with

$$\overline{\rho}_{ij} = \frac{\langle w_\mu |\, \rho_{ij}\, | w_\nu \rangle}{\langle w_\mu | w_\nu \rangle}. \quad \text{(A.52)}$$

Here, $\overline{\rho}_{\mu\nu}$ includes all density contributions, and is defined in equation A.48. Equations A.48 through A.52 represent the foundation of the McWEDA approximation for the calculation of the exchange-correlation matrix elements. To summarize, the initial SN method multi-center expansion combined with the improvements of the McWEDA method, fireball orbitals, and pre-computed data files form the underpinnings of the FIREBALL method and are key to its computational efficiency and accuracy. Note that this approach is independent of the type of functional used, however LDA and Becke exchange (B88) with Lee-Yang-Parr correlation have been used in previous works.

A.7.4 Self-Consistency Implementation

Representing the input electron density by equation A.45 prevents this method from obtaining self-consistency in the usual way where, for each point $\mathbf{r}$, $\rho_{in}(\mathbf{r}) = \rho_{out}(\mathbf{r})$. Instead, this method implements self-consistency on the orbital occupancies. Recall that the occupation numbers are written as $n_i = n_i^0 + \delta n_i$, where n_i^0 is the occupation number that gives a charge density equivalent to that of the neutral atom and δn_i describes the charge transfer between the atoms of the system. Allowing n_i to vary implies that the charge distribution around each atom is in general non-neutral. Now, the total energy is a function of the self-consistent occupation numbers n_i,

$$E_{tot}[\rho_{in}(\mathbf{r})] \equiv E_{tot}[n_i](n_i \neq n_i^0) \quad \text{(A.53)}$$

To find the self-consistent n_i's we first define the output occupation numbers as,

$$n_i^{out} = 2\sum_\alpha |\, \langle \psi_\alpha | \varphi_i \rangle \,|^2, \quad \text{(A.54)}$$

where ψ_α are the occupied eigenstates of equation A.38, and φ_i are the atomic-like orthogonal Löwdin orbitals given by,

$$\varphi_i = \sum_j (S)_{ij}^{-1/2}\phi_j, \quad \text{(A.55)}$$

With S given by equation A.47. Then, the occupation numbers n_i are determined from the self-consistency condition that $n_i^{out} = n_i$ for all i. Recall that these n_i are the input occupation numbers defining the input density from equation A.45, then equation A.54 is a way of projecting the output electron density from equation A.38 into a density of the form given by equation A.45. The problem of finding a self-consistent solution has then changed from matching the input and output densities on the $M \times M \times M$ real space grid, where M are the number of points on the grid, to that of matching $n \times N$ real numbers, where N is the number of atoms, and n is the number of valence shells on each atom. A brief review of the successful applications of FIREBALL, for example as applied to TiO_2, may be found in reference [108]. More detailed descriptions of the FIREBALL method and formulation are found in references [89] and [107].

A.7.5 Simulations of Scanning Tunneling Microscopy Images

Proper theoretical interpretation of STM images requires the inclusion of several effects such as the influence of electronic and atomic structure of the tip and also electron transfer going beyond the first order and image potential effects. Total energy DFT calculations using FIREBALL code combined with Green's function techniques for electron transport calculations provides a path to achieve a more accurate theoretical description of STM images. The practical approach to theoretically modeling STM images is to first treat the tip and sample electronic structures as independent and then coupling both parts using Green's functions. Furthermore, an extended basis formalism that is based on a local basis formalism may be used to calculate the tip and sample electronic structure. In this formalism, the tip-sample interaction is obtained by calculating hopping integrals between orbitals of both sides, tip and sample. This approach addresses both the tunneling and contact electron transfer regimes in similar ways.

The hamiltonian of the tip-sample system may be written as the sum of three terms,

$$\hat{H} = \hat{H}^s + \hat{H}^t + \hat{H}^{t-s}, \tag{A.56}$$

where tip and sample are denoted by superscript t and s, respectively, with the last term taking into account the interaction between the tip and sample. We then can write an expression for the electrical current flowing between the tip and sample involving the calculation of Green's functions for the isolated tip and sample, and use a hopping matrix to couple them,

$$I = \frac{4\pi e}{\hbar} \int_{-\infty}^{+\infty} dE \times [f_t(E) - f_s(E)] \times Tr[\hat{T}_{ts}\hat{\rho}_{ss}(E)\hat{D}^r_{ss}(E)\hat{T}_{st}\hat{\rho}_{tt}(E)\hat{D}^a_{tt}(E)], \tag{A.57}$$

where $\hat{T}_{st}, \hat{T}_{ts}$ are hopping matrices, $f_t(E), f_s(E)$ are the corresponding Fermi-Dirac distribution functions, $\hat{\rho}_{tt}, \hat{\rho}_{ss}$ are density of states matrices associated with the tip and sample, respectively.

Additionally,

$$\hat{D}^r_{ss}(E) = [\hat{1} - \hat{T}_{st}\hat{g}^r_{tt}(E)\hat{T}_{ts}\hat{g}^r_{ss}(E)]^{-1} \tag{A.58}$$

and

$$\hat{D}^a_{tt}(E) = [\hat{1} - \hat{T}_{ts}\hat{g}^a_{ss}(E)\hat{T}_{st}\hat{g}^a_{tt}(E)]^{-1} \tag{A.59}$$

where $\hat{g}^r_{tt}(E)$ and $\hat{g}^a_{ss}(E)$ correspond to the retarded and advanced Green's functions for the tip and sample, respectively, and $\hat{1}$ is the identity matrix. The effectiveness of the FIREBALL method in analyzing atomic scale STM images of semiconductor and metal surfaces has been shown in previous works[27, 47, 94, 132, 165].

A.8 Quantum ESPRESSO

Quantum ESPRESSO is an integrated suite of computer codes for electronic-structure calculations and materials modeling based on DFT using plane wave basis sets, with pseudo-potentials to represent electron-ion interactions.[66] Quantum ESPRESSO is freely available and is an open-source software package. In terms of its relevance to the work shown here, it can calculate the Kohn-Sham orbitals and energies for isolated and extended or periodic systems as well as their ground state energies and can also calculate STM images. It is capable of many other calculation and simulation feats that are not relevant to this work, which are described in detail elsewhere.[66]

Appendix B
UPS Spectrum Calibration and Work Function Measurement

B.1 UPS Calibration: Obtaining Binding Energies

UPS is a useful spectroscopic method to determine information regarding the occupied states of the sample. Recall that ultraviolet photons impinge on the sample, and electrons in the sample occupied states may absorb a photon and eject from the sample and subsequently be detected by a cylindrical mirror analyzer and channeltron. While this detection method does not directly yield binding energies of the electrons, it does provide kinetic energies which can then be converted into the binding energy scale if the appropriate steps are taken.

It is reasonable to assume that the Fermi level of any sample in thermodynamic equilibrium with the measurement equipment (i.e., sample holder, vacuum chamber, etc.) aligns with the Fermi level of the chamber itself. Additionally, since the chamber is massive and conducting enough to be considered an electron reservoir, the Fermi level of the chamber is not significantly altered by the presence of the sample. It follows that the Fermi levels of subsequent samples are aligned with respect to one another.

Samples that have a band gap, such as semiconductors, do not have electrons at the Fermi level, which is located within the band gap, so one cannot directly determine the Fermi level from the electron kinetic energy spectrum. Metals, however, have finite electron occupation at the Fermi level and the Fermi level may be extracted from the UPS spectra. Figure B.1 (a) shows a UPS spectrum of Au foil, dominated by Au 5d states, with a sharp decrease in intensity starting near 34 eV and ending around 34.6 eV on the kinetic energy scale. These are the highest kinetic energy electrons emerging from the sample, and thus originate from the Fermi level of the Au foil. Taking the derivative of the spectrum and fitting this section of the curve with a Gaussian gives the position of the Fermi level on the kinetic energy scale. Since the Fermi energy defines the zero of the binding energy scale, we then apply the following scaling equation to convert kinetic energies to binding energies

$$E_B = E_K - E_{K,F}, \tag{B.1}$$

where E_K is the kinetic energy of the photoelectrons, $\mathrm{E}_{K,F}$ is the kinetic energy of the Fermi level

measured from the Au foil, and E_B is the resulting binding energy of the photoelectrons which is a negative number since $E_K \leq E_{K,F}$. Since the Fermi level is the same for all samples and the position on the kinetic energy scale is known, we then apply this same method to a $TiO_2(110)$ single crystal sample, as shown in figure B.1 (b), to identify the location of the Fermi level in the TiO_2 band gap and convert the kinetic energy scales to binding energy.

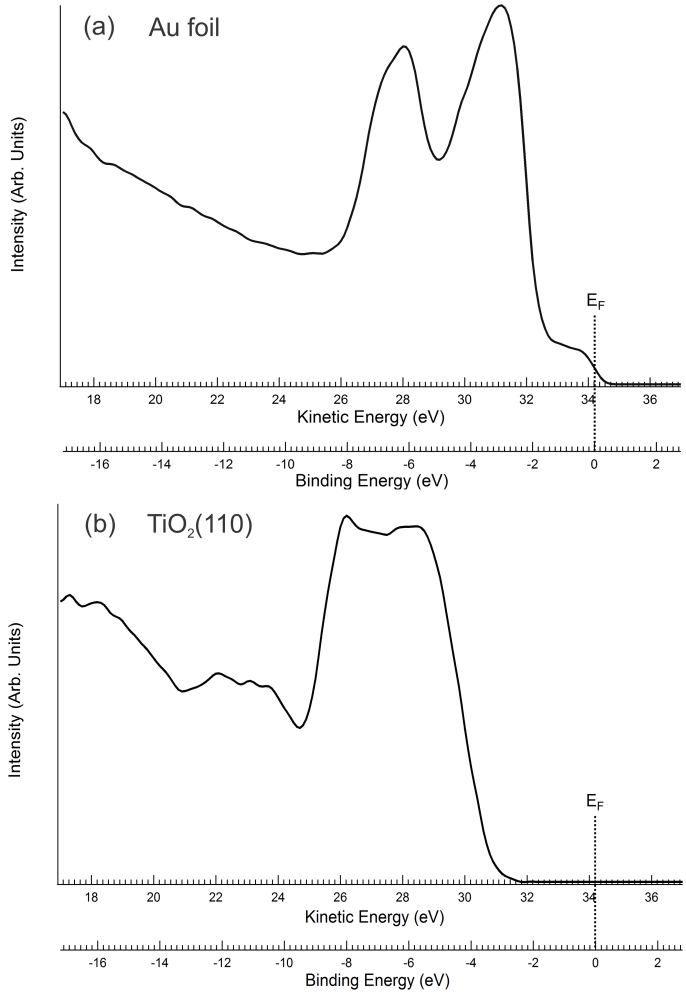

Figure B.1: UPS He II spectrum ($h\nu = 40.8eV$) of (a) Au foil and (b) $TiO_2(110)$ as a function of photoelectron kinetic and binding energies.

B.2 UPS Work Function Measurement: Secondary Electron Cutoff

To obtain a complete description of the occupied states of the system, we must have information regarding the work function and vacuum level in addition to the Fermi energy. With these values determined, we can calculate the ionization potential of the sample and (along with the electron affinity from IPS) draw a complete energy level alignment diagram. We can monitor these values

to establish if an interfacial dipole has formed (possibly indicated by a change in the vacuum level) due changes in the system, such as adsorbing an organic species onto the surface, and obtain greater insight into the fundamental physical interactions at the interface.

In order to determine the vacuum level and work function we must measure the secondary electron cutoff (SECO) of the sample. Primary electrons that are photoexcited out of their occupied states arrive at the detector with some kinetic energy and contribute to the measured spectrum as a peak, for instance. However, there are many primary electrons that interact with the sample inelastically before leaving the sample, and also photoelectrons that lose too much energy in these inelastic interactions to leave the sample at all. These photoelectrons that inelastically interact with the sample after initial photoexcitation, and still have enough energy to leave the sample and reach the detector, contribute to the secondary electron background signal which greatly increases as kinetic energy decreases. Figure B.2 shows a schematic energy level diagram illustrating how this process may occur for two electrons originating from different occupied states. An electron excited from the Fermi level that does not inelastically interact with the sample will arrive with the maximum kinetic energy possible. However, another photoelectron originating from deep within the valence band may, in this case, lose energy before leaving the sample such that it has just enough kinetic energy to reach the detector. Thus there is a minimum amount of energy needed to leave the sample and reach the detector, and the SECO corresponds to this minimum energy.

Figure B.3 shows a HeI UPS spectrum of Au(111) with the sample biased at -5V to observe the SECO, which corresponds to the drastic drop-off in signal at the low-kinetic-energy end of the spectrum. Using a linear extrapolation method, as shown by the two red lines, we obtain the energy position of the SECO (4.5 eV) and the Fermi energy (20.6 eV) to obtain the total energy width of the spectrum, W (16.1 eV).

To make use of these values, we first need to understand the relative energy alignment by considering the energetics of the photoelectrons we detect. Figure B.4 (a) shows a schematic energy level diagram for the SECO measurement of a metallic sample. The energy difference between the incident photon energy, $h\nu$, and the spectrum width, W, gives the work function of the metal, $e\phi$. Written out explicitly, we have

$$h\nu = W + e\phi. \tag{B.2}$$

The spectrum width, W, is simply the kinetic energy separation between the Fermi level and the SECO, or the total kinetic energy range of detected electrons between a maximum at $E_{K,F}$ to a minimum of zero just beyond the SECO. Recall, we bias the sample to -5V to measure the SECO;

the applied bias shifts the spectrum toward greater kinetic energies.

$$h\nu = E_{K,F} + e\phi, \tag{B.3}$$

and finally,

$$h\nu = E_K - E_B + e\phi, \tag{B.4}$$

which can be interpreted as a conservation of energy equation for the incident photon energy ($h\nu$): the photoexcitation releases the electron from its occupied state (E_B), removes the electron from the sample ($e\phi$), and gives enough kinetic energy to reach the sample (E_K).

For a semiconducting sample the presence of a band gap necessitates additional terms, as shown in figure B.4 (b), to give the following relationship

$$h\nu = W + e_\chi + E_{gap}, \tag{B.5}$$

where e_χ is the electron affinity of the semiconductor, and E_{gap} is the width of the band gap between the valence band maximum and conduction band minimum. e_χ can be directly determined using IPS in the same chamber that we perform UPS, and, combined with the UPS valence band measurements, E_{gap} is determined.

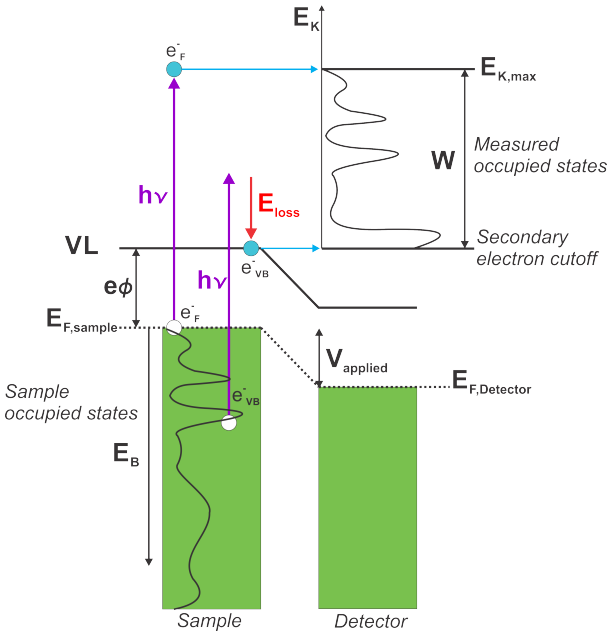

Figure B.2: Schematic energy level diagram illustrating the spectral width (W) measurement, defined by the energy separation between the highest kinetic energy electrons, E_K, max, and the secondary electron cutoff.

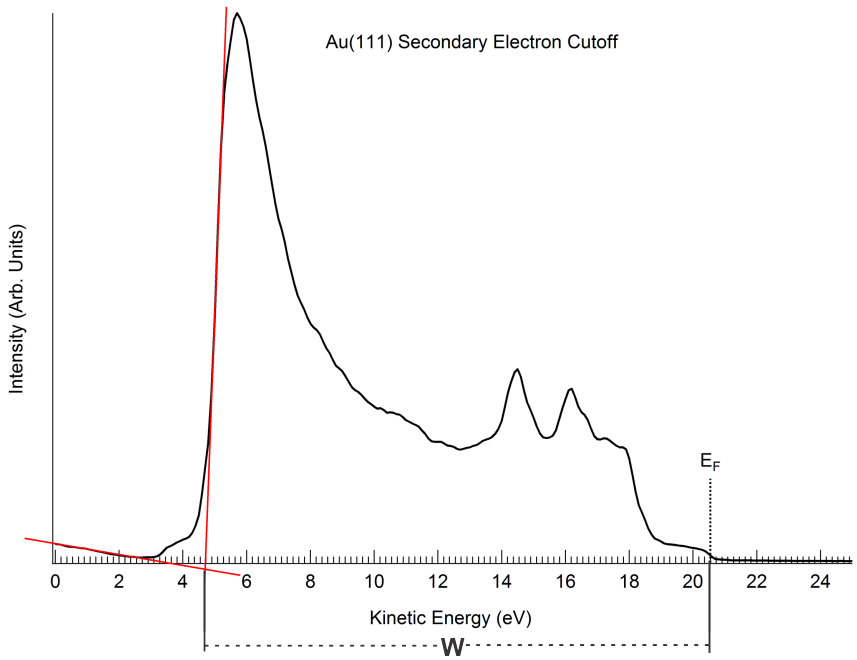

Figure B.3: HeI (21.2 eV) UPS spectrum of Au(111) showing the secondary electron cutoff on the far left. The sample was biased -5V in order to obtain this spectrum. The Fermi energy of the gold sample is located at around 20.6 eV, as indicated by the dotted vertical line. The spectrum width, W, defines the energy separation between the SECO and the highest kinetic energy electrons detected, in this case at the Fermi energy, E_F.

B.3 UPS Molecular States: Subtracting the Substrate Signal

In the thesis are presented UPS spectra from which the substrate contribution has been subtracted in order to extract only the molecular counterpart to the UPS valence band spectra. Here details of the subtraction process are presented.

Figure B.5 contains from top to bottom: a valence band spectrum measured on a ZnTPP monolayer on Ag(111), a valence band spectrum measured on the clean Ag(111) surface and a result of the subtraction of the second spectrum from the first one. Note that the spectra have been normalized so that the Fermi level, clearly visible at 0 eV, coincides in intensity for the first and second spectra. Thus assuming that the Ag surface electronic structure is not significantly modified upon molecular adsorption (which is likely acceptable given the lack of strong chemical bond between ZnTPPs and Ag), the subtraction results should reflect the experimental molecular counterpart to the valence band. This spectrum can be directly compared to the calculated DOS corresponding to the ZnTPP molecule.

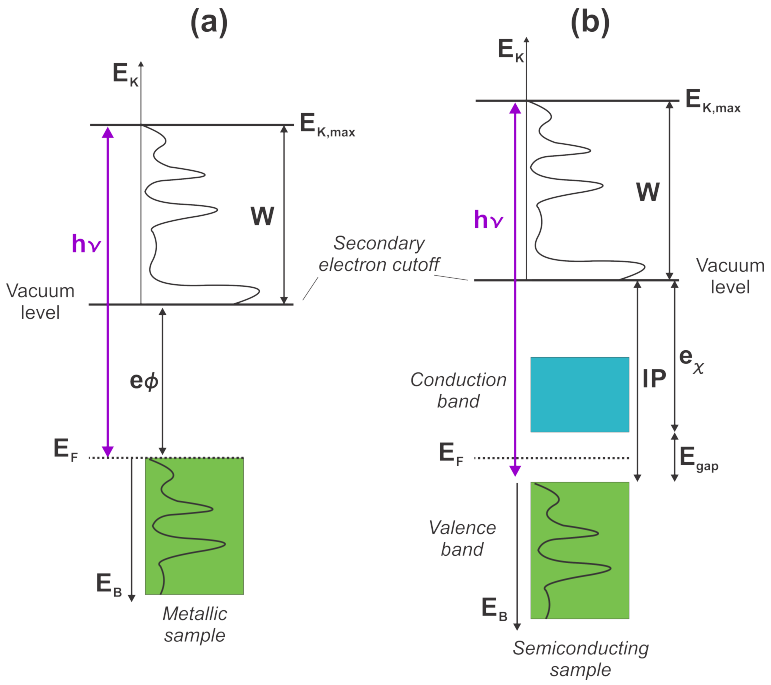

Figure B.4: Schematic energy level diagram depicting the important values in electronic energy level alignment energy diagrams for (a) metals and (b) semiconductors.

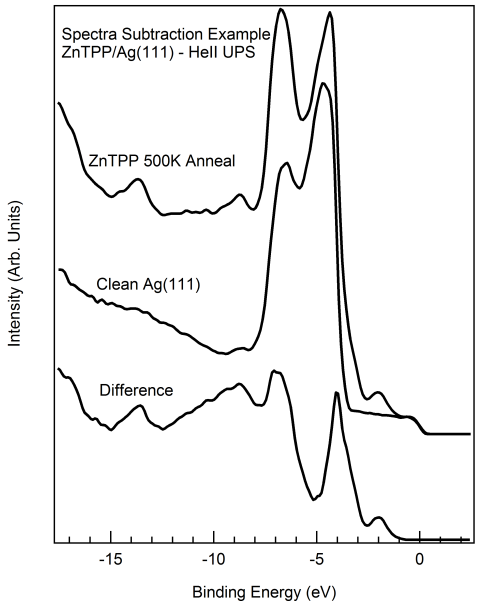

Figure B.5: Example of the subtraction scheme used to obtain the molecular contributions to the UPS HeII spectra.

Appendix C
IPS Spectrum Calibration

C.1 IPS Calibration

Recall that in inverse photoemission spectroscopy (IPS) incident electrons of known energy impinge on the sample, and a fraction of those electrons couple to the sample unoccupied states, decay to lower-lying unoccupied states, and release a photon in the process. This photon is energetically analyzed by way of a spherical diffraction grating and a two-dimensional circular detection plate. The horizontal direction is the direction of photon dispersion and thus indicates the photon energy. The detected events for a given horizontal channel are summed along the vertical channels to yield a photon spectrum. In this way, all photons impinging on the detector are detected at the same time. However, the raw spectrum observed does not directly yield the unoccupied states of the sample; we must first account for contributions from the detector system itself.

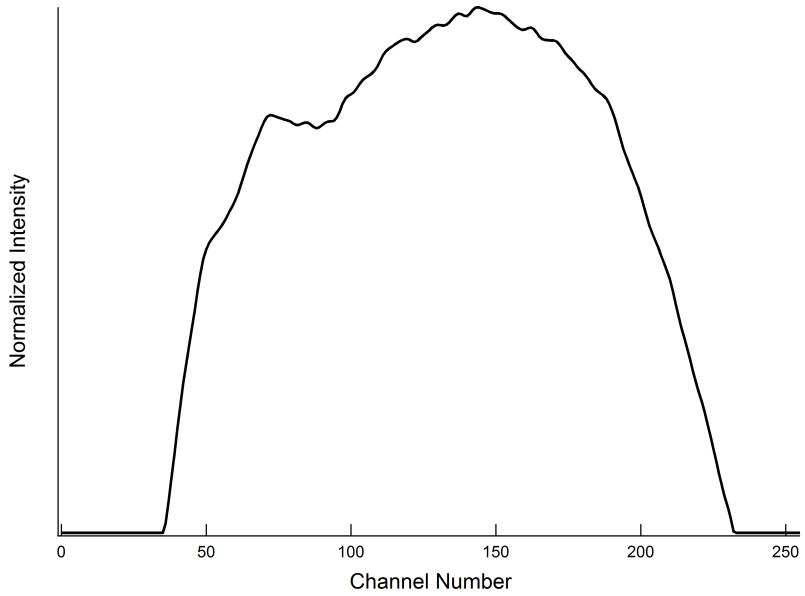

Figure C.1: IPS spectrum of Au foil normalized to the highest intensity feature.

The detector response to incident photons is not uniform across the photon dispersion direction. The detector is circular and thus there are fewer vertical channels for a given horizontal channel at

the extreme ends of the detector compared to the center, resulting in inherently decreased detection probability. Additionally, the spherical diffraction grating may have inhomogeneities that contribute false signals to the spectrum. To account for these artifacts, we create a detector function which maps the sensitivity of the detector as a function of horizontal channel number. This involves taking spectra of an Au foil sample, which has a relatively flat conduction band above the Fermi level, then normalizing the signal by dividing the spectrum by the highest intensity feature, yielding an intensity scale with a maximum value of 1. Figure C.1 shows an example of this normalized spectrum from an Au foil sample. The broad feature from 100 to 150 on the channel number scale indicates that the detector is most sensitive in this region, and provides a striking example of the importance of the detector normalization. Once the normalized detector function is obtained, all sample spectra are divided by it to eliminate the detector's contribution to the spectrum, leaving only the sample's contribution.

The sample spectrum must now be converted from a channel scale to an energy scale. The incident electron energy can be varied and in doing so the highest energy photons produced are varied, and thus the measured Fermi energy is also varied since the photons of highest energy originate from the incident electrons relaxing to the lowest unoccupied levels at the Fermi level in a metal. This is captured in the spectrum since the change in photon energy corresponds to different horizontal channels. Figure C.2 shows multiple spectra taken at varying incident electron energies illustrating how the detected Fermi level shifts due to the different photon energies produced, the Fermi level corresponding to the sloped portion of the spectra on the far left. Note that the sharp decrease in intensity at channel numbers 30 and 240 correspond to the horizontal channel limits of the detection system and are not indicative of the unoccupied states of the sample. By recording at which horizontal channel the Fermi energy is measured for a given incident electron energy (and thus photon energy), the direct relationship between photon energy and channel number is mapped. To more rigorously quantify this relationship we determine the function that relates the photon energy to the horizontal channel number by way of a best-fit curve of the Fermi level measurements as a function of channel number, and then apply this curve to all spectra.

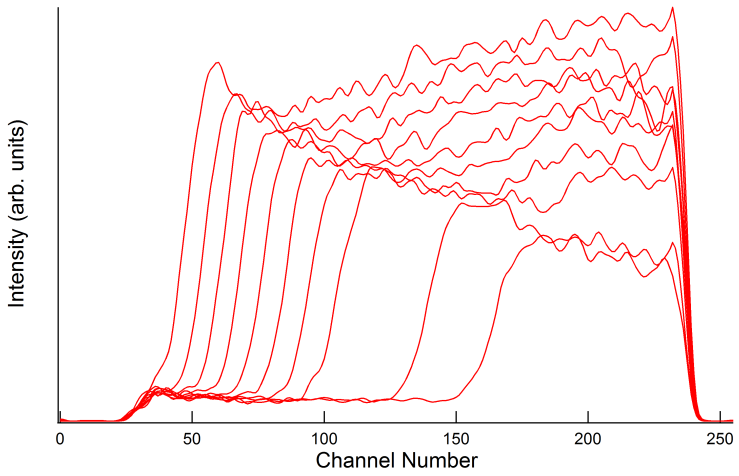

Figure C.2: Au foil IPS spectra taken at varying incident electron energies. Incident electron energies decrease from left to right from 22 eV down to 11 eV.